1-1-2021

COMPUTATIONAL MODELING OF CLIMATE ATTRIBUTES AND CONDITION DETERIORATION OF CONCRETE HIGHWAY PAVEMENTS

Salma Sultana
University of Mississippi

Recommended Citation

Sultana, Salma, "COMPUTATIONAL MODELING OF CLIMATE ATTRIBUTES AND CONDITION DETERIORATION OF CONCRETE HIGHWAY PAVEMENTS" (2021). *Electronic Theses and Dissertations*. 2138.
https://egrove.olemiss.edu/etd/2138

COMPUTATIONAL MODELING OF CLIMATE ATTRIBUTES AND CONDITION DETERIORATION OF CONCRETE HIGHWAY PAVEMENTS

A Dissertation
Presented for the Degree of
Doctor of Philosophy
Department of Civil Engineering
The University of Mississippi

by

SALMA SULTANA

August 2021

ABSTRACT

An efficient and safe road network secures the nation's economy and prosperity by providing public mobility and freight transport. Maintenance and rehabilitation of the road network cost billions of dollars annually. Road and highway infrastructures performance in any country is impacted by load repetitions and it is further compromised by climate attributes and extreme weather events. Damages to roads and bridges are among the infrastructure failures that have occurred during these extreme events. If maintenance and rehabilitation are not done promptly, the damages to the road caused by heavy traffic and extreme climate may lead to life-threatening conditions for road users. A disruption in any one system affects the performance of others. For example, damages in road and bridge infrastructure will delay the recovery operation after a disaster. In 2018, a total of 331 natural disaster occurrences were reported worldwide, which resulted in 14,385 deaths. From 1900 to 2000, in 119 years, 14,854 natural disaster occurrences were reported which caused 32,651,605 deaths. Natural disaster occurrences like hurricanes, floods, droughts, landslides, etc. may be influenced by specific climate mechanisms like El Niño and Southern Oscillation (ENSO).

Several climate attributes models were developed in this research employing Auto-Regressive Integrated Moving Average (ARIMA) methodology. The sea surface temperature data were analyzed and a prediction model was developed to predict future ENSO years. The model successfully predicted the 2018-2019 El Niño year. The model prediction showed that the next El Niño years will be 2021-22 and 2025-26. The model prediction also shows that the next La Niña year will be 2028-29. Global mean sea level (GMSL) data were analyzed and a

prediction model was developed. The predicted annual rate of change in GMSL is 0.6 mm/year from 2013 to 2050. But a higher annual rate of change (1.4 mm/year) is predicted from 2031 to 2050. Northern hemisphere (Arctic) sea ice extent and southern hemisphere (Antarctic) sea ice extent data were investigated and two different models were developed. The model prediction shows that the total loss of northern hemisphere sea ice extent in 2050 will be 1.66 million km^2. But the total gain of southern hemisphere sea ice extent will be 1.24 million km^2. The net change of global sea ice extent will be -0.24 million km^2, which indicates a loss of sea ice. The model predictions of the climate attributes can be used to understand and assess the future climate change in different climate zones worldwide. This understanding of climate changes and future predictions of climate attributes will help to develop climate adaptation strategies and better prepare the communities for extreme weather-related natural disaster occurrences.

The condition deterioration progression of infrastructures, such as roads and bridges, is caused by load repetitions, as well as climate attributes and extreme weather. Pavements undergo maintenance and rehabilitations periodically to provide a smooth riding experience to the riders. Previous researches never considered maintenance and rehabilitation action history in the development of the condition deterioration model. This research considered the maintenance and rehabilitation history in the development and implementation of pavement condition deterioration models. The development of the IRI prediction model using Artificial Neural Network (ANN) and Multiple Linear Regression (MLR) considered the Long Term Pavement Performance (LTPP) climatic region, pavement structural properties, and traffic. The developed models are more objective, incorporate important input variables that are easily available, and

are easy to implement in decision making. The concrete highway pavement IRI deterioration prediction models were developed and evaluated in this research for LTPP datasets of 1,482 for JPCP, 577 for JRCP, and 575 for CRCP. Comparatively, the AASHTO MEPDG performance equations were developed using fewer test sections.

Three performance models were developed for output variable, IRI (outside wheel path) (m/km) for Jointed Plain Concrete Pavement (JPCP), Jointed Reinforced Concrete Pavement (JRCP), and Continuously Reinforced Concrete Pavement (CRCP). The input variables are similar for all the models. An in-depth study of M&R history collected from the LTPP database for all concrete pavement produced several CN_Code. The best models were found with the CN_Code developed based on the IRI value improvement and the type of M&R action and this variable is a continuous variable where number increment indicates the frequency of M&R action provided in the pavement section.

The models' final structure and accuracy statistics can be summarized as: JPCP (13-19-1; ANN R^2 =0.94 and MLR R^2 =0.49), JRCP (11-19-1; ANN R^2 =0.95 and MLR R^2 =0.58), and CRCP (14-19-1; ANN R^2 =0.95 and MLR R^2 =0.83). The ANN models show better accuracy in predicting pavement performance compare to the multiple regression models for all types of concrete pavements. The developed IRI prediction models can successfully characterize the behavior (i.e. the increase of IRI values with time and decrease of IRI value after maintenance and rehabilitation). The ANN models can be used to provide future M&R action by changing CN_Code frequency and the model successfully distinguishes the behavior of IRI (i.e. decrease of IRI after M&R action and increase of IRI with time as CESAL increases). The developed condition deterioration models for concrete highway pavement present a significant improvement on the models currently used in the mechanistic-empirical pavement design method. It is recommended to implement the pavement condition deterioration model developed in this research for life-cycle asset management and M&R programs.

DEDICATION

This dissertation is dedicated to my family and friends who helped me and guided me through my times of stress and anxiety. In particular, my mother Halima Begum, and my brother Md. Mahade Hassan, who supported me during my study. This work would not have been possible without their support.

LIST OF ACRONYMS

AADT	Annual Average Daily Traffic
AASHTO	American Association of State Highway and Transportation Officials
ANN	Artificial Neural Network
ARIMA	Auto Regressive Integrated Moving Average
ASE	Average Squared Error
CAIT	Center for Advanced Infrastructure Technology
CBO	Congressional Budget Office
CESAL	Cumulative ESAL
CIA	Central Intelligence Agency
CN	Construction Number
CRCP	Continuously Reinforced Concrete Pavement
COV	Coefficient of variance
ENSO	El Niño and Southern Oscillation
ESAL	Equivalent Single Axle Load
FFS	Free Flow Speed
FGM	Fuzzy and Gray Models
FHWA	Federal Highway Administration
GM	Gray Model
GMSL	Global Mean Sea Level

GPS	General Pavement Study
HN	Hidden Node
IRI	International Roughness Index
IRI$_o$	Initial International Roughness Index
JPCP	Jointed Plain Concrete Pavement
JRCP	Jointed Reinforced Concrete Pavement
LCC	Life Cycle Cost
LTPP	Long Term Pavement Performance
M&R	Maintenance and Rehabilitation
MARE	Mean Absolute Relative Error
MAPE	Mean Absolute Percentage Error
MEPDG	Mechanistic-Empirical Pavement Design Guide
NCEP	National Centers for Environmental Prediction
NCHRP	National Cooperative Highway Research Program
NOAA	National Oceanic and Atmospheric Administration
NSIDC	National Snow and Ice Data Center
ONI	Oceanic Niño Index
PAM	Pavement Asset Management
PCR	Pavement Condition Rating
PDI	Pavement Distress Index
PMS	Pavement Management System

PSR	Present Serviceability Rating
PSI	Pavement Serviceability Index
PQI	Pavement Quality Index
RMSE	Root Mean Square Error
SD	Standard Deviation
SEE	Standard Error Estimate
SHRP	Strategic Highway Research Program
SLR	Sea Level Rise
SN	Structural Number
SPS	Specific Pavement Studies
SRTM	Shuttle Radar Topography Mission
SST	Sea Surface Temperature
U.S.	United States
USDOT	U.S. Department of Transportation
VMT	Vehicle Miles Traveled

ACKNOWLEDGEMENTS

First and foremost I am expressing my profound gratitude and sincere appreciation to my Ph.D. advisor Professor Dr. Waheed Uddin, the Founder Director of Center for Advanced Infrastructure Technology (CAIT), for his support, patience, motivation, enthusiasm, immense knowledge, constant encouragement, and support, and untiring help, which inspired me through all stages of the work. Dr. Uddin's compliments and encouragement were always important to me. Thank you very much, Dr. Uddin.

I would like to thank the Department of Civil Engineering; I could not have financed my studies without their assistantship. I would like to thank the members of my graduate committee: Dr. Yacoub Najjar as the committee chair, Dr. Hakan Yasarer, Dr. Hunain Alkhateb, and Dr. Tyrus Mc Carty. Thank you very much for the valuable inputs and suggestions that contributed to my dissertation.

Special thanks to Dr. Najjar and Dr. Yasarer for their support during this research and their insight and counsel. I am grateful to my colleague at CAIT, Rulian Barros for helping me when I needed it, regardless of the subject matter.

I am thankful to my family members, my mother Halima Begum and my brother Mahade Hassan, for their continuous support, love, and patience all through my doctoral study. I am also thankful to my husband, Asif Ahmed for his continuous support. I am thankful to other family members and my dear friends Umme Faria Rahim and Maisha Sadia, for their continuous support and love throughout my doctoral study.

TABLE OF CONTENTS

LIST OF TABLES

LIST OF FIGURES

CHAPTER I: INTRODUCTION

1.1 Background

An efficient and safe road network secures the nation’s economy and prosperity by providing public mobility and freight transport. One of the largest public infrastructure assets of a country is the road network. According to the Central Intelligence Agency (CIA), the world fact book [1] 223 countries worldwide reported to the agency a total of 38,800,476 kilometers of road networks for both unpaved and paved roads. According to a recent report of the U.S. Department of Transportation (USDOT), the U.S. road network exceeds 4.09 million miles in total length, which comprises approximately 2.67 million miles of paved roads and 1.41 million miles of unpaved roads, out of which around 65% of roads in every state needs maintenance [2]. Figure 1 shows the concrete pavement length in the U.S. by the state for 2019 [3]. The U.S. has a total 54, 632 miles of concrete pavement all over the country. Texas and Iowa have more than 5,000 miles of concrete pavement. According to the USDOT, about 2,988.3 billion cumulative vehicle miles traveled (VMT) was observed in 2013 [4]. These statistics show that the road infrastructure is imperative to sustain the road user’s movement and ensure a nation’s economic competitiveness. Additionally, efficient and well-maintained road networks are essential for timely response in emergencies. Timely maintenance and rehabilitation treatment is one of the important factors to ensure the road networks are in acceptable condition for the long term.

However, it is well known that the major maintenance and rehabilitation (M&R) of a road network requires huge financial support. For example, out of an average of $50 billion per year allocated by the federal government on surface transportation programs, the highway and mass transit transportation modes dominate the spending financed through the Highway Trust Fund [4].

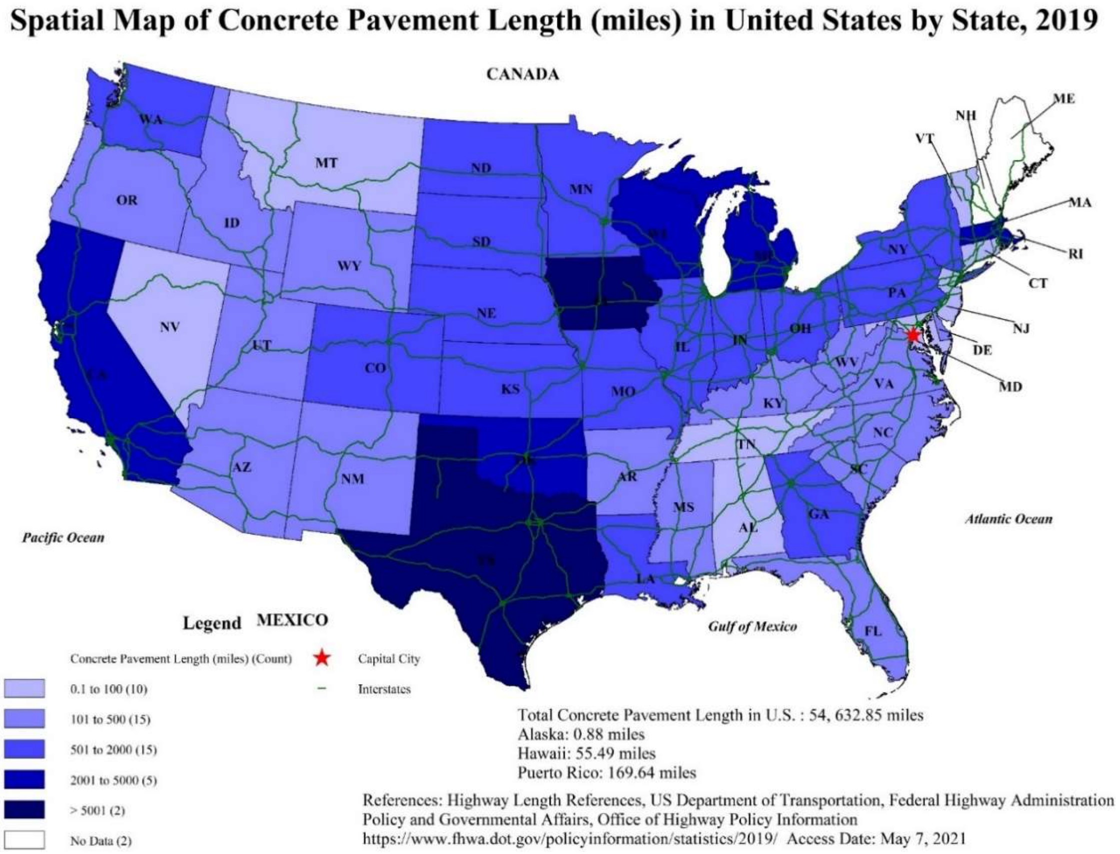
Spatial Map of Concrete Pavement Length (miles) in United States by State, 2019

Total Concrete Pavement Length in U.S. : 54, 632.85 miles
Alaska: 0.88 miles
Hawaii: 55.49 miles
Puerto Rico: 169.64 miles

References: Highway Length References, US Department of Transportation, Federal Highway Administration Policy and Governmental Affairs, Office of Highway Policy Information
https://www.fhwa.dot.gov/policyinformation/statistics/2019/ Access Date: May 7, 2021

Figure 1 Spatial Map of Concrete Pavement Length (miles) in the United States

Recently, the USDOT [5] stated that the highway part of the Highway Trust Fund encountered a shortfall as of July 31, 2015. Only $4.5 billion remained, which was close to the available cash balance level of $4 billion, since most of the funds were transferred to the states for M&R treatments of roads in poor conditions, deficient bridges, and new constructions. Therefore, most state highway agencies face slower rates of reimbursements, which result in delayed M&R actions. Over time, if the required M&R treatments are not performed, road conditions will deteriorate and affect the safety of road users. The deterioration of pavements is imposing approximately $156 billion on the U.S. economy and will continue to do so since the service life of the national, and the state highways are looming to an end. In addition, due to the economic downfall of the last decade, the state, and the local agencies are inclining towards maintaining pavement rather than rehabilitating it. In many cases, state and local agencies do not have sufficient funds to maintain all highway and road pavements. Instead, agencies need to prepare a priority M&R list in the given year and future fiscal years [2].

In 2018, a total of 331 natural disaster occurrences were reported worldwide, which resulted in 14,385 deaths. From 1900 to 2000, in 119 years, 14,854 natural disaster occurrences were reported, which caused 32,651,605 deaths [6]. The average number of weather and climate disasters in the United State from 2015 to 2019 was 14 per year. From 1980 to 2019, 40 years, the United States experienced 258 weather-related disasters, and the total cost of weather and climate-related disaster was $1.75 trillion. In those 40 years, 32 events of floods cost an average of $4.6 billion per event and 174 hurricanes (severe storm, tropical cyclone, and winter storm) cost an average of $26.6 billion per hurricane [6]. All these disasters mostly affect the coastal areas of the country. In the United States, almost 40 percent of the population lives in relatively high population-density coastal areas. Globally, eight of the world's 10 largest cities are near a coast [7]. Natural disaster occurrences like hurricanes, floods, droughts, landslides, etc. may be influenced by specific climate mechanisms like El Niño and Southern Oscillation (ENSO) in the Pacific Ocean [8]. The ENSO event has a global impact through more precipitation, landslide, sedimentation, draught, etc. The ENSO events (El Niño and La Niña) historically led to warming (El Niño) and cooling (La Niña) temperatures. The 1997-1998 El Niño episode led to warm temperatures, and the 2012 La Niña led to cooler temperatures in different parts of the world. ENSO affects extreme weather events, such as torrential rainfall, drought, or extreme snowfall. Because of the global impacts, ENSO drives extreme weather and climate variability, which greatly affect the built environment and human habitants. The extreme weather affects lifeline infrastructure such as roads and bridges. Therefore, forecasting ENSO events a few years in advance is a theme of this doctoral research.

Climate attributes such as precipitation, hot and cold temperature, and freeze-thaw cycles cause pavement distresses. Water seeps through concrete pavement joints and cracks and causes pumping erosion under the slabs. Slabs settle down due to excessive pumping [9]. Moreover, in winter, freezing temperatures cause accumulation of ice lenses in the subbase or subgrade layers and the ice lenses push pavements upward, leading to heaves or undulation of the pavements. On the other hand, in spring, ice lenses melt in the subbase or subgrade layers and make a weak subsurface leading to a downward settlement of the pavements. Freeze-thaw cycles are very detrimental to both flexible and concrete pavements since the foundation of pavements (i.e. base, subbase, and subgrade) becomes soft and unable to carry heavy vehicle loads. Furthermore, concrete pavements expand under hot summer temperatures, and if the contraction joints between two slabs are not adequately connected, then blow-up occurs, and that leads to the breakdown of slabs at the joint locations. Traffic causes edge cracks, corner breaks, and longitudinal cracks in the concrete pavements.

The combination of climate and traffic induced distresses are measured to identify the present condition of the concrete pavements. The maintenance need for pavements is decided based on the present condition. There are several performance scales available such as Present Serviceability Rating (PSR), Present Serviceability Index (PSI), and International Roughness Index (IRI) to access the current condition of the pavement [9]. IRI measures the longitudinal profile of pavement, and the measurement is expressed in a single average number in a unit of in/mile or m/km. A higher IRI number indicates a rough pavement profile and a lower number indicates a smooth pavement profile. IRI provides an overall condition of pavement surfaces due to distresses, and for this reason, IRI is the internationally recognized pavement conditioning rating system. The pavement profile is measured using high-speed vans equipped with lasers, accelerometers, and computers to measure IRI. The highly equipped vans can measure the surface profiles at traffic speeds. The onboard accelerometer gives the necessary data to the computer to calculate changes in the vertical position of the vehicle body as the vehicle moves along the pavement, the laser measures the distance between the vehicle body and the roadway surface. Collected data is stored in the computer at regular intervals. The IRI value increases due to a decrease in pavement smoothness caused by distresses, which are induced by climatic and traffic attributes [9]. Generally, an IRI rating less than 2.68 m/km is acceptable and a rating above 2.68 m/km is considered unacceptable and very poor conditioning rating [10].

1.1.1 Motivation and Goals

The motivation of the research is to: (1) enhance climate modeling, (2) develop the performance modeling to enhance concrete pavement structural design and asset management, and (3) enhance the design of concrete pavements, Numerous factors affect road conditions including heavy traffic flow, environmental effect, material degradation over time, construction quality, and interactions among all these factors. If timely maintenance and rehabilitation are not performed, road surface conditions will deteriorate and in most cases, this deterioration is indicated by the severity of surface cracks and rutting. The focus of this research is on the development of performance models for concrete highway pavements. Additionally, the research will also develop enhanced climate attributes models.

1.2 Research Objectives and Scope

The research objectives are:

1) Complete literature review of climate mechanisms and climate attribute models, and concrete highway pavement performance models.
2) Develop and verify monthly cyclic seasonal predictive models of selected climate attributes using time series data of NOAA and other sources, and make the long-term predictions.
3) Develop performance models for concrete pavement highway sections using the LTPP database and verify the model accuracy for set aside LTPP data and other in-service highway data.

4) Implement the developed performance models to enhance concrete pavement design and asset management.

The scope of this research is as follows:

- The scope of climate models is limited to sea surface temperature, sea-level rise, and sea ice extents in Polar Regions.
- The scope of performance models is limited to concrete pavements, which include Jointed Plain Concrete Pavement (JPCP), Jointed Reinforced Concrete Pavement (JRCP), and Continuously Reinforced Concrete Pavement (CRCP).

1.3 Research Methodology

The research methodology to achieve the objectives consists of the following key steps:

Task 1 Literature Review

An intensive literature review was conducted and will be extended for the following topics: (1) review climate mechanisms and enhancement of selected climate attribute models and (2) the concrete highway pavement performance models including models developed based on datasets from the LTPP database and the Mechanistic-Empirical Pavement Design Guide (MEPDG) models.

Task 2 Models of Climate Attributes

Time series data of selected climate attributes will be accessed from the data collected by NOAA and National Snow and Ice Data Center (NSIDC). Auto-Regressive Integrated Moving Average (ARIMA) modeling method will be used to develop monthly cyclic seasonal predictive models for these climate attributes. The prediction of these climate attributes will be used to assess the impacts of climate change on infrastructure and communities, as well as to develop climate adaptation plans.

Task 3 Performance Models for Concrete Pavement Condition Deterioration

The ANN and multiple regression modeling techniques will be used to develop concrete pavement performance models. The LTPP database will be used to develop the models and set-aside LTPP data will be used to verify the accuracy of the model. The construction number, CN, will be included as a categorical variable to consider maintenance & rehabilitation intervention.

Task 4 Implementation of Developed Models to Enhance Asset Management

The developed climate models along with pavement performance models will be implemented to enhance concrete pavement structural design and asset management.

The research methodology flow chart in Figure 2 shows the milestones of the research topics and their interactions.

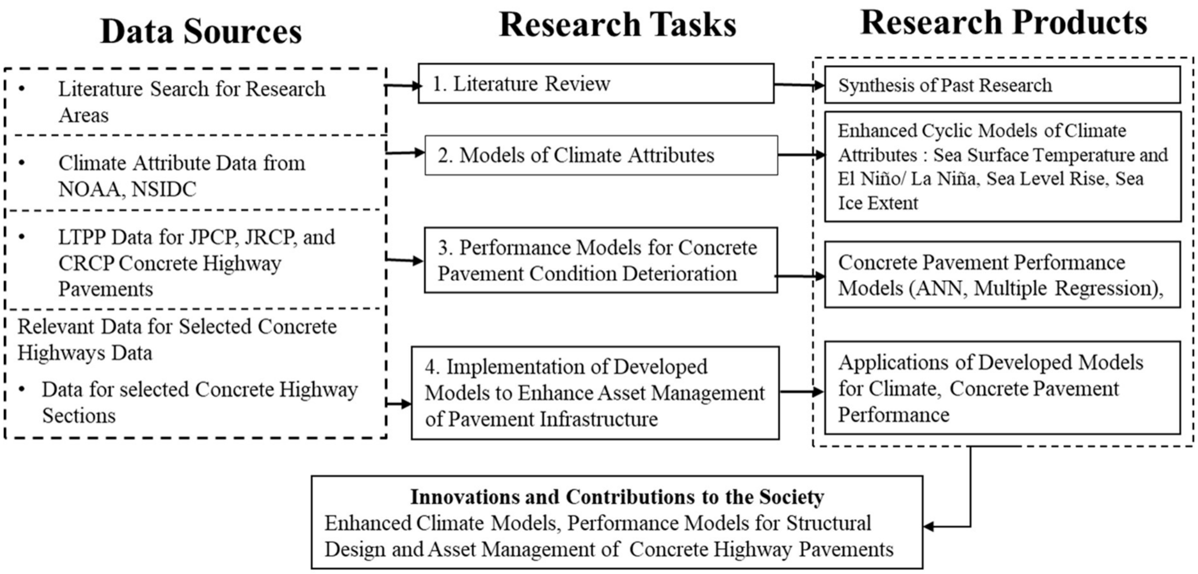

Figure 2 Research Methodology Flowchart

1.4 Synthesis of Literature Review

The ENSO events may touch the lives of more than a billion people around the globe. Their impacts can be devastating, as illustrated by some of the effects of the unusually strong El Niño of 1982–1983: (a) drought and wildfires in many nations of the western and southwestern Pacific Rim, southern Africa, southern India, Spain, Portugal, northern Africa, and South and Central America, (b) severe cyclones that damaged island communities in the Pacific, (c) flooding over wide areas of South America, Western Europe, the Gulf Coast, and some Caribbean islands, and (d) severe storms in the western and northeastern United States [11]. Furthermore, El Niño has been associated with greater landslide occurrence around the world [12]. Currently, the National Oceanic and Atmospheric Administration (NOAA)'s ENSO predictions methodology relies on sea surface temperature data for ENSO prediction a few months ahead only. This doctoral research will enhance ENSO predictions several years in advance. This will be helpful to predict climate changes in climate zones worldwide and implement climate adaptation plans.

Several IRI models were reviewed, which were developed using Artificial Neural Network (ANN) and multiple regression modeling techniques [13-18]. A synthesis of IRI prediction models for concrete highway pavement is shown in Table 1. The Long Term Pavement Performance (LTPP) database was used to develop these models.

Table 1 Summary of IRI Prediction Models using LTPP Data for Concrete Pavement

Ref.	Model Structure	Goodness of fit	Data Points
[13]	$IRI = F\left\{\begin{matrix} Joint\ Faulting, Transverse\ Cracking, \\ and\ Joint\ Spalling \end{matrix}\right\}$	$R^2 = 0.61$	Not Known
[14]	$IRI = F\{Transverse\ Joint\ Faulting\}$	$R^2 = 0.50$	Not Known
NCHRP 1-37 [15]	$IRI = F\left\{\begin{matrix} Initial\ IRI, Joint\ Faulting, Transverse\ Crackin \\ Joint\ Spalling, Patching, Age, Freezing\ Index \\ and\ subgrade\ material \\ passing\ 0.075\ mm\ sieve \end{matrix}\right.$	$R^2 = 0.60$	188
[16]	$IRI = F\left\{\begin{matrix} Initial\ IRI, Joint\ Faulting, Transverse\ Crackin \\ Joint\ Spalling, Patching, Age, Precipitation, \\ and\ Freezing\ Index \end{matrix}\right.$	$R^2 = 0.81$	327
[17]	8 inputs of independent variables, 2 hidden layers (24 and 12 hidden nodes), and 1 output (8-24-12-1)	$R^2 = 0.83$	188
[18]	7 inputs of independent variables, 1 hidden layer (10 hidden nodes), and 1 output (7-10-1)	$R^2 = 0.84$	264

The synthesis of the literature of IRI prediction models established that all the independent variables need to be estimated before making the prediction, which is not easy and can be expensive for federal and state highway agencies.

1.5 Research Needs

The ENSO events affect climate and extreme weather, including more frequency of precipitation, drought or, extreme snowfall. Because of the global impacts of ocean currents, ENSO causes extreme weather and climate variability, which has the greatest impact on the built environment and communities. The summary of the literature review revealed that the prediction of ENSO episodes several years in advance would be helpful to predict climate change worldwide and improve climate adaptation plans. The previous literature review and discussion show that it is imperative to maintain acceptable road conditions over time. This goal is possible if the enhanced prediction models for pavement condition deterioration are used for pavement structural design and asset management. The current literature review indicates that the M&R history was not considered in the concrete pavement condition deterioration progression modeling. In the LTPP database, the M&R sequence is denoted by the construction number (CN). Recently, enhanced performance models for asphalt highway pavements were developed using the CN categorical variable included in the LTPP database [19]. Therefore, this research will consider CN for developing performance models of concrete pavements. The independent variables, used in the previous discussion (Table 1) are mostly distress, age, and environmental data. However, for future prediction of IRI, these distresses need to be predicted as well. The performance models developed in this research will predict the IRI values without using distress data that will help the local and state agencies to prepare M&R programs and budgets without estimating distresses in future years. The only variable that will need to be predicted is traffic and the agency can use the historical traffic data for a particular pavement and project the future traffic data based on the annual traffic growth rate for the highway.

1.6 Research Significance

The following statements describe the significance of the research carried out in this dissertation:

- Synthesis of the past research contains climate models and concrete pavement performance models.
- Enhanced computational models were developed for cyclic climate attributes (sea surface temperature and ENSO episodes, sea-level rise, and sea ice extent). The prediction of the climate attribute models can be used to understand future climate change in climatic zones worldwide. The predicted ENSO episodes can contribute to better predict extreme weather and climate. This understanding of climate mechanisms and future prediction of climate changes will lead to better prepare the communities, harden the critical infrastructure, and enhance disaster resilience management.
- The LTPP database contains the most comprehensive information on road conditions for more than 2000 test sections throughout the U.S. Several prediction equations for pavement distress in the MEPDG were developed based on the LTPP data that has M&R histories. However, the mechanistic-empirical pavement design equations do not consider M&R history. The performance models for concrete pavements using the LTPP database will be for JPCP, JRCP, and CRCP. The performance models will contain cumulative traffic and construction numbers for maintenance and rehabilitation intervention, as an independent variable.

CHAPTER II: REVIEW AND ENHANCEMENT OF MODELS OF CLIMATE ATTRIBUTES

2.1 Introduction

Weather is described in short-term variability of air temperature, precipitation, humidity, cloudiness, air pressure, wind speed, and wind direction. Weather is defined locally. On the other hand, climate describes the “long-term” pattern of weather conditions for specific climate zones. There is no single global climate. The expression “long-term” usually means 30 years or more [20] described climate.

The following attributes affect a region’s climate: (1) latitude, (2) elevation, (3) proximity to oceans and other large water bodies, mountains, or other surface features, (4) ocean current circulation patterns, (5) atmospheric circulation, (6) solar radiation, and, (7) cloud cover. These attributes contribute to climate mechanisms, which control the variations of air temperatures, and the amount of rainfall and/or snowfall received in each region throughout the year. These climate and weather patterns influence the regional biodiversity (forest, vegetation, agriculture, wild animals) and human habitants.

Preliminary statistical inference analysis shows that climate attributes such as monthly global air temperature fails the Normality test and data independence test (shown by high autocorrelation). Therefore, the traditional regression modeling is invalid for this climate attributes. In this study, the ARIMA modeling method has been used to develop prediction models for several climate attributes.

2.2 ARIMA Time Series Modeling

2.2.1 ARIMA Methodology

The Box-Jenkins ARIMA modeling method [22] is the preferred methodology if the time series data shows high autocorrelation. The ARIMA seasonal autoregressive model (p, d, 0) (P, D, 0) can be represented by the following Equation [21, 22]:

$$\nabla^{d}.\nabla_{s}^{D}.\,Y_t = C + (1-\phi_1 B-\phi_2 B^2\ldots-\phi_p B^p)\,(1-\phi_1 B^s-\phi_2\,B^{2s}\ldots-\phi_P B^{Ps}).\,a_t \qquad \text{Eq.1}$$

where,

Y_t = Time series data (dependent or response variable)

∇^{d} = Regular differencing operator of order d

∇_{s}^{D} = Seasonal differencing operator of order D

C = Constant

s = Seasonal length

B = Backward shift operator

$(1-\phi_1 B-\phi_2 B^2\ldots-\phi_p B^p)$ = Regular autoregressive process of order p

$(1-\phi_1 B^s-\phi_2\,B^{2s}\ldots-\phi_P B^{Ps})$ = Seasonal autoregressive process of order P

a_t = Random shock term; normally distributed, independent with zero mean, and variance equal to σ_a

Appendix A presents detailed steps involved in the ARIMA modeling of time series data.

2.2.2 ARIMA Modeling of Natural Disaster Occurrences

This section presents an example of ARIMA modeling for time series data of annual natural disaster occurrences. This time series fails the normality test and independence test (high autocorrelation 0.92 at Lag-1). Natural disaster occurrences like the hurricane, flood, drought, landslide, etc. depend on different climate mechanism such as ENSO events. In 2018, a total of 331 natural disaster occurrences were reported worldwide, which resulted in 14,385 deaths. From 1900 to 2000, in 119 years, a total of 14,854 natural disaster occurrences were reported which caused 32,651,605 deaths [6]. The extent of loss of lives and damages to property by natural disasters largely depends on the built environment. Figure 3 displays worldwide occurrences of natural disasters from the years 1900 to 2018 [6]. An annual mean of 124 natural disasters is calculated for these 119 years.

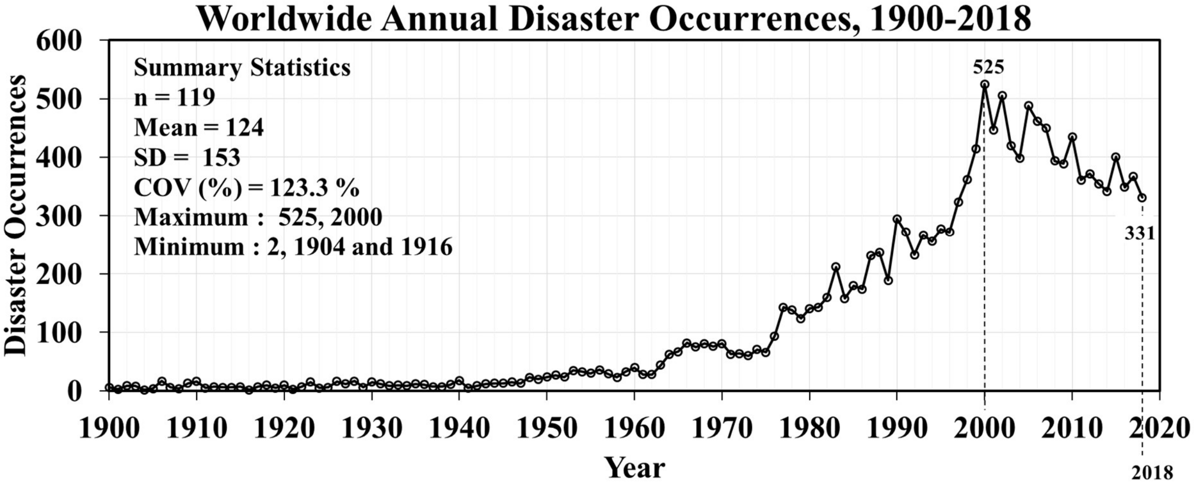

Figure 3 Worldwide Disaster Occurrences, 1900-2018

2.2.2.1 Chi-Square Test of Goodness of Fit to a Normal Distribution

For the Chi-square test, the number of observations has to be 50 or more. In this case, the number of data years is 119.

Null hypothesis, H_0: The population distribution of the worldwide natural disaster occurrences data is normal.

Alternative hypothesis, H_A: The population distribution of the worldwide natural disaster occurrences data is not normal.

Table 2 summarizes the chi-square test results. The observed frequency and expected frequency must be 5 or more.

Table 2 Computation of Chi-square for a Test of Goodness of Fit to a Normal Distribution

	Observed Frequency	Observed Frequency	Normal Dist.	Normal Dist.	Expected Frequency			
Frequency Range	fo	Percentage	z score	Probability	fe*	fo-fe	$(fo-fe)^2$	$(fo-fe)^2/fe$
< 10	30	26%	< -0.7	0.227	26.3	3.714	13.797	0.525
10-100	47	41%	-0.7 to -0.1	0.214	24.8	22.199	492.805	19.871
100-300	20	17%	-0.1 to 1.2	0.454	52.7	-32.664	1066.937	20.259
> 300	19	16%	> 1.2	0.106	12.2	6.8	45.568	3.72
Sum	116	100%		1.000	116			44.375

*fe = Normal dist. Probability * Sum of Observations = 0.227*116 = 26.3

From Table 2, the row number is r = 4. So, df = r-1 = 4-1 = 3

$X^2_{(3, 0.05)}$ critical = 7.81

X^2 test = 44.37

X^2 test (44.37) > X^2 critical (7.81)

Therefore, the null hypothesis is rejected. The data is not normally distributed. Figure 4 shows the observed frequency and expected frequency for the test data.

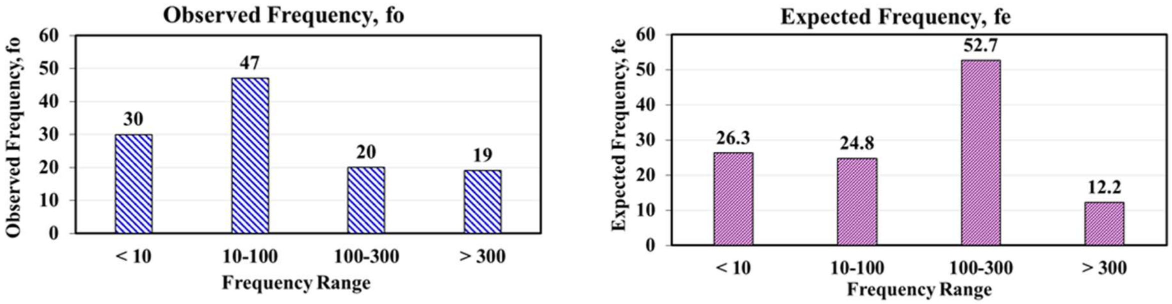

Figure 4 Observed Frequency and Expected Frequency

2.2.2.2 Kolmogorov-Smirnov and Shapiro-Wilk Normality Tests

Kolmogorov-Smirnov is a nonparametric test that is used to test the normality of the data. Shapiro-Wilk test is also used to test the normality of the data. These two Normality tests are generally used for less than 50 datasets. However, for illustration, the results of both Normality tests are conducted using the Statistical Package for the Social Sciences (SPSS) software [23]. For both Kolmogorov-Smirnov and Shapiro-Wilk normality tests the hypotheses are, as follows (for $\alpha = 0.05$):

Null hypothesis, H_0: The distribution of the data is normal

Alternative hypothesis, H_A: The distribution of the data is not normal

Table 3 shows, in the case of worldwide natural disaster occurrences data from 1900 to 2015, the probability of significance, p-value is less than the α level 0.05 probability of chance error. The results are statistically significant for both Kolmogorov-Smirnov and Shapiro-Wilk normality tests. Therefore, the null hypothesis is rejected. The data is not normally distributed.

Table 3 Kolmogorov-Smirnov and Shapiro-Wilk Normality Tests

Tests of Normality

	Kolmogorov-Smirnov[a]			Shapiro-Wilk		
	Statistic	df	Sig.	Statistic	df	Sig.
Occurrence	.254	116	.000	.755	116	.000
a. Lilliefors Significance Correction						

To further examine the data for normality the recommended graphical representations are histograms with the normal curve, normal Q-Q plots, and boxplots.

Next, the SPSS option of the histogram with the normality curve was used for the data. Figure 5 shows that the histogram shape does not approximate a perfect bell curve. Therefore, it confirms that the data is not normally distributed, as shown by the normality tests. The Q-Q plot in Figure 6 shows that the data does not fit the reference distribution (line of equality for observed and expected normal values). The points are not lying in tight random scatter around the reference line, which again indicates that the data is not normally distributed.

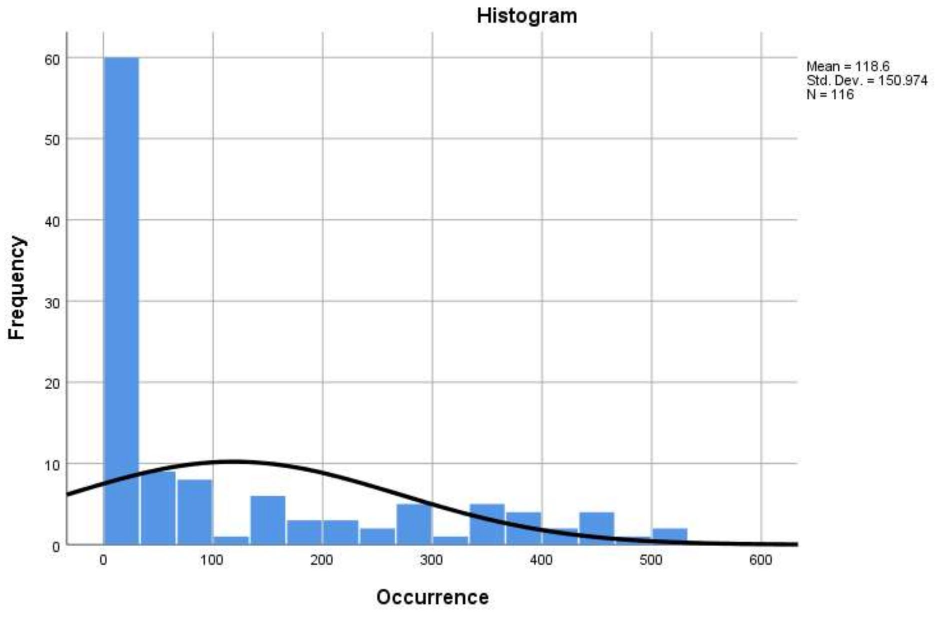

Figure 5 Histogram with Bell-Shaped Curve

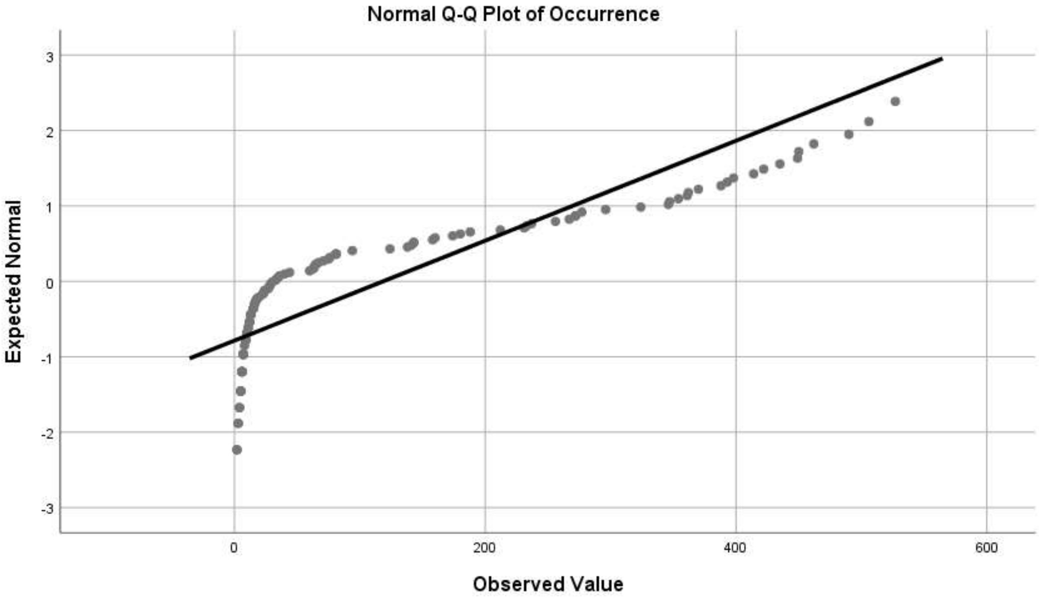

Figure 6 Q-Q Plot

Figure 7 shows the box plot, which is not symmetric to the median line in approximately the center of the box. Therefore, it further indicates that the data is not normally distributed.

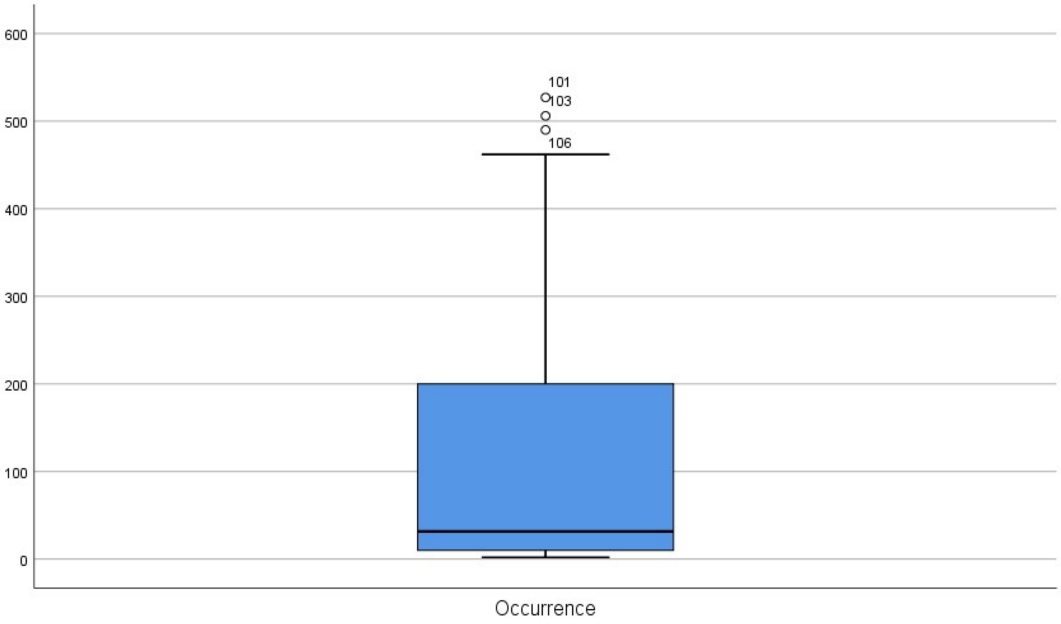

Figure 7 Box Plot

The normality test has been conducted using three different tests, the Chi-square test, Kolmogorov-Smirnov test, and the Shapiro-Wilk test. It is evident from all three tests that the data is not normally distributed. The data also shows a high autocorrelation value of 0.92 at Lag-1, which implies that the data is not independent. Therefore, the regression method is not valid. This time-series data can be modeled using the ARIMA modeling method. The following section shows the procedures of modeling the time-series natural disaster data from 1900 to 2015 and the verification of the model using the data from 2016 to 2018.

2.2.2.3 ARIMA Modeling of Worldwide Disaster Data

The ARIMA model terms were identified using the step-by-step procedure described in Appendix A. The Auto-Correlation Function (ACF) and Partial Auto-Correlation Function (PACF) plots of the original time series are shown in Figure 8 and Figure 9, respectively.

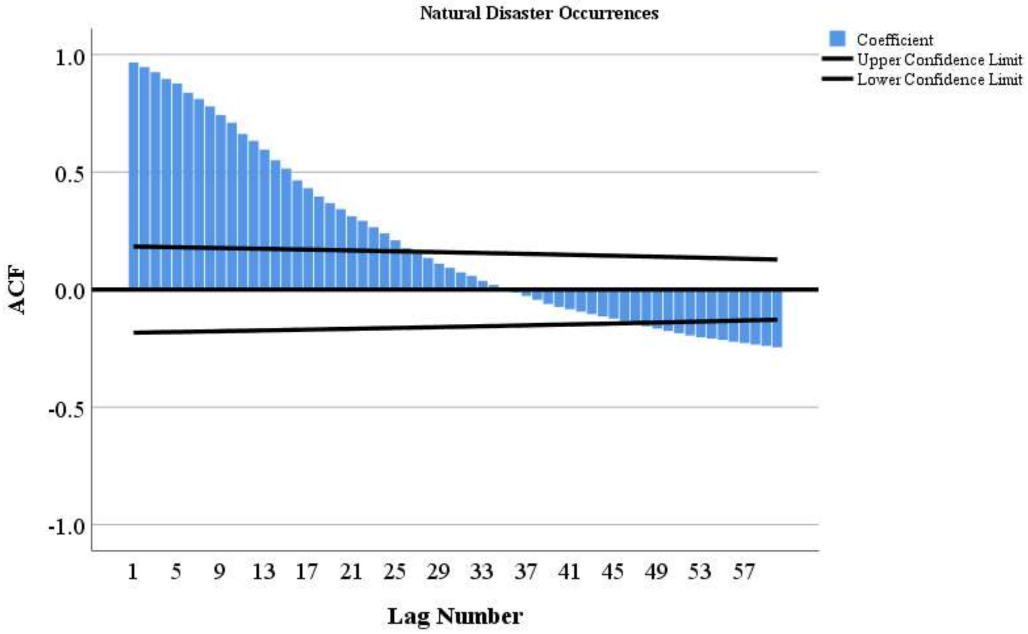

Figure 8 ACF Plot World Disaster Occurrences

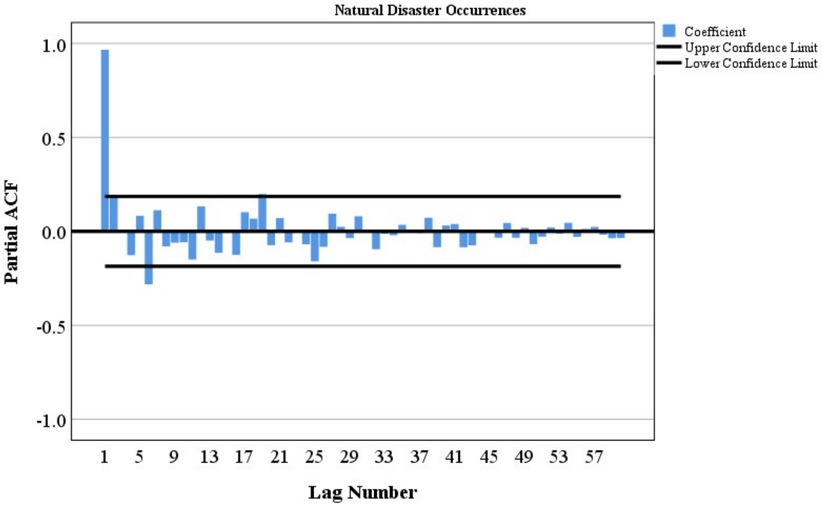

Figure 9 PACF Plot World Disaster Occurrences

Figure 10 shows the differencing order-1 plot for the original time series. The correlation R-value for the differencing order time series and the original time series is 0.035, which is less than 0.2. According to Appendix A, differencing order-1 (d = 1) should be used to make the series stationary. However, Figure 10 shows two distinctive patterns and R-value for two different periods, from 1900 to 1980 (R = -0.09) and from 1981 to 2015 (R = 0.31). Hence, both d=0 and d=1 terms were used to develop the ARIMA model.

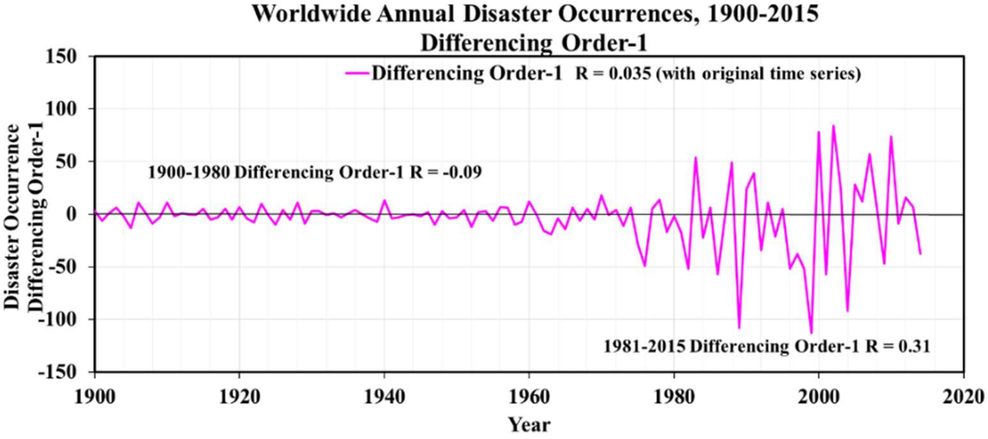

Figure 10 Differencing Order-1 Plot World Disaster Occurrences

Model diagnostics for selecting model terms were based on ACF and PACF plots (Figures 8 and 9) of the original time series. The first ARIMA model (1,1,0) was tried (Figures 11 and 12).

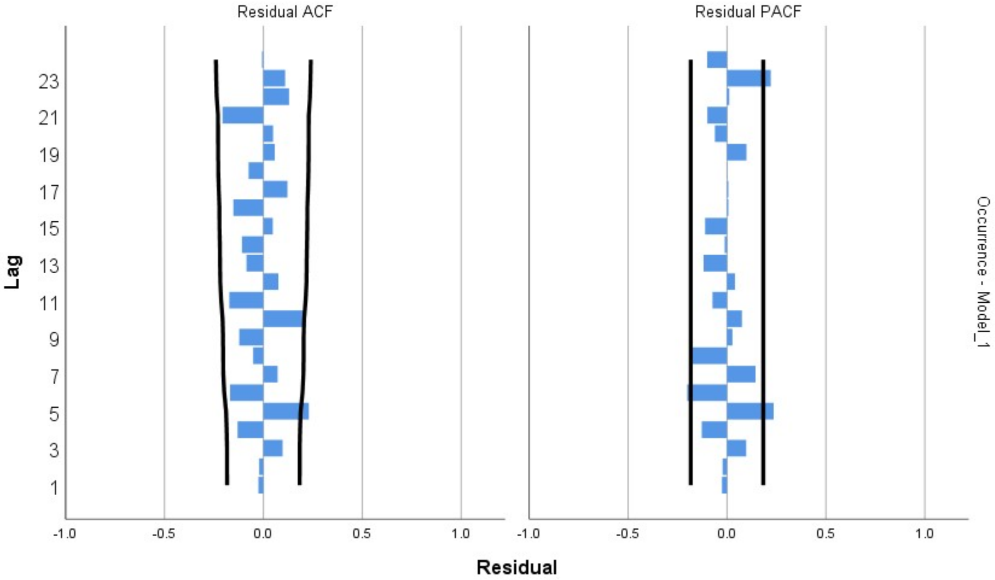

Figure 11 Residual ACF and Residual PACF plot of ARIMA Model (1,1,0)

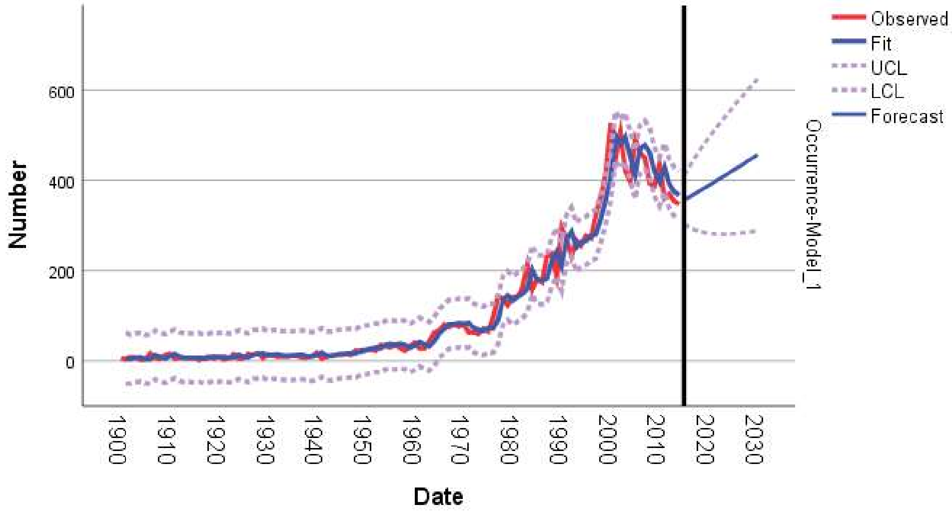

Figure 12 ARIMA Model (1,1,0) Prediction of Worldwide Disaster Occurrences from 2016 to 2030

The residual ACF and PACF (Figure 11) and future prediction pattern (Figure 12) plots indicate the need to improve the prediction pattern in the (1,1,0) model. Subsequently, eight more models were tried using differencing order-1 (d=1) in the model terms. The prediction patterns of the models were not consistent with the pattern of the historic time series. Therefore, more models were tried using without differencing (d = 0) in the model terms, and the residual ACF and PACF plots were examined. Two more ARIMA models with moving average (q) terms (1,0,24) and (1,0,60) were tried without success. The last ARIMA model (1,0,34) trial turned out to be the best model as shown by the residual ACF and PACF plots (Figure 13) and prediction pattern (Figure 14). This ARIMA model included moving average term 34, which was interpreted from Figure 3 that shows the pattern of historic data changes in approximately 34 years.

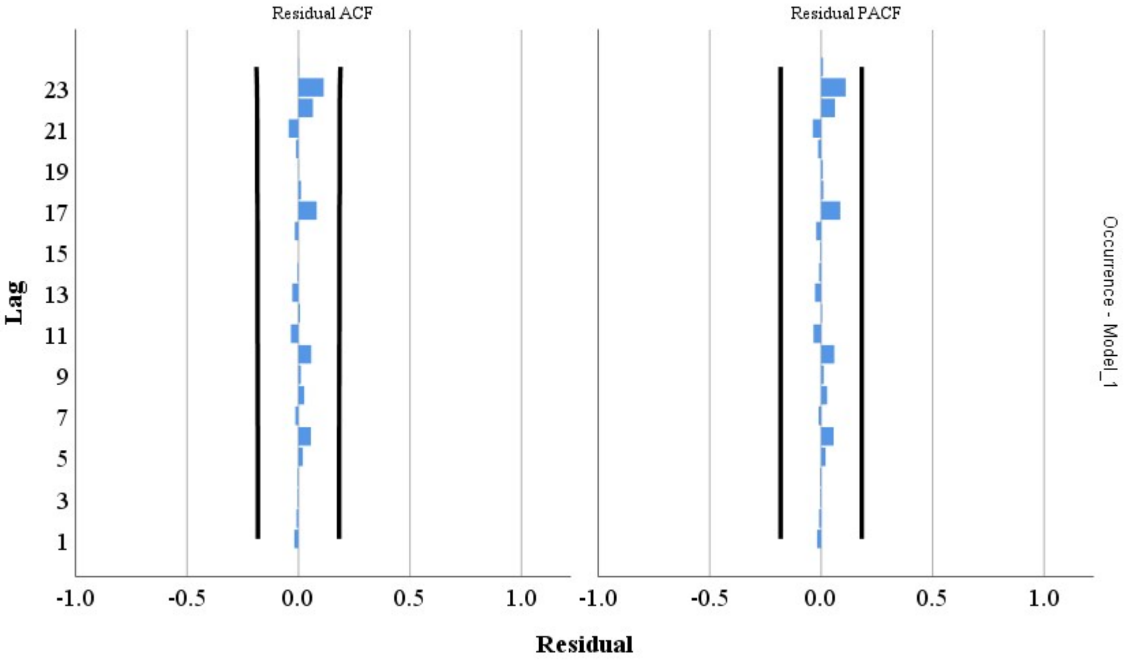

Figure 13 Residual ACF and Residual PACF plot of ARIMA Model (1,0,34)

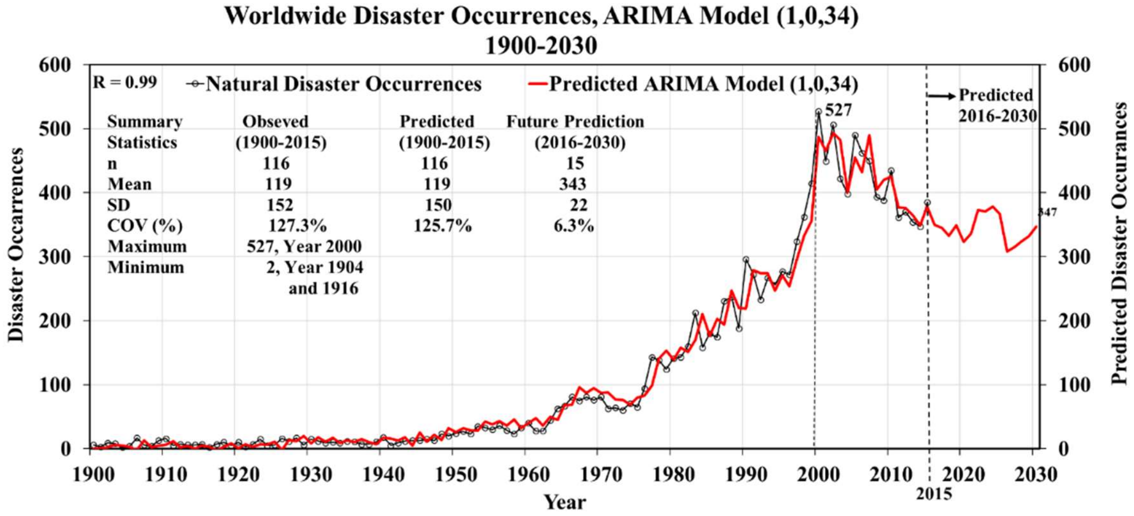

Figure 14 Worldwide Disaster Occurrences from 1900 to 2015 and ARIMA Model (1,0,34) Prediction from 1900 to 2030

The observed vs. predicted worldwide disaster occurrences from 1900 to 2015 using the ARIMA model (1,0,34) are shown in Figure 15 with a high correlation 0.99 R-value.

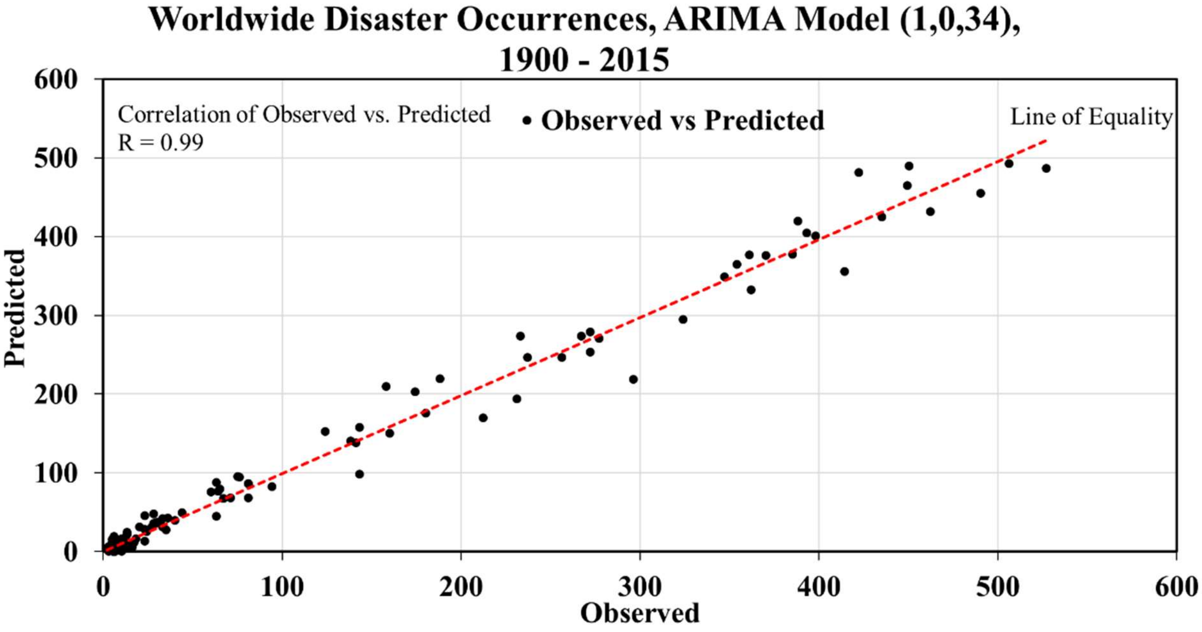

Figure 15 Observed vs. Predicted plot of Worldwide Disaster Occurrences using ARIMA Model (1,0,34)

Table 4 shows the verification for the year 2016 to 2018 using ARIMA Models' prediction. Based on the mean difference, Root Mean Square Error (RMSE), Mean Absolute Relative Error (MARE), and future prediction pattern, the best model is (1,0,34).

Table 4 Verification of ARIMA Models using 2016-2018 Measured Data

Worldwide Disaster Occurrence, 1900-2030					
			$R^2 = 0.99$	R = 0.99	R = 0.99
Number	Year	Measured	Predicted ARIMA Model (1,0,34)	Predicted ARIMA Model (1,0,24)	Predicted ARIMA Model (1,0,60)
117	2016	324	350	369	354
118	2017	335	345	372	389
119	2018	331	333	357	359
120	2019		*349*	*379*	*388*
121	2020		*323*	*380*	*399*
122	2021		*336*	*390*	*406*
123	2022		*373*	*413*	*452*
124	2023		*371*	*398*	*445*
125	2024		*378*	*413*	*465*
126	2025		*367*	*398*	*437*
127	2026		*308*	*337*	*356*
2016-2018	n	3	3	3	3
	Mean	330	343	366	367
	SD	5.57	8.74	7.94	18.93
	COV (%)	1.7%	2.55%	2.17%	5.15%
	Mean Difference		3.8%	10.9%	11.3%
	RMSE		16.12	36.83	39.16
	MARE (%)		3.9%	10.9%	11.3%
			Best Model		

The following results are summarized for the best model (1,0,34).

- the % mean difference in worldwide disaster occurrence: +3.8%
- RMSE: 16.12
- MARE: 3.9%

Equation 2 shows the terms of ARIMA (1,0,34) model.

$$Y_t = C + (1 - \phi_1 B) * (1 - \theta_1 B^1 - \theta_2 B^2 - \ldots\ldots\ldots\ldots\ldots\ldots.. - \theta_{34} B^{34}) * a_t \qquad Eq.2$$

where,

Y_t = Discrete time series

C = Constant

$1 - \phi_1 B$ = Regular Autoregressive process of order one

$1 - \theta_1 B^1 - \theta_2 B^2$ = Regular Moving Average process of order 34

a_t = random shock term; normally distributed, independent with zero mean, and variance equal to σ_a

From the verification results (Figure 15 and Table 4), it is evident that the ARIMA modeling method can be used successfully to predict highly autocorrelated time series data, such as climate attributes.

2.3 Climate Attribute Models

Several climate attributes influence the climate mechanisms which are used to characterize climate zones worldwide. The climate attributes are mostly cyclic data either monthly or annual. The time series data of climate attributes show high autocorrelation values, which indicate that the data are not independent of each other. Therefore, the time series data of climate attributes can be modeled using the ARIMA modeling method. The ARIMA model can be used for long-term future predictions, depending on the variability and pattern of the attributes. The predictions of these climate attributes can lead to assess the climate change mechanisms and used to make climate adaptation decisions accordingly. This research will model some selected climate attributes related to prominent climate mechanisms, such as sea surface temperature (related to ENSO), global mean sea level (related to sea-level change), and sea ice extents (in northern and southern polar regions). The data were accessed from NOAA and NSIDC [24, 25]. The following sections discuss the distinctive features to understand the predictive modeling of these climate attributes.

2.4 Sea Surface Temperature

2.4.1 El Niño-Southern Oscillation (ENSO)

El Niño and La Niña occur in the equatorial Pacific Ocean. These events are characterized by NOAA a five consecutive 3-month running mean of sea surface temperature (SST) anomalies [8] in the Niño 3.4 region (Figure 16) that is above or below the threshold of 0.5°C. This standard of measure is known as the Oceanic Niño Index (ONI) [8].

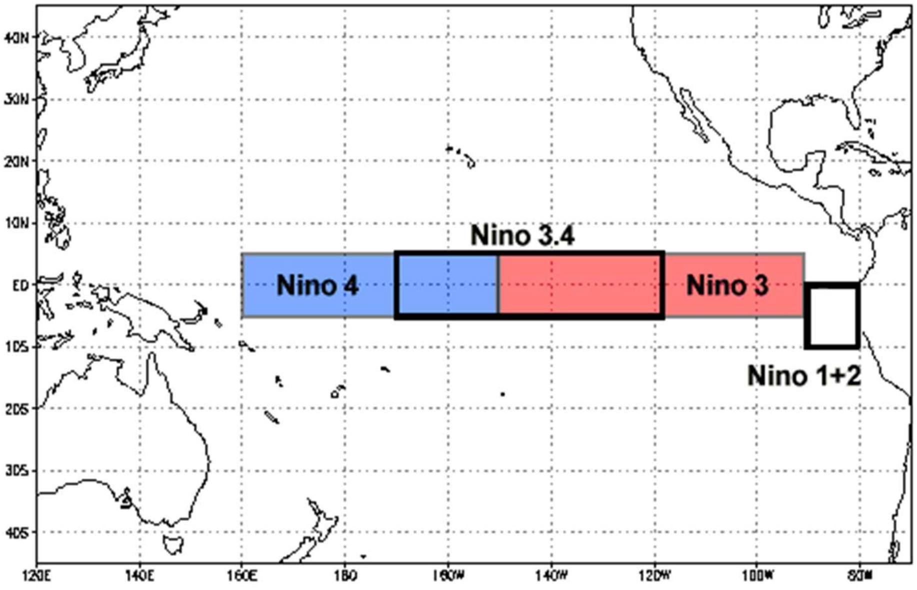

Figure 16 Niño 3.4 Region [8]

Historically, scientists have classified the intensity of El Niño based on SST anomalies exceeding a pre-selected threshold in a certain region of the equatorial Pacific. The most commonly used region is that the Niño 3.4 region and the most commonly used threshold is a positive SST departure from normal greater than or equal to +0.5°C. Since this region encompasses the western half of the equatorial cold tongue region, it provides a good measure of important changes in SST and SST gradients that result in changes in the pattern of deep tropical convection and atmospheric circulation. The criteria, that is often used to classify El Niño episodes, is that five consecutive 3-month running mean SST anomalies exceed the threshold [8].

Because of the strong interactions between oceanic and atmospheric changes, the Southern Oscillation and the El Niño mechanism are strongly coupled. This has led to the selection of the acronym ENSO to refer to the entire process. The ENSO climatic mechanism has been widely stated around the world because of its impact on the economies and activities, such as agriculture and fishing of developing countries. ENSO is a recurring climate pattern involving changes in the temperature of waters in the central and eastern tropical Pacific Ocean. On periods starting from about three to seven years, the surface waters across an oversized swath of the tropical Pacific Ocean warm or cool by anywhere from 1°C to 3°C, compared to normal. This oscillating warming and cooling pattern denoted as the ENSO cycle directly affects rainfall distribution in the tropics and can have a powerful influence on weather across the United States and other parts of the globe. El Niño and La Niña are the acute phases of the ENSO cycle; between these two phases is a third phase called ENSO-neutral. The phases are described below:

El Niño: A warming of the ocean surface, or above-average SST, in the central and eastern tropical Pacific Ocean. Over Indonesia, rainfall tends to reduce while rainfall increases over the central and eastern tropical Pacific Ocean. In general, the warmer the ocean temperature anomalies, the stronger the El Niño [26].

La Niña: A cooling of the ocean surface, or below-average SST, in the central and eastern tropical Pacific Ocean. Over Indonesia, rainfall tends to increase while rainfall decreases over the central and eastern tropical Pacific Ocean. The normal easterly winds along the equator become even stronger. In general, the cooler the ocean temperature anomalies, the stronger the La Niña [26].

Neutral: Neither El Niño or La Niña. Often tropical Pacific SSTs are generally close to average. However, there are some instances when the ocean can look like it is in an El Niño or La Niña state, but the atmosphere is not playing along [26].

2.4.2 Review of Sensor Used for SST Measurements

Before 1997, SSTs were only available globally from IR satellite retrievals [27]. With the launch of the Tropical Rainfall Measuring Mission (TRMM) satellite, which includes TRMM Microwave Imager (TMI), microwave retrievals became possible [28]. Though IR SSTs have a higher resolution than microwave SSTs (1- 4 km for IR as compared to 25 km for microwave), the IR retrieval is prevented by clouds [27]. Microwave SSTs get improved coverage as SST can be measured through clouds [27]. This has proven especially important in tropical cyclone forecasting as the clouds surrounding a cyclone prevented adequate SST [27].

The vertically polarized microwave brightness temperature of ocean areas has an appreciable sensitivity to SST at frequencies between 4 and 11 GHz [27]. “In addition to SST, brightness temperature depends on the sea-surface roughness, the atmospheric temperature, and moisture profile” [27]. The spectral and polarimetric signatures of the surface-roughness and the atmosphere are quite distinct from the SST signature [27]. The influence of these effects can be removed by taking simultaneous measurements at multiple frequencies and polarizations [27]. The microwave instruments TMI, AMSR-E, AMSR2, WindSat, and GMI all measure multiple frequencies that are more than sufficient to remove the surface-roughness and atmospheric effects [27]. Technical specifications of microwave instruments used for sea surface temperature measurements are shown in Table 5.

Table 5 Comparison of Microwave Instruments Used for Measuring SST

Ref.	Satellite	Microwave Instrument Name	Owner	Resolution		Swath width (km)	Footprint (km × km)	Year Launched
				Spectral (bands)	Temporal (days)			
[29]	Global Precipitation Measurement (GPM)	GMI	JAXA and NASA	8	-	931	32×19,18×11,16×10,15×9,7×4,6×4	2014
[30]	GCOM-W1	AMSR2	NASA	7	0.5	1450	62×35,42×24,22×14,19×11,12×7,5×3	2012
[31]	WindSAT	WindSAT	Naval Research Laboratory (NRL), Naval Center for Space Technology, U.S. Navy, and NPOESS	5	0.5	1025	39×71,25×38,16×27,20×30,8×13	2003

Ref.	Satellite	Microwave	Owner	Resolution		Swath	Footprint	Year
[30]	Aqua	AMSR-E	NASA	6	0.5	1450	75×43,51×29,27×16,32×18,14×8,6×4	2002
[28]	Tropical Rainfall Measuring Mission (TRMM)	TMI	JAXA and NASA	5	-	759	72×43,35×21,26×21,18×10,8×6	1997

The additional 7 GHz channel present on AMSR-E and AMSR2, but not TMI, provides improved estimates of sea-surface roughness and improved accuracy for SSTs [27]. “All channels are used simultaneously to retrieve SST, wind speed, columnar water vapor, cloud liquid water, and rain rate. SST retrieval is prevented only in regions with sun-glitter, rain, or proximity to land. Since only a small number of retrievals are unsuccessful, almost complete global coverage is achieved daily” [27].

2.4.3 Literature Review of the Impacts of ENSO

Smith and Sardeshmukh [32] discussed the effect of ENSO on the probability distribution of daily surface air temperature over the Pacific–North American sector. It was investigated using the US National Centers for Environmental Prediction (NCEP) reanalysis data for 1959–1998. In this study, the El Niño response was characterized by reduced intraseasonal variance over most of the US, western Canada, and the Gulf of Alaska, on the other hand, there was a rise of variance during La Niña. The sign of this response was consistent for many individual El Niño and La Niña years in regions with a robust signal. These results were consistent with other studies, suggesting an increased incidence of blocking along the west coast of North America during El Niño, resulting in less storm activity and fewer incursions of warm and cold air over the eastern US.

Lang et al. [33] discussed the effect of ENSO events on the tropical pacific mean climate by an analytical model that has an oscillatory regime that resembles the observations. During this oscillatory regime, the time-mean SST in the eastern equatorial Pacific was found to be significantly different from the corresponding equilibrium SST. In the oscillatory regime, SST is warmer than equilibrium SST. The study found that the difference was proportional to the amplitude of ENSO. The study also discussed the role of ENSO events in shaping the tropical mean climate state and suggested that decadal warming in the recent decades within the eastern tropical Pacific can be more of a consequence than an explanation for the elevated ENSO activity during the same period.

Sun et al. [34] studied the worldwide and regional influence of the ENSO events on extreme precipitation. The analysis was done using a global database comprising over 7000 high-quality observation sites. The study found the influence of ENSO in the extreme precipitation of several regions such as North and South America, southern and eastern Asia, South Africa, Australia, and Europe. The study also found that the effect of ENSO on extreme precipitation was asymmetric, with most parts of the planet experiencing a major effect just for one ENSO phase. These findings have important implications on the current understanding of how ENSO influences extreme precipitation and can enable a more rigorous theoretical foundation for providing quantitative extreme precipitation intensity predictions at seasonal timescales.

Moreiras [35] studied the temporal distribution of landslides that can be verified through climatic anomalies linked to the ENSO events. The study found that an increasing number of landslides triggered by rainfall have been recorded during warm episodes (El Niño) in the Cordillera Frontal, and a decreasing number during cold episodes (La Niña), which concluded that this geological province is principally influenced by the Pacific Anticyclone. However, slope instability in the Precordillera, located east of the Cordillera Frontal, seems to be mainly influenced by the Atlantic Anticyclone. Analysis of variance shows that there was no significant difference between landslide records and cold-warm episodes, and a higher number of landslides were recorded in years linked to wet periods than during dry periods. Furthermore, the precipitation threshold value related to landslide occurrence and antecedent precipitation were analyzed.

Tote et al. [36] studied the effect of ENSO events on sediment production in a very large coastal basin in northern Peru. The effect of ENSO is not limited to changes in sediment mobilization. Since ENSO events can affect terrestrial ecosystems, they may have important effects on sediment production and transport in river basins over periods that are longer than the duration of the event itself. The study found that in strong negative ENSO periods, the mean annual streamflow discharge at the inlet of the Poechos reservoir in the lower basin was 5.4 times over normal annual discharges, while average sediment fluxes exceeded those of normal years by a factor of about 11. In two heavily affected periods, 45.9% of the total sediment yield in the 29 years observation period was generated. Sediment fluxes in the post-ENSO period are lower than expected, which proves post-ENSO event dynamics are significantly different from pre-event dynamics.

From the detailed literature review above, it is profound that the ENSO events, which happen in the Pacific Ocean, have a global impact through drought, extreme precipitation, landslide, sedimentation, etc. Because of the global impacts, ENSO drives extreme weather and climate variability, which greatly affect the built environment and human habitants. The extreme weather affects lifeline infrastructure such as roads and bridges. Therefore, forecasting ENSO events a few years in advance is an intense area of research. Figure 17 shows the monthly sea surface temperature from January 1950 to February 2019. The criteria used by NOAA to classify ENSO episodes is that the five consecutive 3-month running mean SST anomalies exceed the threshold ±0.5. Figure 18 shows El Niño and La Niña years announced by NOAA. The criteria developed in this doctoral research to classify ENSO episodes is that the monthly SST anomalies (calculated using NOAA reference period: 1971-2000, 26.89 °C) exceed the threshold ±1. Figure 19 shows El Niño and La Niña years detected by CAIT Methodology.

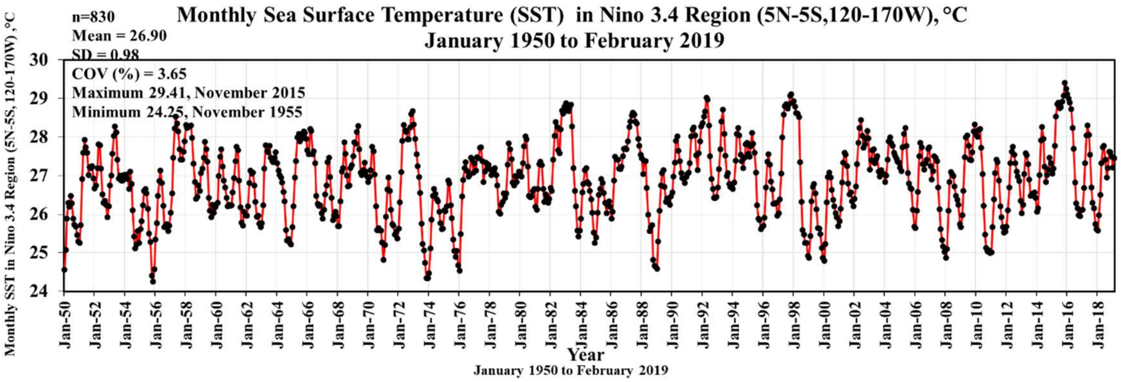

Figure 17 Monthly Sea Surface Temperature, January 1950 to February 2019

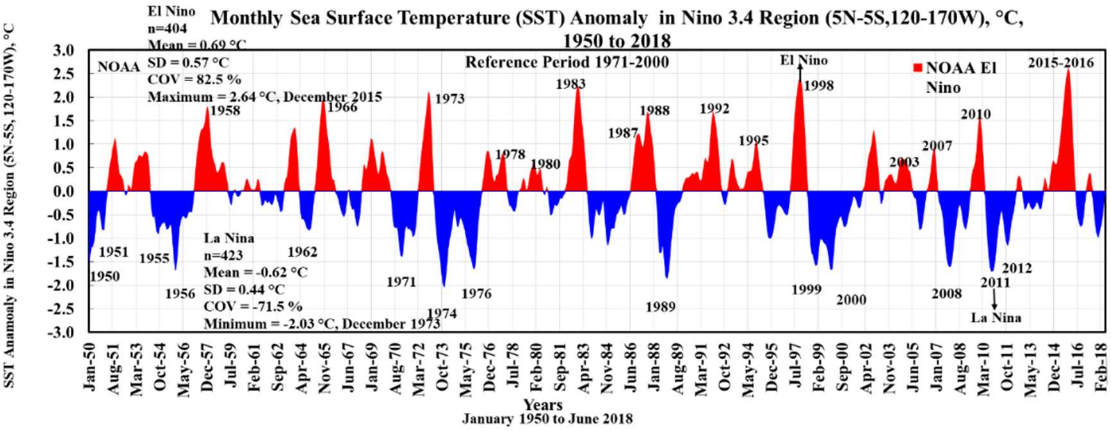

Figure 18 El Niño and La Niña Years by NOAA, January 1950 to February 2019

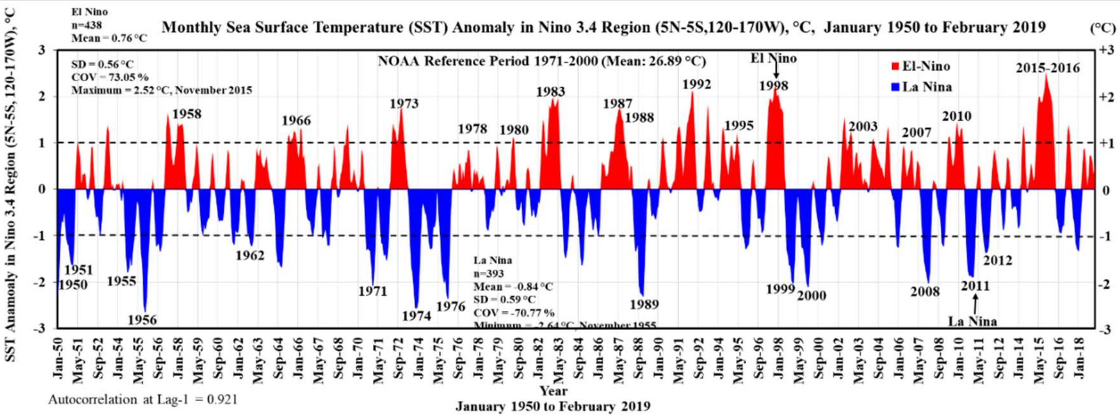

Figure 19 El Niño and La Niña Years Detected by CAIT Methodology, January 1950 to February 2019

2.4.4 ARIMA Modeling of Sea Surface Temperature Data

This section presents ARIMA modeling for time series data of sea surface temperature. This time series fails the Normality test and independence test (high autocorrelation 0.92 at Lag-1). From January 1950 to February 2019, total sea surface temperature data points were 830 with a mean of 26.90 °C. Table 6 shows the maximum (29.41 °C) and minimum (24.25°C) sea surface temperature data were found in November 2015 and November 1955, respectively. For model verification purposes 2018 and 2019 data were kept from the modeling database. Total model data points were 816 with an average of 26.89 °C. SST anomalies were calculated using NOAA reference period (1971-2000) average temperature of 26.89 °C. El-Niño (positive anomalies) and La-Niña (negative anomalies) were identified.

Table 6 Descriptive Statistics of Sea Surface Temperature

Equatorial Pacific Sea Surface Temperatures (°C), 1950 - 2019	
Summary Statistics	Sea Surface Temperature, (°C)
n	830
Mean	26.90
SD	0.98
COV (%)	3.65%
Maximum	29.41
Maximum Date	November, 2015
Minimum	24.25
Minimum Date	November, 1955

The ACF and PACF plots of the original time series are shown in Figure 20 and Figure 21, respectively.

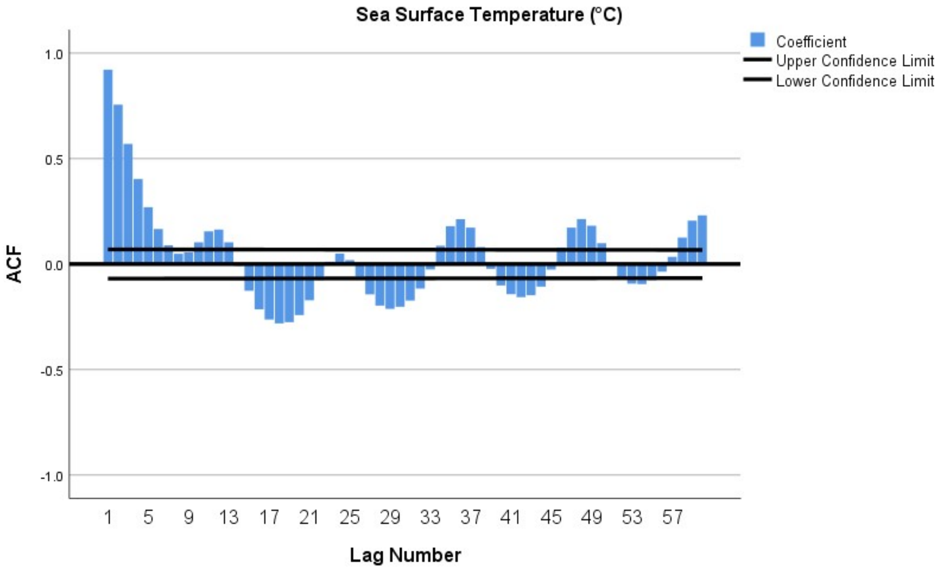

Figure 20 ACF Plot of Sea Surface Temperature

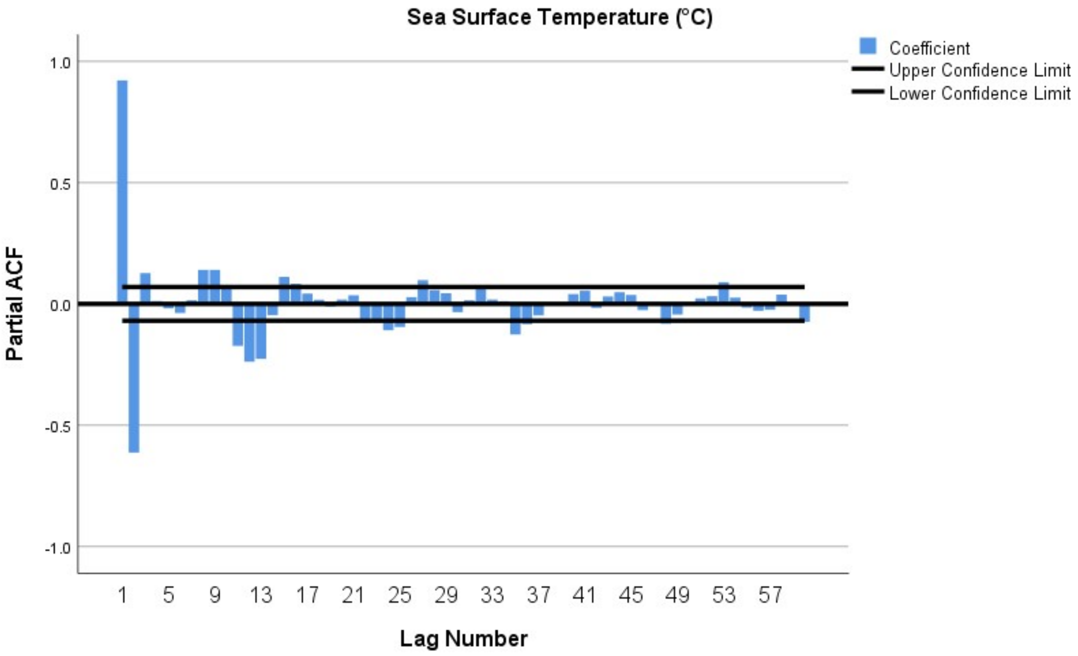

Figure 21 PACF Plot of Sea Surface Temperature

Figure 22 shows the differencing order-1 plot for the original time series. The correlation R-value for the differencing order time series and the original time series is 0.202, which is more than 0.2. According to Appendix A, differencing order-1 (d = 0) should be used to make the series stationary.

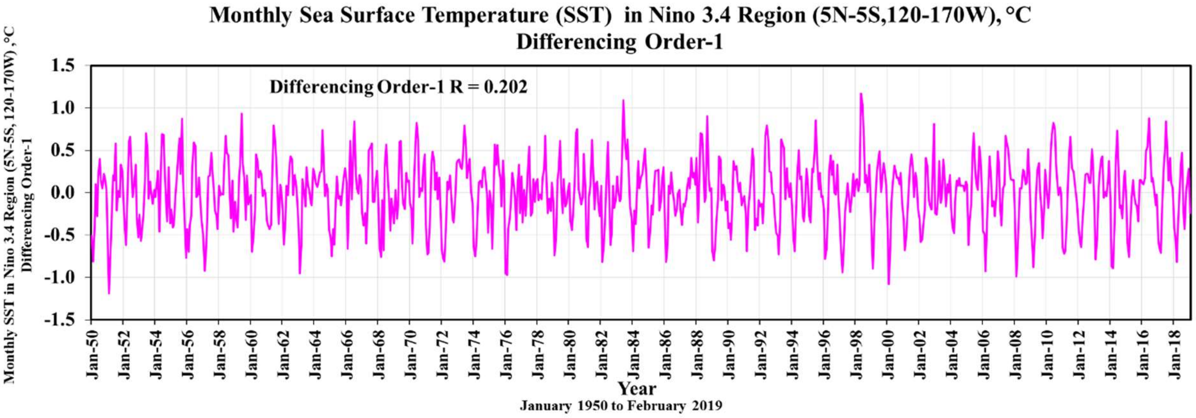

Figure 22 Differencing Order-1 Plot of Sea Surface Temperature

Model diagnostics for selecting model terms were based on ACF and PACF plots (Figures 20 and 21) of the original time series. The first seasonal ARIMA model (1,0,0) (1,0,1) was tried (Figures 23 and 24).

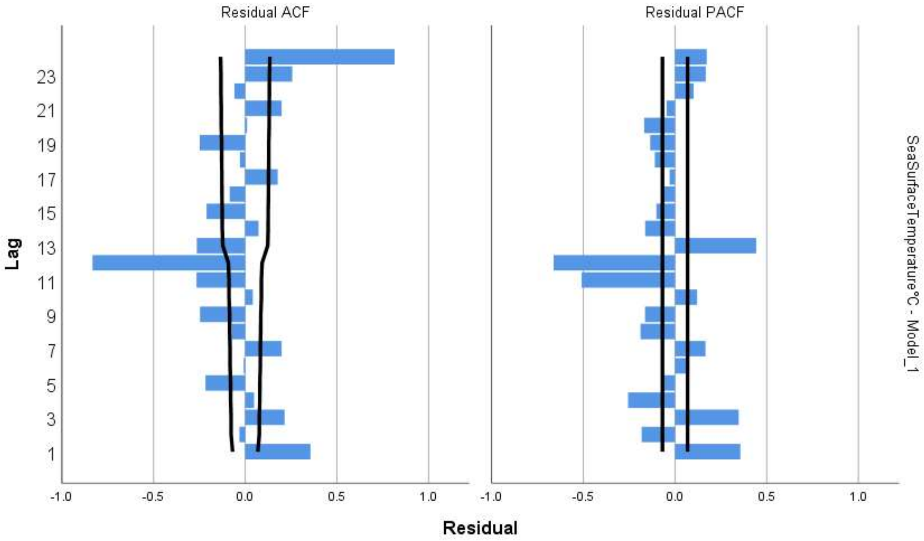

Figure 23 Residual ACF and Residual PACF plot of Seasonal ARIMA Model (1,0,0) (1,0,1)

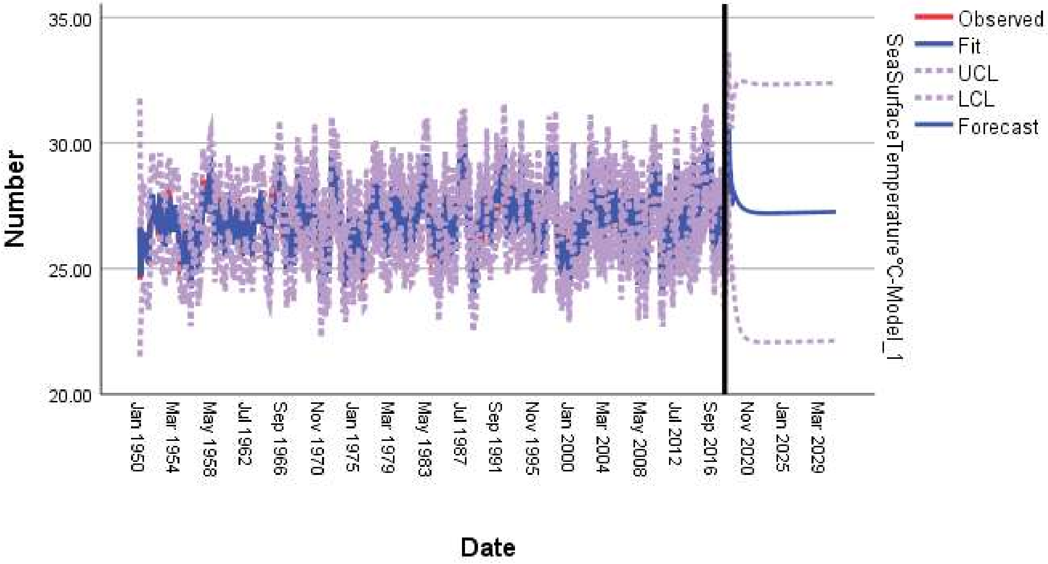

Figure 24 Seasonal ARIMA Model (1,0,0) (1,0,1) Prediction of Sea Surface Temperature from 2018 to 2030

The residual ACF and PACF (Figure 23) and future prediction pattern (Figure 24) plots indicate the need to improve the prediction pattern in the (1,0,0) (1,0,1) model. Subsequently, 24 more models were tried. The prediction patterns of the models were not consistent with the pattern of the historic time series. Therefore, more models were tried and the residual ACF and PACF plots were examined. Two seasonal ARIMA models (24,0,0)(24,0,36) and (9,0,0)(12,0,18) had showed better residual ACF and PACF. The seasonal ARIMA model (24,0,0)(24,0,36) trial turned out to be the best model as shown by the residual ACF and PACF plots (Figure 25) and prediction pattern (Figure 26).

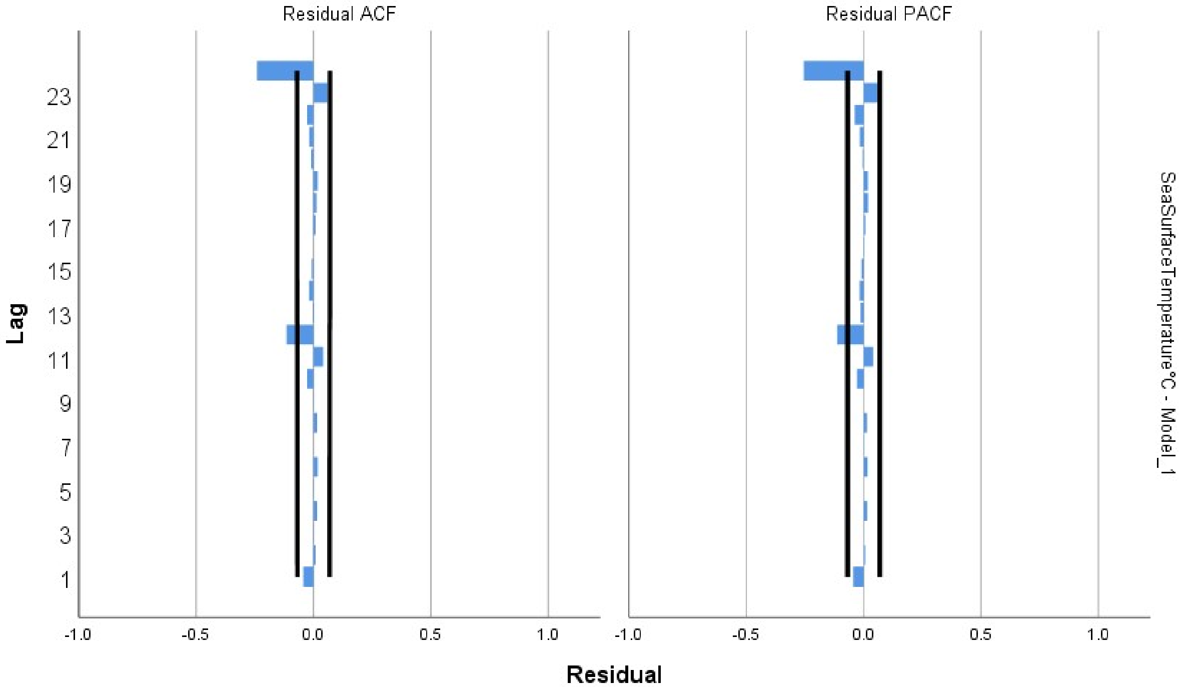

Figure 25 Residual ACF and Residual PACF plot of Seasonal ARIMA Model (24,0,0) (24,0,36)

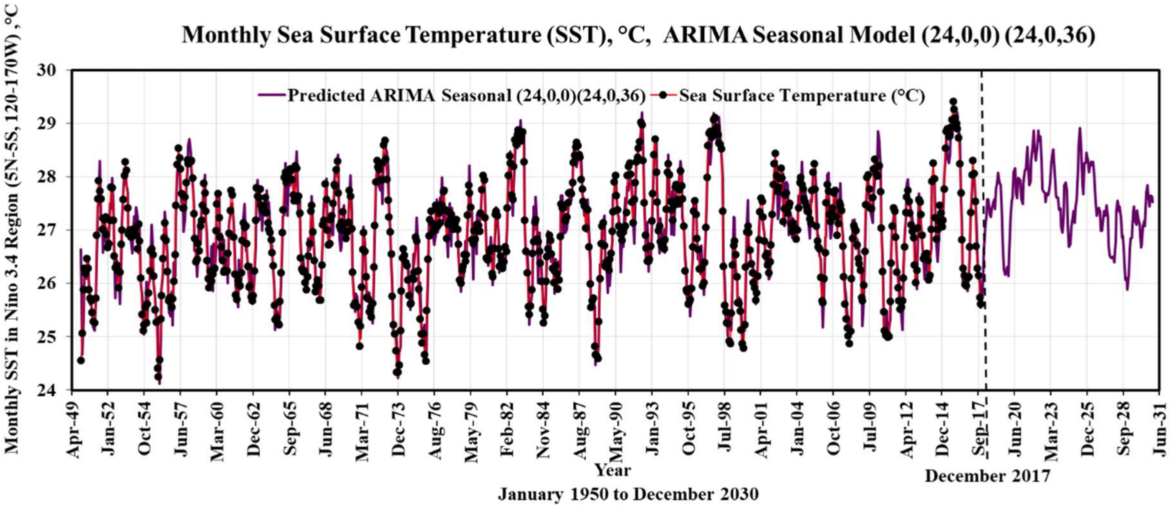

Figure 26 Seasonal ARIMA Model (24,0,0) (24,0,36) Prediction of Sea Surface Temperature from 2018 to 2030

The observed vs. predicted sea surface temperature from 1950 to 2017 using the ARIMA model (24,0,0) (24,0,36) are shown in Figure 27 with a high correlation 0.95 R-value.

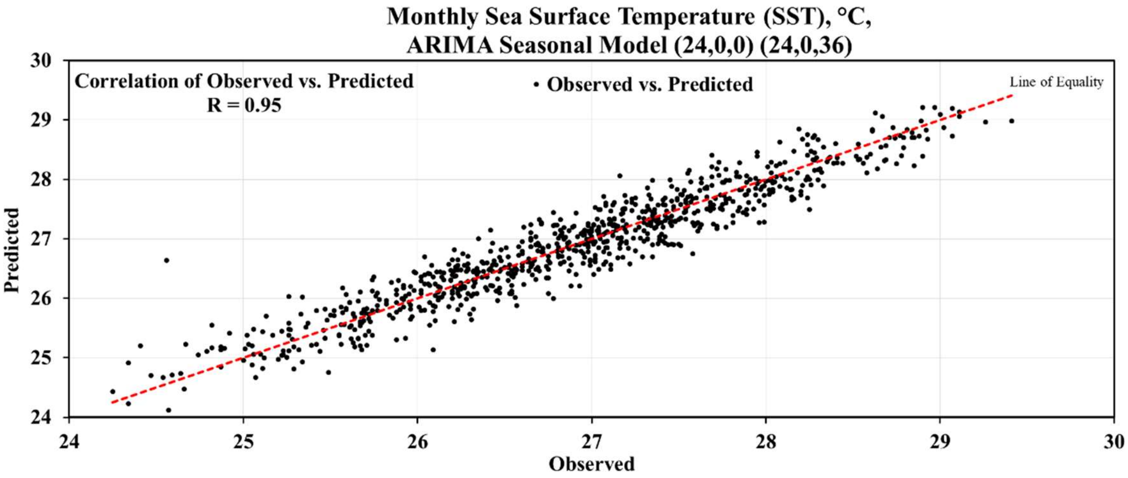

Figure 27 Observed vs. Predicted plot of Sea Surface Temperature using Seasonal ARIMA Model (24,0,0) (24,0,36)

Table 7 shows the verification for the year 2018 using seasonal ARIMA Models' prediction.

Table 7 Verification of Seasonal ARIMA Models using 2018 Measured Data

Equatorial Pacific (Nino 3.4 Region) Monthly Sea Surface Temperatures, °C, January 2018 to December 2018				
			R = 0.95	R = 0.95
Cumulative Month No.	Month	Measured	Predicted ARIMA Seasonal (24,0,0)(24,0,36)	Predicted ARIMA Seasonal (9,0,0)(12,0,18)
817	Jan-18	25.57	25.7	25.48
818	Feb-18	25.98	26.09	25.83
819	Mar-18	26.5	26.63	26.67
820	Apr-18	27.32	27.03	27.48
821	May-18	27.74	27.26	27.56
822	Jun-18	27.77	27.57	27.65
823	Jul-18	27.42	27.57	27.4
824	Aug-18	26.95	27.29	27.27
825	Sep-18	27.19	27.24	27.06
826	Oct-18	27.62	27.4	26.84
827	Nov-18	27.61	27.48	26.72
828	Dec-18	27.49	27.57	26.64
January - December 2018	n	12	12	12
	Mean	27.10	27.07	26.88
	SD	0.72	0.62	0.68
	COV (%)	2.65%	2.28%	2.52%
	Mean Difference (%)		-0.1%	-0.8%
	RMSE		0.07	0.13
	MARE (%)		0.71%	1.18%

The following results are summarized for the better model (24,0,0)(24,0,36) for 2018 verification:

- the % mean difference in sea surface temperature: -0.1%
- RMSE: 0.07
- MARE: 0.71%

Figure 28 and Figure 29 show seasonal ARIMA Model (24,0,0) (24,0,36) and (9,0,0) (12,0,18) prediction for 2018, respectively. Based on the mean difference, RMSE, MARE, and future prediction pattern, the better model is (24,0,0) (24,0,36).

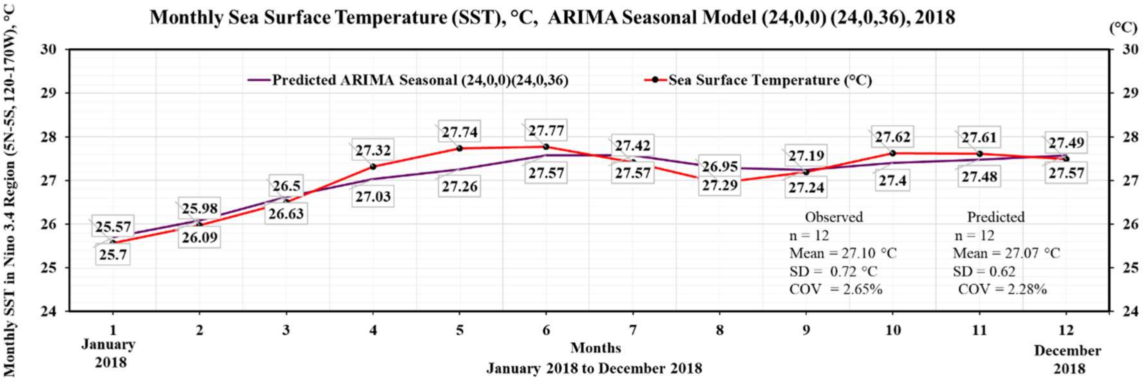

Figure 28 Observed and Seasonal ARIMA Model (24,0,0) (24,0,36) Prediction from January 2018 to December 2018

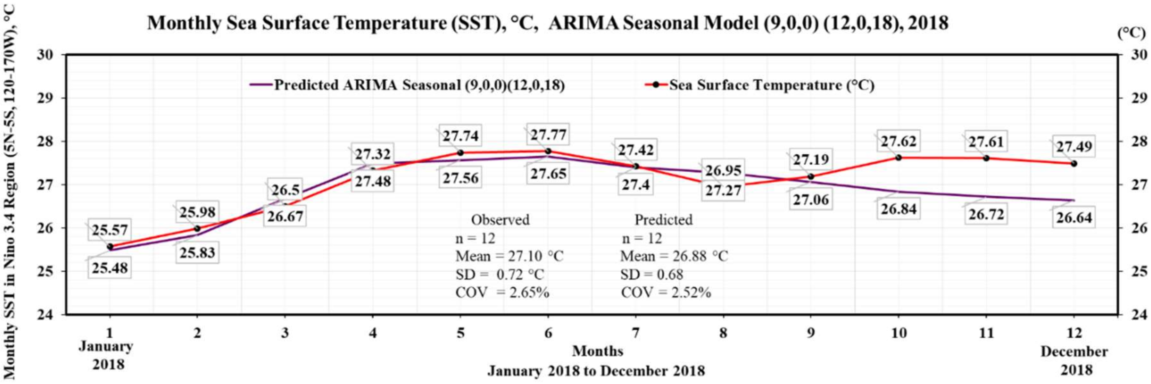

Figure 29 Observed and Seasonal ARIMA Model (9,0,0) (12,0,18) Prediction from January 2018 to December 2018

Table 8 shows the verification for the year 2019 using seasonal ARIMA models' prediction.

Table 8 Verification of Seasonal ARIMA Models using 2019 Measured Data

Equatorial Pacific (Nino 3.4 Region) Monthly Sea Surface Temperatures, °C January 2019 to December 2019				
			R = 0.95	R = 0.95
Cumulative Month No.	Month	Measured	Predicted ARIMA Seasonal (24,0,0)(24,0,36)	Predicted ARIMA Seasonal (9,0,0)(12,0,18)
829	Jan-19	27.2	27.39	26.43
830	Feb-19	27.48	27.78	26.68
831	Mar-19	28.1	27.95	27.13
832	Apr-19	28.45	28.07	27.79
833	May-19	28.49	27.89	28.04
834	Jun-19	28.18	27.84	28.01
835	Jul-19	27.64	27.57	27.72
836	Aug-19	26.9	26.79	27.47
837	Sep-19	26.75	26.26	27.46
838	Oct-19	27.2	26.16	27.5
839	Nov-19	27.23	26.2	27.48
840	Dec-19	27.12	26.31	27.47
January - December 2019	n	12	12	12
	Mean	27.56	27.18	27.43
	SD	0.60	0.78	0.48
	COV (%)	2.19%	2.86%	1.77%
	Mean Difference (%)		-1.4%	-0.5%
	RMSE		0.56	0.57
	MARE (%)		1.67%	1.84%

The following results are summarized for the better model (24,0,0) (24,0,36) for 2019 verification:

- the % mean difference in global mean sea level: -1.4%
- RMSE: 0.56
- MARE: 1.67%

Figure 30 and Figure 31 show seasonal ARIMA Model (24,0,0)(24,0,36) and (9,0,0) (12,0,18) prediction for 2019, respectively. Based on the mean difference, RMSE, MARE, and future prediction pattern, the better model is (24,0,0)(24,0,36).

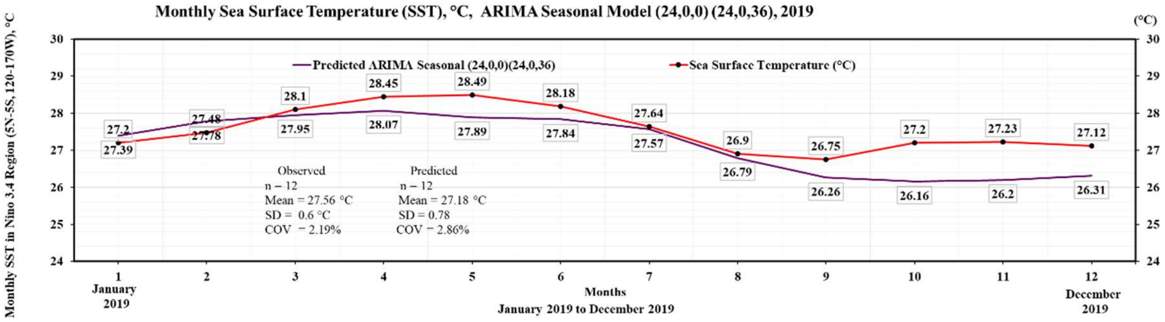

Figure 30 Observed and Seasonal ARIMA Model (24,0,0) (24,0,36) Prediction from January 2019 to December 2019

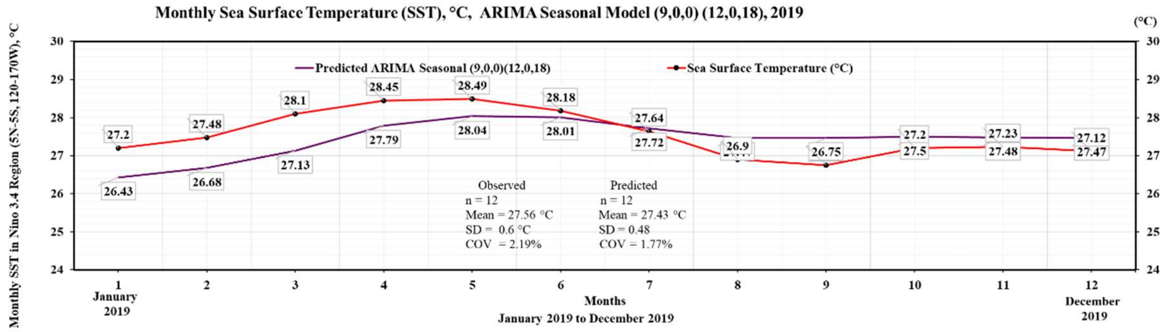

Figure 31 Observed and Seasonal ARIMA Model (9,0,0) (12,0,18) Prediction from January 2019 to December 2019

Based on the observed vs. predicted results from 1950 to 2017 (Figure 27), the future prediction from 2018 to 2050, the verification results of the year 2018 and 2019, the seasonal ARIMA model (24,0,0) (24,0,36) was chosen as the best model. Equation 3 shows the terms of seasonal ARIMA (24,0,0) (24,0,36) model.

$$
\begin{aligned}
Y_t \ = \ C \ + \ (1 - \phi_1 B^1 - \phi_2 B^2 - \cdots \dots \dots - \phi_{24} B^{24}) \\
* \, (1 - \Phi_1 B^S - \Phi_2 B^{2S} - \cdots \dots \dots - \Phi_{24} B^{24} \ ) \\
* \, (1 - \theta_1 B^{1S} - \theta_2 B^{2S} - \cdots \dots \dots - \theta_{36} B^{36S}) \\
* \ a_t \qquad\qquad\qquad\qquad\qquad\qquad Eq.3
\end{aligned}
$$

Y_t = Discrete time series

C = Constant

$1 - \phi_1 B^1 - \phi_2 B^2 - \cdots \dots \dots - \phi_{24} B^{24}$ = Regular Autoregressive process of order 24

$1 - \Phi_1 B^S - \Phi_2 B^{2S} - \cdots \dots \dots - \Phi_{24} B^{24S}$= Seasonal Autoregressive process of order 24

$1 - \theta_1 B^{1S} - \theta_2 B^{2S} - \cdots \dots \dots - \theta_{36} B^{36S}$ = Seasonal Moving Average process of order 36

a_t = random shock term; normally distributed, independent with zero mean, and variance equal to σ_a

As discussed above, the best model found for SST is the seasonal ARIMA model (24,0,0)(24,0,36). The future prediction of this model was used to predict the future El Niño and La Niña years. The criteria developed in this doctoral research to classify ENSO episodes is that the monthly SST anomalies (calculated using NOAA reference period: 1971-2000, 26.89 °C) exceed the threshold ±1 was applied to the future prediction of the final model. Figure 32 shows the future El Niño and La Niña years detected by CAIT Methodology. The model successfully predicted the 2018-2019 El Niño year. The model prediction shows that the next El Niño years will be 2021-22 and 2025-26. The model prediction also shows that the next La Niña year will be 2028-29.

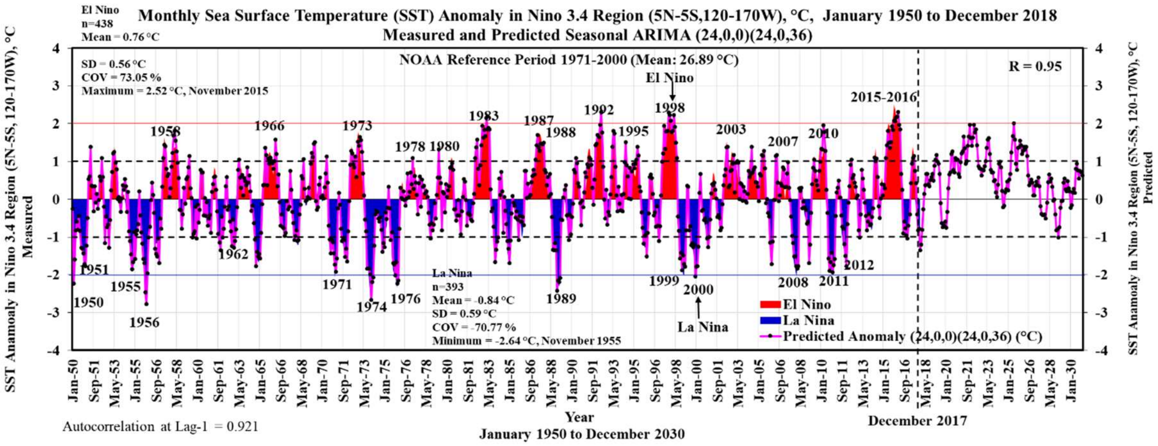

Figure 32 Future El Niño and La Niña Years Detected by CAIT Methodology, January 2018 to December 2030

2.5 Sea Level Rise

According to the U.N. Atlas of the Oceans, globally, eight of the world's 10 largest cities are near a coast. In the United States, almost 40 percent of the population lives in relatively high population-density coastal areas, where sea level plays a role in flooding, shoreline erosion, and hazards from storms [7]. In the urban area along coastlines around the world, rising seas threaten the infrastructure necessary for local jobs and regional industries. In the natural world, rising sea level creates stress on coastal ecosystems that provide recreation, protection from storms, and habitat for fish and wildlife, including commercially valuable fisheries. As seas rise, saltwater is also contaminating fresh-water aquifers, many of which sustain municipal and agricultural water supplies and natural ecosystems [7].

2.5.1 Global Mean Sea Level

Sea level is measured by two main methods: tide gauges and satellite altimeters. Tide gauge stations from around the world have measured the daily high and low tides for more than a century, using a variety of manual and automatic sensors. Using data from scores of stations around the world, a global average is calculated and adjusted for seasonal differences. High-quality measurements of (near)-global sea level have been made since late 1992 by satellite altimeters, in particular, TOPEX/Poseidon (launched August 1992), Jason-1 (launched December 2001), Jason-2 (launched June 2008), and Jason-3 (launched January 2016) [37]. There are several changes in slope over short periods in the global mean sea level record. This variability is partly related to El Niño and La Niña (sea level rises during El Niño and falls during La Niña) and associated changes in the hydrological cycle [37].

The Global Mean Sea Level (GMSL) time series (Figure 33) is collected tide gauge data around the world. The total GMSL change from January 1880 to December 2009 is about 210 mm over 130 years. The average annual rate of change over 130 years is 1.7 mm/year. The IPCC Fourth Assessment Report described studies that estimated sea-level rise for the 20th century between 0.5 and 3.0 mm a year. The most likely range, according to the IPCC, was between 1.0 and 2.0 mm a year [38].

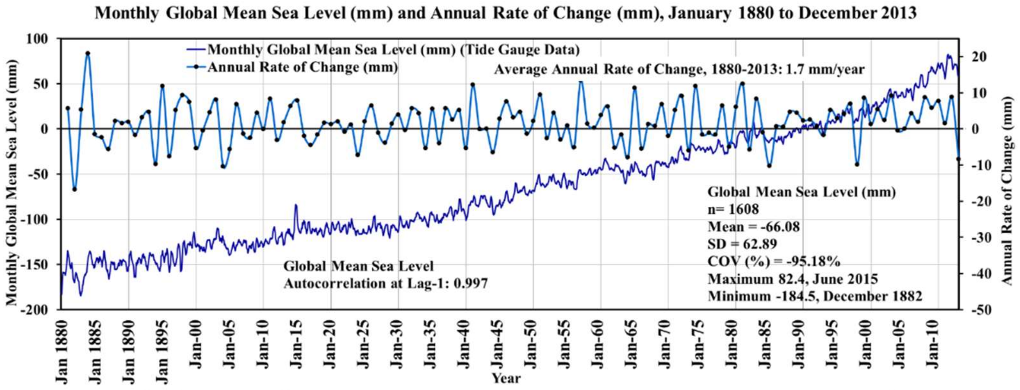

Data Source: CSIRO. Coastal Tide Gauge Records. http://www.cmar.csiro.au/sealevel/sl_data_cmar.html Accessed 22 March 2019

Figure 33 Monthly Global Mean Sea Level and Annual Rate of Change, January 1880 to December 2013

2.5.2 ARIMA Modeling of Global Mean Sea Level Data

This section presents ARIMA modeling for time series data of global mean sea level. This time series fails the Normality test and independence test (high autocorrelation 0.997 at Lag-1). From January 1880 to December 2013, total global mean sea level data points were 1,608 with a mean of -66.08 mm. Table 9 shows the maximum (82.4 mm) and minimum (-184.5 mm) global mean sea level data were found in June 2012 and December 1882, respectively. For model verification purposes 2012 and 2013 data were kept from the modeling database. Total model data points were 1,596 with an average of -67.09 mm.

Table 9 Descriptive Statistic of Monthly Global Mean Sea Level

Monthly Global Mean Sea Level (mm) January 1880 to December 2013	
Summary Statistics	Monthly Global Mean Sea Level (mm)
n	1608
Mean	-66.08
SD	62.89
COV (%)	-95.18%
Maximum	82.4
Maximum Date	June, 2012
Minimum	-184.5
Minimum Date	December, 1882
Autocorrelation at Lag-1	0.997
Normality Test	Significant (Not Normal)

The ACF and PACF plots of the original time series are shown in Figure 34 and Figure 35, respectively.

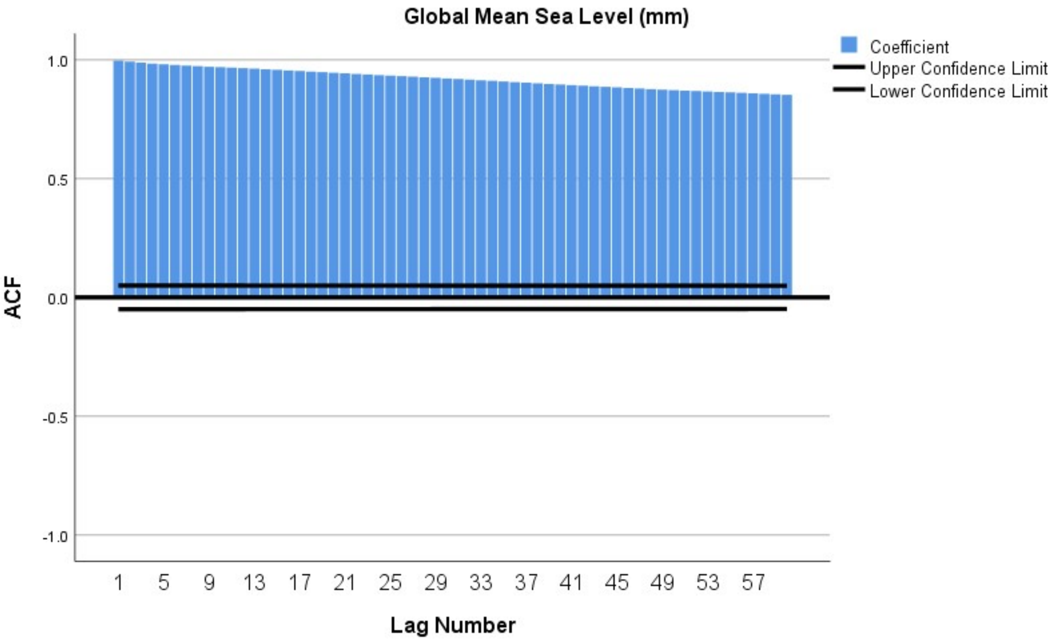

Figure 34 ACF Plot of Global Mean Sea Level

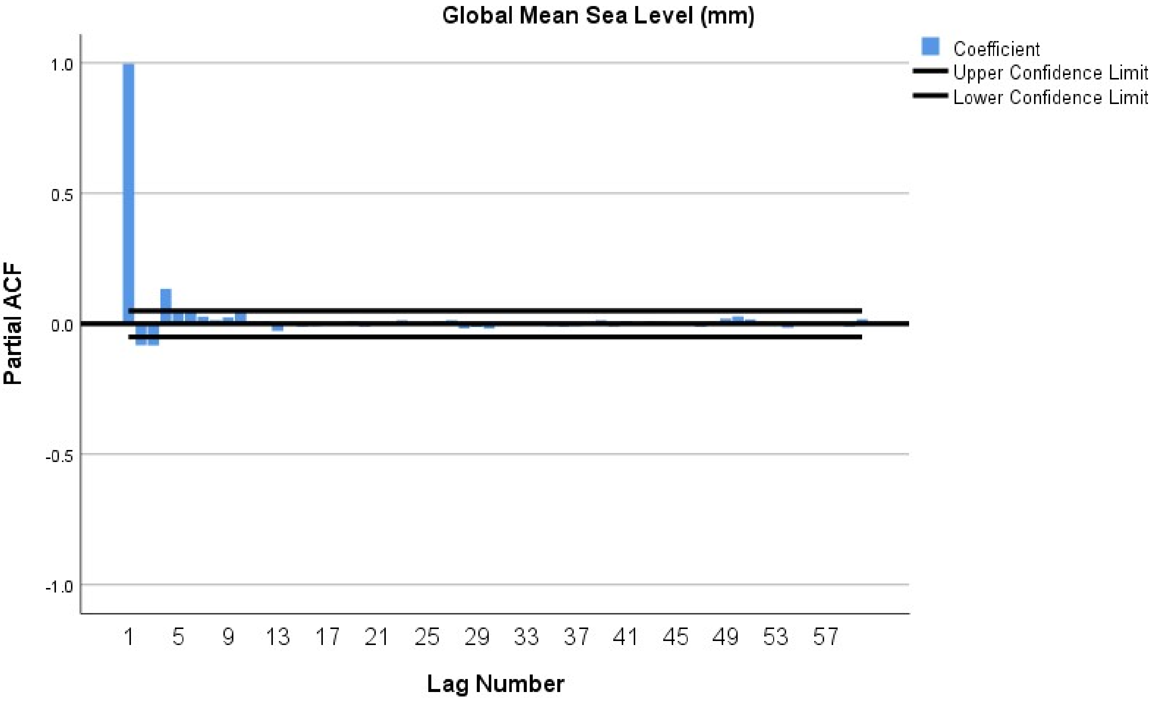

Figure 35 PACF Plot of Global Mean Sea Level

Figure 36 shows the differencing order-1 plot for the original time series. The correlation R-value for the differencing order time series and the original time series is -0.021, which is less than 0.2. According to Appendix A, differencing order-1 (d = 1) should be used to make the series stationary. However, Figure 36 shows two distinctive patterns and R-values for two different periods, from 1880 to 1914 (R = 0.115) and from 1915 to 2013 (R = -0.0000127). Hence, both d=0 and d=1 terms were used to develop the ARIMA model.

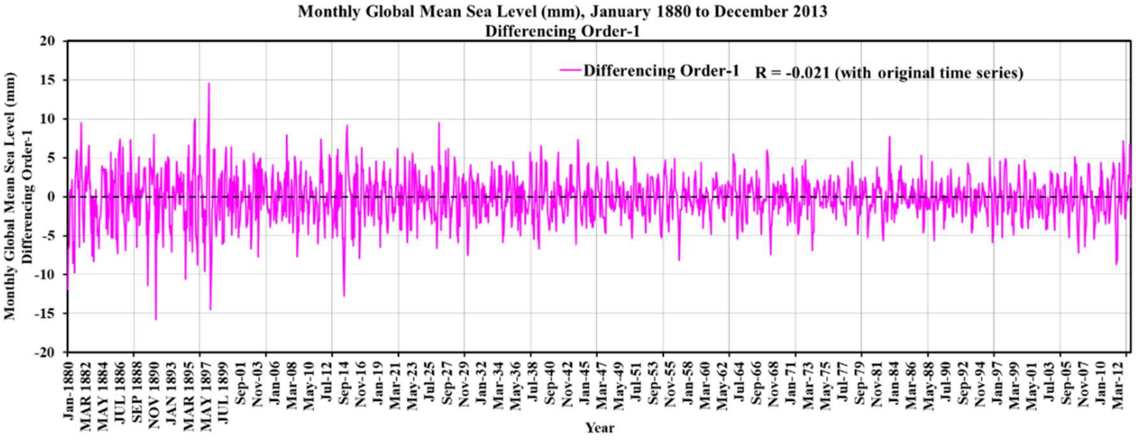

Data Source: CSIRO. Coastal Tide Gauge Records. Australia. http://www.cmar.csiro.au/sealevel/sl_data_cmar.html Accessed 22 March 2019

Figure 36 Differencing Order-1 Plot of Global Mean Sea Level

Model diagnostics for selecting model terms were based on ACF and PACF plots (Figures 34 and 35) of the original time series. The first seasonal ARIMA model (1,1,0) (1,1,3) was tried (Figures 37 and 38).

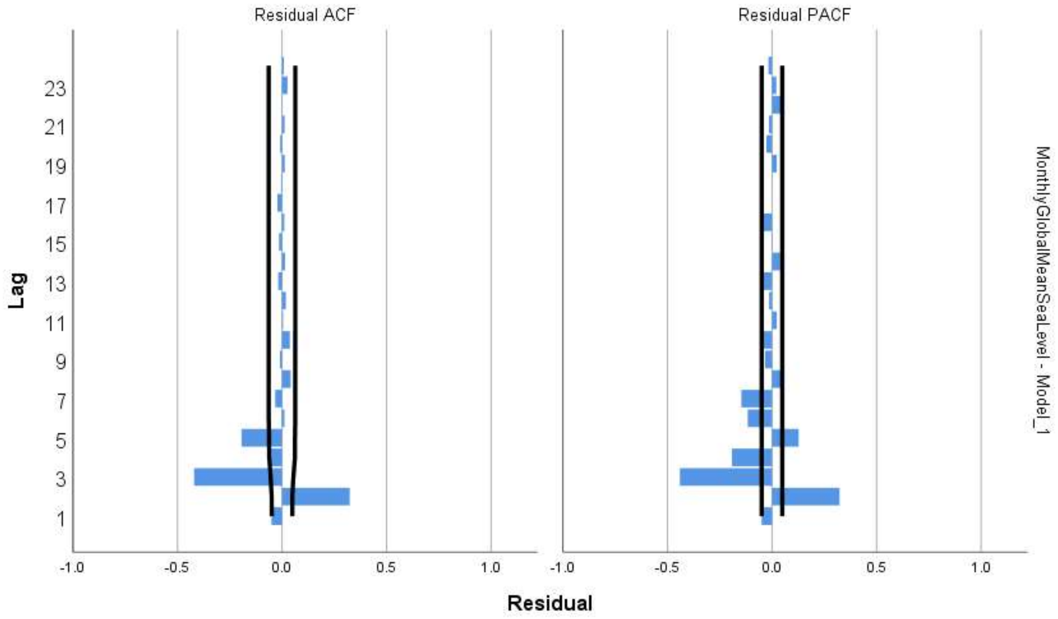

Figure 37 Residual ACF and Residual PACF plot of Seasonal ARIMA Model (1,1,0) (1,1,3)

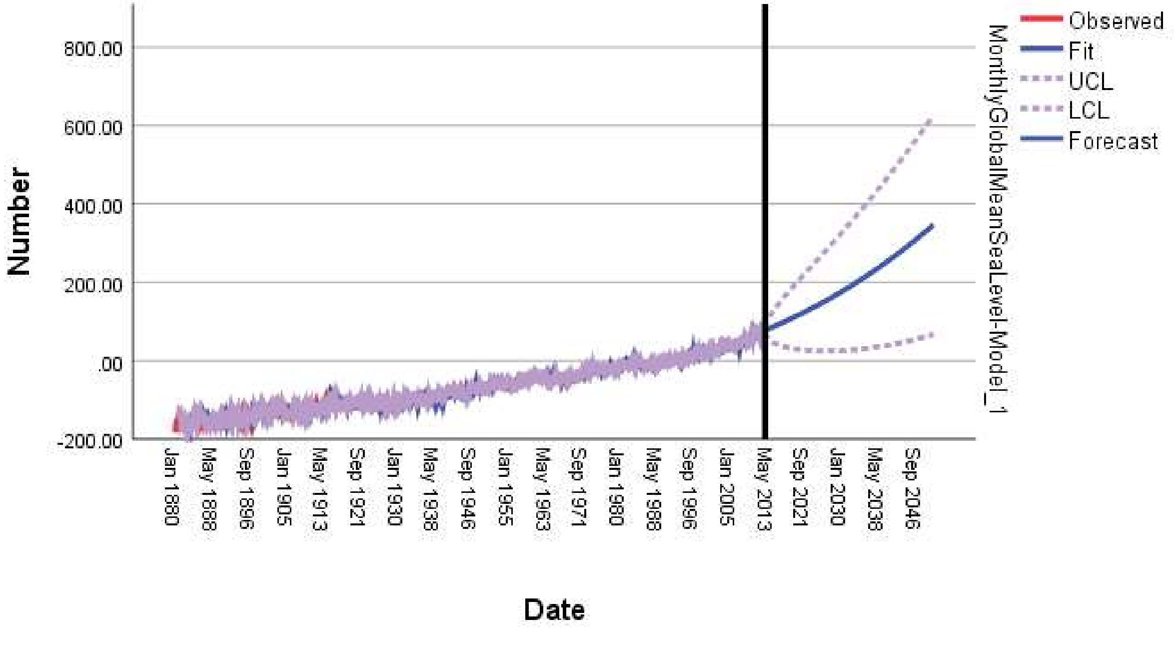

Figure 38 Seasonal ARIMA Model (1,0,0) (1,0,3) Prediction of Global Mean Sea Level from 2012 to 2050

The residual ACF and PACF (Figure 37) and future prediction pattern (Figure 38) plots indicate the need to improve the prediction pattern in the (1,1,0) (1,1,3) model. Subsequently, nine more models were tried using differencing order-1 (d=1) in the model terms. The prediction patterns of the models were not consistent with the pattern of the historic time series. Therefore, more models were tried using without differencing (d = 0) in the model terms, and the residual ACF and PACF plots were examined. Two seasonal ARIMA models (6,0,0) (6,0,6) and (12,0,0) (12,0,36) were tried without success. The last ARIMA model (12,0,0) (12,0,24) trial turned out to be the best model as shown by the residual ACF and PACF plots (Figure 39) and prediction pattern (Figure 40).

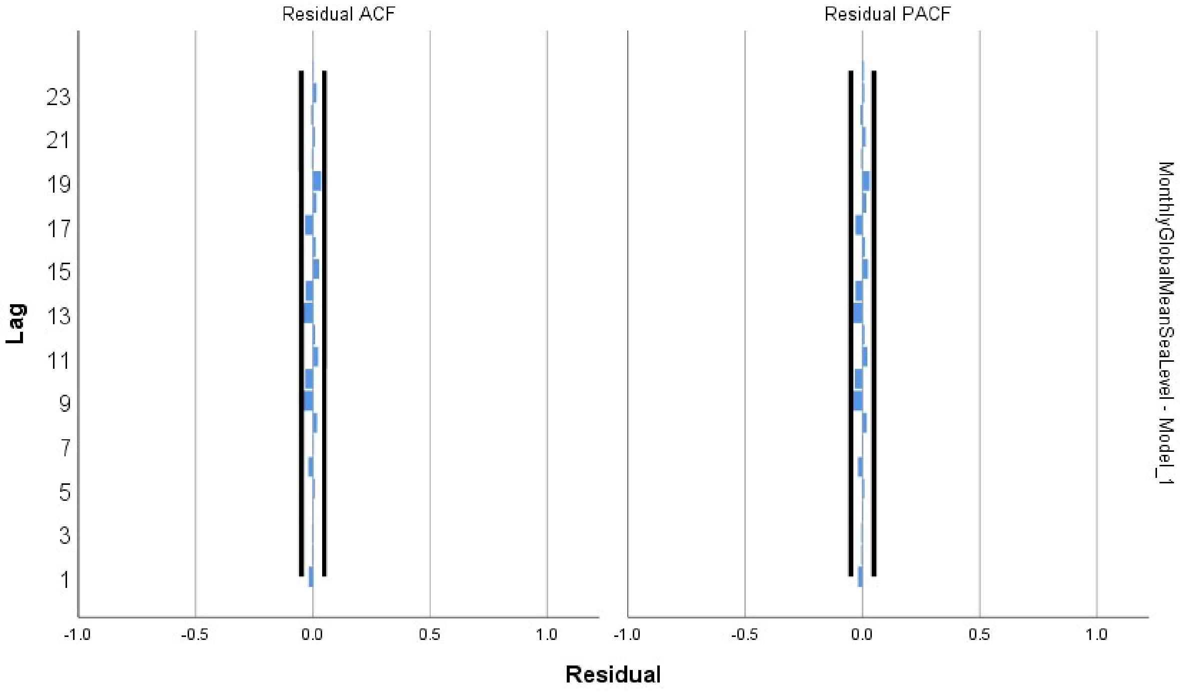

Figure 39 Residual ACF and Residual PACF plot of Seasonal ARIMA Model (12,0,0) (12,0,24)

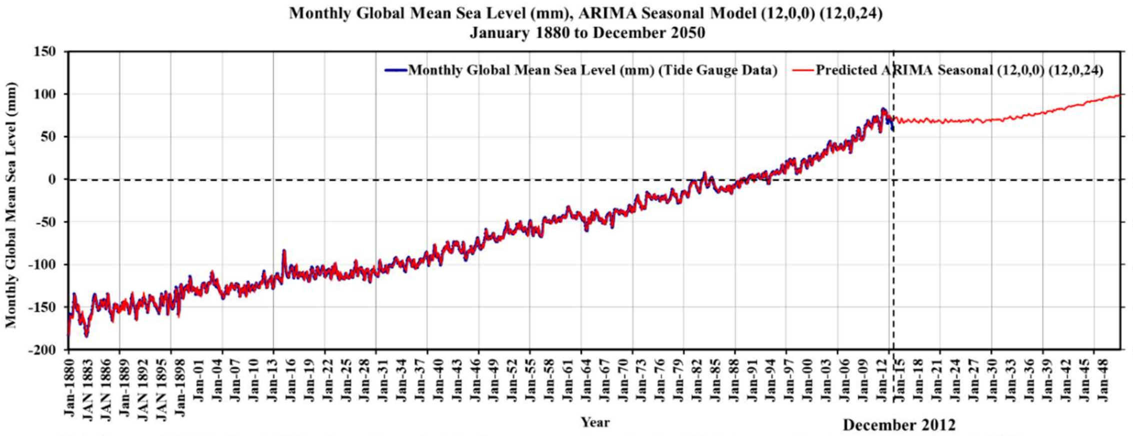

Data Source: CSIRO. Coastal Tide Gauge Records. http://www.cmar.csiro.au/sealevel/sl_data_cmar.html Accessed 22 March 2019

Figure 40 Seasonal ARIMA Model (12,0,0) (12,0,24) Prediction of Global Mean Sea Level from 2012 to 2050

The observed vs. predicted monthly global mean sea level from 1880 to 2012 using the ARIMA model (12,0,0) (12,0,24) are shown in Figure 41 with a high correlation 0.95 R-value.

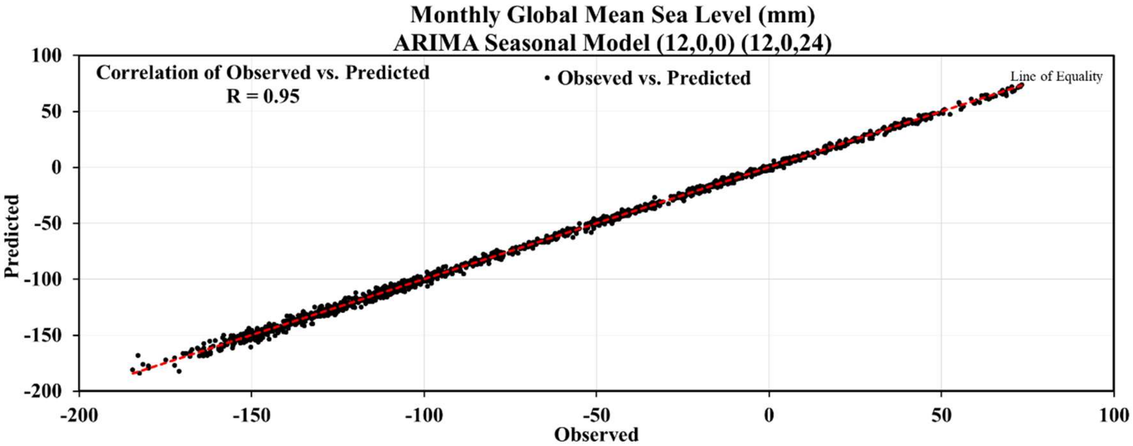

Figure 41 Observed vs. Predicted plot of Monthly Global Mean Sea Level using Seasonal ARIMA Model (12,0,0) (12,0,24)

Table 10 and Table 11 show the verification for the years 2012 and 2013, respectively using seasonal ARIMA Models' prediction. Based on the mean difference, RMSE, MARE, and future prediction pattern, the best model is (12,0,0) (12,0,24).

Table 10 Verification of Seasonal ARIMA Models using 2012 Measured Data

Monthly Global Mean Sea Level (mm) **January 2012 to December 2012**					
			R = 0.99	R = 0.99	R =0.95
Cumulative Month No.	Month	Measured	Predicted ARIMA Seasonal (6,0,0) (6,0,6)	Predicted ARIMA Seasonal (12,0,0) (12,0,36)	Predicted ARIMA Seasonal (12,0,0) (12,0,24)
1585	Jan-12	58.5	54.9	55.6	55.7
1586	Feb-12	63.8	59.2	60.0	59.7
1587	Mar-12	72.5	67.8	69.0	69.8
1588	Apr-12	80.4	75.1	75.1	76.3
1589	May-12	82	82.1	82.7	82.0
1590	Jun-12	82.4	80.0	81.2	80.6
1591	Jul-12	78.1	77.5	77.3	77.8
1592	Aug-12	78.8	75.4	75.9	75.3
1593	Sep-12	78.6	76.6	77.2	76.8
1594	Oct-12	80.8	79.9	79.7	79.5
1595	Nov-12	79.4	79.5	79.1	79.6
1596	Dec-12	77.7	77.5	77.9	77.7
January - December 2012	n	12	12	12	12
	Mean	76.08	73.78	74.23	74.24
	SD	7.51	8.66	8.45	8.36
	COV (%)	9.87%	11.74%	11.39%	11.27%
	Mean Difference (%)		-3.0%	-2.4%	-2.4%
	RMSE		0.86	0.73	0.69
	MARE (%)		3.23%	2.74%	2.60%

The following results are summarized for the best model (12,0,0) (12,0,24):

- the % mean difference in global mean sea level: -2.4%
- RMSE: 0.69
- MARE: 2.6%

Table 11 Verification of Seasonal ARIMA Models using 2013 Measured Data

Monthly Global Mean Sea Level (mm) **January 2013 to December 2013**					
			R = 0.99	R = 0.99	R = 0.95
Cumulative Month No.	Month	Measured	Predicted ARIMA Seasonal (6,0,0) (6,0,6)	Predicted ARIMA Seasonal (12,0,0) (12,0,36)	Predicted ARIMA Seasonal (12,0,0) (12,0,24)
1597	Jan-13	70.5	74.4	74.8	74.3
1598	Feb-13	65.7	71.9	72.9	71.7
1599	Mar-13	67	70.4	72.1	71.5
1600	Apr-13	69.8	70.4	73.2	73.0
1601	May-13	72	70.3	73.7	74.5
1602	Jun-13	71.5	70.1	73.7	74.7
1603	Jul-13	71.2	69.0	72.9	73.7
1604	Aug-13	71.6	67.5	72.6	72.5
1605	Sep-13	68.8	66.0	72.1	70.7
1606	Oct-13	66.4	64.5	71.3	69.4
1607	Nov-13	59.7	63.3	70.6	69.5
1608	Dec-13	58.5	61.8	70.3	69.3
January - December 2013	n	12	12	12	12
	Mean	67.73	68.30	72.50	72.06
	SD	4.56	3.76	1.31	2.02
	COV (%)	6.73%	5.50%	1.81%	2.81%
	Mean Difference (%)		0.8%	7.1%	6.4%
	RMSE		0.94	1.69	1.51
	MARE (%)		4.39%	7.42%	6.71%

The following results are summarized for the best model (12,0,0) (12,0,24):

- the % mean difference in global mean sea level: 6.4%
- RMSE: 1.51
- MARE: 6.71%

Figures 42 and 43 presented the observed and predicted global mean sea level data of 12 months for 2013. Figure 29 shows that the seasonal ARIMA model (6,0,0) (6,0,6) prediction did not follow the same pattern as the observed data. Although, % mean difference, RMSE, and MARE statistics were the lowest for the seasonal ARIMA model (6,0,0) (6,0,6), the seasonal ARIMA model (12,0,0) (12,0,24) was chosen as the best model based on the verification of 2012 and 2013 monthly global mean sea level data.

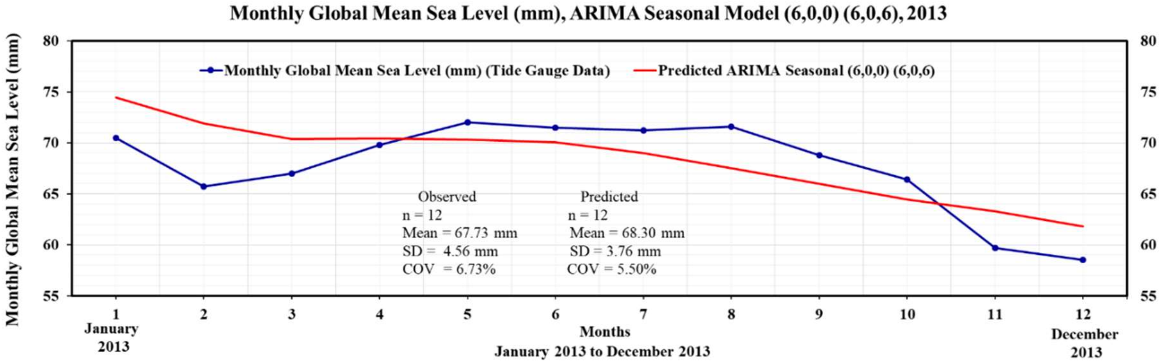

Figure 42 Observed and Seasonal ARIMA Model (6,0,0) (6,0,6) Prediction from January 2013 to December 2013

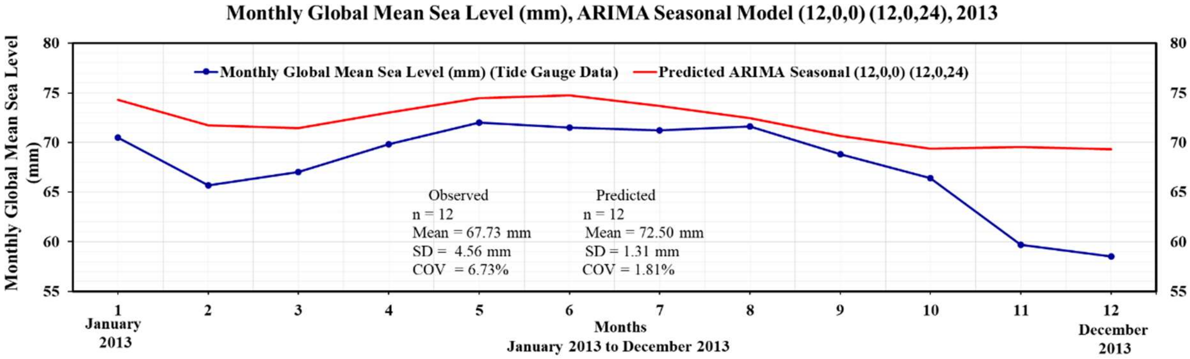

Figure 43 Observed and Seasonal ARIMA Model (12,0,0) (12,0,24) Prediction from January 2013 to December 2013

Equation 4 shows the terms of seasonal ARIMA (12,0,0) (12,0,24) model.

$$\begin{aligned} Y_t = C + (1 - \phi_1 B^1 - \phi_2 B^2 - \cdots \ldots \ldots - \phi_{12} B^{12}) \\ * (1 - \Phi_1 B^S - \Phi_1 B^{2S} - \cdots \ldots \ldots - \Phi_{12} B^{12S}) \\ * (1 - \theta_1 B^{1S} - \theta_2 B^{2S} - \cdots \ldots \ldots - \theta_{24} B^{24S}) \\ * a_t \end{aligned} \qquad Eq. 4$$

Y_t = Discrete time series

C = Constant

$1 - \phi_1 B^1 - \phi_2 B^2 - \cdots \ldots \ldots - \phi_{12} B^{12}$ = Regular Autoregressive process of order 12

$1 - \Phi_1 B^S - \Phi_1 B^{2S} - \cdots \ldots \ldots - \Phi_{12} B^{12S}$ = Seasonal Autoregressive process of order 12

$1 - \theta_1 B^{1S} - \theta_2 B^{2S} - \cdots \ldots \ldots - \theta_{24} B^{24}$ = Seasonal Moving Average process of order 24

a_t = random shock term; normally distributed, independent with zero mean, and variance equal to σ_a

As discussed above, the best model found for GMSL is the seasonal ARIMA model (12,0,0) (12,0,24). The future prediction of this model was used to predict the annual rate of change in GMSL. Figure 44 shows the predicted monthly global mean sea level and the annual rate of change from January 2013 to December 2050. The predicted annual rate of change in GMSL is 0.6 mm/year from 2013 to 2050. This contradicts the prediction from IPCC, which is between 1.0 and 2.0 mm a year [38]. But a higher annual rate of change (1.4 mm/year) is predicted from 2031 to 2050.

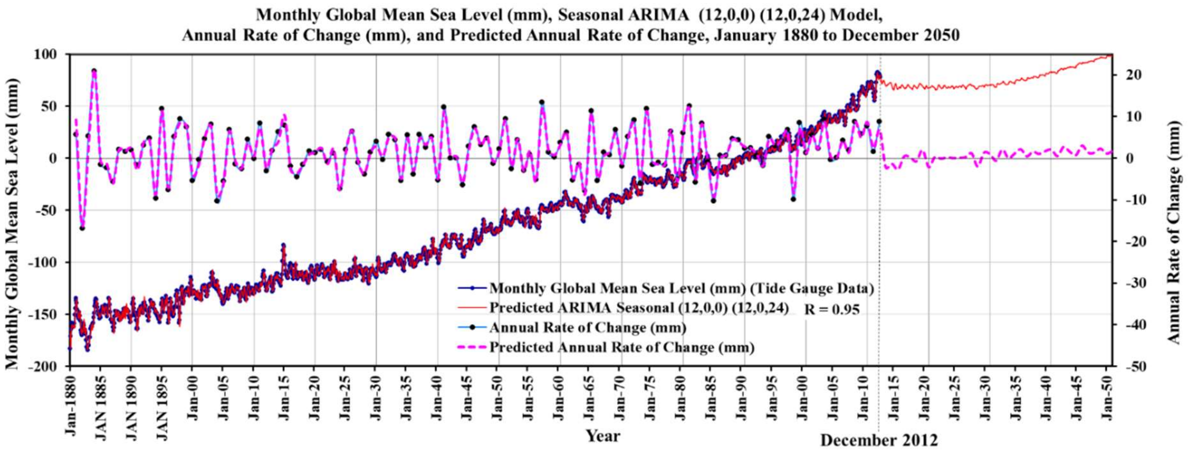

Data Source: CSIRO. Coastal Tide Gauge Records. http://www.cmar.csiro.au/sealevel/sl_data_cmar.html Accessed 22 March 2019

Figure 44 Predicted Monthly Global Mean Sea Level and Annual Rate of Change, January 2013 to December 2050

2.6 Sea Ice Extent

Sea ice extent is defined as the total surface area covered by sea ice above a certain concentration threshold (usually 15%) [39]. It has most commonly been derived from passive microwave imagery. Sea ice extent is a widely used polar climate indicator. Sea ice affects both global ocean temperatures and the global movement of ocean waters. The ocean is salty and when sea ice forms, much of the salt is pushed into the ocean water below the ice, although some salt may become trapped in small pockets between ice crystals. Water below sea ice has a higher concentration of salt and is denser than the surrounding ocean water, so it sinks and moves from the surface. In this way, sea ice contributes to the circulation of the global ocean conveyor belt. Cold, dense polar water descends from the surface and circulates along the ocean bottom toward the equator, while the warm water from mid-depth to the surface travels from the equator toward the poles [40].

2.6.1 ARIMA Modeling of Northern Hemisphere Monthly Sea Ice Extent

This section presents an example of ARIMA modeling for time series data of northern hemisphere monthly sea ice extent. The northern hemisphere sea ice extent is also known as the arctic sea ice extent. Figures 45 show the time series data of the northern hemisphere sea ice extent. This time series fails the Normality test and independence test (high autocorrelation 0.86 at Lag-1). From January 1979 to July 2019, total northern hemisphere monthly sea ice extent data points were 487 with a mean of 11.48 million km^2. Table 12 shows the maximum (16.34 million km^2) and minimum (3.57 million km^2) northern hemisphere monthly sea ice extent data were found on March 1979 and September 2012, respectively. For model verification purposes 2018 and 2019 data were set aside from the modeling database. Total model data points were 468 with an average of 11.49 million km^2.

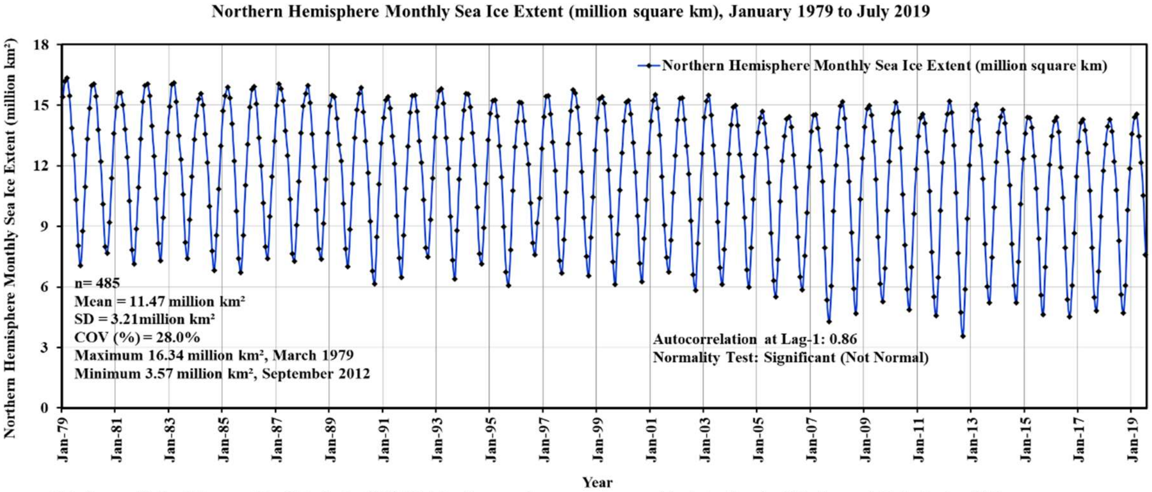
Northern Hemisphere Monthly Sea Ice Extent (million square km), January 1979 to July 2019

Data Source: National Snow and Ice Data Center (NSIDC) https://www.ncdc.noaa.gov/snow-and-ice/extent/sea-ice/N/0 Accessed 11 September 2019

Figure 45 Northern Hemisphere Monthly Sea Ice Extent, January 1979 to July 2019

Table 12 Descriptive Statistics of Northern Hemisphere Monthly Sea Ice Extent

Northern Hemisphere Sea Ice Extent (million square km), January 1979 to July 2019	
Summary Statistics	Northern Hemisphere Sea Ice Extent (million km²)
n	487
Mean	11.48
SD	3.21
COV (%)	28.0%
Maximum	16.34
Maximum Date	March, 1979
Minimum	3.57
Minimum Date	September, 2012
Autocorrelation at Lag-1	0.86
Normality Test	Significant (Not Normal)

The ACF and PACF plots of the original time series are shown in Figure 46 and Figure 47, respectively

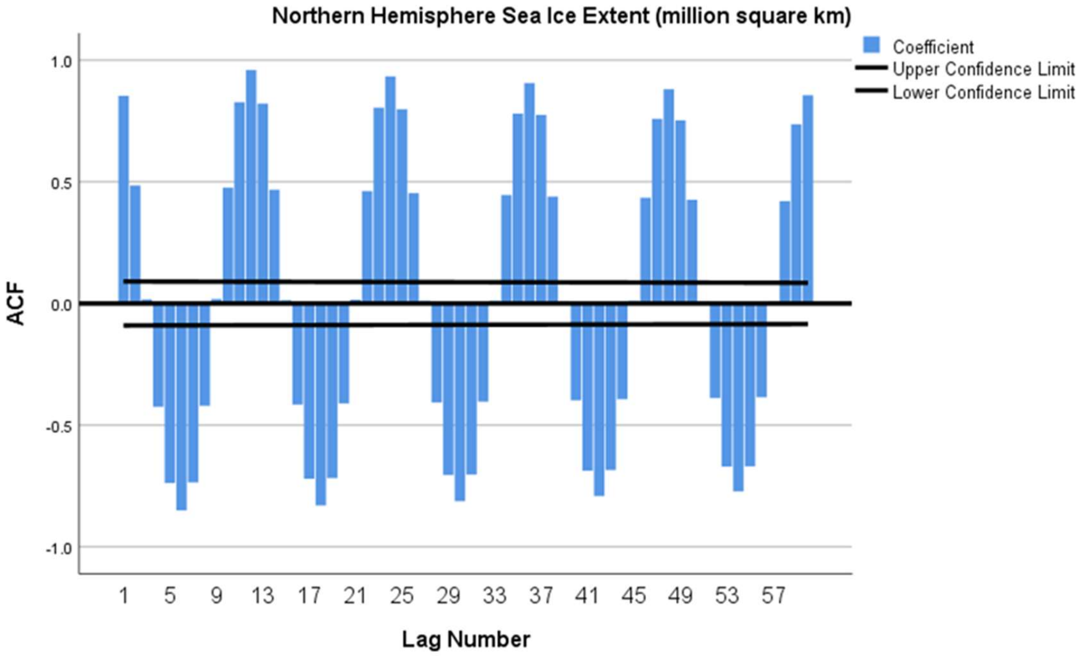

Figure 46 ACF Plot Northern Hemisphere Sea Ice Extent

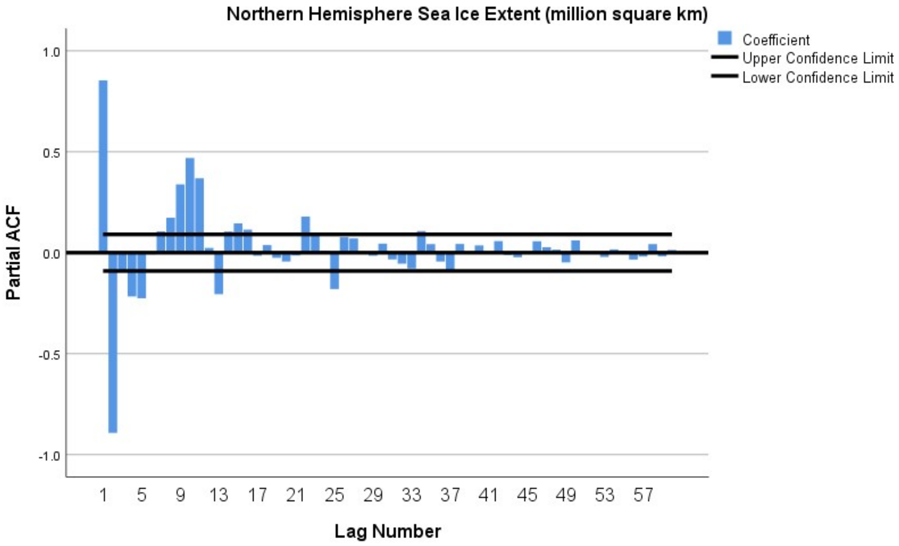

Figure 47 PACF Plot Northern Hemisphere Sea Ice Extent

Figure 48 shows the differencing order-1 plot for the original time series. The correlation R-value for the differencing order time series and the original time series is 0.27, which is more than 0.2. According to Appendix A, differencing order-1 (d = 0) should be used to make the series stationary.

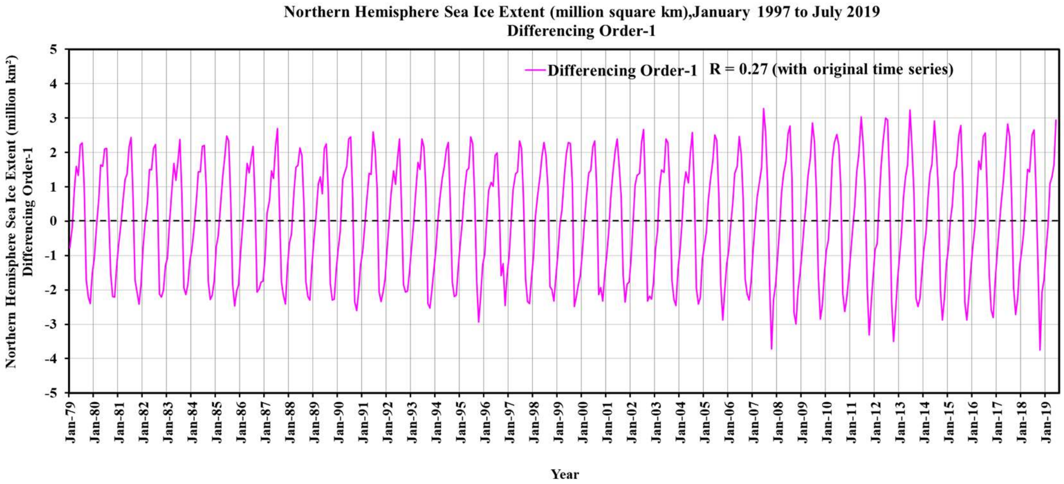

Figure 48 Differencing Order-1 Plot Northern Hemisphere Sea Ice Extent

Model diagnostics for selecting model terms were based on ACF and PACF plots (Figures 46 and 47) of the original time series. The first seasonal ARIMA model (1,0,2) (1,0,12) was tried (Figures 49 and 50).

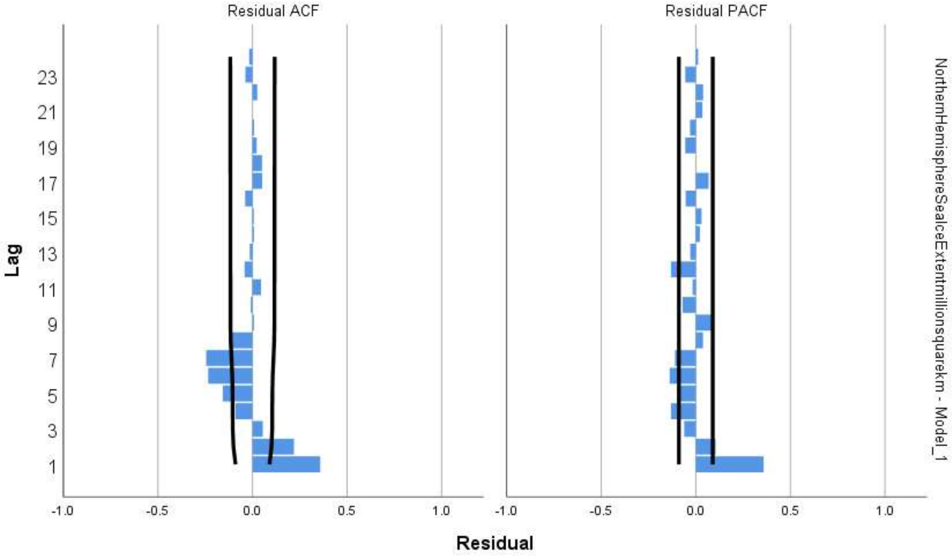

Figure 49 Residual ACF and Residual PACF plot of seasonal ARIMA Model (1,0,2) (1,0,12)

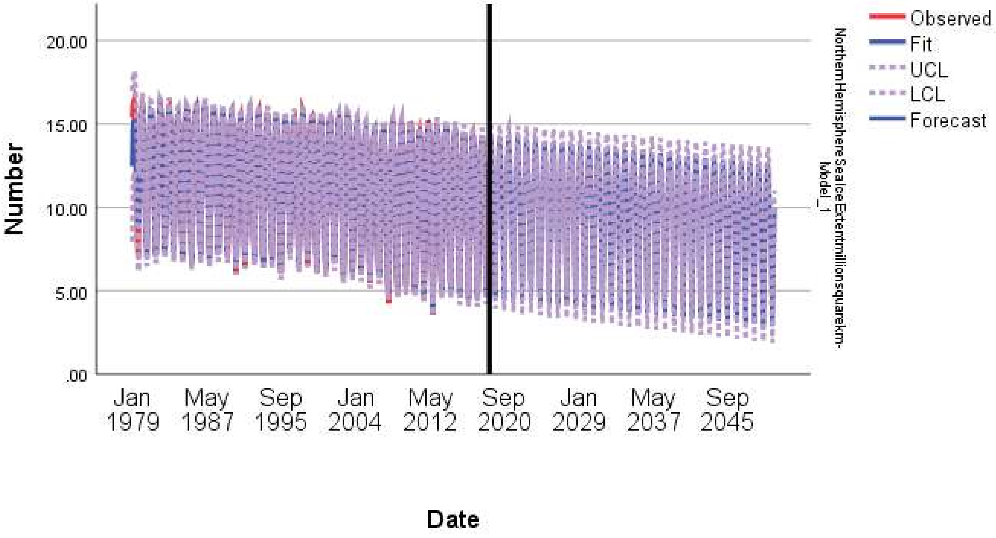

Figure 50 Seasonal ARIMA Model (1,0,2) (1,0,12) Prediction of Northern hemisphere Monthly Sea Ice Extent from January 2018 to December 2050

The residual ACF and PACF (Figure 49) and future prediction pattern (Figure 50) plots indicate the need to improve the prediction pattern in the (1,0,2) (1,0,12) model. Subsequently, 11 more models were tried. The prediction patterns of the models were not consistent with the pattern of the historic time series. Therefore, more models were tried and the residual ACF and PACF plots were examined. Two seasonal ARIMA models (1,0,18) (1,0,24) and (2,0,18) (2,0,24) had showed better residual ACF and PACF. The seasonal ARIMA model (1,0,18) (1,0,24) trial turned out to be the best model as shown by the residual ACF and PACF plots (Figure 51) and prediction pattern (Figure 52).

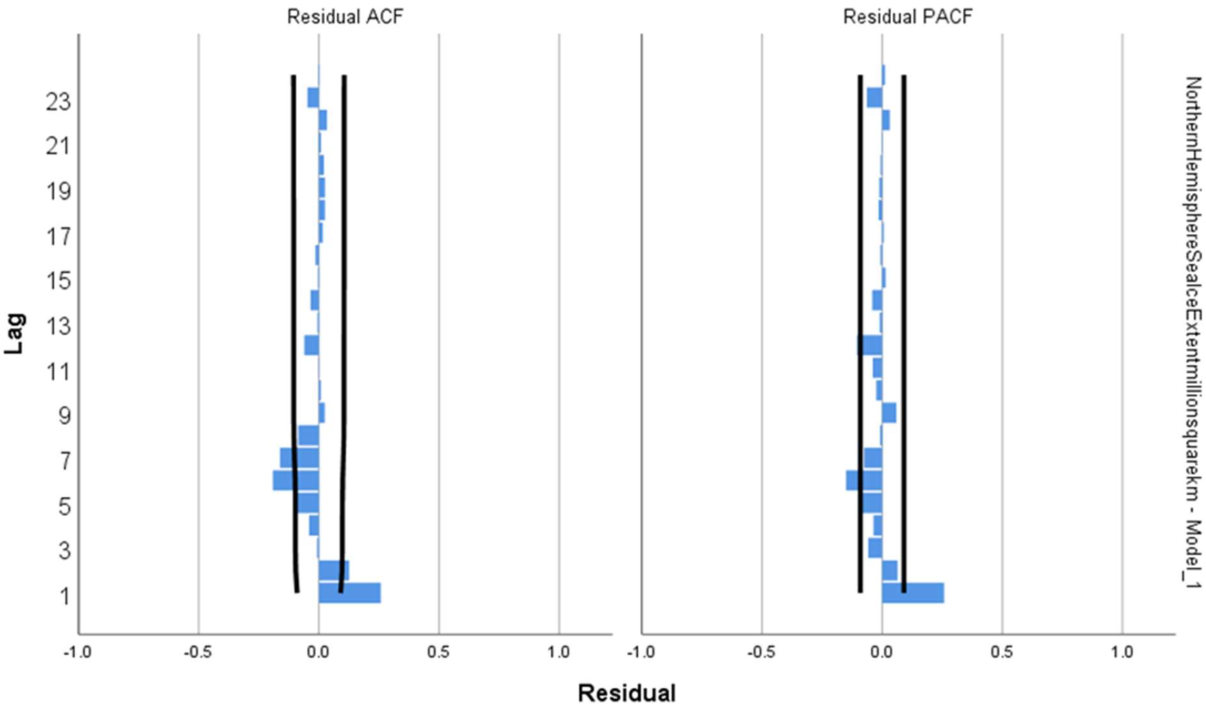

Figure 51 Residual ACF and Residual PACF plot of seasonal ARIMA Model (1,0,18) (1,0,24)

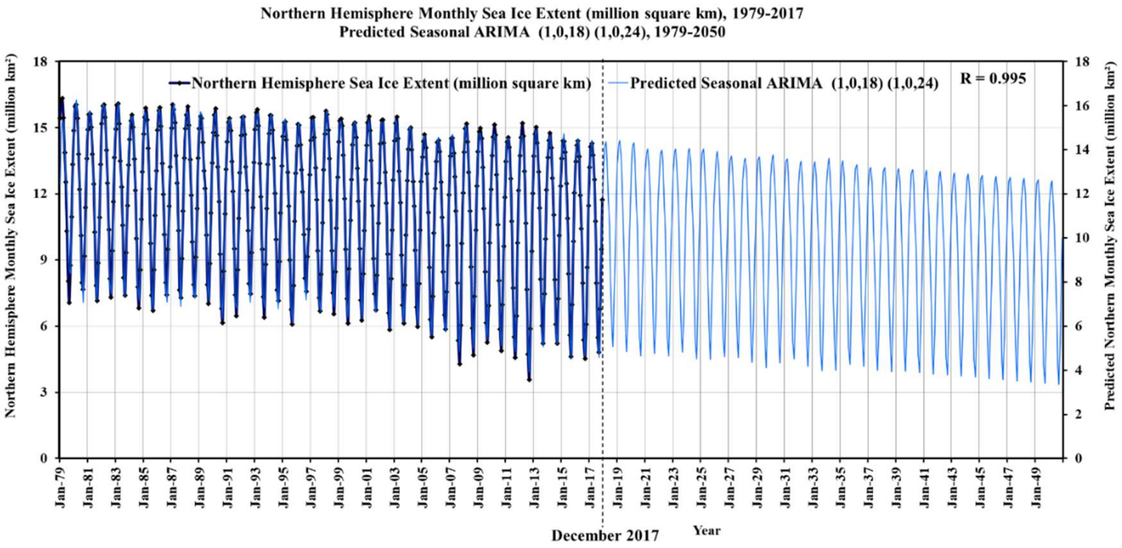

Figure 52 Seasonal ARIMA Model (1,0,18) (1,0,24) Prediction of Northern Hemisphere Monthly Sea Ice Extent from January 2018 to December 2050

The observed vs. predicted northern hemisphere monthly sea ice extent from 1979 to 2017 using the ARIMA model (1,0,18) (1,0,24) are shown in Figure 53 with a high correlation 0.995 R-value.

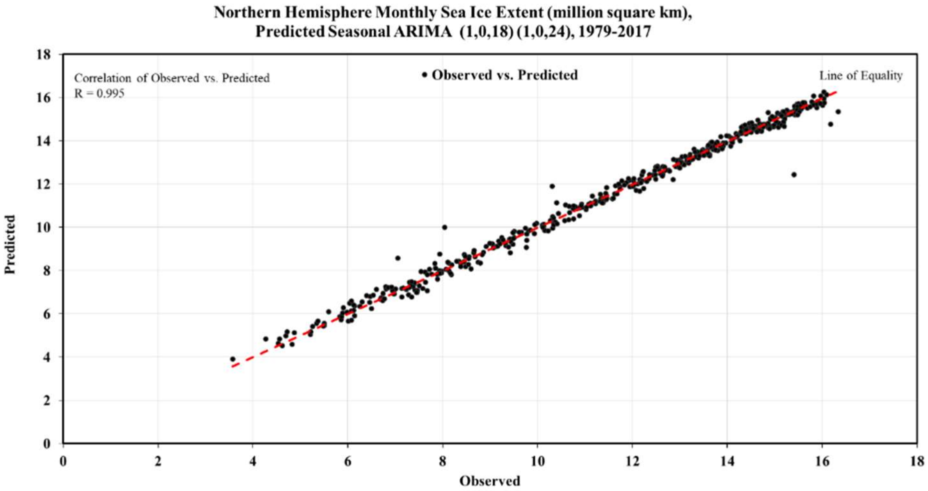

Figure 53 Observed vs. Predicted plot of Northern Hemisphere Monthly Sea Ice Extent using Seasonal ARIMA Model (1,0,18) (1,0,24)

Table 13 shows the verification for the year 2018 using seasonal ARIMA Models' prediction.

Table 13 Verification of Seasonal ARIMA Models using 2018 Measured Data

Northern Hemisphere Sea Ice Extent (million square km), January 2018 to December 2018				
			R = 0.995	R = 0.995
Cumulative Month No.	Month	Measured	Predicted Seasonal ARIMA (1,0,18) (1,0,24)	Predicted Seasonal ARIMA (2,0,18) (2,0,24)
469	Jan-18	13.06	13.23	13.28
470	Feb-18	13.95	14.13	14.12
471	Mar-18	14.3	14.36	14.26
472	Apr-18	13.71	13.55	13.52
473	May-18	12.21	12.14	12.12
474	Jun-18	10.78	10.65	10.56
475	Jul-18	8.27	8.14	8.03
476	Aug-18	5.61	5.85	5.75
477	Sep-18	4.71	5.07	5.05
478	Oct-18	6.06	6.99	6.92
479	Nov-18	9.8	9.47	9.45
480	Dec-18	11.86	11.86	11.86
January - December 2018	n	12	12	12
	Mean	10.4	10.5	10.4
	SD	3.4	3.3	3.3
	COV (%)	33.2%	31.5%	31.8%
	Mean Difference (%)		0.90%	0.48%
	RMSE		0.33	0.32
	MARE (%)		3.18%	3.14%

The following results are summarized for the better model (2,0,18) (2,0,24) for 2018 verification:

- the % mean difference in sea ice extent: 0.48%
- RMSE: 0.32
- MARE: 3.14%

Figure 54 and Figure 55 show seasonal ARIMA Model (1,0,18) (1,0,24) and (2,0,18) (2,0,24) prediction for 2018, respectively. Based on the mean difference, RMSE, MARE, and future prediction pattern, the better model is (2,0,18) (2,0,24).

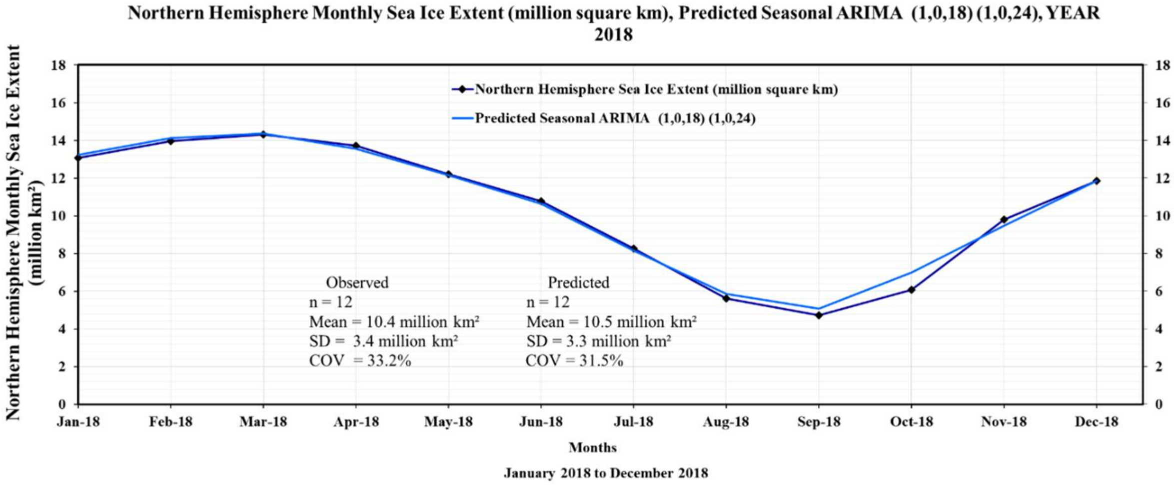

Figure 54 Observed and Seasonal ARIMA Model (1,0,18) (1,0,24) Prediction from January 2018 to December 2018

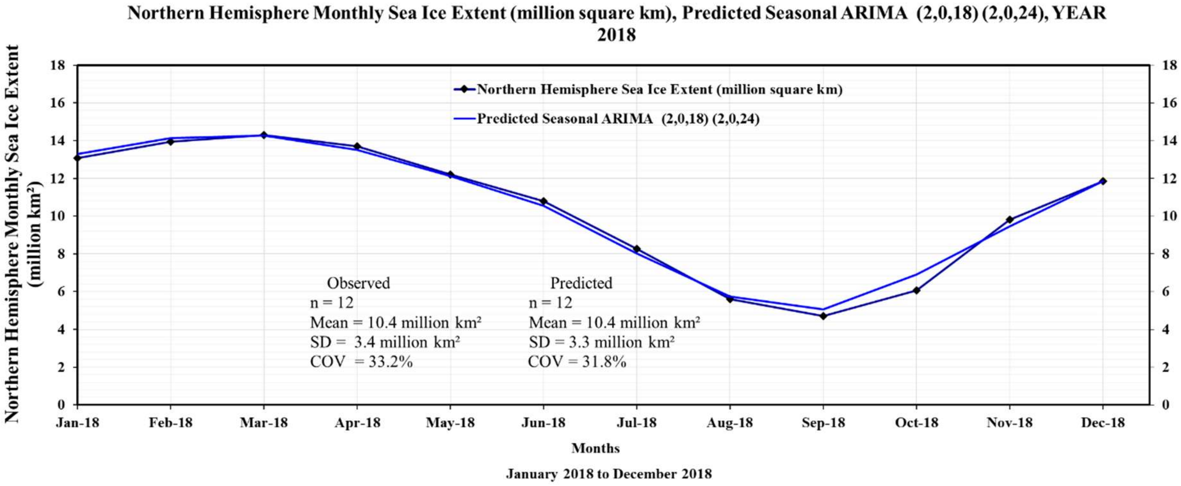

Figure 55 Observed and Seasonal ARIMA Model (2,0,18) (2,0,24) Prediction from January 2018 to December 2018

Table 14 shows the verification for the year 2019 using seasonal ARIMA Models' prediction.

Table 14 Verification of Seasonal ARIMA Models using 2019 Measured Data

Northern Hemisphere Sea Ice Extent (million square km), January 2019 to December 2019				
			R = 0.995	R = 0.995
Cumulative Month No.	Month	Measured	Predicted Seasonal ARIMA (1,0,18) (1,0,24)	Predicted Seasonal ARIMA (2,0,18) (2,0,24)
481	Jan-19	13.6	13.4	13.4
482	Feb-19	14.4	14.3	14.3
483	Mar-19	14.6	14.4	14.5
484	Apr-19	13.5	13.6	13.7
485	May-19	12.2	12.3	12.3
486	Jun-19	10.5	10.7	10.7
487	Jul-19	7.6	8.0	8.1
488	Aug-19	5.0	5.6	5.7
489	Sep-19	4.3	4.9	4.9
490	Oct-19	5.7	6.7	6.8
491	Nov-19	9.3	9.4	9.4
492	Dec-19	12.0	11.8	11.8
January - December 2019	n	12	12	12
	Mean	10.2	10.4	10.5
	SD	3.8	3.4	3.4
	COV (%)	36.8%	32.9%	32.8%
	Mean Difference (%)		1.98%	2.38%
	RMSE		0.42	0.44
	MARE (%)		4.80%	5.05%

The following results are summarized for the better model (1,0,18) (1,0,24) for 2019 verification:

- the % mean difference in sea ice extent: 1.98%
- RMSE: 0.42
- MARE: 4.80%

Figure 56 and Figure 57 show seasonal ARIMA Model (1,0,18) (1,0,24) and (2,0,18) (2,0,24) prediction for 2019, respectively. Based on the mean difference, RMSE, MARE, and future prediction pattern, the better model is (1,0,18) (1,0,24).

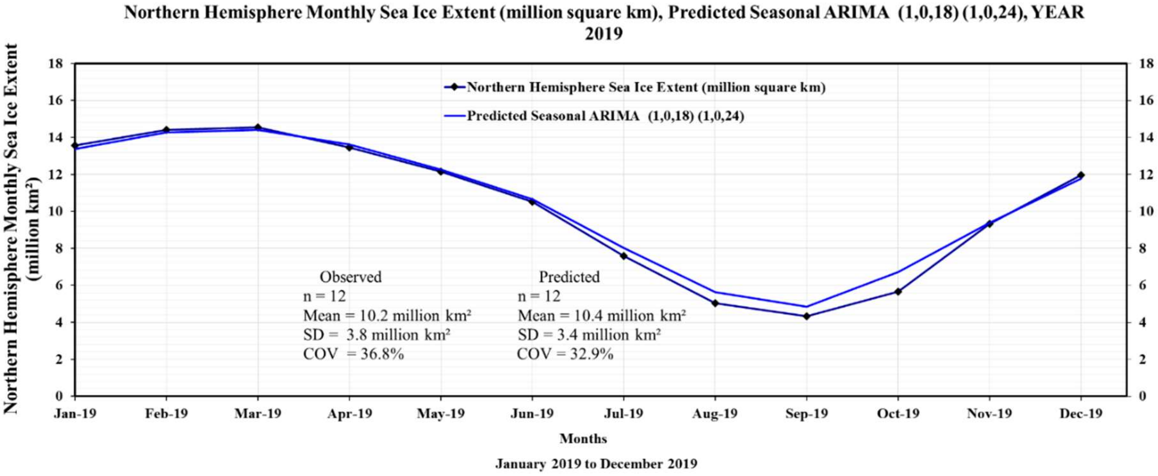

Figure 56 Observed and Seasonal ARIMA Model (1,0,18) (1,0,24) Prediction from January 2019 to December 2019

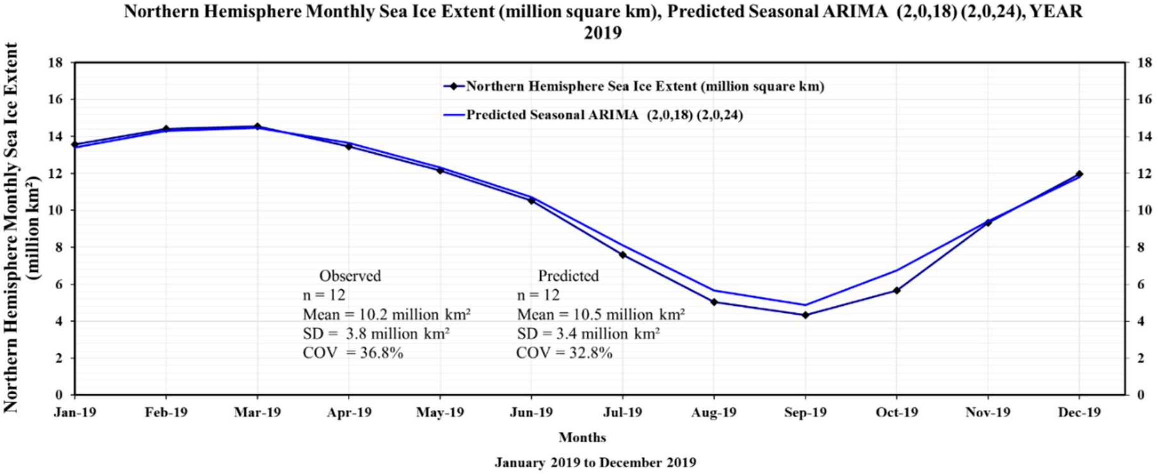

Figure 57 Observed and Seasonal ARIMA Model (2,0,18) (2,0,24) Prediction from January 2019 to December 2019

Based on the observed vs. predicted results from 1979 to 2017 (Figure 53), the future prediction from 2018 to 2050, the verification results of the year 2018 and 2019, the seasonal ARIMA model (1,0,18) (1,0,24) was chosen as the best model. Equation 5 shows the terms of seasonal ARIMA (1,0,18) (1,0,24) model.

$$
\begin{aligned}
Y_t = C + (1 - \phi_1 B^1) * (1 - \Phi_1 B^S) * (1 - \theta_1 B^1 - \theta_2 B^2 - \cdots \ldots \ldots - \theta_{18} B^{18}) \\
* (1 - \theta_1 B^{1S} - \theta_2 B^{2S} - \cdots \ldots \ldots - \theta_{24} B^{24S}) \\
* a_t \qquad\qquad Eq. 5
\end{aligned}
$$

Y_t = Discrete time series

C = Constant

$1 - \phi_1 B^1$ = Regular Autoregressive process of order 1

$1 - \Phi_1 B^S$ = Seasonal Autoregressive process of order 1

$1 - \theta_1 B^1 - \theta_2 B^2 - \cdots \ldots \ldots - \theta_{18} B^{18}$ = Regular Moving Average process of order 18

$1 - \theta_1 B^{1S} - \theta_2 B^{2S} - \cdots \ldots \ldots - \theta_{24} B^{24S}$ = Seasonal Moving Average process of order 24

a_t = random shock term; normally distributed, independent with zero mean, and variance equal to σ_a

2.6.2 ARIMA Modeling of Southern Hemisphere Monthly Sea Ice Extent

This section presents an example of ARIMA modeling for time series data of southern hemisphere monthly sea ice extent. Southern hemisphere sea ice extent is also known as Antarctic sea ice extent. Figures 58 shows the time series data of southern hemisphere sea ice extent. This time series fails the Normality test and independence test (high autocorrelation 0.85 at Lag-1). From January 1979 to July 2019, total southern hemisphere monthly sea ice extent data points were 487 with a mean of 11.55 million km^2. Table 15 shows the maximum (19.76 million km^2) and minimum (2.29 million km^2) northern hemisphere monthly sea ice extent data were found on September 2014 and February 2017, February 2018, respectively. For model verification purposes 2018 and 2019 data were set aside from the modeling database. Total model data points were 468 with an average of 11.62 million km^2.

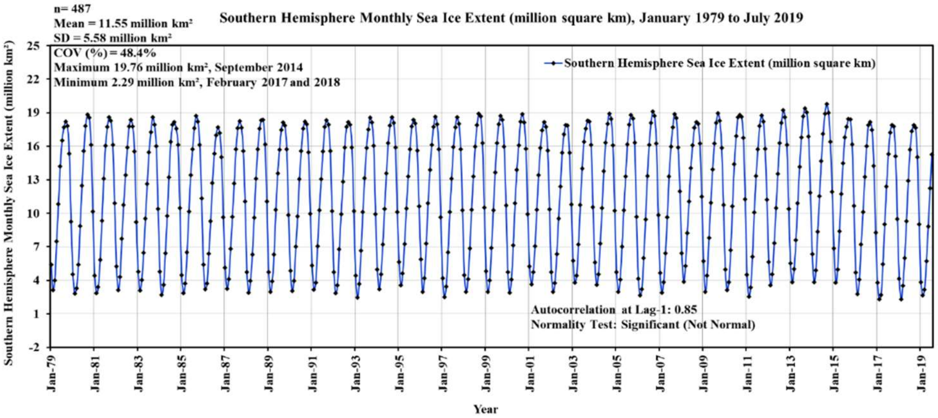

Figure 58 Southern Hemisphere Monthly Sea Ice Extent, January 1979 to July 2019

Table 15 Descriptive Statistics of Southern Hemisphere Monthly Sea Ice Extent

Southern Hemisphere Sea Ice Extent (million square km), January 1979 to July 2019	
Summary Statistics	Southern Hemisphere Sea Ice Extent (million km²)
n	487
Mean	11.55
SD	5.58
COV (%)	48.4%
Maximum	19.76
Maximum Date	September, 2014
Minimum	2.29
Minimum Date	February 2017 and February 2018
Autocorrelation at Lag-1	0.85
Normality Test	Significant (Not Normal)

The ACF and PACF plots of the original time series are shown in Figure 59 and Figure 60, respectively

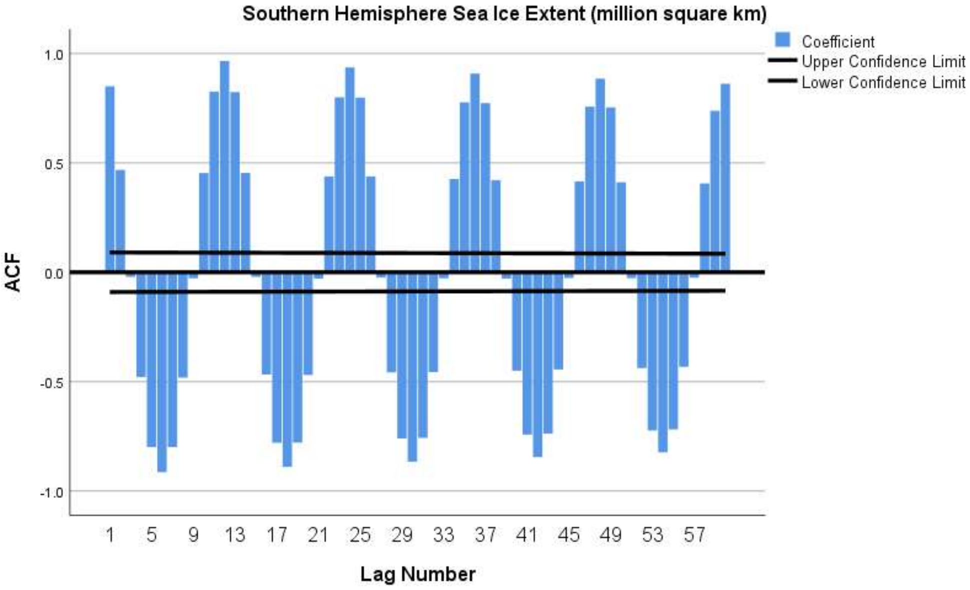

Figure 59 ACF Plot Southern Hemisphere Sea Ice Extent

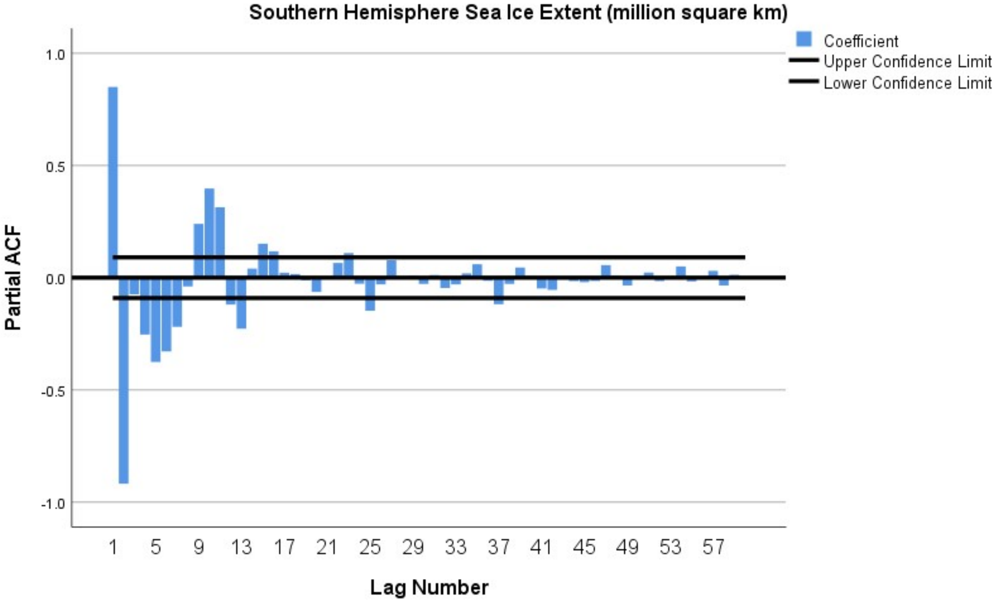

Figure 60 PACF Plot Southern Hemisphere Sea Ice Extent

Figure 61 shows the differencing order-1 plot for the original time series. The correlation R-value for the differencing order time series and the original time series is 0.27, which is more than 0.2. According to Appendix A, differencing order-1 (d = 0) should be used to make the series stationary.

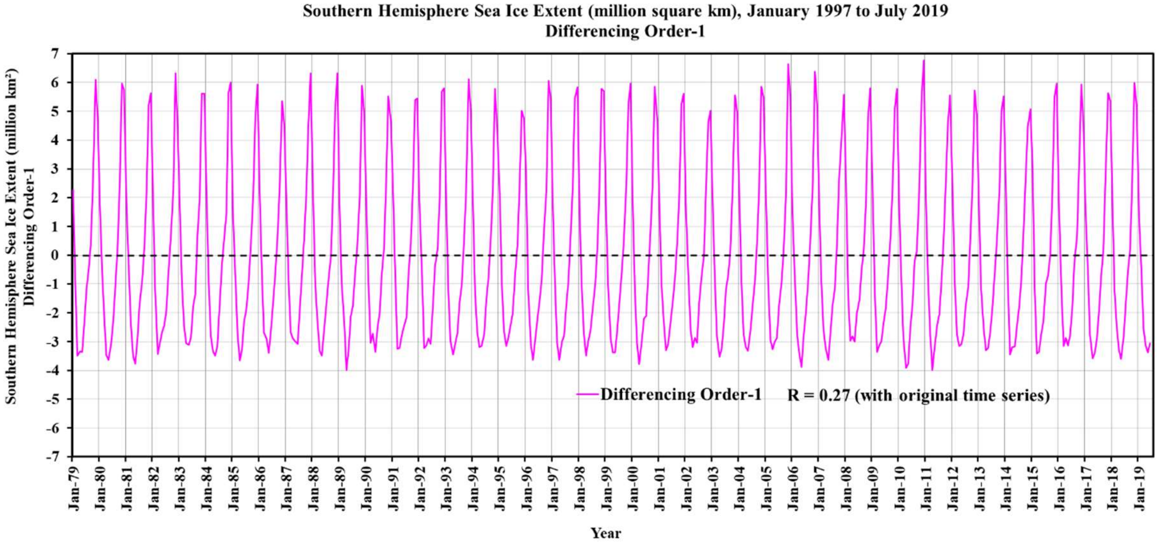

Figure 61 Differencing Order-1 Plot Southern Hemisphere Sea Ice Extent

Model diagnostics for selecting model terms were based on ACF and PACF plots (Figures 59 and 60) of the original time series. The best model for the Northern Hemisphere Monthly Sea Ice Extent was the seasonal ARIMA model (1,0,18) (1,0,24). Since, the original time series of Southern Hemisphere Monthly Sea Ice Extent, ACF, and PACF plot was following the same pattern as Northern Hemisphere Monthly Sea Ice Extent, the first seasonal ARIMA model (1,0,18) (1,0,24) was tried (Figures 62 and 63).

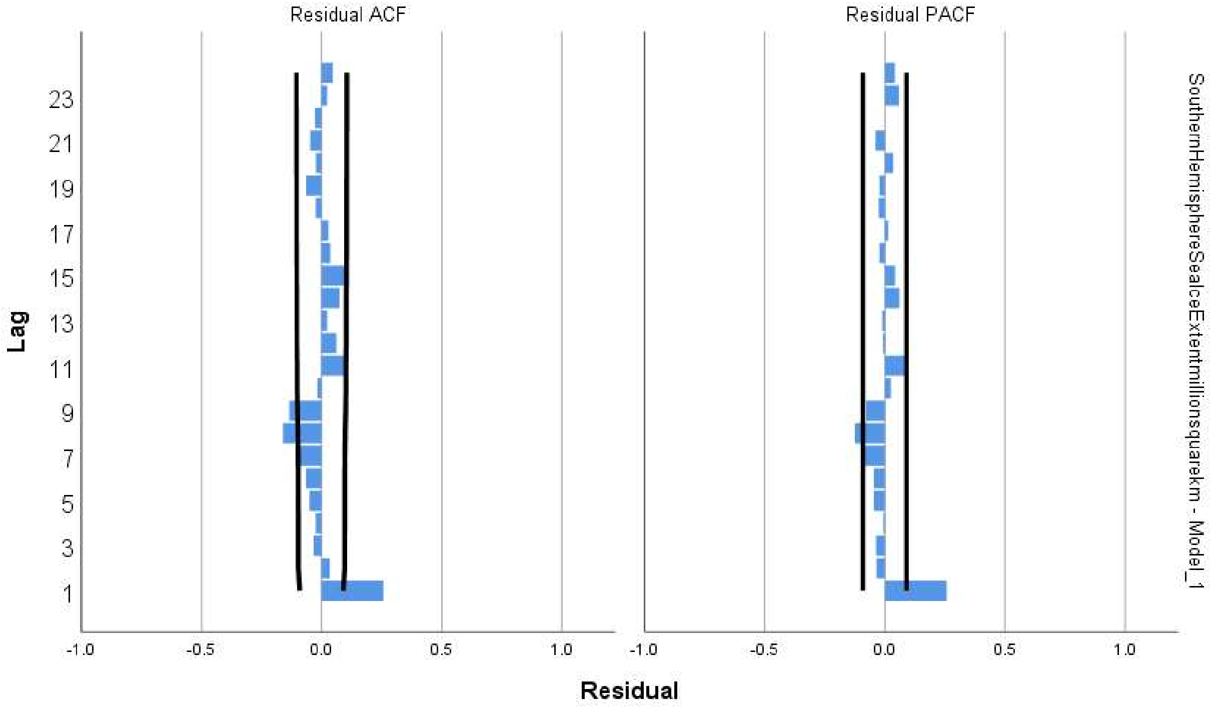

Figure 62 Residual ACF and Residual PACF plot of seasonal ARIMA Model (1,0,18) (1,0,24)

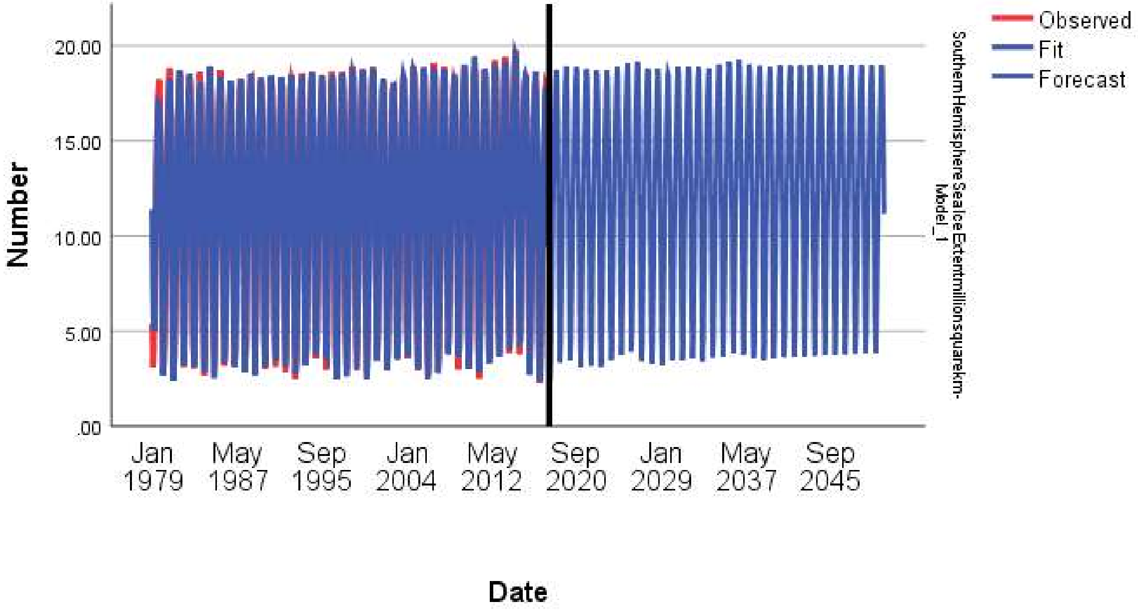

Figure 63 Seasonal ARIMA Model (1,0,18) (1,0,24) Prediction of Southern hemisphere Monthly Sea Ice Extent from January 2018 to December 2050

The residual ACF and PACF (Figure 62) and future prediction pattern (Figure 63) plots indicate the need to improve the prediction pattern in the (1,0,18) (1,0,24) model. Subsequently, three more models were tried. The prediction patterns of the models were not consistent with the pattern of the historic time series. Therefore, more models were tried and the residual ACF and PACF plots were examined. Two seasonal ARIMA models (8,0,18) (8,0,24) and (12,0,18) (12,0,24) had showed better residual ACF and PACF. The seasonal ARIMA model (12,0,18) (12,0,24) trial turned out to be the best model as shown by the residual ACF and PACF plots (Figure 64) and prediction pattern (Figure 65).

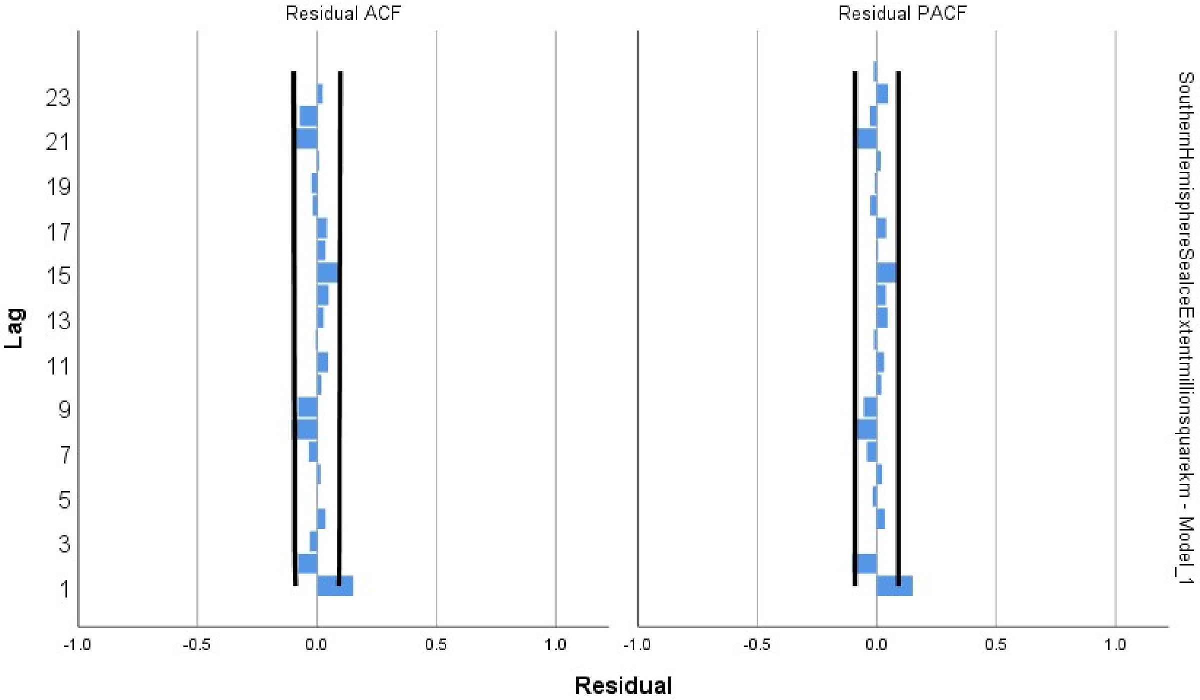

Figure 64 Residual ACF and Residual PACF plot of seasonal ARIMA Model (12,0,18) (12,0,24)

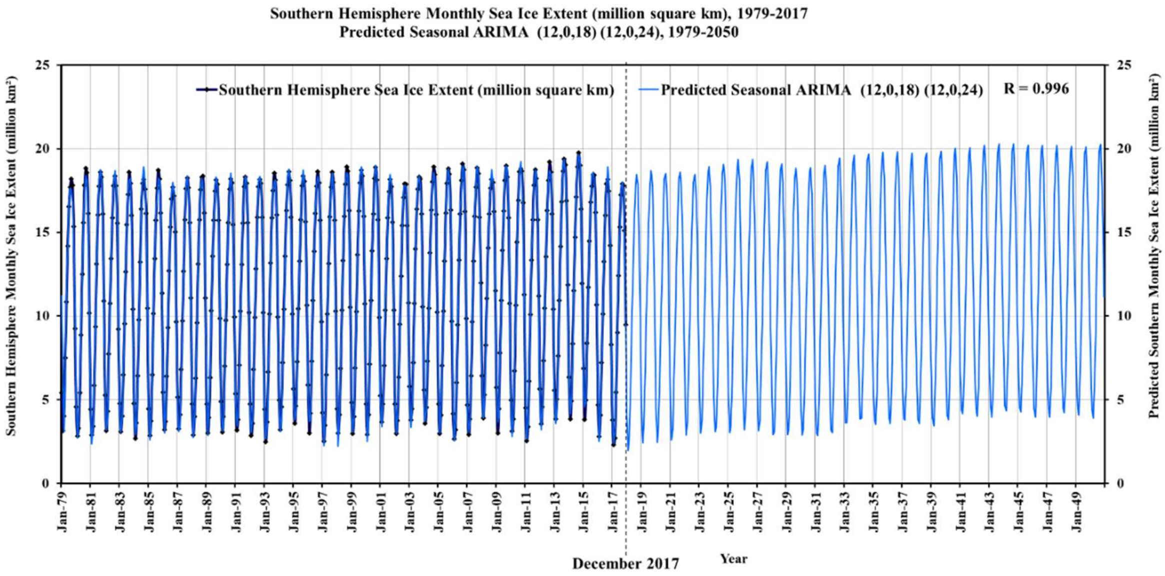

Data Source: National Snow and Ice Data Center (NSIDC) https://www.ncdc.noaa.gov/snow-and-ice/extent/sea-ice/S/0 Accessed 11 September 2019

Figure 65 Seasonal ARIMA Model (12,0,18) (12,0,24) Prediction of Southern Hemisphere Monthly Sea Ice Extent from January 2018 to December 2050

The observed vs. predicted northern hemisphere monthly sea ice extent from 1979 to 2017 using the ARIMA model (12,0,18) (12,0,24) are shown in Figure 66 with a high correlation 0.995 R-value.

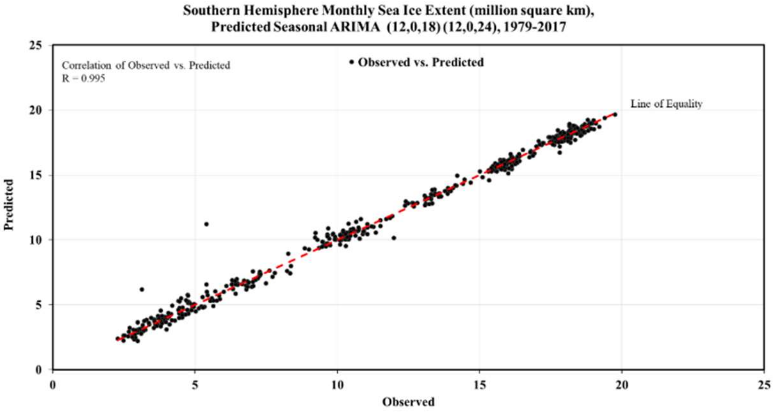

Figure 66 Observed vs. Predicted plot of Southern Hemisphere Monthly Sea Ice Extent using Seasonal ARIMA Model (12,0,18) (12,0,24)

Table 16 shows the verification for the year 2018 using seasonal ARIMA Models' prediction.

Table 16 Verification of Seasonal ARIMA Models using 2018 Measured Data

Southern Hemisphere Sea Ice Extent (million square km), January 2018 to December 2018				
			R = 0.996	R = 0.995
Cumulative Month No.	Month	Measured	Predicted Seasonal ARIMA (12,0,18) (12,0,24)	Predicted Seasonal ARIMA (8,0,18) (8,0,24)
469	Jan-18	4.13	4.04	4.10
470	Feb-18	2.29	1.94	2.19
471	Mar-18	3.53	2.76	3.32
472	Apr-18	6.01	5.8	6.27
473	May-18	9.29	9.23	9.92
474	Jun-18	12.89	12.54	13.07
475	Jul-18	15.7	15.32	15.50
476	Aug-18	17.34	17.57	17.44
477	Sep-18	17.88	18.46	18.58
478	Oct-18	17.66	17.85	18.32
479	Nov-18	15.01	14.91	15.95
480	Dec-18	9.03	9.82	10.99
January - December 2018	n	12	12	12
	Mean	10.9	10.9	11.3
	SD	5.9	6.1	6.1
	COV (%)	54.2%	56.4%	53.9%
	Mean Difference (%)		-0.4%	3.7%
	RMSE		0.42	0.72
	MARE (%)		5.30%	5.08%

The following results are summarized for the better model (12,0,18) (12,0,24) for 2018 verification:

- the % mean difference in sea ice extent: 0.4%
- RMSE: 0.42
- MARE: 5.30%

Figure 67 and Figure 68 show seasonal ARIMA Model (12,0,18) (12,0,24) and (8,0,18) (8,0,24) prediction for 2018, respectively. Based on the mean difference, RMSE, MARE, and future prediction pattern, the better model is (12,0,18) (12,0,24).

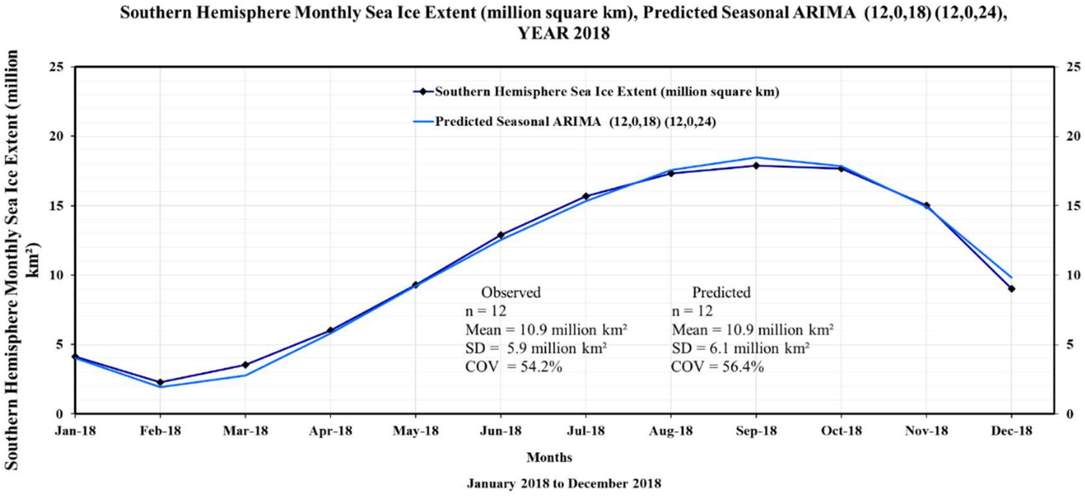

Figure 67 Observed and Seasonal ARIMA Model (12,0,18) (12,0,24) Prediction from January 2018 to December 2018

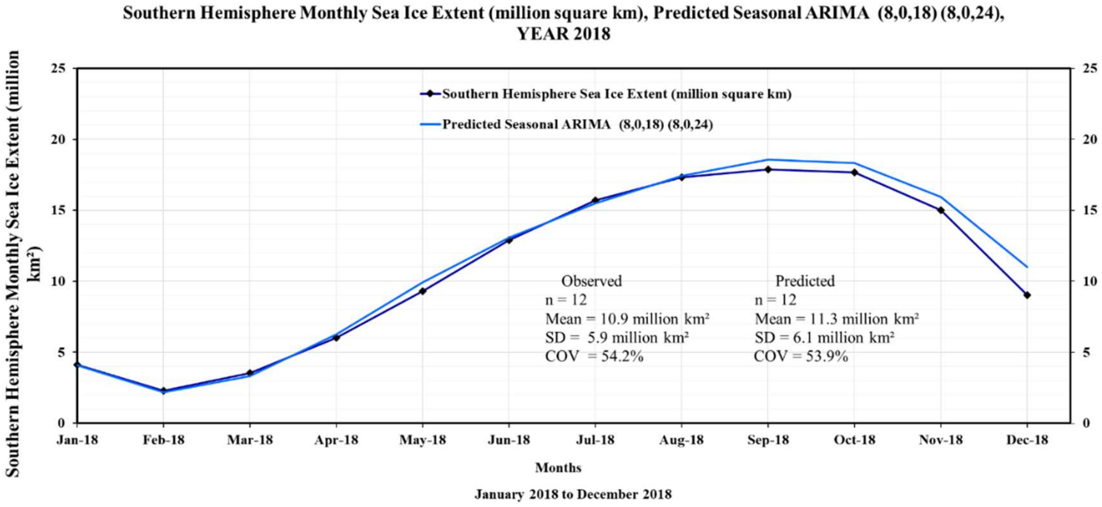

Figure 68 Observed and Seasonal ARIMA Model (8,0,18) (8,0,24) Prediction from January 2018 to December 2018

Table 17 shows the verification for the year 2019 using seasonal ARIMA Models' prediction.

Table 17 Verification of Seasonal ARIMA Models using 2019 Measured Data

Southern Hemisphere Sea Ice Extent (million square km), January 2019 to December 2019				
			R = 0.996	R = 0.995
Cumulative Month No.	Month	Measured	Predicted Seasonal ARIMA (12,0,18) (12,0,24)	Predicted Seasonal ARIMA (8,0,18) (8,0,24)
481	Jan-19	3.83	4.63	5.68
482	Feb-19	2.66	2.42	3.12
483	Mar-19	3.16	3.42	4.38
484	Apr-19	5.71	6.74	7.62
485	May-19	8.84	9.92	10.83
486	Jun-19	12.22	12.92	13.9
487	Jul-19	15.27	15.66	16.36
488	Aug-19	17.48	17.9	18.0
489	Sep-19	18.24	18.7	18.9
490	Oct-19	17.85	17.8	18.3
491	Nov-19	14.89	14.9	15.8
492	Dec-19	9.3	9.5	10.3
January - December 2019	n	12	12	12
	Mean	10.8	11.2	11.9
	SD	6.0	5.9	5.7
	COV (%)	55.5%	52.9%	48.0%
	Mean Difference (%)		3.87%	10.54%
	RMSE		0.58	1.27
	MARE (%)		6.98%	17.20%

The following results are summarized for the better model (12,0,18) (12,0,24) for 2019 verification:

- the % mean difference in sea ice extent: 3.57%
- RMSE: 0.58
- MARE: 6.98%

Figure 69 and Figure 70 show seasonal ARIMA Model (12,0,18) (12,0,24) and (8,0,18) (8,0,24) prediction for 2019, respectively. Based on the mean difference, RMSE, MARE, and future prediction pattern, the better model is (12,0,18) (12,0,24).

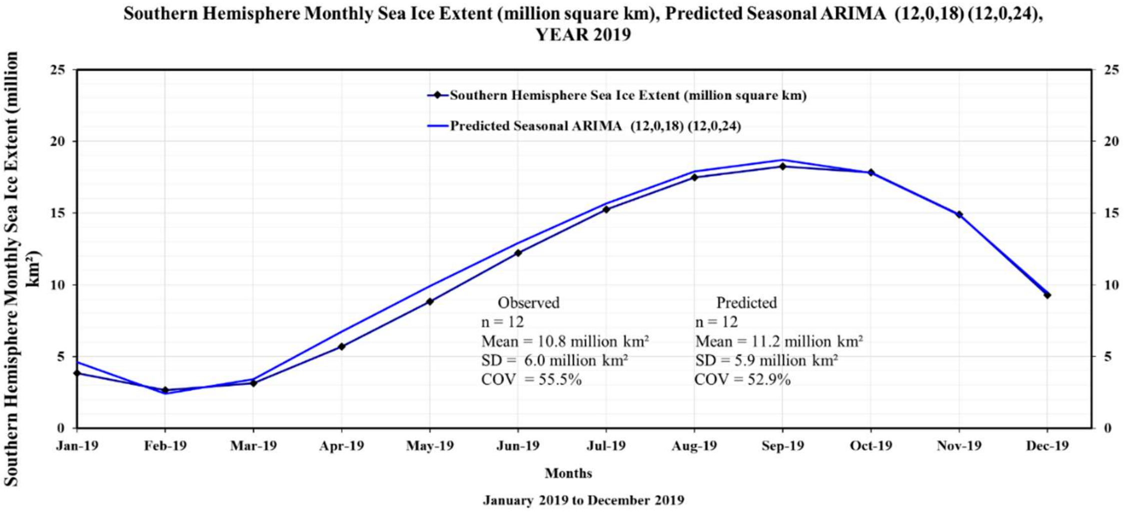

Figure 69 Observed and Seasonal ARIMA Model (12,0,18) (12,0,24) Prediction from January 2019 to December 2019

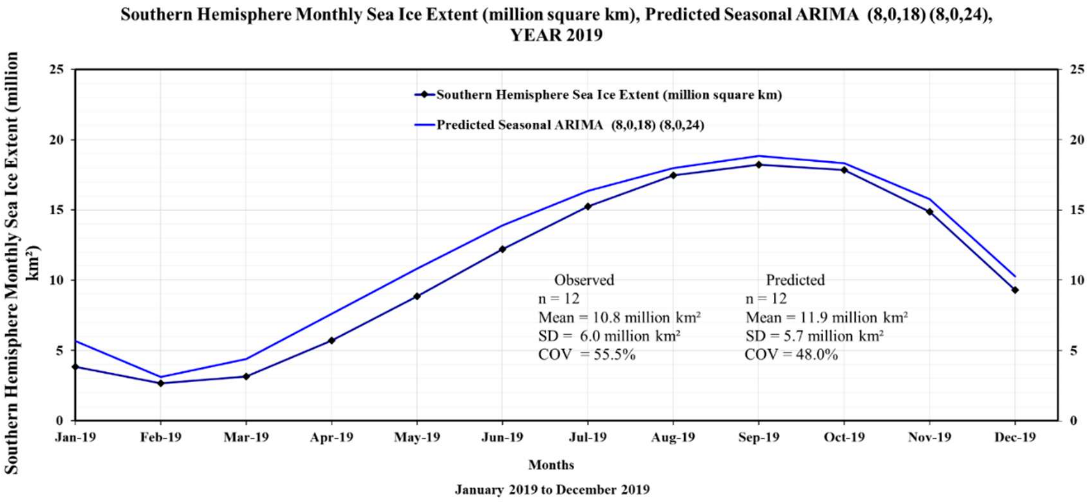

Figure 70 Observed and Seasonal ARIMA Model (8,0,18) (8,0,24) Prediction from January 2019 to December 2019

Based on the observed vs. predicted results from 1979 to 2017 (Figure 66), the future prediction from 2018 to 2050, the verification results of the year 2018 and 2019, the seasonal ARIMA model (12,0,18) (12,0,24) was chosen as the best model. Equation 6 shows the terms of seasonal ARIMA (12,0,18) (12,0,24) model.

$$\begin{aligned} Y_t \; = \; C \; + \; & (1 - \phi_1 B^1 - \phi_2 B^2 - \cdots \ldots \ldots - \phi_{12} B^{12}) \\ & * (1 - \Phi_1 B^S - \Phi_2 B^{2S} - \cdots \ldots \ldots - \Phi_{12} B^{12} \;) \\ & * (1 - \theta_1 B^1 - \theta_2 B^2 - \cdots \ldots \ldots - \theta_{18} B^{18}) \\ & * (1 - \theta_1 B^{1S} - \theta_2 B^{2S} - \cdots \ldots \ldots - \theta_{24} B^{24} \;) \\ & * \; a_t \qquad\qquad\qquad\qquad\qquad\qquad\qquad\qquad Eq. 6 \end{aligned}$$

Y_t = Discrete time series

C = Constant

$1 - \phi_1 B^1 - \phi_2 B^2 - \cdots \ldots \ldots - \phi_{12} B^{12}$ = Regular Autoregressive process of order 12

$(1 - \Phi_1 B^S - \Phi_2 B^{2S} - \cdots \ldots \ldots - \Phi_{12} B^{12S})$= Seasonal Autoregressive process of order 12

$1 - \theta_1 B^1 - \theta_2 B^2 - \cdots \ldots \ldots - \theta_{18} B^{18}$ = Regular Moving Average process of order 18

$1 - \theta_1 B^{1S} - \theta_2 B^{2S} - \cdots \ldots \ldots - \theta_{24} B^{24S}$ = Seasonal Moving Average process of order 24

a_t = random shock term; normally distributed, independent with zero mean, and variance equal to σ_a

As discussed above, the best model found for Northern hemisphere sea ice extent and southern hemisphere sea ice extent is the seasonal ARIMA model (1,0,18) (1,0,24) and (12,0,18) (12,0,24), respectively. The future predictions of these models were used to calculate the net change in global sea ice extent in 2050. The model prediction shows that the total loss of northern hemisphere sea ice extent in 2050 will be 1.66 million km^2. But the total gain of southern hemisphere sea ice extent will be 1.24 million km^2. The net change of global sea ice extent will be -0.24 million km^2, which indicates a loss of sea ice. The calculation process is given below:

2050 predicted average annual Northern hemisphere sea ice extent = 8.74 million km^2

2018 average annual Northern hemisphere sea ice extent = 10.4 million km^2

2050 vs. 2018 change = (8.74-10.4) = -1.66 million km^2

2050 vs. 2018 percent change = ((8.74-10.4)/10.4)*100 = -16%

2050 predicted average annual Southern hemisphere sea ice extent = 12.14 million km^2\

2018 average annual Southern hemisphere sea ice extent = 10.9 million km^2

2050 vs. 2018 change = (12.14-10.9) = 1.24 million km^2

2050 vs. 2018 percent change = ((12.14-10.9)/10.9)*100 = 11.4%

Total 2017 for global sea ice extent = 10.42+10.7 = 21.12 million km^2

Total 2050 for global sea ice extent = 8.74+12.14 = 20.88 million km^2

Net Change 2050 vs 2017 = 20.88-21.12 = -0.24 million km^2

2.7 Implementation of Models for Climate Attributes

The model predictions of the climate attributes can be used to understand and assess the future climate change in different climate zones worldwide. The predicted ENSO episodes can contribute to better predict long-term weather and climate changes. This understanding of climate changes and future predictions of climate attributes will help to develop climate adaptation strategies and better prepare the communities for extreme weather-related natural disaster occurrences.

2.8 Concluding Remarks

Several climate attribute models were developed in this chapter. The key concluding remarks for these models are discussed below:

- The best model found for SST is the seasonal ARIMA model (24,0,0) (24,0,36). The model successfully predicted the 2018-2019 El Niño year. The model prediction shows that the next El Niño years will be 2021-22 and 2025-26. The model prediction also shows that the next La Niña year will be 2028-29.
- The best model found for GMSL is the seasonal ARIMA model (12,0,0) (12,0,24). The predicted annual rate of change in GMSL is 0.6 mm/year from 2013 to 2050. This contradicts the prediction from IPCC, which is between 1.0 and 2.0 mm a year [42]. But a higher annual rate of change (1.4 mm/year) is predicted from 2031 to 2050.
- The best model found for northern hemisphere sea ice extent and southern hemisphere sea ice extent is the seasonal ARIMA model (1,0,18) (1,0,24) and (12,0,18) (12,0,24), respectively. The model prediction shows that the total loss of northern hemisphere sea ice extent in 2050 will be 1.66 million km^2. But the total gain of southern hemisphere sea ice extent will be 1.24 million km^2. The net change of global sea ice extent will be -0.24 million km^2, which indicates a loss of sea ice.

CHAPTER III: ARTIFICIAL NEURAL NETWORKS (ANNS)

3.1 Overview of ANN

3.1.1 Definition

Artificial Neural Network, ANN, is an information processing computational tool during which highly interconnected processing neurons work together to investigate and solve a complex problem in a nontraditional manner [41]. The unique power of ANNs, which emulate the biological nervous system, lies in the tremendous number of interconnections between their neurons or processing elements because they provide significant advantages by learning from examples, producing meaningful and cost-effective solutions to numerous problems, neglecting the minor errors such as a small difference between the predicted and measured value [41]. ANNs adapt themselves to changing circumstances and process information quickly to come up with desired outputs [41]. ANNs store data among the individual neurons of the network and process data in a parallel and distributed manner.

The following explanation of the ANN modeling method is discussed by Hossain et al. [42]:

- ANN consists of three building blocks (1) input neurons or processing elements, representing the input for the problem, (2) connecting links known as axons, which connect input and output neurons and represent the connection weights that associate the input with the output, and (3) output neurons, or processing elements representing the output for the problem.

- ANNs can be composed of a single layer or many layers, depending on the complexity of the data.
- Multilayered neural networks have more than one hidden layer consisting of neurons with no direct connection to either the input or the output of the network, preferably they are used to further refine the training process by adjusting the connecting weights for the networks. These connection weights are applied to the links connecting the input to the output.
- Overall, ANNs are a proven alternative to conventional function approximation methods, which are very often limited by strict assumptions of normality, linearity, and variable independence.
- The power of ANNs to capture different relationships allows users to quickly and comparatively easily develop the specified model.
- ANNs offer some advantages. They require less formal statistical training, they can implicitly detect complex nonlinear relationships between dependent and independent variables, they can detect all possible interactions between predictor variables, and there are multiple training algorithms available.

3.1.2 Elements

The architecture of a typical ANN consists of some hidden nodes that are usually arranged in layers such as an input layer, hidden layers, and an output layer [10]. Figure 71 shows a typical ANN model structure. These layers are described as follows:

- Input Layer: This layer consists of independent variables used in the model.
- Hidden Layer: This layer consists of hidden nodes. The hidden layer can be one or more and each hidden layer can contain a different number of hidden nodes.
- Output Layer: This layer consists of the dependent variable used in the model.

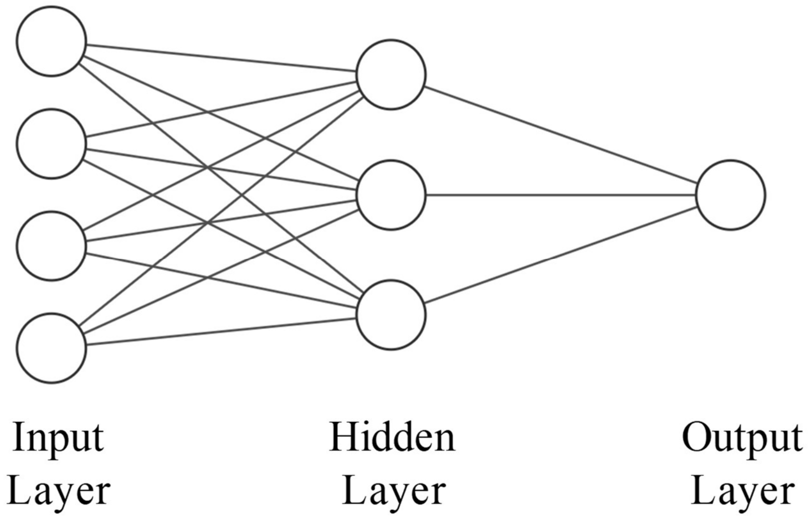

Figure 71 Typical ANN Model Structure

3.2 Feed-Forward Network and Error Backpropagation Learning Algorithm

There are several layers and a specific number of neurons in a neural network with a backpropagation algorithm. The inputs directly affect the output phenomenon. The output neuron(s) which signifies the solution of the phenomenon is contained by the output layer. The hidden layer is in between the input and output layers. It is designed to not have contact with the outside environment. Numerous studies have discovered only one hidden layer can approximate any function with finitely many discontinuities to arbitrary precision [43]. But the activation functions of that hidden layer must be non-linear.

A sigmoidal function is employed to adjust the connection weights by determining the error. It is the most widely used function to calculate the output of the neuron at the hidden and output layers. The connection weights are not known in the beginning. Thus, the connection weights linked to the input values are assigned randomly. The output value using these initial connection weights may not be close to the target value. The output value is compared to the actual value and error is calculated. This error is propagated backward through the network and the initial connection weights are adjusted. These adjusted weights are used to calculate the new output and then the comparison of new output with actual value is done again. Then, the new error is determined and the connection weights are adjusted similarly. All training datasets are continuously subjected to the forward activation of signals and the backpropagation of errors. This is continued until the error is reduced to a predetermined minimum or an allowed tolerance [44, 45]. Connection weights that produce an error within the allowable range are considered to be the final connection weights and are stored to represent the network.

3.3 Learning Algorithm

3.3.1 Nodal Input Values

All the nodes are connected: the nodes in the input layer are connected to all of the nodes in the hidden layer and the nodes in the hidden layer are all connected to the nodes in the output layer (Figure 71). In each node, the node values are multiplied by their corresponding connection weights and added up to calculate the sum of weights. This is the new input value for the next node. The bias is an additional set of weights. The sum of weights along with bias is used to It adjusts the output. This is the new input value for the next node.

For example, for an arbitrary node “A” at a hidden layer, the node value is the sum of the value of the weights from the input layer. The following equation expresses the input value for a node “A” [43]:

$$Node_A = \sum_{i=1}^{n}[(Input\ Node\ value)_i \times (connection\ weight)_i] + bias \qquad Eqn. 7$$

3.3.2 Activation Function: Sigmoidal Function

Several active functions can be used in neural networks like Identity function, Binary step function, Logistic sigmoidal function, and Bipolar sigmoidal function. For specific applications, specific functions can be used as these functions have different ranges, and each one has its properties. The activation function must be continuous, differentiable, and monotonically non-decreasing to be used in the backpropagation neural network [46].

Feed forwarded information at the nodes in the hidden and output layer(s) must pass through this activation function, which is to introduce nonlinearity into the model. The node’s input is subjected to the nonlinear transformation in all the nodes at the hidden and output layers, which can be simplified with the following equation for the node “A” [43]:

$$Out_A = f(Net_j^L)_A \qquad Eqn. 8$$

Where f is the activation function and $(\text{input})_A$ is the input for node A, which is computed using equation 9.

In this study, the sigmoidal function was used as the activation function. The sigmoidal function is one of the most common activation functions and is the most widely used in backpropagation networks. The final output signal is positive and has a specified interval between 0 and 1. Figure 72 shows the sigmoidal activation function. The sigmoidal function is expressed as

$$y(x) = \frac{1}{1 + e^{-x}} \qquad Eqn. 9$$

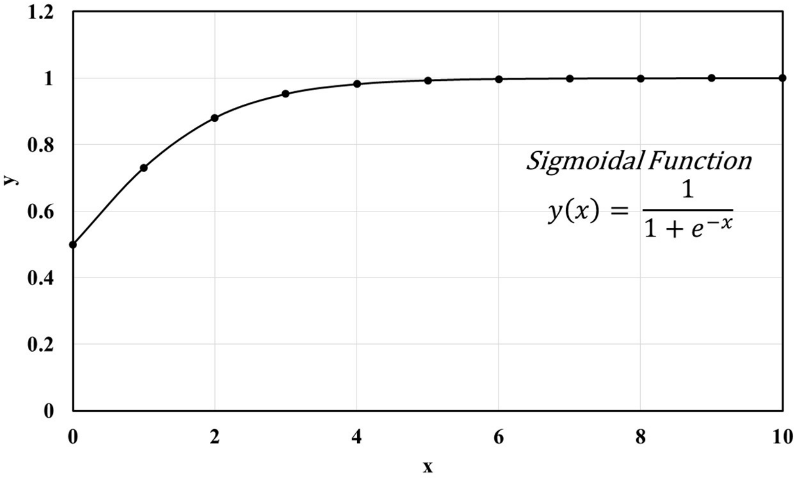

Figure 72 Sigmoid Activation Function

3.3.3 Weight Adjustment

The result from the output node (i.e., the predicted value) is compared with the actual value/targeted value. The error calculated from these two values is used to adjust the connection weights. There are different methods of propagating this error (i.e., Error Back-Propagation) to adjust the connection weights, such as; Perceptron's, Gradient Descent, Levenberg-Marquardt, and many others. Due to its simplicity, stability, and effectiveness, the most popular learning method is the Gradient Descent method [47].

The Gradient Descent method propagates the error from the output layer to the previous layers utilizing the derivatives of the activation function. The weight adjustments are calculated using equations 10 and 11 [43].

$$\Delta w_{ji}^{L} = w_{ji}^{L(new)} - w_{ji}^{L(old)} \qquad Eqn.10$$

According to Zupan and Gasteiger's backpropagation neural network algorithm, incremental change,Δw_{ji}^{L}, can be calculated using the Delta rule [48]:

$$\Delta w_{ji}^{L} = n\delta_j^L Out_i^{L-1} \qquad Eqn.11$$

Where new and old stand for the current and previous iterations; n is the learning rate that moderates the amount of data being updated. The weighted error of the connection ji is represented by the error functionδ. The outcome from the ith neuron in the (L-1)th layer is represented by the Out_i^{L-1} term [43].

3.3.4 Learning Process

The entire learning process of a one output neural network is outlined in the following six steps [43]:

(1) Input vectors are marked as X_1, X_2, X_3, …, X_n, where n refers to the total number of variables

(2) Propagate the input vectors, X_1, X_2, X_3, …, X_n via the connection weights to compute the output vectors.

(3) Itemize the initial weights and update connection weights on the output layer.

(4) All weights on any hidden layers are updated.

(5) Steps A through D are repeated for each training dataset.

(6) Steps A through E are repeated until the predicted output meets the corresponding target output within a predetermined tolerance or the training iterations reach the maximum limit [43, 49].

3.4 Number of Hidden Nodes

The number of initial hidden nodes and the maximum allowed hidden nodes in ANN model development are specified by the user. The user specifies an initial hidden node and the ANN progresses to the maximum allowed number of hidden nodes. The formula to compute the maximum number of hidden nodes (HN) is as follows:

$$HN \leq \frac{(number\ of\ training\ datasets)-(number\ of\ output\ variables)}{(number\ of\ input\ variables)+(number\ of\ output\ variables)+1} \qquad Eqn.12$$

An important note when choosing the maximum allowed hidden nodes, an overtraining situation can be caused by choosing too many hidden nodes. Yet, for a complex phenomenon, having too few hidden nodes may not allow the model to capture the phenomenon. Networks with one hidden layer were chosen for this study to utilize the generalization capability of neural network modeling [43].

3.5 Model Selection Criteria

The comparison among networks is done using three statistical accuracy measures. The three measures are the Coefficient of Determination (R^2), the Mean Absolute Relative Error (MARE), and the Average Square Error (ASE). In order to completely evaluate each network, the training, testing, validation, and overall performance statistics should be considered. The statistical measures of the network producing the minimum values of ASE and MARE and the highest R^2 indicate a level of agreement between predicted and actual output values. The ASE value is computed by the equation [50]:

$$ASE = \frac{\sum_{i=1}^{N}\sum_{j=1}^{n}\left(Y_{ij}^{P}-Y_{ij}^{o}\right)^{2}}{N.n} \qquad Eqn.13$$

The MARE value is expressed by the following equation [50]:

$$MARE = \frac{\sum_{i=1}^{N}\sum_{j=1}^{n}\left|\frac{Y_{ij}^{P} - Y_{ij}^{o}}{Y_{ij}^{O}}\right|}{N.n} \qquad Eqn. 14$$

Where, Y_{ij}^{P} = Predicted output; Y_{ij}^{O} = Actual output; N = number of dataset; and n = number of outputs.

To prevent the ANN models from being biased towards a specific input, the values of all the inputs are normalized. The data were normalized using equations 15 and 16 for input variables and Equations 17 and 18 for output variables.

$$\frac{X_{Max}-ANN_{XMin}}{ANN_{XMax}-ANN_{XMin}} = 0.8 \qquad \text{Eqn. 15}$$

$$\frac{X_{Min}-ANN_{XMin}}{ANN_{XMax}-ANN_{XMin}} = 0.2 \qquad \text{Eqn. 16}$$

$$\frac{Y_{Max}-ANN_{YMin}}{ANN_{YMax}-AN\ \ _{YMin}} = 0.9 \qquad \text{Eqn. 17}$$

$$\frac{Y_{Min}-ANN_{YMin}}{ANN_{YMax}-ANN_{YMin}} = 0.1 \qquad \text{Eqn. 18}$$

Where, X = value of each independent variable, X_{max} = Maximum X, X_{min} = Minimum X

Y = value of dependent variable, Y_{max} = Maximum Y, Y_{min} = Minimum Y

ANN_{xmax} = Maximum X value normalized with respect to the value on the right side of Equation

ANN_{xmin} = Minimum X value normalized with respect to the value on the right side of Equation

ANN_{Ymax} = Maximum Y value normalized with respect to the value on the right side of Equation

ANN_{Ymin} = Minimum Y value normalized with respect to the value on the right side of Equation

3.6 Summary of ANN Model Development

The development of the ANN model includes five sequential stages. The ANN architecture is determined based on parameter characteristics and ANN knowledge in the first stage. In this step, the datasets are divided into three different sub-datasets: training, testing, and validation. In Yaserer's study, the network was trained and tested, in the second stage using the optimum number of hidden nodes and iteration, attained from the first stage [51]. The best performing networks are determined in this stage based on the lowest ASE, lowest MARE, and highest R^2 values. The best performing network obtained from the second stage was validated using validation sub-datasets in the third stage. The best performing networks attained from the second stage were retrained using all the data, in the fourth stage [51]. Normally, retraining the network with all experimental data is expected to provide reliable predictions and overall better accuracy measures. However, it has been shown through several research studies [51-54] that stage four is recommended to arrive at a better performing network model. Stage five involves selecting the best network based on the statistical accuracy measures, which are ASE, MARE, and R^2. It should be noted that the best performing models to predict multiple output phenomena are selected based on the "average" statistical values as oppose to individual output statistics. The modeling sequence explained in this section was employed to develop all the models in this doctoral dissertation [43]. In this research, the development of ANN models was carried out using the ANN TRSEQ1 computer program [53].

CHAPTER IV: DEVELOPMENT OF PERFORMANCE MODELS FOR JOINTED PLAIN CONCRETE HIGHWAY PAVEMENTS

4.1 Background

The LTPP program was established to monitor and collect pavement performance data during 1987-1991 under the Strategic Highway Research Program (SHRP) of the National Academy of Science [55]. Since 1992, the Federal Highway Administration (FHWA) has continued the management and funding of the program [56]. The LTPP program has two vital classes of studies and several other smaller studies to investigate specific pavement-related details that are critical to pavement performance. The vital classes of study are the General Pavement Study (GPS) and the Specific Pavement Studies (SPS). The combined GPS and SPS programs involve over 2,500 test sections located on in-service highways throughout the United States and Canada. The LTPP program monitors and collects pavement performance data on all active sites. The collected data include information in seven modules: Inventory, Maintenance, Monitoring (Deflection, Distress, and Profile), Rehabilitation, Materials Testing, Traffic, and Climatic.

The LTPP data is collected at different spatial locations that exhibit values that are different across the LTPP regions. The following LTPP climate zone classification map (Figure 73) was created during the initial recruitment phases of the LTPP test sections [15, 57], which indicates spatial and temporal variability that applied to the collected pavement attributes. Four different climates zones were identified, namely wet-freeze, wet-non-freeze, dry-freeze, and dry-non-freeze zones. In certain areas, the regional contractors altered this map to state boundaries to ease data collection processes.

Figure 73 LTPP Climate Zones [15]

Pavement smoothness is one of the foremost important measures of pavement performance. Within the MEPDG study of NCHRP 1–37 A [15], pavement smoothness is defined by the IRI. The IRI statistic is generally used as an internationally recognized pavement conditioning rating system. The IRI is calculated from the measured longitudinal profile of a pavement. It mathematically represents the reaction of a single tire on a vehicle suspension to roughness in the pavement surface traveling at 50 mph. The measurement is expressed in a single number with a unit of in/mile or m/km. A higher IRI number indicates a rough pavement profile and, a lower number indicates a smooth pavement profile [58]. The pavement profile is measured using high-speed vans equipped with lasers, accelerometers, and computers to measure IRI. The highly equipped vans can measure the surface profiles at traffic speeds. The onboard accelerometer gives the necessary data to the computer to calculate changes in the vertical position of the vehicle body as the vehicle moves along the pavement, and the laser measures the distance between the vehicle body and the roadway surface. Collected data is stored in the computer at regular intervals. The IRI value increases due to a decrease in pavement smoothness caused by distresses, which are triggered by climatic and traffic attributes. Generally, an IRI rating less than 2.68 m/km is acceptable, and a rating above 2.68 m/km is considered unacceptable and very poor conditioning rating [10].

In the MEPDG study of NCHRP 1–37 A [15], the IRI measurement of longitudinal roughness was adopted to indicate pavement smoothness for the following reasons:

- It is time stable and can be reproduced easily from longitudinal profile elevation data since it is just a computed statistic of the road profile.
- It gives consistently high correlations with the outputs of other roughness measuring devices at different speeds.
- It has been shown to correlate well with the user serviceability rating, such as PSR.

Jointed plain concrete pavements (JPCP) contain several joints to control the location of the expected natural cracks. The cracking occurs at joints and not elsewhere in the slabs. JPCP does not contain any steel reinforcement unlike reinforced concrete pavement (JRCP, CRCP). However, there may be load transfer devices (e.g., dowel bars) at transverse joints and deformed steel bars (e.g., tiebars) at longitudinal joints. The spacing between transverse joints is typically about 15 feet for slabs 7-12 inches thick. Figure 74 shows the top-view and cross-section view of a JPC pavement [59].

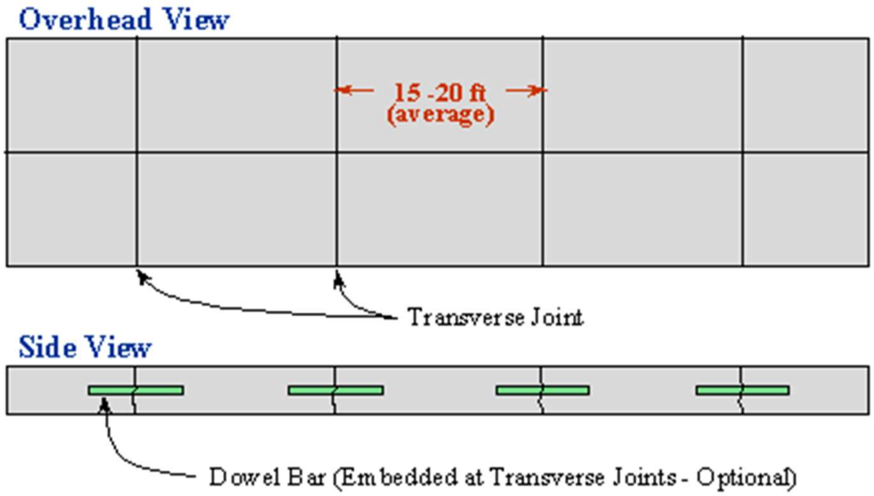

Figure 74 Cross-section and Top-view of Jointed Plain Concrete Pavement [59]

4.2 Methodology

The prediction of IRI value is important to estimate condition deterioration and timely maintenance and/or major rehabilitation actions, as well as associated budget. Pavement performance (condition attributes of IRI and distresses) can be predicted using computational models. Mechanistic-Empirical pavement performance models can evaluate the deterioration process of pavement conditions, identify the major load and environmental attributes that affect the service life, provide forecasts over time, and play an essential role in the pavement asset management system. Figure 75 shows the pavement performance modeling methodology using the LTPP database.

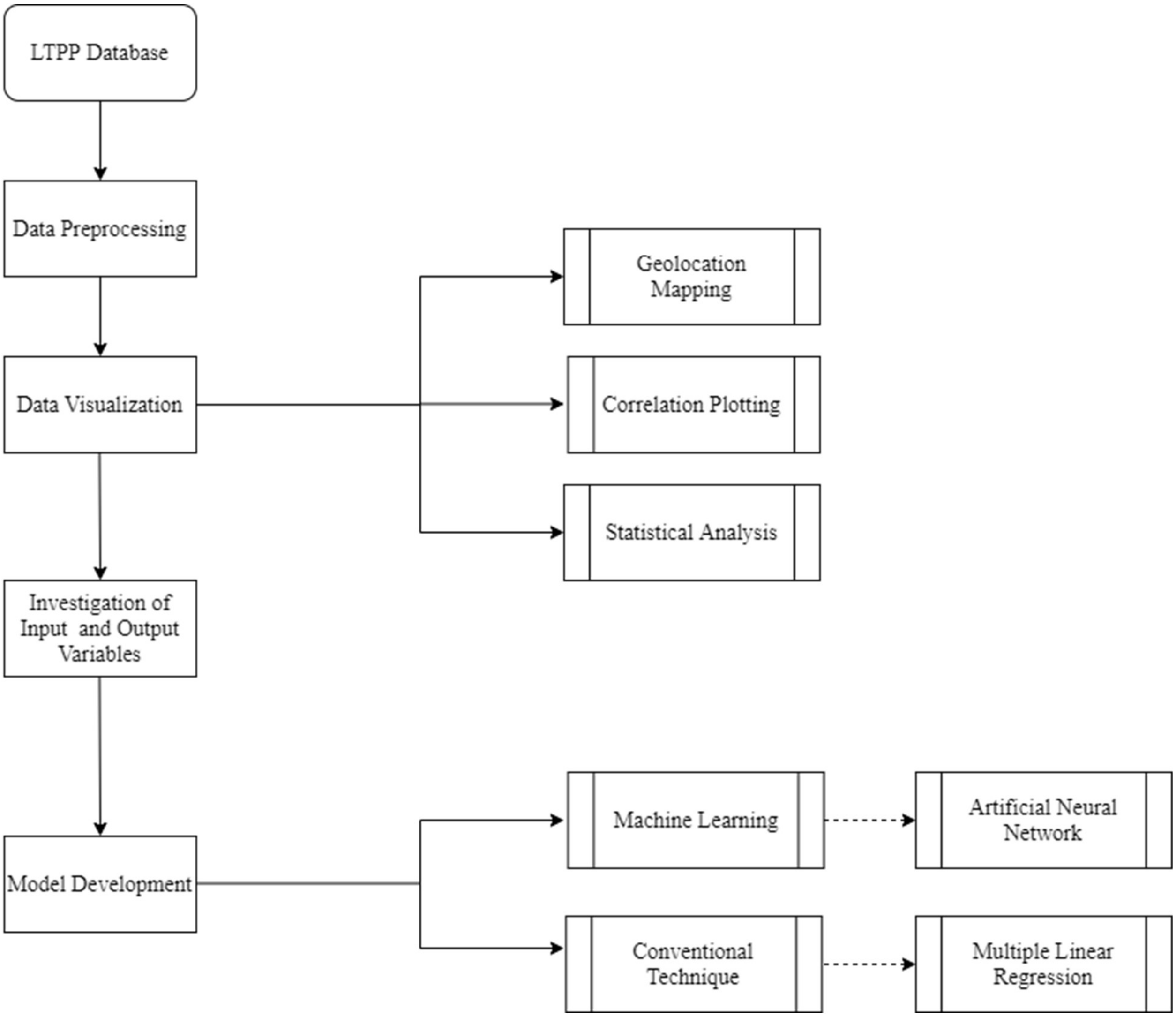

Figure 75 Pavement Performance Modeling Methodology Flow Chart using the LTPP Database

The model development process is, as follows:

(1) Conduct a literature review of past research studies to identify independent and categorical variables that influence pavement performance.
(2) Assemble databases for JPCP model development from the LTPP database, which must include the variables identified in step (1).
(3) Evaluate the quality of databases and identify missing/erroneous data items.
(4) Develop procedures for estimating important missing data in the time series.
(5) Develop pavement performance models using ANN and multiple linear regression modeling techniques.
(6) Select the appropriate IRI model form (should be capable of estimating the increase of IRI value with time and decrease of IRI value after maintenance and rehabilitation).
(7) Evaluate accuracy and verification of developed performance prediction models for JPCP.
(8) Perform sensitivity analysis for developed performance models.
(9) Implement selected performance models.

4.3 Literature Review of IRI Prediction Models

Oh et al. [60] analyzed the long-term performance of JPCP in line with changes in standard mix design using evaluation of concrete properties based on Korea HPMS (highway pavement management system) and Korea LTPP data accumulated for over 15 years. The study found that the concrete pavements built in the 2010s by the specification of a durability-based mix design adopted in 2010 performed better with much fewer surface distresses than the concrete pavements built before 2010 using the specification of classical strength-based mix design.

Zhizhong and Zhongyin [61] developed an IRI prediction model by using the Markov approach. The data employed in this study is based on the field IRI dates obtained from test sections TXLF210016 locate on Highway 281 in the US from 1997-2005. This study used a combined approach by empirical regression and Markov to predict the IRI data from 2005 to 2011.

Wang and Li [62] developed a pavement smoothness prediction model employing a Gray Theory-based technique. In this study, rather than using the conventional least square method to determine the coefficients for Gray Models (GM), the fuzzy regression method is proposed to solve this gray problem. With pavement, IRI and distresses data exported from the LTPP database, Fuzzy and Gray Model (FGM)-based smoothness predictions are established using influencing factors like those in MEPDG. Based on the comparisons among results originated from MEPDG models, conventional GM models, FGM models, and actual LTPP data, the study found that the FGM method is promising for performance modeling.

Naguib et al. [63] developed a regression model for IRI prediction for JPCP using the data from the LTPP Project. A total of 327 data points from 81 pavement sections distributed all over the U.S. were used for model development. The model predicts IRI as a function of pavement age, initial IRI, faulting, number of spalled joints, number of transverse cracks, precipitation, and freezing index. The goodness of fit statistics of the model shows excellent improvement over the model implemented within the MEPDG. The model has a high coefficient of determination (R^2) of 0.80. In addition, the bias in the predicted values of IRI was significantly lower compared to the MEPDG regression model.

Rahman et al. [64] developed pavement performance evaluation models using data from primary and interstate highway systems in the state of South Carolina, USA. Historical pavement performance data were collected from 25 pavements across the state. A total of 8 models were developed based on regression techniques, which include 4 for Asphalt Concrete (AC) pavements and 4 JPCP and 4 Asphalt Concrete (AC) models were developed using regression technique. The input variables were Annual Average Daily Traffic (AADT), Free Flow Speed (FFS), precipitation, temperature, and soil type (soil Type A from Blue Ridge and Piedmont Region, and soil Type B from Coastal Plain and Sediment Region) and the output variables were Present Serviceability Index (PSI), Pavement Distress Index (PDI), Pavement Quality Index (PQI), and International Roughness Index (IRI). The results showed that AADT, FFS, and precipitation have statistically significant effects on PSI and IRI for both JPCP and AC pavements.

4.4 Related Studies on ANN-Based IRI Prediction Models

Relatively few studies have been conducted in recent years to predict the roughness of asphalt and concrete pavements, and selected studies are reviewed in the following paragraphs.

Attoh-Okine [65] developed an IRI prediction model of asphalt pavements by using data from the LTPP database. The study used a backpropagation neural network algorithm and aimed toward developing a roughness prediction model and applying sensitivity analysis to spot the relative significance of material and construction variables on the roughness. The independent variables were the asphalt content, asphalt layer thickness, cumulative equivalent single axle load, structural number (SN), and also the percentage of fines passing through the No. 200 sieve. The IRI was the output variable. The study revealed that the predicted neural network model was a useful alternative required for performance-related specifications such as measuring IRI for a newly constructed pavement.

Lin et al. [66] studied the relationship between asphalt pavement distresses and IRI based on ANNs. The ANN architecture used included fourteen independent variables, two hidden layers with six hidden nodes, and one output (14-6-6-1 ANN model). The independent variables were stripping, alligator cracking, cracking, rutting on the left wheel path, rutting on the right wheel path, road level, corrugation, potholes (mild and severe), road level, manholes (mild and severe), bleeding, and patching. The output variable was IRI. The study conducted a sensitivity analysis that found rutting, potholes, and patching were the most relevant independent variables.

Mazari and Rodriguez [67] conducted a study that found correlations between IRI with pavement age, equivalent single axle load (ESAL), and SN employing a hybrid gene expression programming ANN model (GEP-ANN). The GEP-ANN structure included one hidden layer with twenty hidden nodes and one output (4-20-1 ANN model). The data was collected from eight U.S. states and two Canadian provinces using the LTPP databases of asphalt pavement. The study found that GEP-ANN provides a better IRI prediction model than a GEP-only prediction model.

Ziari et al. [68] developed a model predicting IRI using pavement structure, traffic, and climate data collected from the LTPP database and using ANN and group method of data handling (GMDH) techniques. The used input variables in this study were surface, base, and sub-base thickness, ESAL, annual average daily traffic (AADT), annual average daily truck traffic (AADTT), annual average precipitation (AAP), annual average temperature (AAT), annual average freezing index (AAFI), and pavement age. The study modeled IRI for both flexible and rigid highway pavements employing a large 9-100-50-30-1 ANN model in addition to other ANN models. The study used the ANN model for both short- and long-term IRI predictions.

Georgiou et al. [69] developed a model for the prediction of pavement roughness in terms of the IRI using ANNs and support vector machines (SVMs). The modeling is based on pavement roughness data collected periodically for a high-volume motorway during a seven-year period, on a yearly basis. The comparative study of the developed models concludes that the performance of the ANN model is slightly better compared to the SVM in terms of prediction accuracy.

Hossain et al. [42] developed a prediction model for IRI for flexible pavements using climate and traffic data by employing ANN modeling. The climate and traffic data were collected from the LTPP database. The ANN model was trained using 50% of climate, traffic, and IRI data, and the other 50% of data was employed to validate the model by comparing ANN predicted IRI and measured IRI for flexible pavement under a climatic zone. The trained model and the validated model were compared by calculating the RMSE of ANN predicted IRI and measured IRI. The study developed a model for a flexible pavement located at the wet-freeze climatic zone, employing a 7-7-1 ANN structure and using the Pure Linear transfer function, the

RMSE generated was 0.055. A better prediction ANN model was generated using 7-9-9-1 architecture using a nonlinear transfer function and the RMSE further improved to 0.012.

Hossain et al. [70] developed a prediction model for IRI for rigid pavement using climate and traffic data by employing Artificial Neural Network (ANN) modeling. The climate and traffic data were collected from the LTPP database. The ANN model was trained using 70% of climate, traffic, and IRI data, 15% of data was used to test the model, and the other 15% of the data was employed to validate the model. The trained model and the validated model were compared by calculating the Root Mean Square Error (RMSE) and Mean Absolute Percentage Error (MAPE) of ANN predicted IRI and measured IRI. The study developed a model for rigid pavement located at the wet no-freeze climatic zone, employing 7-9-9-1 ANN structure and using hyperbolic tangent sigmoidal transfer function, the RMSE value and MAPE value generated was 0.01 and 0.01 (1% error), respectively.

Mohamed Jaafar [19] developed mechanistic-empirical models for predicting IRI, rutting, and cracking for asphalt pavements using pavement structural, traffic, and climate data extracted from the LTPP database. The models were developed using ANN and multiple linear regression techniques. The ANN architecture for IRI modeling used included seven independent variables, one hidden layer with five hidden nodes, and one output (7-5-1 ANN model). The independent variables used for IRI modeling were initial IRI, pavement age, SN, CESAL, air temperature, precipitation, and CN (an indicator of major maintenance and/or rehabilitation). The ANN model had a high coefficient of correlation (R) of 0.72. The model implemented in MEPDG had a coefficient correlation of 0.75, but the MEPDG model does not consider pavement M&R history as an independent variable, which was included in this study. This study also developed a multiple linear regression model, and this model includes Region as an independent variable with other variables that were used in the ANN model. The multiple regression model had a correlation coefficient of 0.63. The model verification showed a -22.6% difference in the means of measured and predicted IRI values. The ANN model verification showed a -25.3% difference in the means of measured and predicted IRI values. It is evident from the study that the ANN model and the multiple regression model of IRI are reasonably accurate for predicting future IRI values within the LTPP database used. This study [19] of mechanistic-empirical pavement performance models of asphalt pavement is the first and only study that embedded M&R intervention compared to the above literature review. Table 18 shows the summary of IRI prediction models for concrete pavement using the LTPP data employing ANN and multiple regression modeling techniques.

Table 18 Summary of IRI Prediction Models using LTPP Data for Concrete Pavement

Reference	Model Structure	Goodness of fit	Data Points
[13]	$IRI^2 = 99.59 + 2.6098 \times FaulTT + 2.2802 * T - Crack^3 + 1.8407 \times Spall$	$R^2 = 0.61$	Not Known
[14]	$IRI = 1.471 + 0.2794 \times F$	$R^2 = 0.50$	Not Known
NCHRP 1-37 [15]	$IRI = IRI1 + 0.013 \times TC + 0.007 \times SPALL + 0.005 \times PATCH + 0.0015 \times TFAULT + 0.4 \times SF$	$R^2 = 0.60$	188

Reference	Model Structure	Goodness of fit	Data Points
[16]	$IRI = 0.142 + 0.78 \times IRI1 + 0.013 \times Age + 0.000152 \times Fault + 0.018 \times Tcrack + 0.014 \times Spall + 0.000109 \times prec. + 0.000072 \times FI$	$R^2 = 0.81$	327
[17]	8 inputs of independent variables, 2 hidden layers (24 and 12 hidden nodes), and 1 output (8-24-12-1)	$R^2 = 0.83$	188
[18]	7 inputs of independent variables, 1 hidden layer (10 hidden nodes), and 1 output (7-10-1)	$R^2 = 0.84$	264

Where, IRI = International Roughness Index, in/mile, FaulTT = total accumulated joint faulting, in/mile, T-crack = amount of transverse cracking, number of cracks per mile, Spall = percentage of joints spalled , F = Transverse joint Faulting, IRI1= initial smoothness measured as IRI, m/km, TC = percentage of slabs with transverse cracking (all severities), SPALL = percentage of joints with spalling (all severities), PATCH = pavement surface area with flexible and rigid patching (all severities), percent, TFAULT = total joint faulting cumulated per km, mm, SF = site factor = Age*(1+FI)*(1+P200)/1000000, Age = pavement age in years, FI = freezing index, °C days, P200 = percent subgrade material passing the 0.075-mm sieve, perc.=annual average precipitation in mm.

The previous literature review indicates that the M&R history was not considered in the concrete pavement condition deterioration progression modeling. Recently, enhanced performance models for asphalt highway pavements were developed using M&R history [19]. Therefore, this research will consider M&R history for developing performance models for concrete pavements. The independent variables used in the previously developed models are mostly distress, age, and environmental data. However, for future prediction of IRI, these distresses need to be predicted as well. The performance models developed in this research will predict the IRI values using easily available variables that will help the local and state agencies to prepare M&R programs and budgets without estimating distresses in future years.

4.5 Data Collection for Jointed Plain Concrete Pavement using LTPP Database

The data were collected from the LTPP database of JPCP, which is GPS-3 [71]. A total of 107 GPS-3 JPCP pavement sections are included in the LTPP that are located throughout the United States. The IRI measurements are from 1989 to 2018. A total of 7,982 measurements are for 107 sections. By averaging the IRI value from one run, a dataset was created which has 1,486 data points. Figure 76 shows the spatial map of JPCP sections included in the LTPP database.

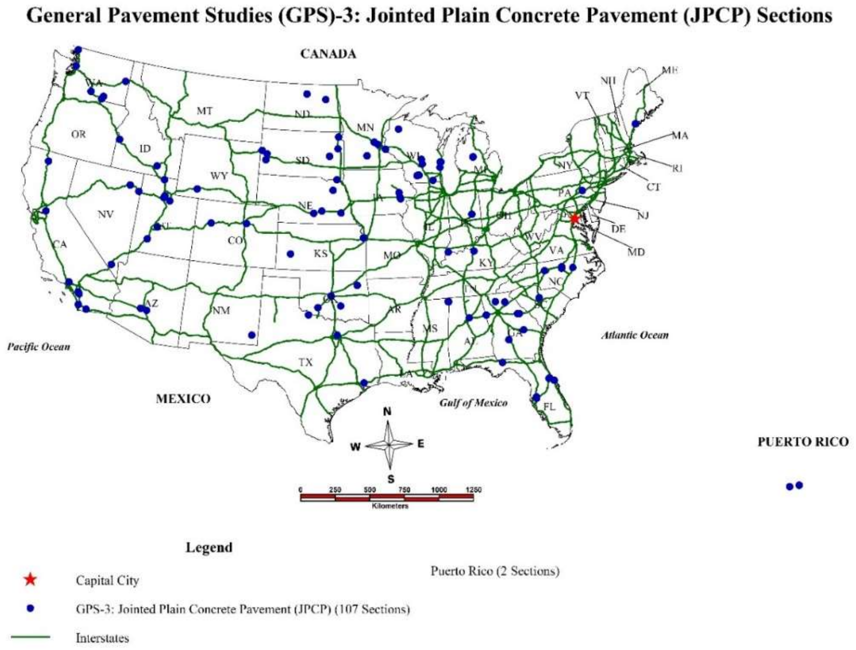

General Pavement Studies (GPS)-3: Jointed Plain Concrete Pavement (JPCP) Sections

Figure 76 Spatial Map of JPCP Sections in the USA

JPCP sections included in the LTPP database are located in four climatic regions. Table 19 shows that 43% (46 of 107) sections are in the wet, freeze climatic region and 31.8% (34 of 107) sections are in the wet, non-freeze climatic region. The IRI data points follow the same statistics, higher in wet, freeze (44.9%, 665 of 1,482) region than wet, non-freeze (25.4%, 376 of 1,482) region.

Table 19 Distribution of Pavement Sections and IRI Data Points in Different Climatic Region

Climatic Region	Number of Sections	% of Sections	Number of Data Points	% of Data points
Wet, Non-Freeze	34	31.8%	376	25.4%
Dry, Non-Freeze	13	12.1%	210	14.2%
Dry, Freeze	14	13.1%	231	15.6%
Wet, Freeze	46	43.0%	665	44.9%
Total	107	100%	1482	100%

Table 20 shows the distribution of pavement sections and IRI data points by state. Wisconsin has the highest 13 pavement sections out of 107 and 12.1% (209 of 1,482) IRI data points. California has 8 sections and it contains the second highest IRI data points of 9.6% (143 of 1,482).

Table 20 Distribution of Pavement Sections and IRI Data Points by States

State Code	State Name	Climate Zone	Number of Sections	% of Sections	Number of Data points	% of Data points
1	Alabama	Wet, Non-Freeze	1	0.9%	9	0.6%
4	Arizona	Dry, Non-Freeze, Dry, Freeze	2	1.9%	16	1.1%
6	California	Wet, Non-Freeze, Dry, Non-Freeze,	8	7.5%	143	9.6%
8	Colorado	Dry, Freeze, Wet, Freeze,	2	1.9%	36	2.4%
12	Florida	Wet, Non-Freeze	6	5.6%	69	4.7%
13	Georgia	Wet, Non-Freeze	7	6.5%	89	6.0%
16	Idaho	Wet, Non-Freeze, Dry, Non-Freeze, Dry, Freeze	2	1.9%	43	2.9%
18	Indiana	Wet, Freeze, Wet, Non-Freeze	2	1.9%	30	2.0%
19	Iowa	Wet, Freeze	3	2.8%	46	3.1%
20	Kansas	Wet, Freeze, Wet, Non-Freeze	2	1.9%	27	1.8%

State Code	State Name	Climate Zone	Number of Sections	% of Sections	Number of Data points	% of Data points
21	Kentucky	Wet, Freeze, Wet, Non-Freeze	1	0.9%	17	1.1%
23	Maine	Wet, Freeze	2	1.9%	28	1.9%
26	Michigan	Wet, Freeze	2	1.9%	17	1.1%
27	Minnesota	Wet, Freeze	7	6.5%	75	5.1%
28	Mississippi	Wet, Non-Freeze	2	1.9%	21	1.4%
31	Nebraska	Dry, Freeze, Wet, Freeze	4	3.7%	74	5.0%
32	Nevada	Dry, Non-Freeze, Dry, Freeze	3	2.8%	26	1.8%
35	New Mexico	Dry, Non-Freeze, Dry, Freeze	1	0.9%	12	0.8%
37	North Carolina	Wet, Non-Freeze	4	3.7%	48	3.2%
38	North Dakota	Wet, Freeze	2	1.9%	26	1.8%
40	Oklahoma	Wet, Non-Freeze	4	3.7%	39	2.6%
42	Pennsylvania	Wet, Freeze, Wet, Non-Freeze	1	0.9%	23	1.6%
45	South Carolina	Wet, Non-Freeze	1	0.9%	9	0.6%
46	South Dakota	Dry, Freeze, Wet, Freeze	7	6.5%	97	6.5%
48	Texas	Wet, Non-Freeze, Dry, Non-Freeze	3	2.8%	33	2.2%
49	Utah	Dry, Non-Freeze, Dry, Freeze, Wet, Freeze	6	5.6%	89	6.0%
53	Washington	Wet, Non-Freeze, Dry, Non-Freeze, Dry, Freeze	6	5.6%	105	7.1%
55	Wisconsin	Wet, Freeze	13	12.1%	209	14.1%
56	Wyoming	Dry, Freeze	1	0.9%	12	0.8%
72	Puerto Rico	Wet, Non-Freeze	2	1.9%	14	0.9%
Total 107 Sections and 1482 Data Points						

4.6 Preliminary ANN Models

The data used for the model are 590 data points from 43 JPCP sections from all over the United States. IRI measurements are measured left (inside) wheel path and right (outside) wheel path. The mean IRI is the average of IRI measurement in right (outside) and left (inside) wheel path. Figure 77 shows the mean IRI measurement of 43 sections of JPCP pavement.

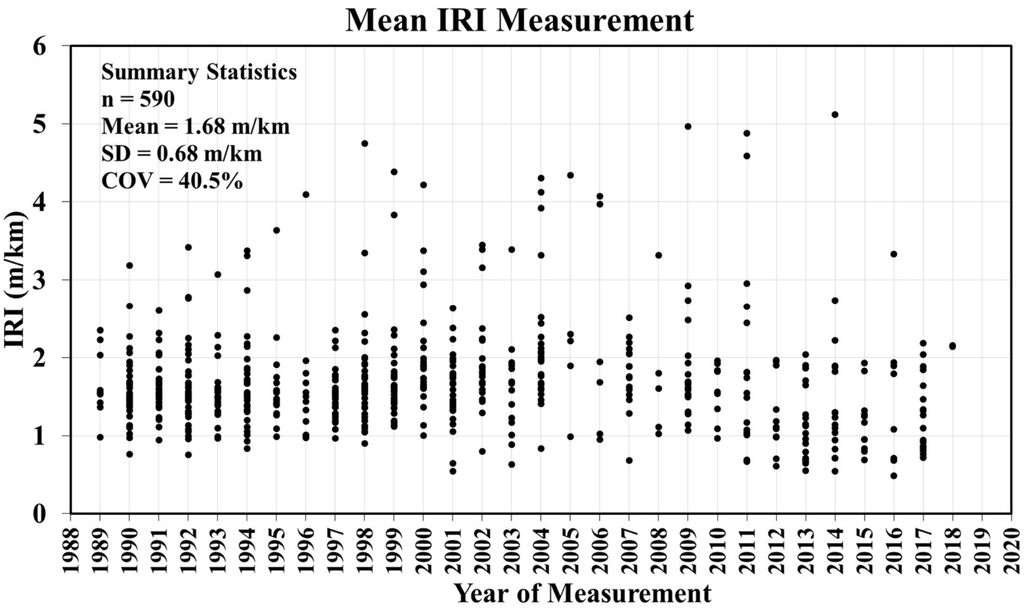

Figure 77 Mean IRI Distribution over the Years

4.6.1 Preliminary ANN Model Architecture

In the preliminary research, using the selected JPCP section of the LTPP database, several models were tried with varying numbers of inputs and outputs variables. The first model had six inputs variables but CN was a categorical variable with two categories 0 for CN1 and 1 for any other CN number. The region was also assigned as a categorical variable with four categories. Therefore, the first model had 10 input and 2 output variables (i.e. IRI for inside and outside wheel path). The second model had the same number of input variables but the output variable was mean IRI (MRI). The third model had 13 input variables (including 4 climatological variables) and one output variable (mean IRI). Table 21 shows the input variables used in this study for the ANN model. The independent variables used in the MEPDG model are related to distresses, which need to be measured or predicted for future years, to predict the IRI. On the other hand, the ANN model developed in this research used easily available input variables.

Table 21 Input and Output Variables Used in Preliminary ANN Models

Input Variables	**Model 1**	**Model 2**	**Model 3**
IRI_0 (Initial IRI m/km)	Initial IRI Right Wheel Path, m/km	Initial Mean IRI, m/km	Initial Mean IRI, m/km
	Initial IRI Left Wheel Path, m/km		
Age (Pavement age, years)	Age	Age	Age
h (Concrete pavement thickness, in)	*h*	*h*	*h*
ESAL (Equivalent Single Axel Load)	ESAL	ESAL	ESAL
Climatic Region (Categorical variable for LTPP climatic region)	Wet, Non-Freeze Dry, Non-Freeze Wet, Freeze Dry, Freeze	Wet, Non-Freeze Dry, Non-Freeze Wet, Freeze Dry, Freeze	Wet, Non-Freeze Dry, Non-Freeze Wet, Freeze Dry, Freeze
CN (Construction Number, Categorical variable for M & R)	No Intervention 0 Any Intervention 1	No Intervention 0 Any Intervention 1	No Intervention 0 Any Intervention 1
Climatological Inputs			Mean Annual Temperature (°C) Total Annual Precipitation (in) Freezing Index Year Freeze-Thaw (days)
Output Variables			
	IRI Right Wheel Path, m/km IRI Left Wheel Path, m/km	Mean IRI, m/km	Mean IRI, m/km

4.6.2 Preliminary ANN Model Selection

Three best performing networks from each model (Model 1, Model 2, and Model 3) were selected based on statistical measures such as minimum values of MARE, ASE, and maximum values of Coefficient of Determination (R^2). A total of 590 datasets were used to build the desired database; 302, 144, and 144 subdatabases were used, respectively, for training, testing, and validation purposes. Datasets that include minimum and maximum values of each variable were included in the training phase for the network to represent the characteristics of the response. The maximum and minimum ranges of each input/output variable for ANN model development were chosen on purpose to be wider than their actual ranges for better mathematical mapping [54]. The statistical measures of the best performing network for Model 1, Model 2, and Model 3 are shown in Table 22. With the lowest ASE value of 0.001766, the lowest MARE value of 10.437, and the highest R^2 value of 0.87169 in all data stages, Model 2 was selected to be the best performing model.

Table 22 Best Networks from Each Model

Dataset	Statistical Error Measures	Model 1	Model 2	Model 3
		4-6-20000	6-9-20000	3-5-20000
Training	MARE	15.745	10.668	12.693
	R^2	0.76194	0.85476	0.8527
	ASE	0.003375	0.002127	0.00217
Testing	MARE	13.934	13.096	13.516
	R^2	0.65816	0.79938	0.7513
	ASE	0.004032	0.002644	0.003282
Validation	MARE	15.327	14.465	15.292
	R^2	0.7403	0.7413	0.74104
	ASE	0.002882	0.003545	0.00403
All Data	MARE	12.98	10.437	11.822
	R^2	0.80226	0.87169	0.85598
	ASE	0.002526	0.001766	0.001986
Final Network Structure		10-6-2	**9-9-1**	13-5-1

4.6.3 Preliminary ANN Model Results

Model 2 was chosen as the best performing network based on statistical measures (ASE, MARE, and R^2 value) of all data. This model will be discussed further to explain the considerations made to choose the best model. The comparison of the prediction accuracy measures for ANN Model 2 is graphically presented in Figure 78. From Figure 78 it is evident that once observed IRI rises above 3.0, the model steadily underestimates the prediction output.

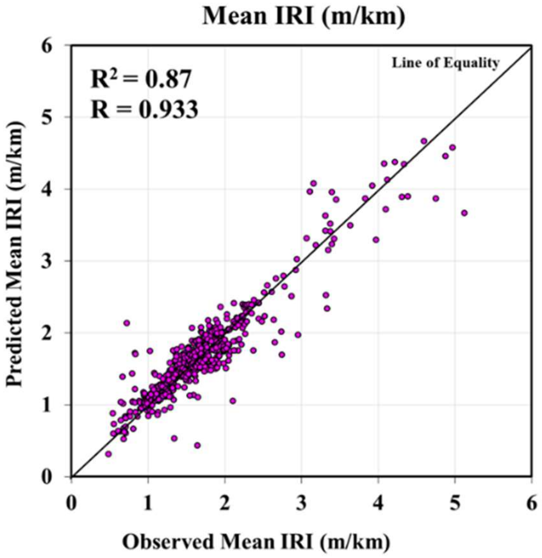

Figure 78 Observed Mean IRI (m/km) vs. Predicted Mean IRI (m/km)

4.6.4 Sensitivity Analysis for Preliminary ANN Models

The 590 data points are assigned section sequence numbers from 1 to 590. Figure 79 shows the observed and Model 2 predicted mean IRI values. From Figure 79, it is demonstrated that the predicted IRI has apprehended most of the variability in the IRI observed values.

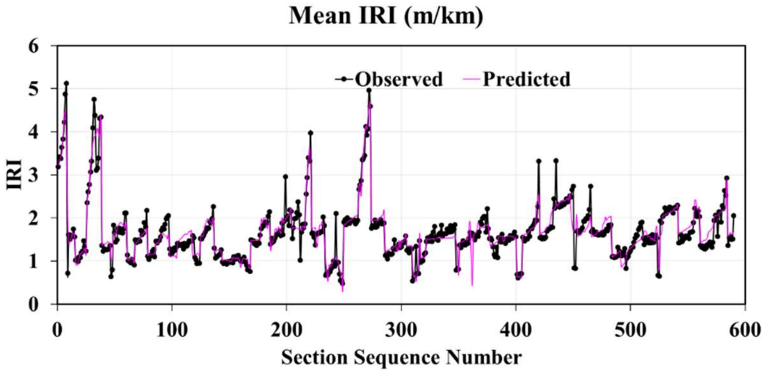

Figure 79 Observed and Predicted Mean IRI (m/km) plot

Figure 80 shows the observed and predicted IRI for Section 06-3017, in California. The predicted values follow the observed values closely. The difference in the mean values of observed and predicted is -3.1%.

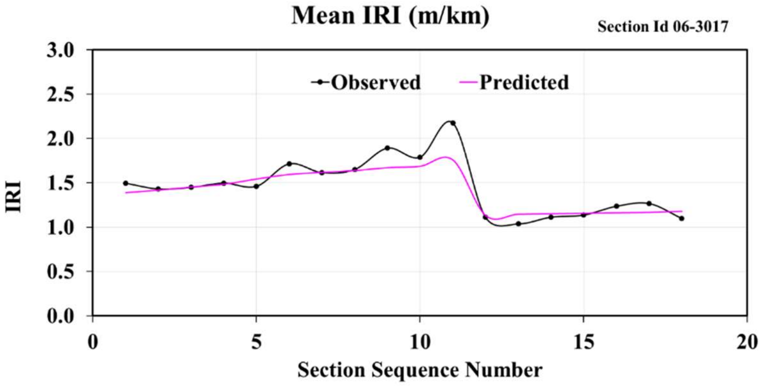

Figure 80 Observed and Predicted Mean IRI Plot of JPCP Section in California

Randomly selected sections with different M&R types (CN1 and CN2) were used to generate IRI predictions for future years. For IRI predictions, the ESAL values were assumed with an annual growth rate of 1%. Figure 81 shows that the IRI prediction model follows the trend of the observed values. Additionally, it can estimate the increase of IRI values with time and decrease of IRI value after maintenance and rehabilitation.

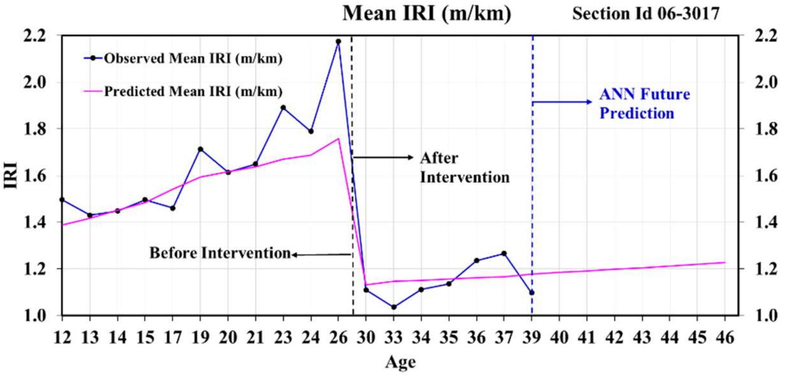

Figure 81 ANN Future Prediction Plot of Mean IRI for JPCP Section in California

4.6.5 Recommendations from Preliminary Study

(1) In the preliminary study, ESAL was used as an independent variable. The cumulative ESAL (CESAL) should be used as an independent variable to incorporate the accumulated traffic load for better performance prediction.

(2) The developed IRI prediction models in this study used 590 data points. All data points should be used to develop models for better characterization.

(3) Further study on exploring M&R types and their classifications need to be done.

4.7 Consideration of M&R Treatment in the Development of IRI Roughness Prediction Models

The current literature review indicated that none of the equations developed from previous studies considered M&R history in the equations. Therefore, this research proposes the use of CN as a categorical variable in the IRI roughness prediction models. This approach was used in a recent asphalt highway pavement performance study at the University of Mississippi [19]. The CN categorical variable is one of the attributes available in the LTPP pavement monitoring database. In the LTPP study, a test section on the road network was assigned CN1 when it was opened to the traffic. When the first M&R treatment was conducted, the construction number changed to CN2. The CN values increase as a result of more frequent M&R treatments. The CN factor indicates that a major M&R treatment was conducted on the pavement section. Generally, the M&R treatment intervention improves the pavement condition with respect to longitudinal roughness, cracking, rutting, and other surface defects for asphalt pavements. On the JPCP highway, the M&R treatment intervention improves the pavement condition with respect to longitudinal roughness, cracking, faulting, joint deterioration, and other surface defects. In the data analysis to develop the condition prediction equation, it is imperative to consider the CN intervention factor for realistic modeling of pre- and post-M&R practice. The CN intervention factor is considered as a categorical variable with zero or one value. The zero value means no M&R, and a value of one for CN implies some M&R treatment has taken place. By using this dichotomous (dummy) variable in the regression analysis, the models are more realistic since the modeling approach considers the actual M&R treatment conducted in the field. This concept of using the CN in the regression models was not discussed in AASTHO's MEPDG model development and implementation [72].

4.8 Database Development for JPCP Final Performance Models

4.8.1 Data Processing

Output Variables

International Roughness Index (IRI) is considered as the output variable in the pavement performance modeling process for this research. The IRI measurements are from 1989 to 2018. A total of 7,982 measurements are for 107 sections. Each section has two types of IRI measurements, IRI inside/left wheel path and IRI outside/right wheel path. A mean roughness index Mean IRI is calculated by averaging the IRI inside/left wheel path and IRI outside/right wheel path measurements. In each visit date, several IRI measurement runs were completed for each section. By averaging the IRI measurement runs, a single IRI measurement was obtained for IRI inside/left wheel path, IRI outside/right wheel path, and mean IRI for each visit date. By doing this, a dataset was created which has 1,486 data points for 107 JPCP sections. After further study of the IRI data collection, it was found that two pavement sections later became asphalt overlaid concrete pavement and four data points were collected after the section became asphalt overlaid concrete pavement. These four data points were excluded from the dataset and the final dataset came to have 1,482 data points. Figure 82 shows the IRI Measurements for Inside Wheel Path and Outside Wheel Path.

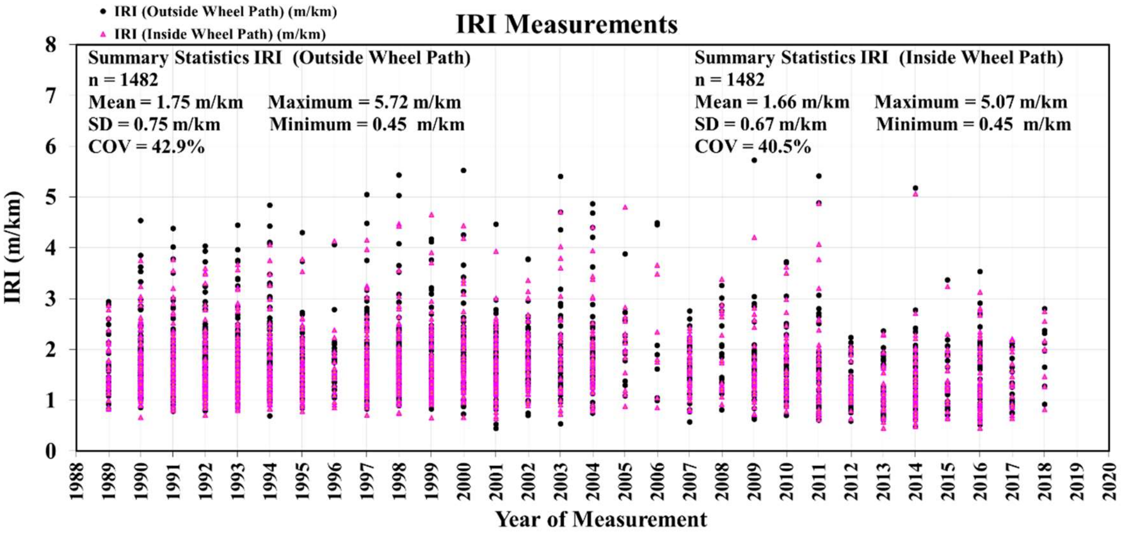

Figure 82 IRI Measurements for Inside Wheel Path and Outside Wheel Path

Hypothesis Testing Using T-Test for IRI Inside Wheel Path (IRI Left) and Outside Wheel Path (IRI Right) for Jointed Plain Concrete Pavements using LTPP Database

Step by Step procedure

Step 1: Set up the null hypothesis and alternative hypothesis.

Null Hypothesis: H_0: $\mu 1 = \mu 2$

Where:

$\mu 1$ = Mean of Population 1 for IRI inside wheel path

$\mu 2$ = Mean of Population 2 for IRI outside wheel path

The population means of the two samples (IRI inside wheel path and IRI outside wheel path) are equal. This implies that both samples are from the same population.

Alternative Hypothesis: H_A: $\mu 1 \neq \mu 2$

The population means of the two samples (IRI inside wheel path and IRI outside wheel path) are not equal. This implies that both samples are from different populations.

Step 2: Select α probability of Type 1 chance error for α level of statistical significance.

$\alpha = 0.05$

$\alpha/2 = 0.025$ (for two-tailed test)

Figure 83 shows the two-tailed t-test probability distribution.

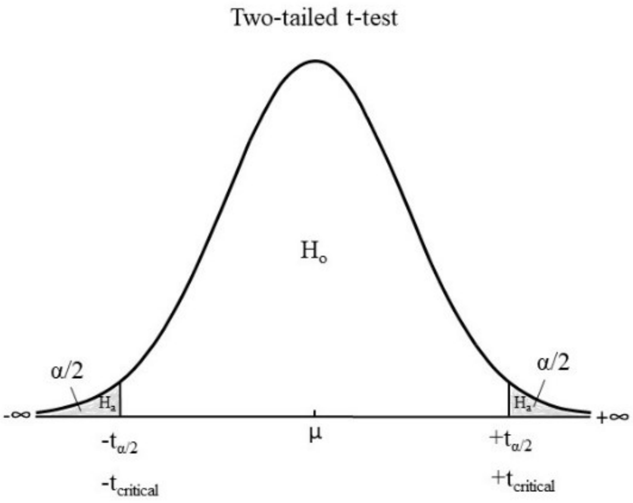

Figure 83 Two-tailed t-test Probability Distribution Graph

Step 3: Define test criteria and the decision rule for rejecting H_0.

Test criteria: $t_{critical} = 1.96$ for degree of freedom (dof) = 2962 and $\alpha/2 = 0.025$

Decision Rule: Reject H_0 if t-test statistics t_{test} exceeds the absolute value of $t_{critical}$ ($t_{test} > t_{critical}$) and probability of significance value, $p \leq$ Probability of Type-1 chance error, α.

Step 4: Calculate t test statistics, t_{test}, and p-significance value.

$t_{\text{test}} = 3.30$

Probability of significance, p-value < 0.001

Step 5: Interpret the results.

t_{test} (3.30) $>$ t_{critical} (1.96) and p (< 0.001) $< \alpha$ (0.05)

Therefore, the t-test rejects the null hypothesis. The results show that the difference in the means of IRI inside wheel path and IRI outside wheel path is statistically significant at α 0.05 probability of chance error. This implies that both samples (IRI inside wheel path and IRI outside wheel path) are from different populations. The results show that that the IRI outside wheel path is significantly higher than the IRI inside wheel path. Hence, this research developed pavement performance models using IRI (outside wheel path) (m/km) as the output variable across all concrete pavement types.

Input Variables

An input or independent variable is also known as a predictor variable is used to predict the output variable. Pavement deterioration is affected by several factors such as pavement structure, climate, traffic, and maintenance over the years. In this research, an extensive literature review was done to identify the key input variables that influence pavement performance. This research also identified the input variables that were used in previously developed pavement performance models. In addition to using these input variables, other easily available input variables were used to develop the pavement condition deterioration model. The input variables were collected from the LTPP database corresponded to the output variable (IRI outside wheel path) measurement taken date (visit date). The relationship between each input variable and output variable (IRI outside wheel path) was studied by creating several plots.

Initial IRI (Outside Wheel Path) (m/km):

The initial IRI outside wheel path (m/km) represents the first IRI value measured in the outside wheel path for a specific pavement section of the LTPP database. The first measurement is usually done when the pavement was built and opened to traffic or the pavement was first included in the LTPP study. It indicates the road surface condition at the beginning of the analysis period. Initial IRI has a range of a minimum of 0.83 to a maximum of 4.53. Figure 84 shows the plot of the initial IRI outside wheel path (m/km) against the IRI outside wheel path (m/km).

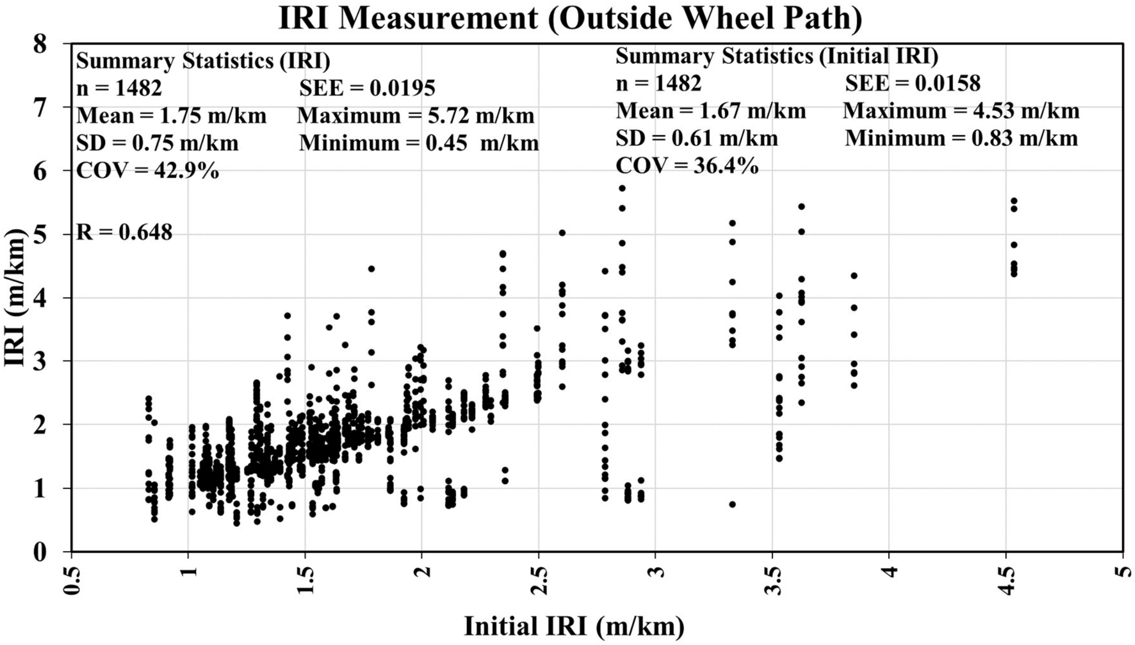

Figure 84 Initial IRI vs. IRI Measurement (Outside Wheel Path) of JPCP Sections

Age:

The variable age is calculated by subtracting the year when the section was opened to traffic from the year IRI measurement was collected. This variable represents the time pavement was expose to climate and traffic loads. Age is also a fundamental variable to be used as an input variable to predict pavement performance for future years. The mean pavement age 107 JPCP section is 19 years. But for some pavement sections, some IRI data were collected when the pavement age was as little as one year, and for some pavement sections that age was as high as 46 years. Figure 85 shows the pavement age when IRI measurements were collected.

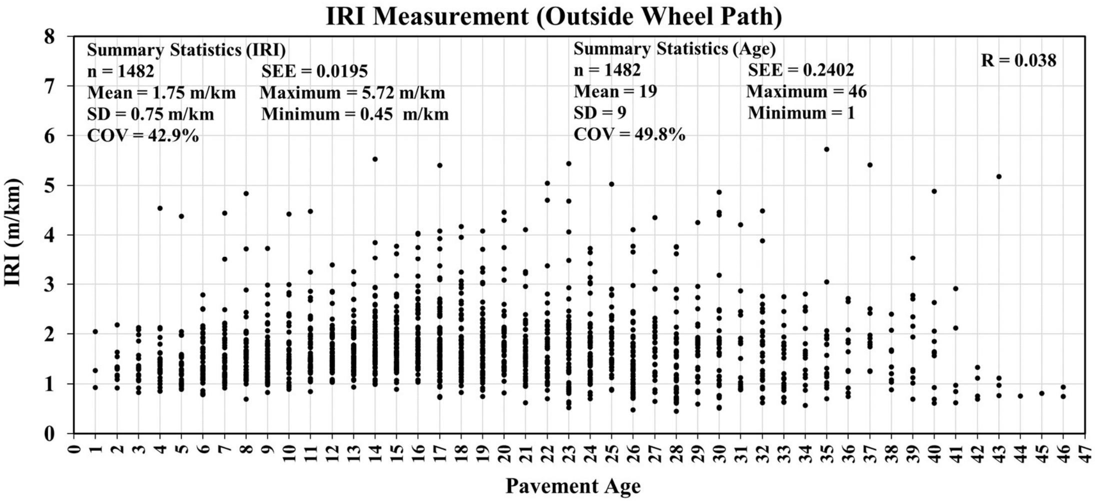

Figure 85 Age vs. IRI Measurement (Outside Wheel Path) of JPCP Sections

Concrete Pavement Thickness (in):

Concrete pavement thickness represents the thickness of the concrete layer in a JPCP pavement section that is laid over the base/subbase layer. This layer is exposed to climate and endures the traffic loads throughout pavements life. Concrete layer thickness plays an important role in JPCP performance. The average concrete layer thickness is 9.5 in with a standard deviation of 1.22 in. The maximum concrete layer thickness is 13.2 in and the minimum is 7 in. Figure 86 shows the concrete layer thickness of JPCP sections and IRI outside wheel path measurements.

Base/Subbase Thickness (in):

Base/subbase pavement thickness represents the thickness of the base/subbase layer in a JPCP pavement section that is laid over the subgrade layer. Some JPCP sections have both base and subbase layers, on the other hand, some JPCP sections have only a base layer underneath the concrete layer, over the subgrade layer. Traffic loads transfer from concrete layer to base/subbase layer and this layer is also affected by precipitation. Therefore, base/ subbase thickness is an important input variable for JPCP performance modeling. The average base/subbase thickness is 5.3 in. The maximum base/subbase thickness is 23.2 in.

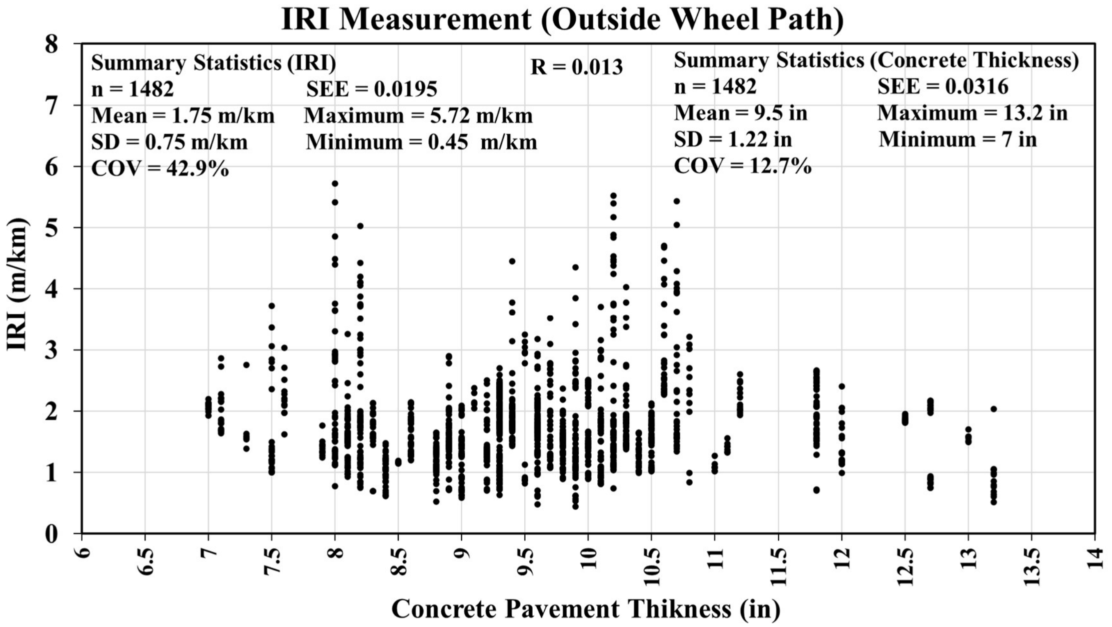

Figure 86 Concrete Pavement Thickness vs. IRI Measurement (Outside Wheel Path) of JPCP Sections

Average Contraction Spacing (m)

The average contraction spacing represents the joint spacing in JPCP sections. This joint spacing controls the natural cracks in a pavement section. Therefore, it will be useful to use the average contraction spacing of joints as an input variable for JPCP performance modeling. The mean average contraction spacing is 4.94 m with a standard deviation of 0.99 m. The maximum average contraction spacing is 9.14 m and the minimum is 3.51 m. Figure 87 shows the average contraction spacing of JPCP sections and IRI outside wheel path measurements.

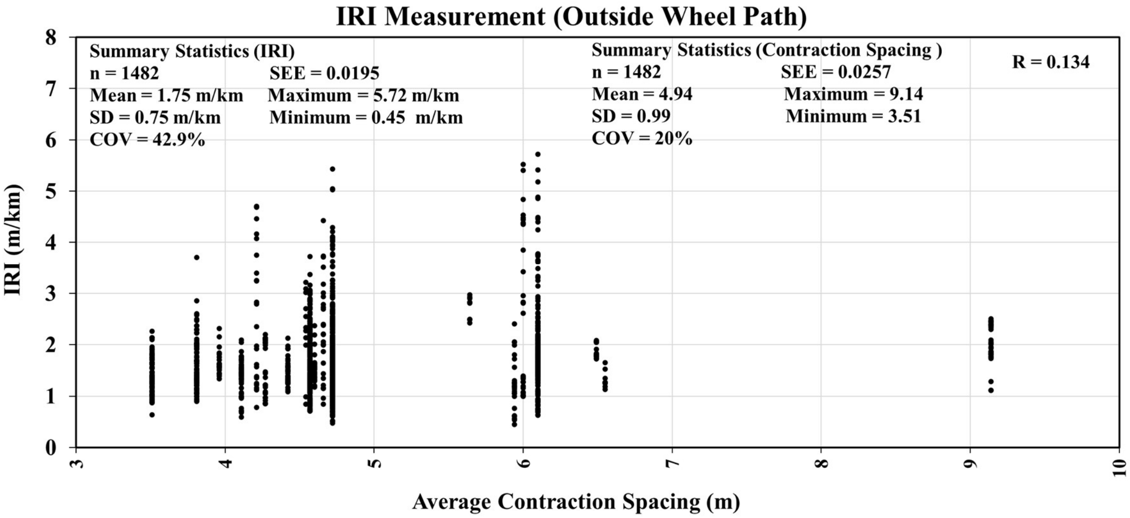

Figure 87 Average Contraction Spacing vs. IRI Measurement (Outside Wheel Path) of JPCP Sections

Cumulative ESAL:

Cumulative ESAL (CESAL) is the sum of annual ESAL data over the years. ESAL represents a mixed stream of traffic of different axle loads and axle configurations predicted over the design or analysis period and then converted into an equivalent number of 18,000-lb. single axle loads summed over that period. ESAL represents the effects of traffic loads on the pavement over time. In some years, the LTPP database did not have ESAL information corresponding to the IRI measurements data. Interpolation and extrapolation procedures were applied using known data points to compute ESAL for the missing years. Cumulative ESAL represents the cumulative traffic load that was endured by the pavement over pavements' life. CESAL has one of the most important effects on pavement deterioration. Hence, it is vital to use in performance modeling. CESAL has a mean of 5,519,198 and a standard deviation of 7,631,630. Figure 88 shows the CESAL values corresponded to the IRI outside wheel path measurements for JPCP sections included in this study.

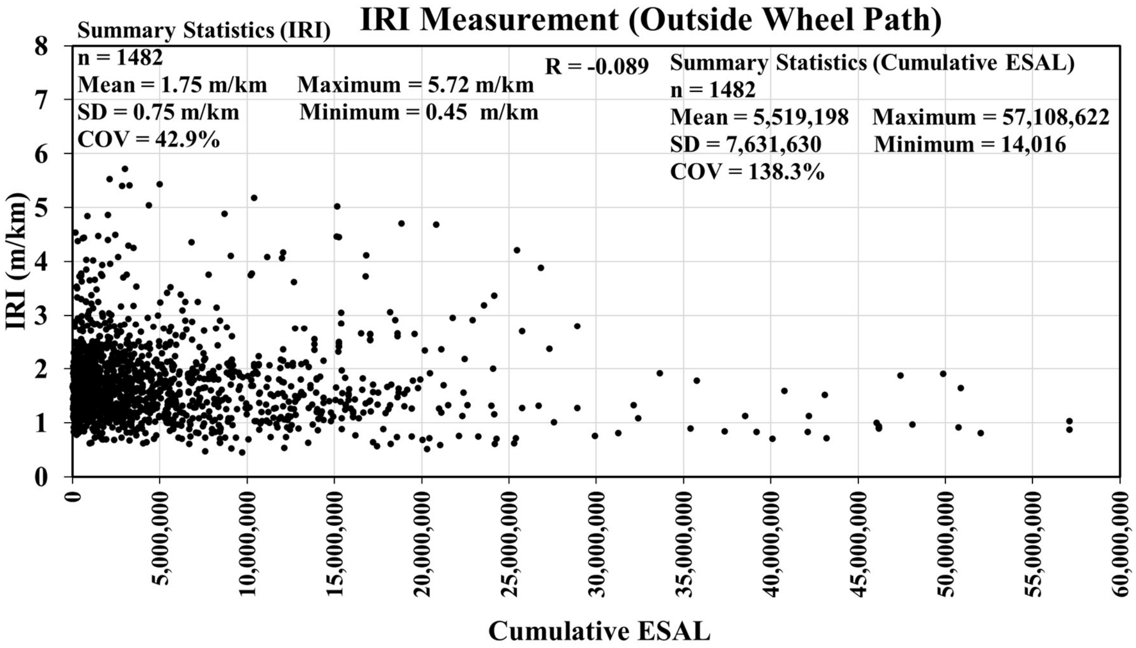

Figure 88 Cumulative ESAL vs. IRI Measurement (Outside Wheel Path) of JPCP Sections

Average Annual Temperature:

Average annual temperature represents the average daily mean air temperatures for the year. The temperature data were collected corresponding to each IRI outside wheel path measurement collection year (visit year). The temperature changes affect the material properties of pavements and contribute to the pavement deterioration process. Thus, this climatological variable is used in pavement performance modeling. The collected data has a mean of 12.25 °C and a standard deviation of 4.89 °C average annual temperature. The maximum temperature is 26.6 °C and the minimum temperature is 2.5 °C. Figure 89 shows the average annual temperature and IRI outside wheel path measurements for JPCP sections.

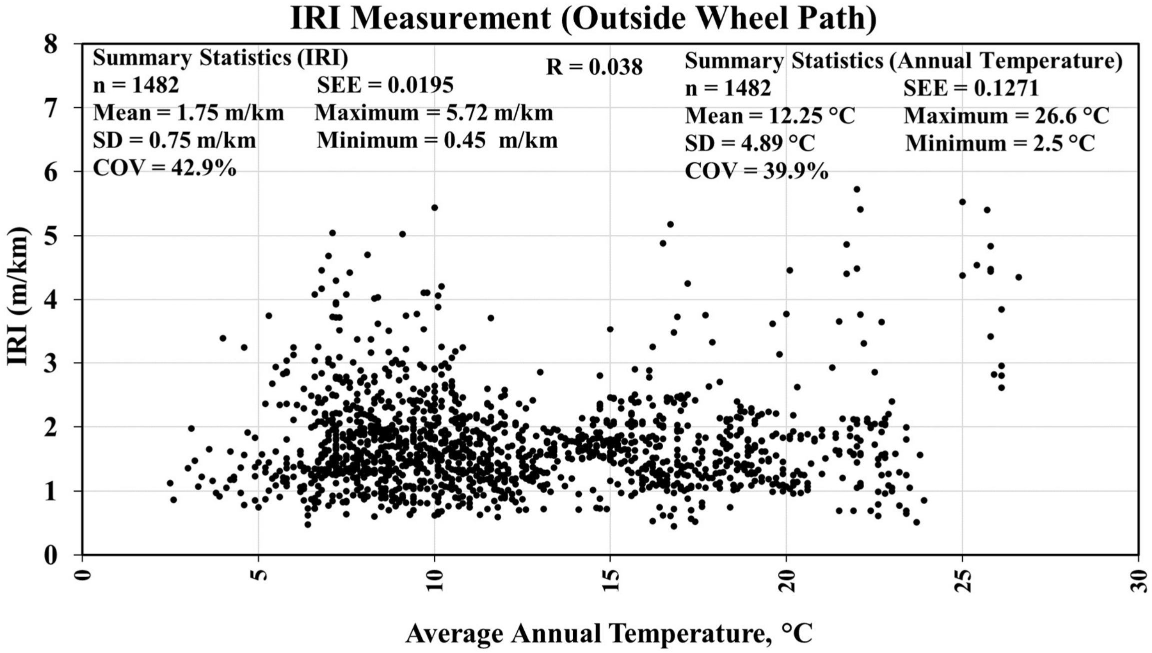

Figure 89 Average Annual Temperature vs. IRI Measurement (Outside Wheel Path) of JPCP Sections

Total Annual Precipitation:

Total annual precipitation represents the sum of monthly precipitation for the year. The precipitation data were collected corresponding to each IRI outside wheel path measurement collection year (visit year). The amount of precipitation affects the material properties of pavements' base/ subbase and subgrade layer hence, also has effects on the pavement deterioration process. Thus, this climatological variable is used in pavement performance modeling. The collected data has a mean of 793.16 mm with a standard deviation of 423.85 mm total annual precipitation. The maximum total annual precipitation is 2,235 mm and the minimum is 59 mm. Figure 90 shows the total annual precipitation and IRI outside wheel path measurements for JPCP sections.

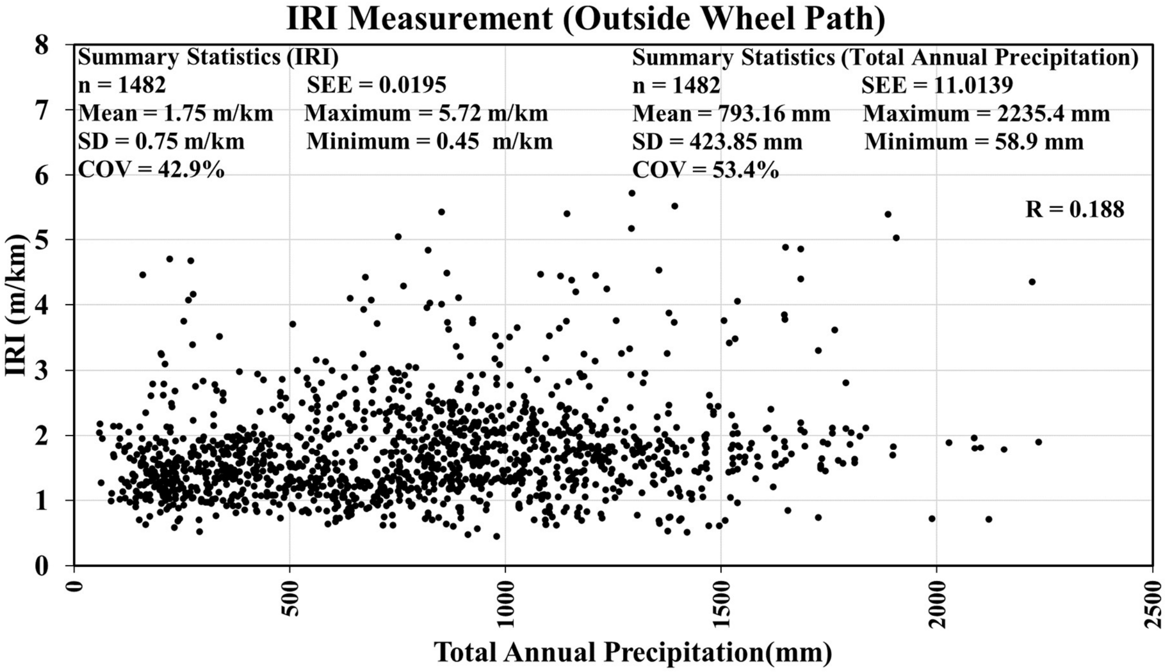

Figure 90 Total Annual Precipitation vs. IRI Measurement (Outside Wheel Path) of JPCP Sections

Annual Freezing Index:

The annual freezing index represents the sum of the difference between 0 and mean daily air temperature, when the mean daily air temperature is less than 0 °C, for each day of the month. This signifies the freezing of pavement sections thus freezing of pavement materials which affect the pavement performance. The annual freeze index data were collected corresponding to each IRI outside wheel path measurement collection year (visit year). The collected data has a mean of 333.8 and a standard deviation of 357.96 for the annual freezing index. The maximum annual freezing index is 1937. Figure 91 shows the annual freezing index and corresponded IRI outside wheel path measurements.

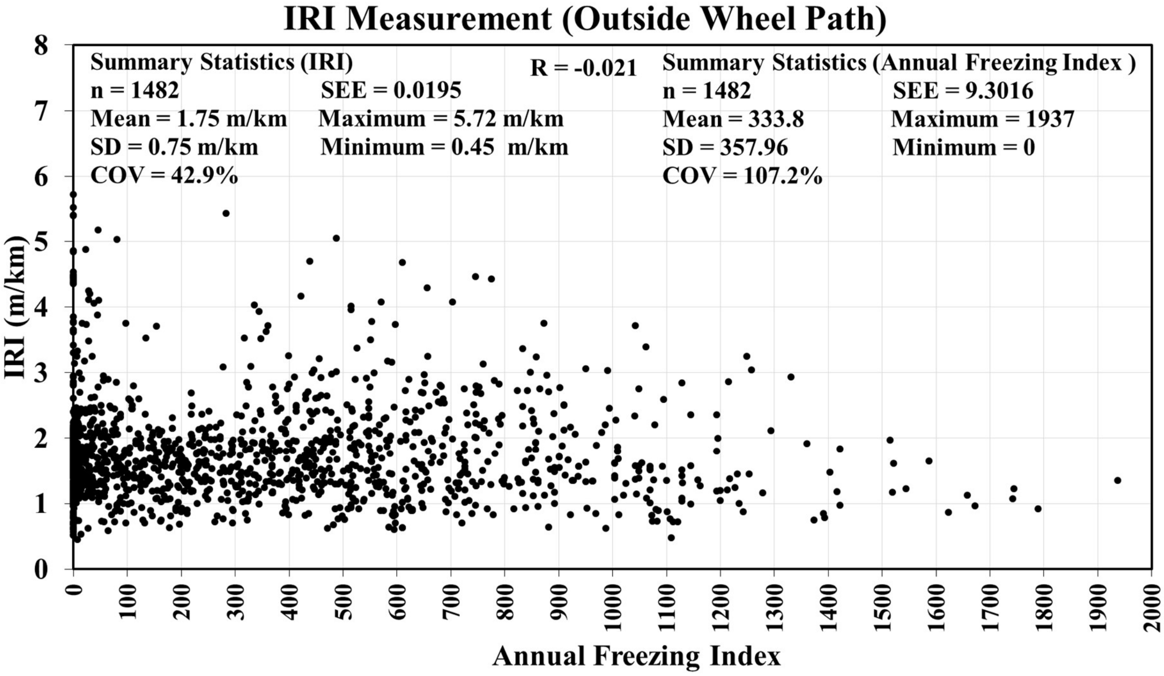

Figure 91 Annual Freezing Index vs. IRI Measurement (Outside Wheel Path) of JPCP Sections

Annual Freeze-Thaw (days):

Annual freeze-thaw (days) represents the number of days in the year when the air temperature goes from less than 0 °C to greater than 0 °C, assumes minimum daily temperature occurs before maximum daily temperature. This signifies that the number of days pavement sections undergo a freeze-thaw process which affects the pavement materials hence pavement performance. The annual freeze-thaw has a mean of 77.45 days with a standard deviation of 43.4

days. The maximum annual freeze-thaw days are 204 days. Figure 92 shows the annual freeze-thaw and corresponded IRI outside wheel path measurements.

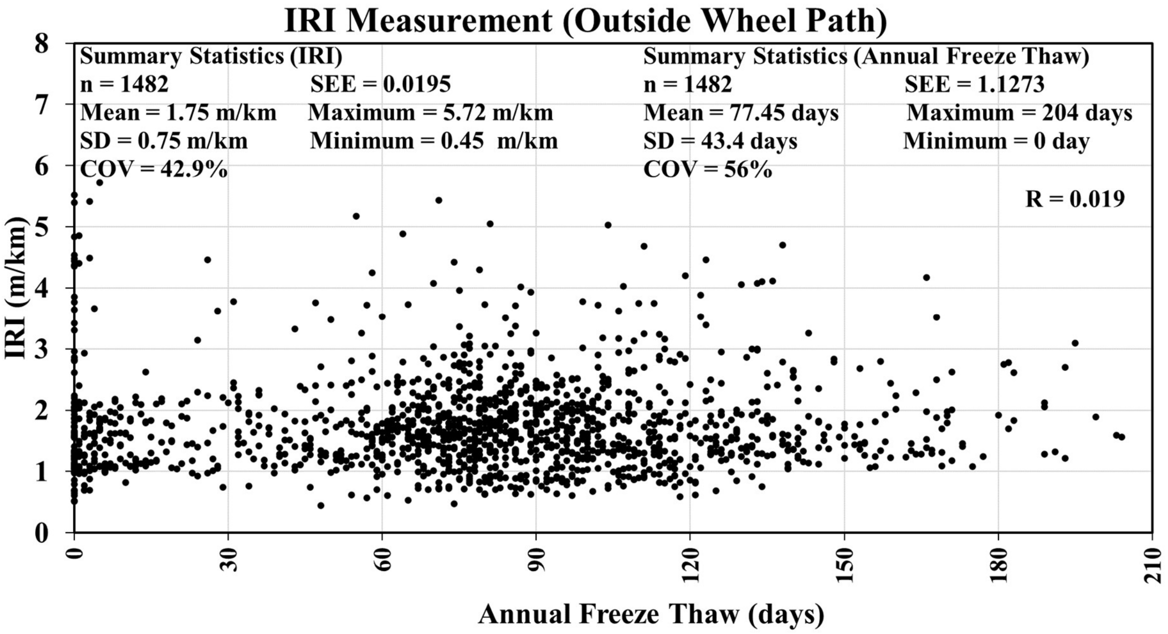

Figure 92 Annual Freeze-Thaw vs. IRI Measurement (Outside Wheel Path) of JPCP Sections

A correlation analysis was performed to obtain the Pearson correlation coefficient (r) between all variables. The correlation matrix summarizes the correlation coefficient (r) values between all the variables and it is easy to observe if the variables are correlated with each other. This correlation coefficient (r) only provides a linear association between variables, if the data is not linearly correlated it will have a low correlation value. Table 23 summarizes the descriptive statistics of input variables used in this study and the correlation between each input variable and the output variable (IRI outside wheel path).

The three highest correlations between input variables and IRI outside wheel path (m/km) were observed with the variable initial IRI (outside wheel path) (m/km) (0.65) followed by total annual precipitation (mm) (0.188), and average contraction spacing (m) (0.134). Other variables show low correlation coefficient (r) values, which means they are not linearly correlated with the output variable. However, these variables might follow a non-linear correlation with IRI outside wheel path (m/km) that cannot be identified by the correlational analysis. Therefore, even though some correlation coefficient values were low, all input variables were used in this study for the development of ANN models.

Table 23 Descriptive Statistics of Input Variables for JPCP Model

Statistics	Mean	SD	COV (%)	Maximum	Minimum	Correlation with IRI outside wheel path (m/km), r
Initial IRI (Outside Wheel Path) (m/km)	1.66	0.6078	36.6%	4.53	0.83	0.650
Age	19	9.2438	49.8%	46	1	0.038
Cumulative ESAL	5,519,198	7,631,630	1	57,108,622	14,016	-0.089
Concrete Pavement Thickness (in)	9.6	1.2174	12.7%	13.2	7	0.013
Base/Subbase Thickness (in)	5.3	2.9018	54.5%	23.2	0	0.096
Average Contraction Spacing (m)	4.9416	0.9900	20.0%	9.14	3.51	0.134
Average Annual Air Temperature (°C)	12.2472	4.8935	40.0%	26.6	2.5	0.038
Total Annual Precipitation (mm)	793.1601	423.8546	53.4%	2235.3999	58.9	0.188
Annual Freezing Index	333.8036	357.9607	107.2%	1937	0	-0.021
Annual Freeze-Thaw (days)	77.4480	43.3860	56.0%	204	0	0.019

Some variables were dummy coded as 0 and 1 for modeling purposes. The categorical variables used in this study are summarized in Table 24.

The climatic region represents the climate zone defined by the LTPP which consists of four different regions, wet non-freeze, dry non-freeze, dry freeze, wet freeze. Correlation analysis shows a correlation coefficient value of 0.18 between wet, non-freeze climate zone and IRI outside wheel path (m/km) and a negative correlation coefficient value of -0.2 between dry, non-freeze climate zone and IRI outside wheel path (m/km).

Season characterizes the month in which the measurements were collected, and it consists of four seasons, spring (March, April, May), summer (June, July, August), autumn (September, October, November), and winter (December, January, February). The summer season has the highest correlation (0.11) with IRI outside wheel path (m/km).

The base/subbase materials represent the type of base/subbase materials used in the pavement section which consists of two types, unbound (granular) or bound (stabilized).

Table 24 Correlation between IRI (Outside Wheel Path) (m/km) with Categorical Variables

Categorical Variables	Categories	Correlation with IRI outside wheel path (m/km), r
Climatic Region (Categorical variable for LTPP climatic region)	Wet, Non-Freeze	0.18
	Dry, Non-Freeze	-0.20
	Dry, Freeze	-0.02
	Wet, Freeze	0.00
Seasons (Categorical variable for the season)	Winter	0.00
	Spring	-0.07
	Summer	0.11
	Autumn	-0.03
Base/Subbase Material (Categorical variable for Base/Subbase materials)	Unbound (Granular) Base/ Subbase	0.05
	Bound (Treated) Base/ Subbase	-0.03

The annual average temperature, total annual precipitation, annual freezing index, and annual freeze-thaw are responsible to represent the effect of climate variables in the model. Concrete, base, and subgrade layers' properties are susceptible to both temperature and moisture variations, which makes the use of climate variables crucial for more accurate pavement performance models. Table 25 shows that there is a high linear association between climate variables and climate zones defined by the LTPP. For this reason, climate variables were not included in the process of developing final models. The climate zones were used as a categorical variable.

Table 25 Correlation between Climatological Variables and LTPP Climate Zones

Input Variables	Wet, Non-Freeze	Dry, Non-Freeze	Dry, Freeze	Wet, Freeze
Average Annual Air Temperature (°C)	0.62	0.40	-0.22	-0.66
Total Annual Precipitation (mm)	0.65	-0.45	-0.47	0.10
Annual Freezing Index	-0.50	-0.35	-0.06	0.73
Annual Freeze-Thaw (days)	-0.43	-0.48	0.48	0.36

4.8.2 Maintenance and Rehabilitation Actions

In a previous study to develop an IRI roughness prediction model using the LTPP database for Southern U.S. states, Mohamed Jaafar and Uddin [73] discussed the effect of the CN on asphalt highway pavement roughness. As an illustration, for JPCP Figure 93 shows different CN values for section 06-3042 located in California. This test section has four construction numbers (CN1, CN2, CN3, CN4), which were assigned in 1989, 1996, 2008, and 2010. It was observed that the IRI values at each subsequent CN decreased as seen in CN2 year and more sharply decreased in CN4 year, and then increased again until the subsequent maintenance and rehabilitation year. Another example of JPCP highway section 06-3013 is shown in Figure 94, which has only CN1 (starting year) and CN2 (year 2007) interventions. The IRI shows a significant reduction in the year 2009.

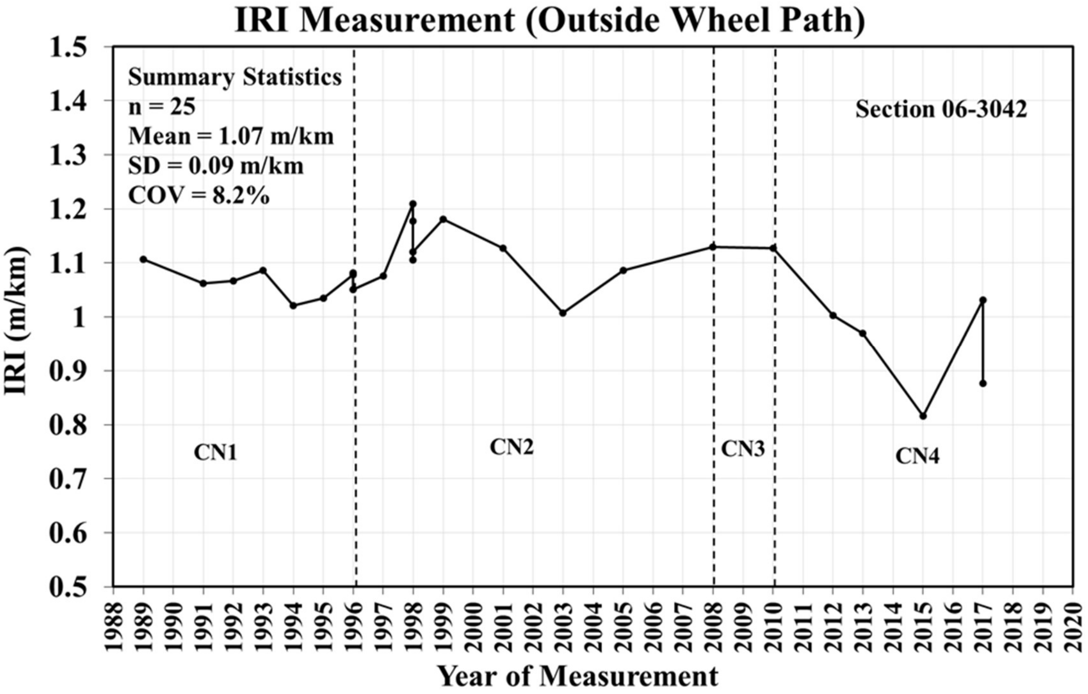

Figure 93 IRI Data for JPCP Section 06-3042 in California

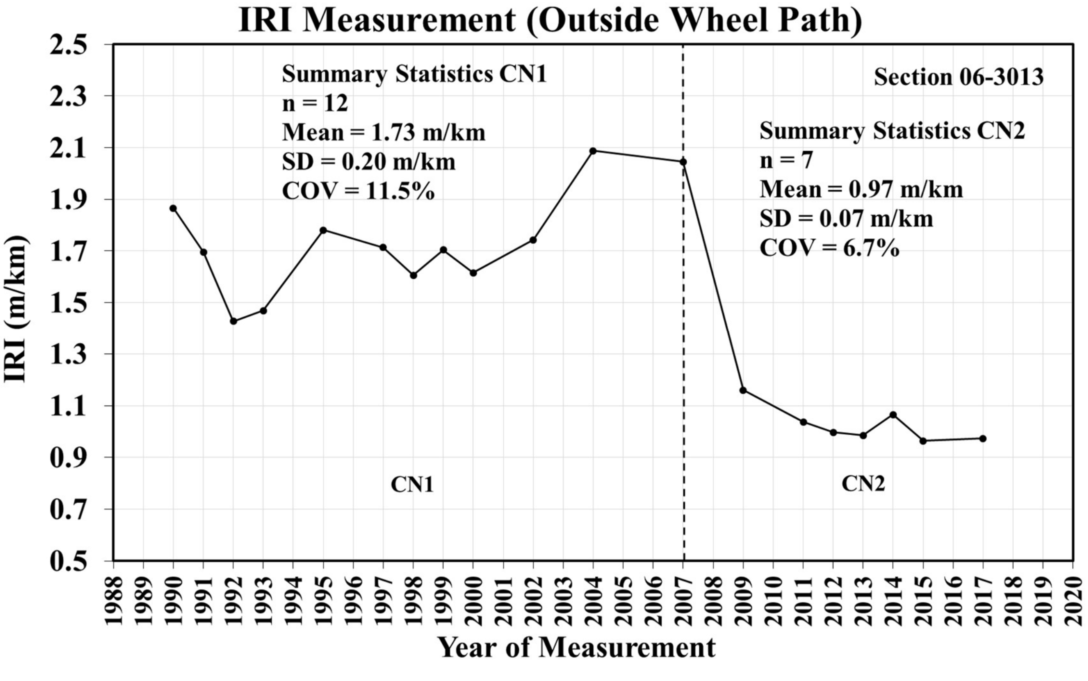

Figure 94 IRI Data for JPCP Section 06-3013 in California

It is evident from Figure 94 that the M&R treatments improved the JPCP surface condition, which contributed to lower IRI roughness values. This statement is supported by an independent sample t-test described below. The t-test compared whether there are statistically significant differences between the means of yearly IRI between CN1 and CN2 (pre- and post-CN2).

Step-by-Step Procedure

Step 1: Setup null hypothesis and alternative hypothesis.

Null Hypothesis: H_0: $\mu 1 = \mu 2$

Where:

$\mu 1$ = Mean of Population 1 for CN1 IRI

$\mu 2$ = Mean of Population 2 for CN2 IRI

The population means of the two samples (CN1 IRI and CN2 IRI) are equal. This implies that both samples are from the same population.

Alternative Hypothesis: H_A: $\mu 1 \neq \mu 2$

The population means of the two samples (CN1 IRI and CN2 IRI) are not equal. This implies that both samples are from different populations.

Step 2: Select α probability of Type 1 chance error for α level of statistical significance.

$\alpha = 0.05$; $\alpha/2 = 0.025$ (for two-tailed test)

Figure 83 shows the two-tailed t-test probability distribution.

Step 3: Define test criteria and decision rule for rejecting H_0.

Test criteria: $t_{critical} = 2.11$ for degree of freedom (dof) = 17 and $\alpha/2 = 0.025$

Decision Rule: Reject H_0 if t-test statistics t_{test} exceeds the absolute value of $t_{critical}$ ($t_{test} > t_{critical}$) and probability of significance value, $p \leq$ Probability of Type-1 chance error, α.

Step 4: Calculate t test statistics, t_{test}, and p-significance value.

$t_{test} = 8.92$

Probability of significance, p-value < 0.001

Step 5: Interpret the results.

t_{test} (8.92) > $t_{critical}$ (2.11) and p (<0.001) < α (0.05)

Therefore, the t-test rejects the null hypothesis. The results show that the difference in the means of CN1 IRI and CN2 IRI are statistically significant at α 0.05 probability of chance error. This implies that both IRI samples (CN1 and CN2) are from different populations. This confirmed that the mean IRI value for CN2 (0.97 m/km) is statistically significant and lower, compared to the mean IRI value for CN1 (1.73 m/km).

The t-test established that there is a significant change in IRI value after M&R actions are done on a pavement section. Hence, it is important to incorporate pavement M&R history in the JPCP performance model. An in-depth study of M&R history provided in the LTPP database concrete pavement has been carried out in this research. The process is as follows:

- The M&R actions (improvement done on pavement) history was collected from the LTPP database. The M&R action was provided as IMP_TYPE code that is assigned by the LTPP. The description of IMP_TYPE code is described in Table 26 gathered from the LTPP user guide [74]. This table contained the type of improvements for both concrete and asphalt pavement. For this research, only concrete pavement improvement types (M&R actions) were further investigated.

Table 26 IMP_Type and Improvement Description collected from LTPP User Guide [74]

IMP_Type	Type of Improvement
1	Crack Sealing
2	Transverse Joint Sealing
3	Lane-Shoulder Longitudinal Joint Sealing
4	Full-Depth Transverse Joint Repair Patch
5	Full-Depth Patching of PCC Pavement Other Than at Joint
6	Partial-Depth Patching of PCC Pavement Other Than at Joint
7	PCC Slab Replacement
8	PCC Shoulder Restoration
9	PCC Shoulder Replacement
10	AC Shoulder Restoration
11	AC Shoulder Replacement
12	Grinding Surface
13	Grooving Surface
14	Pressure Grout Subsealing
16	Asphalt Subsealing
19	AC Overlay
20	PCC Overlay
21	Mechanical Premix Patch
22	Manual Premix Spot Patch
23	Machine Premix Patch
24	Full-Depth Patch of AC Pavement
25	Patch Pot Holes: Hand Spread, Compacted with Truck
26	Skin Patching
27	Strip Patching
28	Surface Treatment, Single Layer
29	Surface Treatment, Double Layer
30	Surface Treatment, Three or More Layers
31	Aggregate Seal Coat
32	Sand Seal Coat
33	Slurry Seal Coat
34	Fog Seal Coat
35	Prime Coat
36	Tack Coat
37	Dust Layering
38	Longitudinal Subdrainage
39	Transverse Subdrainage

IMP_Type	Type of Improvement
40	Drainage Blankets
41	Well System
42	Drainage Blankets with Longitudinal Drains
43	Hot-Mix Recycled AC
44	Cold-Mix Recycled AC
45	Heater Scarification, Surface-Recycled AC
46	Crack-and-Seat PCC Pavement + AC Surface
47	Crack-and-Seat PCC Pavement + PCC Surface
48	Recycled PCC
49	Pressure Relief Joints in PCC Pavements
50	Joint Load-Transfer Restoration in PCC
51	Mill Off AC and Overlay with AC
52	Mill Off AC and Overlay with PCC
53	Other
54	Partial-Depth Joint Patching of PCC Pavement
55	Mill Existing Pavement and Overlay with Hot-Mix AC
56	Mill Existing Pavement and Overlay with Cold-Mix AC
57	Saw and seal

- The M&R action corresponded to each IRI data point was obtained from Table 26. The IMP_TYPE and the description for the type of improvements for concrete pavements are described in Table 27. The M&R actions can be characterized in two categories: major M&R and local/minor M&R. Table 27 described the designation of M&R categories for the different types of improvement [75]. The improvement description and designated M&R action category were obtained for each IRI data point using Table 27.

Table 27 Designation of Major M&R and Minor M&R for Different Type of Improvement [75]

IMP_Type	Type of Improvement	M&R Definitions Local/Minor = L_Minor Major = M
1	Crack Sealing	L_Minor
2	Transverse Joint Sealing	L_Minor (less than or equal to 50% slabs) Major (more than 50% slabs)
3	Lane-Shoulder Longitudinal Joint Sealing	L_Minor
4	Full-Depth Transverse Joint Repair Patch	Major

IMP_Type	Type of Improvement	M&R Definitions Local/Minor = L_Minor Major = M
5	Full-Depth Patching of PCC Pavement Other Than at Joint	Major
6	Partial-Depth Patching of PCC Pavement Other Than at Joint	L_Minor (less than or equal to 10% slabs) Major (more than 10% slabs)
7	PCC Slab Replacement	Major
8	PCC Shoulder Restoration	L_Minor
9	PCC Shoulder Replacement	Major
10	AC Shoulder Restoration	L_Minor
11	AC Shoulder Replacement	L_Minor
12	Grinding Surface	L_Minor
13	Grooving Surface	Major
14	Pressure Grout Subsealing	L_Minor (less than or equal to 10% slabs) Major (more than 10% slabs)
16	Asphalt Subsealing	L_Minor
38	Longitudinal Subdrainage	L_Minor
39	Transverse Subdrainage	L_Minor
40	Drainage Blankets	L_Minor
41	Well System	L_Minor
42	Drainage Blankets with Longitudinal Drains	L_Minor
47	Crack-and-Seat PCC Pavement + PCC Surface	Major (if recorded)
48	Recycled PCC	Major (if recorded)
49	Pressure Relief Joints in PCC Pavements	L_Minor
50	Joint Load-Transfer Restoration in PCC	Major
53	Other	L_Minor (If IRI Improves)
54	Partial-Depth Joint Patching of PCC Pavement	L_Minor

The CN_Code categorical variable was developed to represent the M&R action done on a pavement section. The LTPP database has the Construction Number (CN) corresponded to each IRI data point and the description is given in Section 4.7. But this CN is not an accurate representation of the improvement action done on pavement. For this reason, this doctoral research assigned CN_Code for each IRI data point based on IRI value improvement, the M&R action done before the collection of IRI measurements, and the type of M&R action (major, local/minor). Several CN_Code were developed to achieve the most accurate model that will provide an accurate future prediction of IRI and incorporate the M&R actions in the developed model. The description of each CN_Code is given below:

(1) The first CN_Code was developed based on the original CN collected from the LTPP database corresponded to each IRI data point. If no M&R action (CN1 in the original LTPP database) was done, the CN_Code was categorized as '0', and this 0 was continued until an M&R action was performed. The first M&R action (CN2 in the original LTPP database) was categorized as '1', and this 1 was continued until the second M&R action. The second M&R action (CN3 in the original LTPP database) was categorized as '2', and this 2 was continued until the third M&R action. This CN_Code assignment continued until all the M&R actions done on a pavement section were categorized.

(2) The second CN_Code was also developed based on the original CN collected from the LTPP database corresponded to each IRI data point. If no M&R action (CN1 in the original LTPP database) was done, the CN_Code was categorized as '1', and this 1 was continued until an M&R action was performed. The first M&R action (CN2 in the original LTPP database) was categorized as '2', and this 2 was continued until the second M&R action. The second M&R action (CN3 in the original LTPP database) was categorized as '3', and this 3 was continued until the third M&R action. This CN_Code assignment continued until all the M&R actions done on a pavement section were categorized.

(3) The third CN_Code was developed based on the improvement of IRI values for each IRI data point. If the IRI value change was less than 0.1 m/km, the CN_Code was assigned as ‘0’. If the IRI value change was more than 0.1 m/km, the CN_Code was assigned as ‘1’, and when the next IRI value change was more than 0.1 m/km, the CN_Code was assigned as ‘2’. In between CN_Code ‘1’ and CN_Code ‘2’, the CN_Code for other data points was assigned as ‘0’. This CN_Code assignment continued until all the IRI data points were categorized.

(4) The fourth CN_Code was also developed based on the improvement of IRI values for each IRI data point. If the IRI value change was less than 0.1 m/km, the CN_Code was assigned as ‘0’, and this 0 was continued until the IRI value change was more than 0.1m/km. If the IRI value change was more than 0.1 m/km, the CN_Code was assigned as ‘1’, and this 1 was continued until the next IRI value change was more than 0.1m/km. When the next IRI value change was more than 0.1 m/km, the CN_Code was assigned as ‘2’, and this 2 was continued until the next IRI value change was more than 0.1m/km. This CN_Code assignment process continued until all the IRI data points were categorized.

(5) The fifth CN_Code was developed based on the IRI value improvement and the type of M&R action provided in Table 27. If no M&R action was done and the improvement of IRI value was very low, the CN_Code was categorized as ‘0’, and this 0 continued until an M&R action was performed or the IRI value improved significantly. The first data point found with an M&R action done or a significant improvement of IRI value was assigned as ‘1’ CN_Code and this 1 continued until the end of IRI data points for this pavement section.

(6) The sixth and the last CN_Code was also developed based on the IRI value improvement and the type of M&R action provided in Table 27. If no M&R action was done and the improvement of IRI value was very low, the CN_Code was categorized as ‘0’, and this 0 continued until an M&R action was performed or the IRI value improved significantly. The first data point found with an M&R action done or a significant improvement of IRI values was assigned as ‘1’ CN_Code and this 1 continued until the next M&R action was performed or the IRI value improved significantly. The next data point found with an M&R action done or a significant improvement of IRI value was assigned as ‘2’ CN_Code and this 2 continued until the next M&R action was found or the IRI value improved significantly. This CN_Code assignment process continued until all the IRI data points were categorized for a pavement section.

4.8.3 Database Summary

The input and output variables are thoroughly discussed in section 4.8.1. Table 28 shows the key input variables for the final JPCP models. As discussed above, the climate variables show a high linear association with climatic regions. For this reason, for JPCP final models only climatic regions were used as input variables. The climate variables are also needed to be predicted for future prediction of the output variable (IRI outside wheel path).

Table 28 Input Variables for JPCP Performance Models

No.	**Input Variables**	
1	IRI_0 (Initial IRI Outside Wheel Path) (m/km)	Initial IRI Outside Wheel Path (m/km)
2	Age (Pavement age, years)	Age

No.	**Input Variables**	
3	$h_{concrete}$ (Concrete pavement thickness, in)	$h_{concrete}$
4	$h_{base/subbase}$ (Base/Subbase thickness, in)	$h_{base/subbase}$
5	Average Contraction spacing (m)	Average Contraction spacing (m)
6	CESAL (Cumulative Equivalent Single Axel Load)	CESAL
7	Base/Subbase Materials (Categorical variable for Base/Subbase materials)	Unbound (Granular) Base/ Subbase Bound (Treated) Base/ Subbase
8	Climatic Region (Categorical variable for LTPP climatic region)	Wet, Non-Freeze Dry, Non-Freeze Wet, Freeze Dry, Freeze
9	Seasons (Categorical variable for the season)	Winter (Dec-Feb) Spring (Mar-May) Summer (June-Aug) Autumn (Sept-Nov)

The maintenance and rehabilitation (M&R) history is represented as CN_Code. Table 29 shows the CN_Code used in these final models. CN_Code descriptions are discussed in section 4.8.2. Six models were tried to find the most accurate model that can predict IRI incorporating the M&R history of the pavement sections.

Table 29 CN_Code used in JPCP Perfomance Models

Models	**CN (Construction Number, variable for M & R)**
Model A	CN Original Continuous: (0,0,1,1,2,2…) No M&R Action 0 M&R Action 1,2….
Model Aa	CN Original Continuous: (1,1,2,2…) No M&R Action 1 M&R Action 2,3,4….
Model A1	CN Continuous if more than 0.1m/km IRI change: (0,0,1,0,2,0...) No IRI Improvement 0 IRI Improvement 1,2….

Models	CN (Construction Number, variable for M & R)
Model A2	CN Continuous if more than 0.1m/km IRI change: (0,0,1,1,2,2...) No IRI Improvement 0 IRI Improvement 1,2….
Model A3	CN Categorical: (0,1) (Based on IRI value improvement and the type of M&R action provided in Table 27) No IRI Improvement and/or M&R Action 0 Any IRI Improvement and/or M&R Action 1
Model A4	CN Continuous: (1,1,2,2,3,3,…..) (Based on IRI value improvement and the type of M&R action provided in Table 27) No IRI Improvement and/or M&R Action 1 IRI Improvement and/or M&R Action 2,3,4

This research also developed the Multiple Linear Regression (MLR) model using the same input variables to compare with the ANN model. For verification of the MLR model, the database was divided into two parts: model database and verification database. The verification pavement sections were randomly selected using some guidelines to ensure these pavement sections were collected from all climate zones. The guidelines are described below:

- If less than 5 LTPP sections in one climate zone do not pick any sections for verification.
- If 5 to 10 LTPP sections in one climate zone pick up one section for verification.
- If 11 to 20 LTPP sections in one climate zone pick up two sections for verification.
- If more than 20 LTPP sections pick up a minimum of three sections for verification

Nine JPCP sections were randomly selected from all climate zones following the above guidelines for the verification database. These nine pavement sections have 127 data points. So, the final model database contains 1,355 data points.

Table 30 Randomly Chosen JPCP Sections for Verification Database

No.	Section	Climate Region
1	37-3807	Wet, Non-Freeze
2	40-4157	Wet, Non-Freeze
3	35-3010	Dry, Non-Freeze
4	53-3014	Dry, Non-Freeze
5	19-3033	Wet, Freeze
6	26-3068	Wet, Freeze
7	27-3005	Wet, Freeze
8	16-3017	Dry, Freeze
9	32-3010	Dry, Freeze

4.9 Final ANN Models

4.9.1 ANN Model Architecture

In the final research, using the developed model database, six models were tried with the same input variables from Table 28 only changing CN_Code described in Table 29. The output variable is IRI outside wheel path (m/km) for all six models. These six models have six continuous variables, three categorical variables, and CN_Code.

4.9.2 ANN Model Selection

Six best performing networks from each model (Model A, Model Aa, Model A1, Model A2, Model A3, and Model A4) were selected based on statistical measures such as minimum values of MARE, ASE, and maximum values of R^2. A total of 1355 datasets were used to build the desired database. Datasets that include minimum and maximum values of each variable were included in the training phase for the network to represent the characteristics of the response. The maximum and minimum ranges of each input/output variable for ANN model development were chosen on purpose to be wider than their actual ranges for better mathematical mapping (30).

Model A

The inputs for Model A are initial IRI, age, concrete pavement thickness, base/subbase thickness, average contraction spacing, CESAL, base/subbase materials type, climatic region, seasons, and CN_Code and output is IRI (outside wheel path) (m/km) as shown in Table 28. The CN_Code is shown in Table 29. This CN_Code is based on the original CN collected from the LTPP database. No M&R action was assigned as 0 and M&R actions were assigned as 1,2 and so on. This CN_Code is a continuous variable where 1, 2 is the frequency of M&R actions done on pavement. Table 31 shows the statistical accuracy of Model A. The ASE values for training, testing, validation, and all data are 0.001938, 0.004707, 0.006162, and 0.001417, respectively. R^2 values for this model are as follows: 0.897 for the training, 0.701 for the testing, 0.623 for the validation, and 0.899 for all data. The final architecture of this model is 17-18-1, where 17 is the number of inputs, 18 is the number of hidden nodes and 1 is the number of output.

Model Aa

The inputs and output of this model are very similar to model A. The CN_Code used in Model Aa is shown in Table 29. This CN_Code is also based on the original CN collected from the LTPP database. No M&R action was assigned as 1 and M&R actions were assigned as 2,3 and so on. This CN_Code is a continuous variable where 2, 3 is the frequency of M&R actions done on pavement. Table 31 shows the statistical accuracy of Model Aa. The ASE values for the selected network are as follows: 0.001201 for the training, 0.004609 for the testing, 0.007607 for the validation, and 0.001409 for all data. The R^2 for training, testing, validation, and all data are

0.920, 0.683, 0.514, and 0.901, respectively. The final architecture of this model is 17-18-1 where, 17 inputs, 18 hidden nodes, and 1 output.

Model A1

The inputs and output of this model are very similar to model Aa. The CN_Code used in Model A1 is shown in Table 29. This CN_Code was developed based on the improvement of IRI values for each IRI data point. If the IRI value change was less than 0.1 m/km, the CN_Code was assigned as '0'. If the IRI value change was more than 0.1 m/km, the CN_Code was assigned as 1, 2, and so on. In between CN_Code '1' and CN_Code '2', the CN_Code for other data points was assigned as '0'. This CN_Code is a continuous variable where 1, 2 is the frequency IRI value improvements. Table 31 shows the statistical accuracy of Model A1. The ASE values for training, testing, validation, and all data are 0.001632, 0.005224, 0.006835, and 0.001718, respectively. R^2 values for this model are as follows: 0.897 for the training, 0.658 for the testing, 0.577 for the validation, and 0.875 for all data. The final architecture of this model is 17-19-1, where 17 is the number of inputs, 19 is the number of hidden nodes and 1 is the number of output.

Model A2

The inputs and output of this model are very similar to model A1. The CN_Code used in Model A2 is shown in Table 29. This CN_Code was also developed based on the improvement of IRI values for each IRI data point. If the IRI value change was less than 0.1 m/km, the CN_Code was assigned as '0'. If the IRI value change was more than 0.1 m/km, the CN_Code was assigned as 1, 2, and so on. This CN_Code is a continuous variable where 1, 2 is the frequency of IRI value improvements. Table 31 shows the statistical accuracy of Model A2. The ASE values for the selected network are as follows: 0.002054 for the training, 0.004246 for the testing, 0.004444 for the validation, and 0.001638 for all data. The R^2 for training, testing, validation, and all data are 0.865, 0.695, 0.709, and 0.882, respectively. The final architecture of this model is 17-13-1 where, 17 inputs, 13 hidden nodes, and 1 output.

Model A3

The inputs and output of this model are very similar to model A2. The CN_Code used in Model A3 is shown in Table 29. This CN_Code was developed based on the IRI value improvement and the type of M&R action provided in Table 27. If no M&R action was done and the improvement of IRI value was very low, the CN_Code was categorized as '0'. If any M&R action was done or there was a significant improvement of IRI value, the CN_Code was assigned as '1' This CN_Code is a categorical variable. Table 31 shows the statistical accuracy of Model A3. The ASE values for training, testing, validation, and all data are 0.001062, 0.003779, 0.004751, and 0.001354, respectively. R^2 values for this model are as follows: 0.932 for the training, 0.724 for the testing, 0.689 for the validation, and 0.904 for all data. The final architecture of this model is 17-17-1, where 17 is the number of inputs, 17 is the number of hidden nodes and 1 is the number of output.

Model A4

The inputs and output of this model are very similar to model A3. The CN_Code used in Model A4 is shown in Table 29. This CN_Code was also developed based on the IRI value improvement and the type of M&R action provided in Table 27. If no M&R action was done and the improvement of IRI value was very low, the CN_Code was categorized as ‘1’. If M&R action was done or there was a significant improvement of IRI value, the CN_Code was assigned as 2, 3, and so on. This CN_Code is a continuous variable where 2, 3 is the frequency of M&R actions and/or IRI value improvements. Table 31 shows the statistical accuracy of Model A4. The ASE values for the selected network are as follows: 0.001485 for the training, 0.003835 for the testing, 0.005116 for the validation, and 0.001630 for all data. The R^2 for training, testing, validation, and all data are 0.900, 0.740, 0.680, and 0.881, respectively. The final architecture of this model is 17-13-1 where, 17 inputs, 13 hidden nodes, and 1 output.

Table 31 Best Networks from Each Model

Models		Model A	Model Aa	ModelA1	ModelA2	ModelA3	Best Model ModelA4
Structure Initial Nodes-Final Nodes-Iterations		14-18-20000	1-18-20000	4-19-20000	5-13-20000	3-17-20000	2-13-20000
Training	MARE	15.357	11.277	13.420	15.490	11.109	13.246
	R^2	0.897	0.920	0.897	0.865	0.932	0.900
	ASE	0.001938	0.001201	0.001632	0.002054	0.001062	0.001485
Testing	MARE	22.175	18.163	21.877	19.798	18.748	18.251
	R^2	0.701	0.683	0.658	0.695	0.724	0.740
	ASE	0.004707	0.004609	0.005224	0.004246	0.003779	0.003835
Validation	MARE	22.575	20.863	23.964	21.614	18.469	20.245
	R^2	0.623	0.514	0.577	0.709	0.689	0.680
	ASE	0.006162	0.007607	0.006835	0.004444	0.004751	0.005116
All Data	MARE	12.376	12.582	12.841	13.008	12.115	12.634
	R^2	0.899	0.901	0.875	0.882	0.904	0.881
	ASE	0.001417	0.001409	0.001718	0.001638	0.001354	0.001630
Final Structure Input Variables-Final Nodes-Iterations		17-18-20000	17-18-20000	17-19-20000	17-13-20000	17-17-20000	17-13-20000

Model A3 has the lowest ASE for training, testing, and all data. Model A3 also has the lowest MARE for training, validation, and all data. Model Aa has the lowest MARE and model A4 has the highest R^2 for testing. Model A3 has the highest R^2 for training and all data. Figure

95 shows that model A2 has the lowest ASE and highest R^2 for validation.

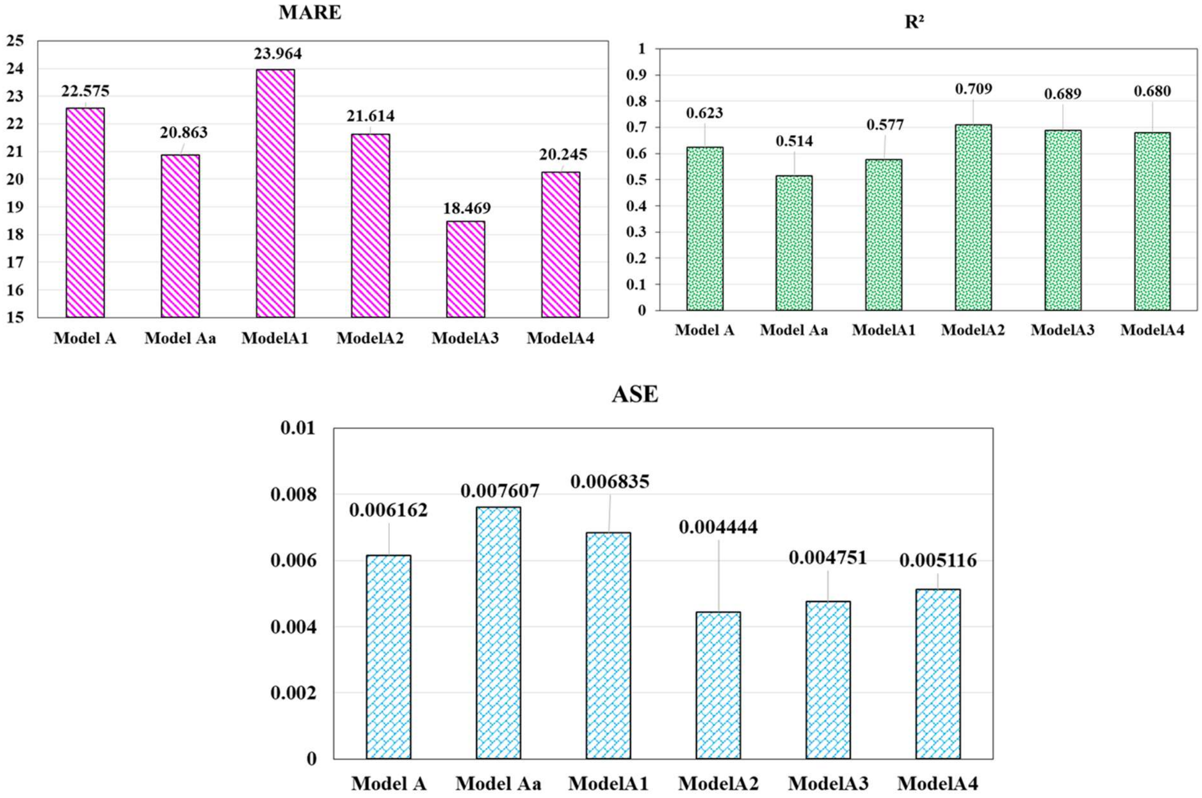

Figure 95 Comparison of Model Accuracy across All Models for Validation

Figure 96 shows that model A3 has the lowest ASE, MARE, and highest R^2 for all data. Based on the statistical accuracy, Model A3 is the best performing network. But as discussed above, the CN_Code used in Model A3 is a categorical variable with 0 and 1 where M&R action and/or IRI improvement frequency cannot be added for future prediction. Model A4 has very similar statistical accuracy and the CN_Code is a continuous variable where M&R action and/or IRI improvement frequency can be added for future prediction. For this reason, Model A4 has been chosen as the best network. Further investigation into the input variables was done using Model A4 input variables and CN_Code.

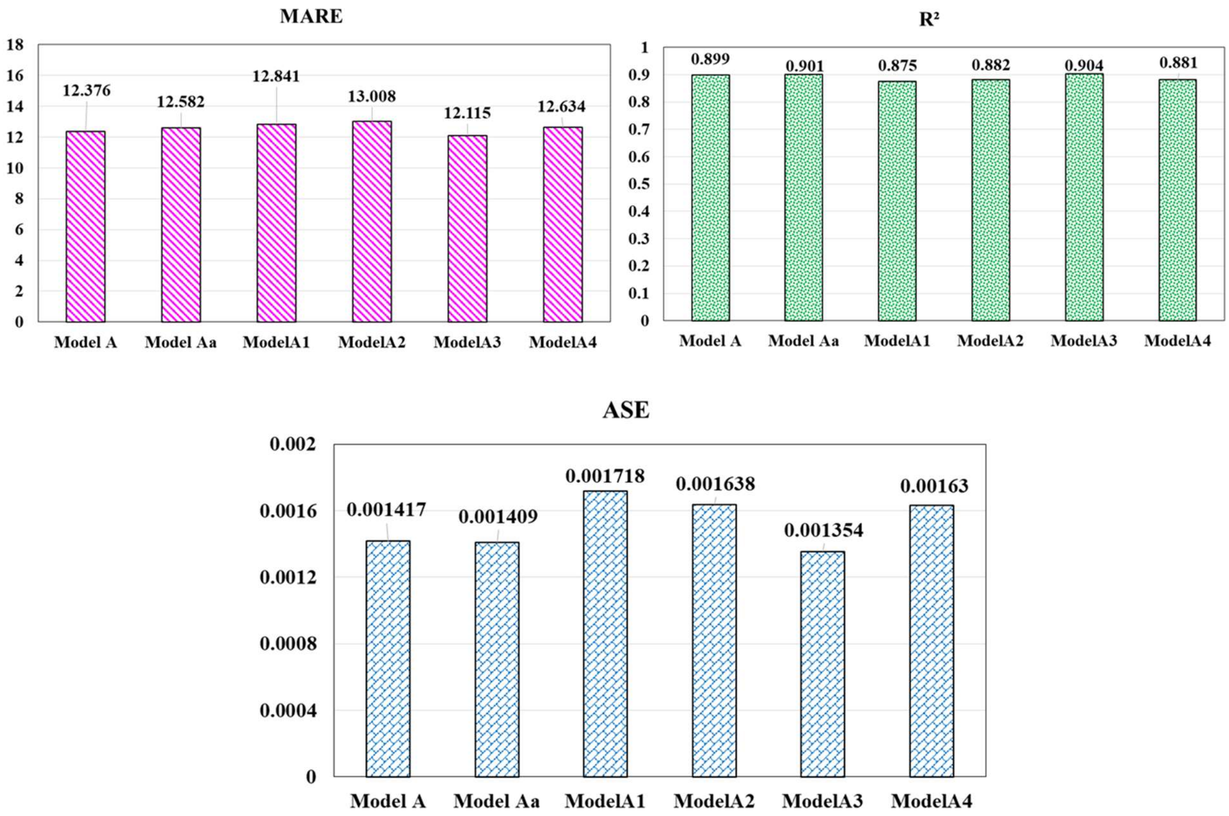

Figure 96 Comparison of Model Accuracy across All Models for All Data

Model A4a

A new model, model A4a was tried using the same input variable as model A4 excluding seasons categorical variable. The CN_Code is also the same as model A4. Table 32 shows the statistical accuracy of Model A4a. The ASE values for the selected network are as follows: 0.001037 for the training, 0.002567 for the testing, 0.002141 for the validation, and 0.000922 for all data. The R^2 for training, testing, validation, and all data are 0.934, 0.805, 0.850, and 0.933, respectively. The final architecture of this model is 13-19-1 where, 13 inputs, 19 hidden nodes, and 1 output.

Table 32 Statistical Accuracy Measures of Five Chosen Model Networks for Model A4a

Dataset	Statistical Error Measures	2-19-20000	7-19-20000	1-14-20000	1-19-20000	Best Model 11-19-20000
Training	MARE	11.791	10.556	13.026	11.877	11.039
	R^2	0.928	0.937	0.920	0.929	0.934
	ASE	0.001166	0.000967	0.001324	0.001153	0.001037
Testing	MARE	15.331	13.759	16.352	15.104	14.779
	R^2	0.836	0.834	0.830	0.826	0.805
	ASE	0.002279	0.002289	0.002378	0.002414	0.002567
Validation	MARE	15.986	15.231	16.025	15.452	14.510
	R^2	0.849	0.837	0.851	0.858	0.850
	ASE	0.002316	0.002404	0.002316	0.002331	0.002141
All Data	MARE	9.825	9.639	11.276	9.954	9.543
	R^2	0.932	0.931	0.911	0.930	0.933
	ASE	0.000961	0.000960	0.001238	0.000978	0.000922
Final Structure		13-19-20000	13-19-20000	13-14-20000	13-19-20000	13-19-20000
						Best Model

Table 33 shows that Model A4a has lower ASE, MARE, and higher R^2 across all datasets. The exclusion of input variable season helped to develop a better model. For this reason, the season was not used as an input variable in the model developing process for other types of concrete pavement.

Table 33 Comparison of Statistical Accuracy Measures between Model A4 and Model A4a

Models		ModelA4	Best Model ModelA4a
Input Variables		**With Independent Variable Seasons**	**Without Independent Variable Seasons**
Structure Initial Nodes-Final Nodes-Iterations		2-13-20000	11-19-20000
Training	MARE	13.246	11.039
	R^2	0.900	0.934
	ASE	0.001485	0.001037
Testing	MARE	18.251	14.779
	R^2	0.740	0.805

Models		ModelA4	Best Model ModelA4a
Input Variables		**With Independent Variable Seasons**	**Without Independent Variable Seasons**
Structure Initial Nodes-Final Nodes-Iterations		2-13-20000	11-19-20000
	ASE	0.003835	0.002567
Validation	MARE	20.245	14.510
	R^2	0.680	0.850
	ASE	0.005116	0.002141
All Data	MARE	12.634	9.543
	R^2	0.881	0.933
	ASE	0.001630	0.000922
Final Structure Input Variables-Final Nodes-Iterations		17-13-20000	13-19-20000

Model B

Table 33 shows that the best performing model is Model A4a. Another model has been tried using the same input variable as Model A4a and included four more climatological variables average annual air temperature (°C), total annual precipitation (mm), annual freezing index, annual freeze-thaw (days). The CN_Code is the same as Model A4a. Table 34 shows the statistical accuracy of Model B. The ASE values for the selected network are as follows: 0.000754 for the training, 0.001982 for the testing, 0.002592 for the validation, and 0.000803 for all data. The R^2 for training, testing, validation, and all data are 0.949, 0.869, 0.837, and 0.942, respectively. The final architecture of this model is 17-19-1 where, 17 inputs, 19 hidden nodes, and 1 output.

Table 34 Statistical Accuracy Measures of Five Chosen Model Networks for Model B

Dataset	Statistical Error measure	Best Model 6-19-20000	10-18-20000	8-19-20000	5-19-20000	11-19-20000
Training	MARE	9.415	10.504	10.560	10.691	9.622
	R^2	0.949	0.934	0.945	0.938	0.948
	ASE	0.000754	0.001005	0.000907	0.001017	0.000836
Testing	MARE	13.062	15.076	15.594	14.712	16.289
	R^2	0.869	0.832	0.854	0.844	0.826
	ASE	0.001982	0.002474	0.002493	0.002572	0.002579
Validation	MARE	13.660	15.584	16.999	16.407	17.063
	R^2	0.837	0.831	0.806	0.817	0.824
	ASE	0.002592	0.002661	0.002943	0.002991	0.002943
All Data	MARE	9.037	9.407	9.644	9.596	9.841
	R^2	0.942	0.935	0.939	0.937	0.935
	ASE	0.000803	0.000910	0.000857	0.000871	0.000915
Final Structure		17-19-20000	17-18-20000	17-19-20000	17-19-20000	17-19-20000

Table 35 shows that Model B has lower ASE and MARE for training, testing, and all data. The R^2 values are also higher for Model B than Model A4a for training, testing, and all data. But Model A4a has a lower MARE, ASE, and higher R^2 value for the validation dataset. For this reason, Model A4 was still chosen as bet performing model. Another reason for choosing model A4a will be that all climatological variables need to be predicted before using in the models for future prediction of IRI. The climatological variables were not used in this doctoral research for the development of other types of concrete pavement performance models.

Table 35 Comparison of Statistical Accuracy Measures between Model A4a and Model B

Models		Best Model ModelA4a	Model B
Structure Initial Nodes-Final Nodes-Iterations		11-19-20000	6-19-20000
Training	MARE	11.039	9.415
	R^2	0.934	0.949
	ASE	0.001037	0.000754
Testing	MARE	14.779	13.062
	R^2	0.805	0.869
	ASE	0.002567	0.001982
Validation	MARE	14.510	13.660
	R^2	0.850	0.837
	ASE	0.002141	0.002592
All Data	MARE	9.543	9.037
	R^2	0.933	0.942
	ASE	0.000922	0.000803
Final Structure Input Variables-Final Nodes-Iterations		13-19-20000	17-19-20000

4.9.3 ANN Model Results

The discussion in the previous section establishes that Model A4a is the best performing network based on all statistical measures (ASE, MARE, and R^2 value). The final model structure has 13 inputs of independent variables, 19 hidden nodes, and 1 output (13-19-1) (Figure 97). The comparison of the prediction accuracy measures for ANN Model A4a is graphically presented in Figure 98. From Figure 98, it is evident that once observed IRI rises above 3.0, the model steadily underestimates the prediction output.

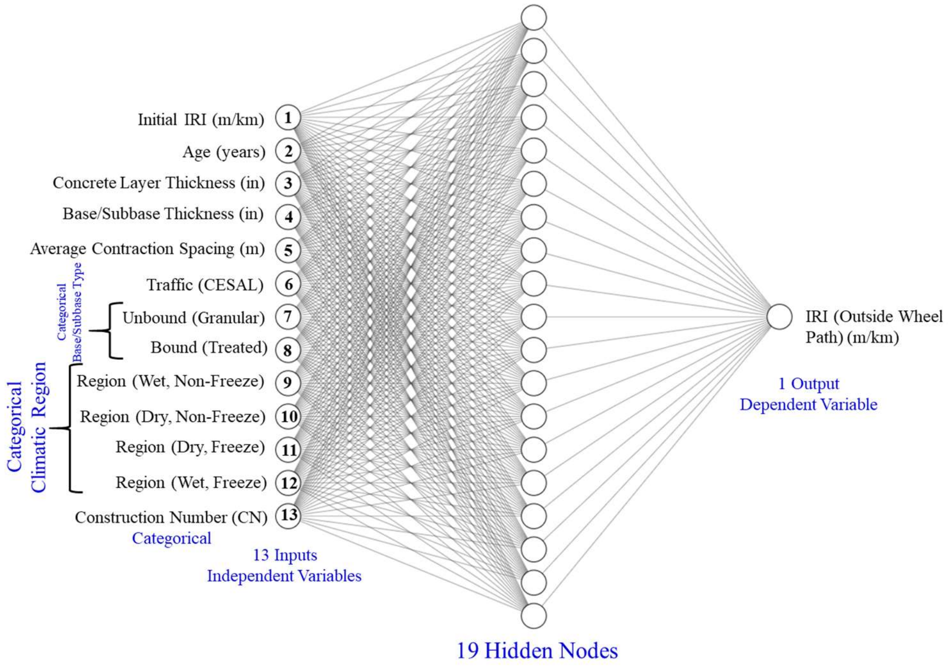

Figure 97 Network Architecture for Best Model (Model A4a, Structure: 13-19-1)

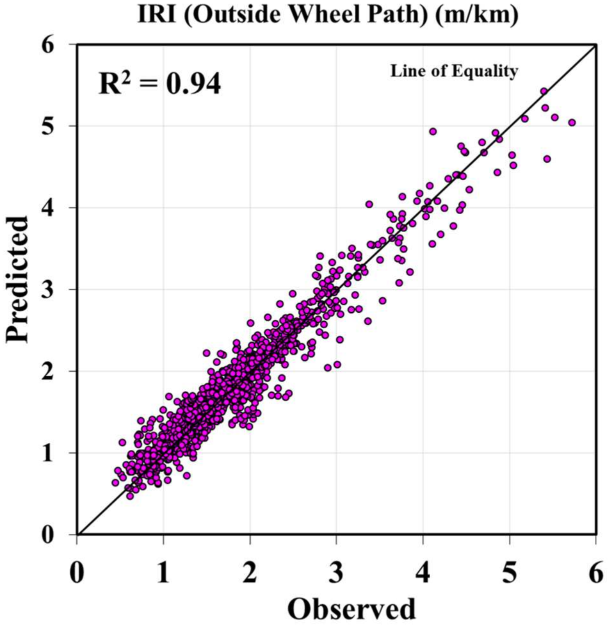

Figure 98 Observed IRI (Outside Wheel Path) (m/km) vs. Predicted IRI (Outside Wheel Path) (m/km)

The 1,355 data points are assigned section sequence numbers from 1 to 1,355. Figure 99 shows the observed and Model A4a predicted IRI (outside wheel path) values. From Figure 99, it is demonstrated that the predicted IRI has apprehended most of the variability in the IRI observed values.

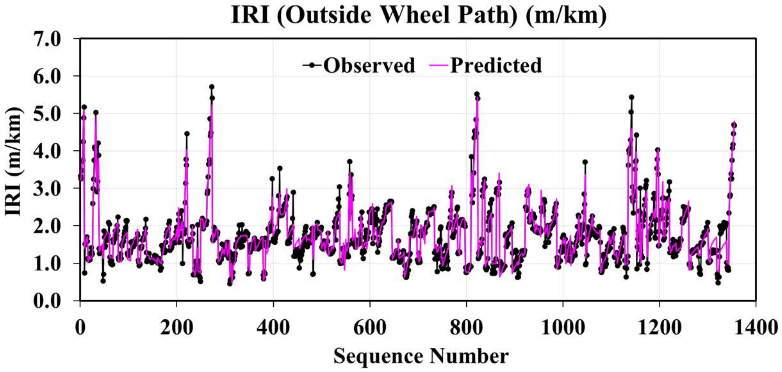

Figure 99 Observed and Predicted IRI (Outside Wheel Path) (m/km) Plot

Figure 100 shows the observed and predicted IRI for Section 27-3012, in Minnesota. The predicted values follow the observed values closely. The difference in the mean values of observed and predicted is 0.23%.

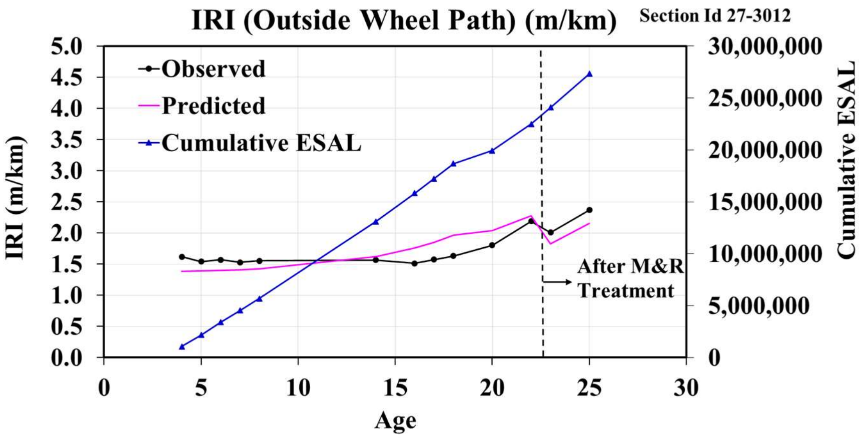

Figure 100 Observed and Predicted IRI (Outside Wheel Path) (m/km) Plot of JPCP section in Minnesota

4.9.4 Sensitivity Analysis

A sensitivity analysis was carried out to evaluate the significance of the inputs on the output. A Graphical User Interface (GUI) was developed by importing all the final ANN model parameters into an excel spreadsheet. To examine the models, some input was changed while keeping the other inputs constant. In this paper, the sensitivity analysis of model A4a is presented since it is the best model in terms of statistical accuracy measures. All model A4a inputs were kept constant except age and CESAL that were changed to generate predictions of IRI. The CESAL values were calculated using the previous year's data. A randomly selected section with one M&R action done was used to show the sensitivity analysis. Figure 101 that the IRI prediction model follows the trend of the observed values. Additionally, it can estimate the increase of IRI values with time and decrease of IRI value after M&R action. Usually, without any rehabilitation, pavement deteriorates over time, therefore, IRI increases.

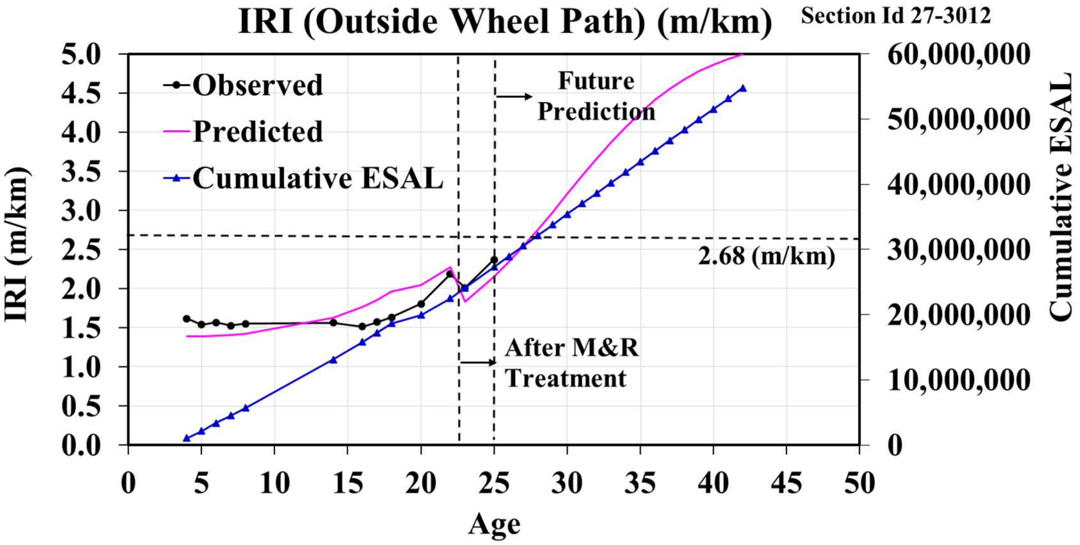

Figure 101 ANN Future Prediction Plot of IRI (Outside Wheel Path) (m/km) for JPCP Section in Minnesota

Figure 101 shows that with the increase of CESAL value, the IRI value increases more than 2.68 m/km when a pavement is considered as very poor condition [10]. At this point, a new M&R action should be done to improve pavement performance. By changing CN_Code frequency using GUI, a future M&R action was provided in the section. Figure 102 shows that with CESAL value increasing over time in the future, the IRI value decreased when future M&R action was done, which means pavement condition improved.

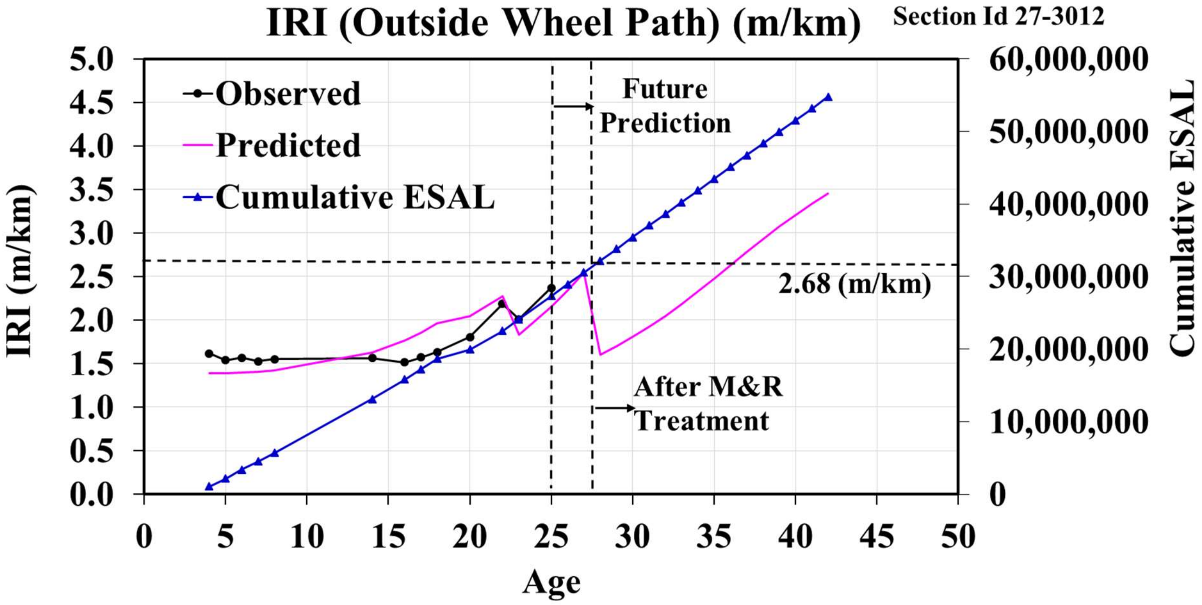

Figure 102 ANN Future Prediction Plot of IRI (Outside Wheel Path) (m/km) after First M&R Action

Figure 102 shows that after one future M&R action has been taken, the IRI value went down, and then the IRI value is increasing with time as CESAL is increasing in the future. The IRI value increases more than 2.68 m/km again at age 36. Another M&R action was provided using the CN_Code frequency and the IRI value plummeted. Figure 103 shows the IRI value drop after the second M&R action in the future.

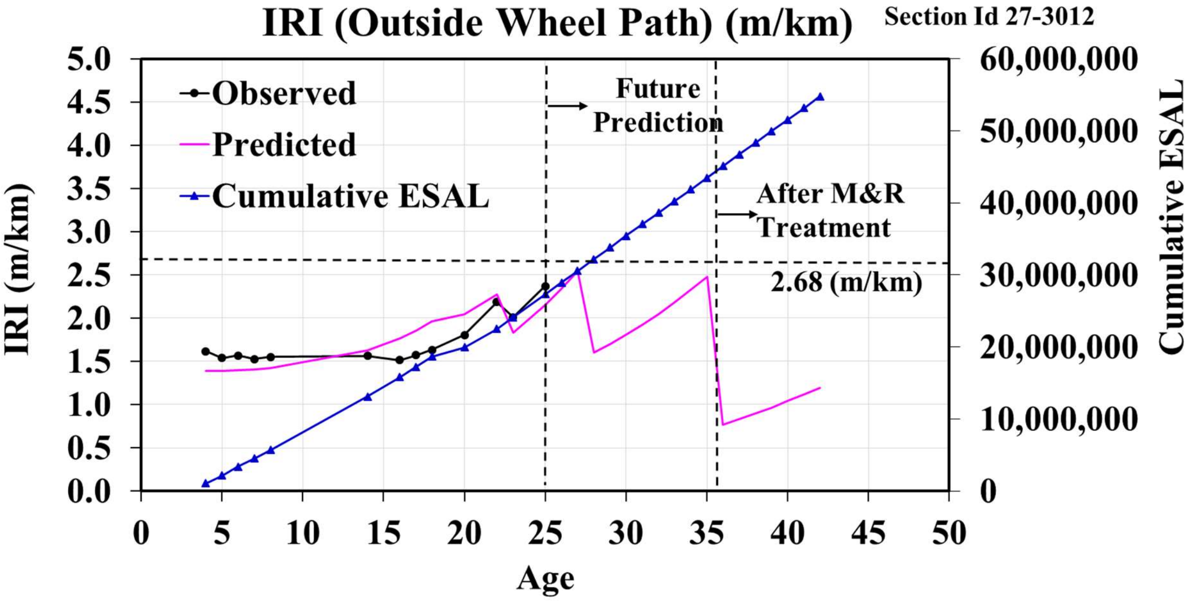

Figure 103 ANN Future Prediction Plot of IRI (Outside Wheel Path) (m/km) after Second M&R Action

4.10 Multiple Linear Regression Analysis for JPCP Performance Model

A multiple linear regression (MLR) analysis was conducted to develop the JPCP performance model. This MLR model will be compared with the best model developed using the ANN modeling technique. The best performing model was model A4a for JPCP discussed in section 4.9.3. The input and output variables are the same as model A4a. The input variables are initial IRI, age, concrete pavement thickness, base/subbase thickness, average contraction spacing, CESAL, base/subbase materials type, climatic region, and CN_Code. The output variable is IRI (outside wheel path) (m/km). The input variables have six continuous variables, two categorical variables, and CN_Code. The CN_Code was developed based on the IRI value improvement and the type of M&R action provided in Table 27. If no M&R action was done and the improvement of IRI value was very low, the CN_Code was categorized as ‘1’. If M&R

action was done or there was a significant improvement of IRI value, the CN_Code was assigned as 2, 3, and so on. This CN_Code is a continuous variable where 2, 3 is the frequency of M&R actions and/or IRI value improvements.

IRI (outside wheel path) (m/km) was normally distributed. Standard residuals were normally distributed. Scatterplots were analyzed, and no curvilinear relationships between the criterion variable and predictor variables or heteroscedasticity were evident. There was a statistically significant relationship between input variables and output variable, F (12, 1354) = 108.557, $p < 0.001$. The MLR model accounted for 49% of the variance in the model with $R^2 = 0.493$.

4.10.1 MLR Model Results and Comparison between Final ANN Model and MLR Model

The developed MLR model equation is given below:

$$\begin{aligned} IRI\ (Outside\ Wheel\ Path)(m/km) \\ &= 1.537 + 0.866 \times IRI_0 + [(-0.001) \times Age] + 0.159 \times Wet, Non-Freeze \\ &+ [(-0.272) \times Dry, Non-Freeze] + [(-0.011) \times Dry, Freeze] \\ &+ 0 \times Wet, Freeze + [(-0.229) \times Granular\ Base/\ Subbase \\ &+ 0.064 \times Treated\ Base/\ Subbase + [(-0.267) \times CN_{Code}] \\ &+ [(-0.056) \times h_{concrete}] + 0.031 \times h_{base/subbase} \\ &+ [(-0.087) \times Average\ Contraction\ Spacing\ (m)] + 6.711 \times 10^{-9} \times CESAL \end{aligned}$$

Where, IRI_0 = Initial IRI Outside Wheel Path (m/km); Wet, Non-Freeze, Dry, Non-Freeze, Wet, Freeze, and Dry, Freeze = Categorical variable for climatic region; Granular Base/Subbase, Treated Base/Subabse = Categorical variable for base/subbase material type; CN_Code =

Continuous variable for Maintenance and Rehabilitation (M&R) frequency; $h_{concrete}$ = Concrete pavement thickness, in; $h_{base/subbase}$ = Base/Subbase thickness, in; CESAL = Cumulative Equivalent Single Axel Load.

The comparison of the prediction accuracy measures for the MLR model is graphically presented in Figure 104. From Figure 104, it is evident that the model prediction is scattered and far away from the line of equality. The MLR model accounted for only 49% variability whereas the final ANN model accounted for 94% variability in the model.

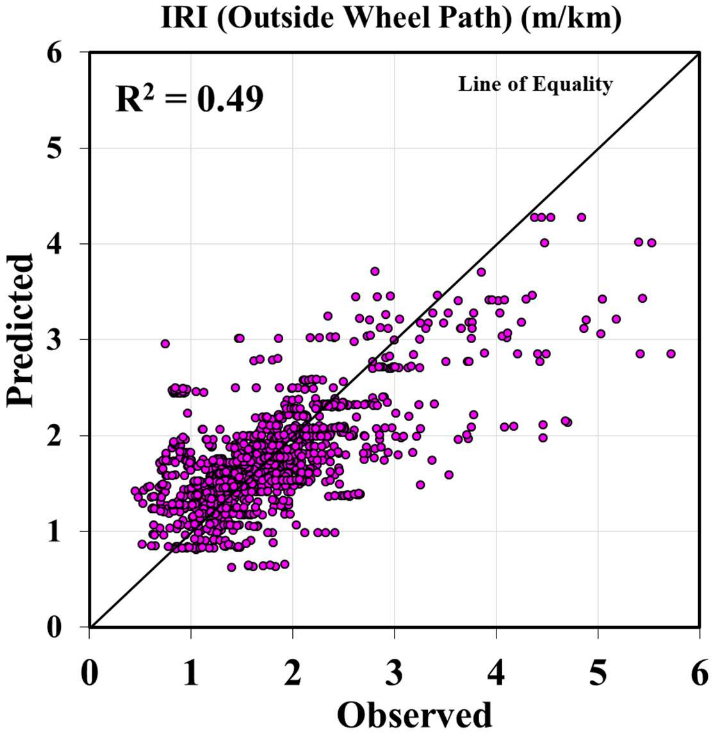

Figure 104 Observed IRI (Outside Wheel Path) (m/km) vs. Predicted IRI (Outside Wheel Path) (m/km)

The 1,355 data points are assigned section sequence numbers from 1 to 1,355. Figure 105 shows the observed and MLR model predicted IRI (outside wheel path) values. From Figure 105, it is demonstrated that the predicted IRI could not capture most of the variability in the IRI observed values.

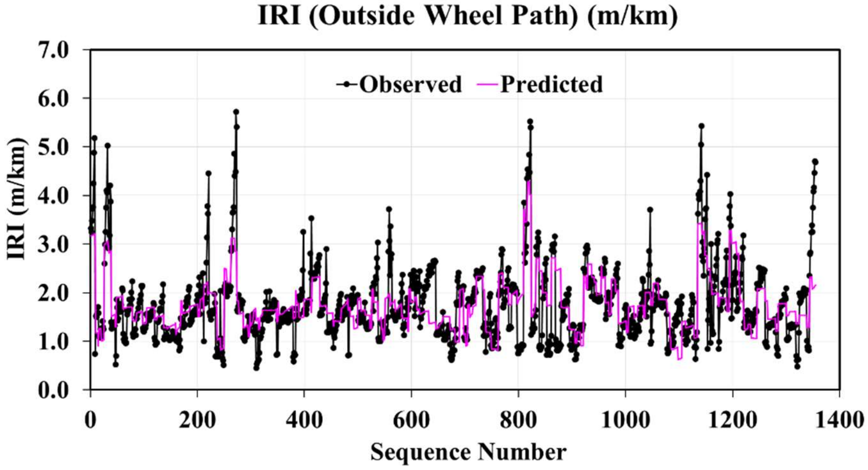

Figure 105 Observed and Predicted IRI (Outside Wheel Path) (m/km) Plot

Figure 106 shows the observed and predicted IRI for Section 27-3012, in Minnesota. The predicted values do not follow the observed values closely. The difference in the mean values of observed and predicted is -2.8% whereas the difference is 0.23% for the final ANN Model.

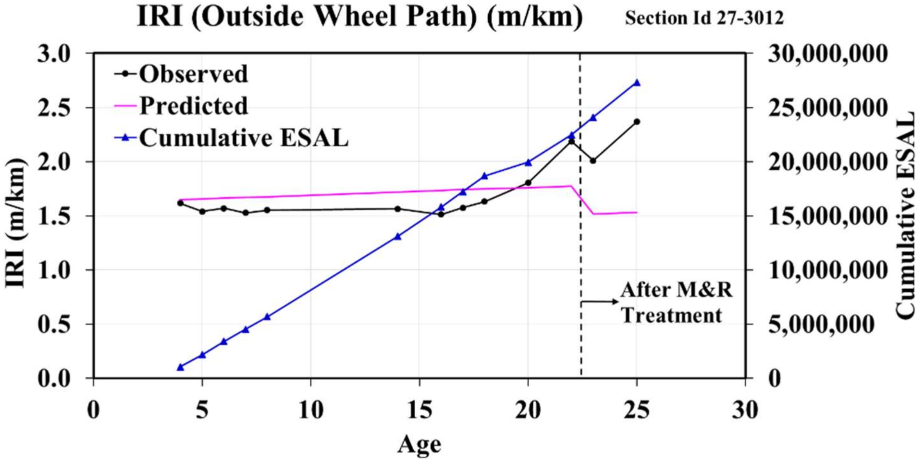

Figure 106 Observed and Predicted IRI (Outside Wheel Path) (m/km) Plot of JPCP Section in Minnesota

The model was verified using the verification database described in section 4.8.3. Figure 107 shows the observed and predicted value against the line of equality. Model verification results are summarized below:

- the % mean difference in IRI outside wheel path (m/km): 1.49%
- RMSE: 0.370
- MARE: 19.3%

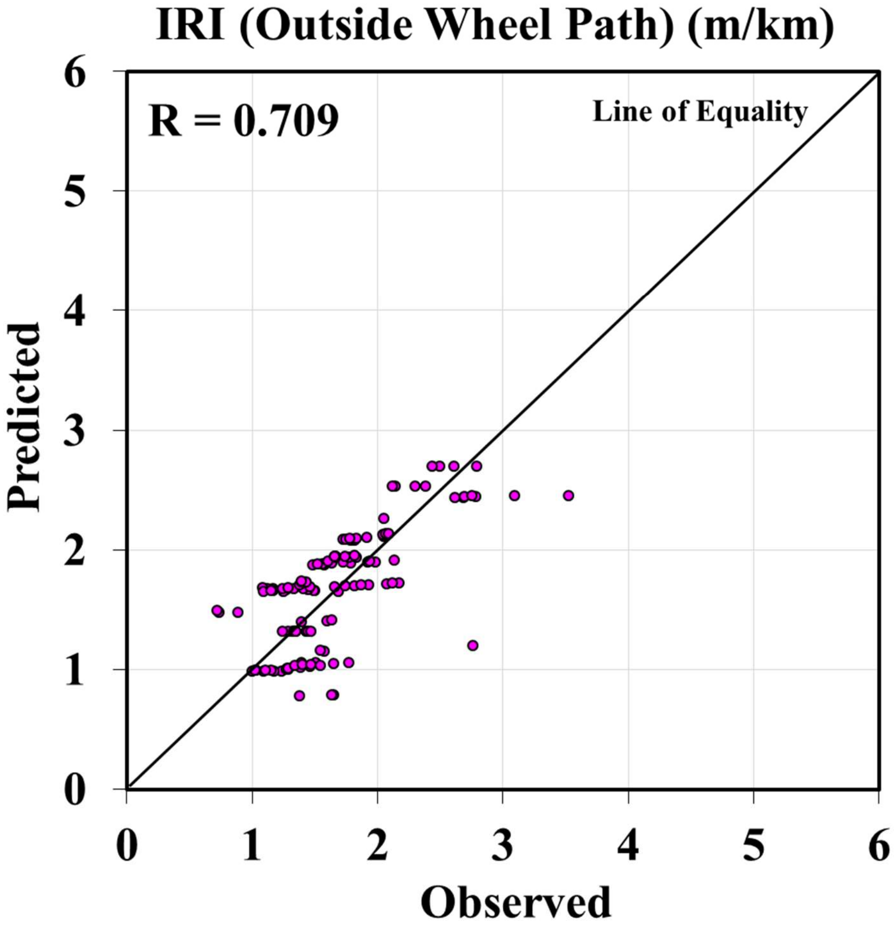

Figure 107 Observed IRI (Outside Wheel Path) (m/km) vs. Predicted IRI (Outside Wheel Path) (m/km) using Verification Database

4.11 Concluding Remarks

Based on the materials discussed in this chapter, the key concluding remarks are summarized below:

- The LTPP database contained 107 JPCP sections under the GPS-3 study. Most data points are from the wet, freeze and wet, non-freeze climatic regions.
- Preliminary research showed that reasonably better IRI models can be developed using readily available input variables collected from the LTPP database employing the ANN modeling technique.
- The hypothesis testing in this study confirmed that IRI outside wheel path has significantly higher values than IRI inside wheel path. Therefore, the ANN and MLR models were developed for IRI outside wheel path.
- The climatological variables have a strong linear association with climatic regions. The climatological variables also need to be predicted before using in the prediction models for future IRI predictions. Hence, climatological variables were not used in the model development.
- The exclusion of categorical variable season helped to develop a better ANN performance model for JPCP.
- The hypothesis testing in this study demonstrated that it is imperative to use the maintenance and rehabilitation history of the pavement in the development of the IRI prediction model. An in-depth study of M&R history collected from the LTPP database for JPC pavement produced several CN_Code. The best model was found with the CN_Code developed based

on the IRI value improvement and the type of M&R action provided in Table 27 and the variable is a continuous variable where number increment indicates the frequency of M&R action provided in the pavement section.

- The best performing ANN model has a network structure of 13-19-1 (i.e. 13 inputs, 19 hidden nodes, and 1 output). The ANN model to predict IRI has an R^2 value of 0.94. The total data points used to develop the IRI prediction ANN model were 1,355. From Table 18, it is evident that the developed ANN model in this study has higher accuracy than the previously developed models via multiple regression and ANN models.
- The developed IRI prediction model can successfully characterize the behavior (i.e. the increase of IRI values with time and decrease of IRI value after maintenance and rehabilitation). The ANN model can be used to provide future M&R action by changing CN_Code frequency and the model successfully distinguishes the behavior of IRI (i.e. decrease of IRI after M&R action and increase of IRI with time as CESAL increases).
- The developed MLR model to predict IRI has an R^2 value of 0.49. The verification of this MLR model generated a mean difference of 1.49%, RMSE of 0.370, and MARE of 19.3%.
- The ANN model shows better accuracy compared to the MLR model developed in this study. The ANN model accounted for 94% variability in the model whereas the MLR model accounted for only 49% variability.

CHAPTER V: DEVELOPMENT OF PERFORMANCE MODELS FOR JOINTED REINFORCED CONCRETE PAVEMENTS

5.1 Background

Jointed reinforced concrete pavements (JRCP) are a type of concrete pavement that contains steel mesh reinforcement. In JRCP, the joint spacing is higher than JPCP pavement, and to hold the mid-panel cracks reinforcing steels are provided. The spacing between transverse joints is typically 30 feet or more. Figure 108 shows the average joint spacing and average mid-panel crack [76].

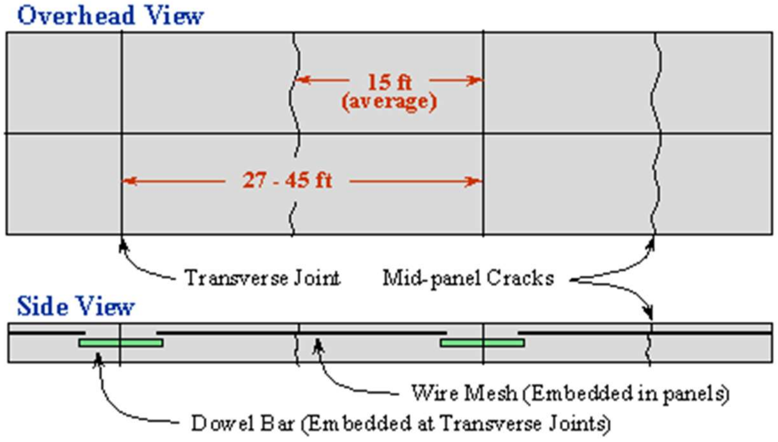

Figure 108 Cross-section and top view of Jointed Reinforced Concrete Pavement [76]

5.2 Methodology

The methodology of developing the JRCP performance model is similar to the JPCP performance model described in section 4.2. The model development process for JRCP is, as follows:

(1) Conduct a literature review of past research studies to identify independent and categorical variables that influence pavement performance.
(2) Assemble databases for JRCP model development from the LTPP database, which must include the variables identified in step (1).
(3) Evaluate the quality of databases and identify missing/erroneous data items.
(4) Develop procedures for estimating important missing data in the time series.
(5) Develop pavement performance models using ANN and multiple linear regression modeling techniques.
(6) Select the appropriate IRI model form (should be capable of estimating the increase of IRI value with time and decrease of IRI value after maintenance and rehabilitation).
(7) Evaluate accuracy and verification of developed performance prediction models for JRCP.
(8) Perform sensitivity analysis for developed performance models.
(9) Implement selected performance models.

5.3 Literature Review

There were not many smoothness (IRI) models found for JRCP pavements. Some models were developed only for specific states of a specific area. The FHWA RPPR study [77] investigated the effect of distress on both serviceability (PSR) and smoothness (IRI) for JRCP. The model developed for IRI as part of the RPPR study is as follows:

$$IRI^2 = 99.59 + 2.6098 * FaulTT + 2.2802 * T - crack_3 + 1.8407 * Spall$$

Where,

IRI = International Roughness Index, in/mile

FaulTT = total accumulated joint faulting, in/mile

T-crack = amount of transverse cracking, number of cracks per mile

Spall = percentage of joints spalled

$R^2 = 0.61$, SEE = 64.11 in/mile, N = 144

5.4 Data Collection for JRCP Performance Models

The data were collected from the LTPP database of JRCP, which is GPS-4 [71]. A total of 49 GPS-4 JRCP pavement sections are included in the LTPP that are located throughout the United States. The IRI measurements are from 1989 to 2017. By averaging the IRI value from one run, a dataset was created which has 577 data points. Figure 109 shows the spatial map of JRCP sections included in the LTPP database.

JRCP sections included in the LTPP database are located in two climatic regions (Wet, Non-Freeze, and Wet, Freeze). Table 36 shows that 36.37% (18 of 49) sections are in the wet, non-freeze climatic region and 63.27% (31 of 49) sections are in the wet, freeze climatic region. The IRI data points follow the same statistics, higher in the wet, freeze (69.5%, 401 of 577) region than the wet, non-freeze (30.5%, 176 of 577) region.

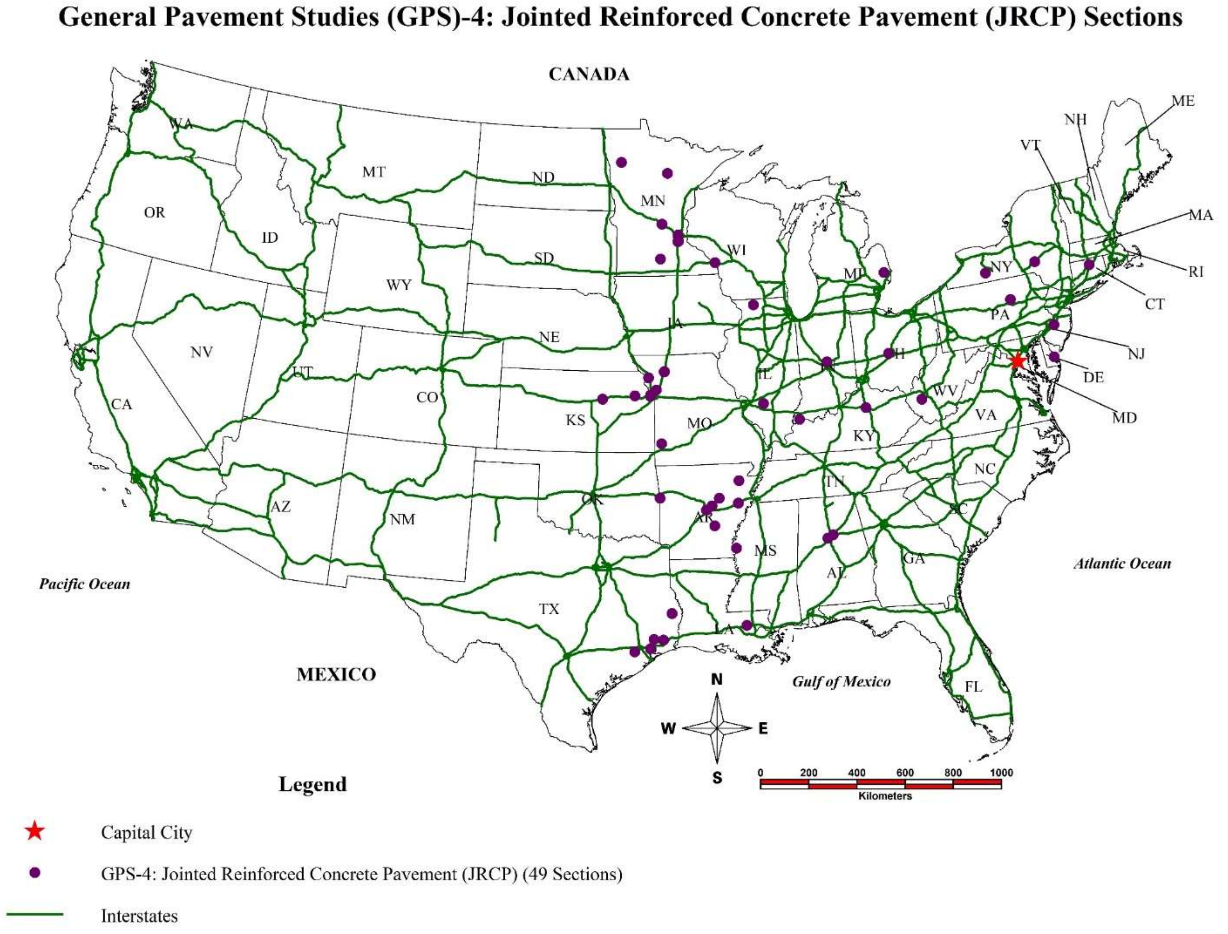

Figure 109 Spatial Map of JRCP Sections in the USA

Table 36 Distribution of Pavement Sections and IRI Data Points in Different Climatic Region

Climatic Region	Number of Sections	% of Sections	Number of Data Points	% of Data Points
Wet, Non-Freeze	18	36.73%	176	30.50%
Dry, Non-Freeze	0	0.00%	0	0.00%
Dry, Freeze	0	0.00%	0	0.00%
Wet, Freeze	31	63.27%	401	69.50%
Total	49	100.00%	577	100.00%

Table 37 shows the distribution of pavement sections and IRI data points by state. Minnesota State has the highest eight pavement sections out of 49 and 17.5% IRI data points. Though Kansas has only five sections, and it contains the second highest IRI data points of 13.69%.

Table 37 Distribution of Pavement Sections and IRI Data Points by States

State Code	State Name	Climatic Zone	Number of Sections	% of Sections	Number of Data Points	% of Data points
1	Alabama	Wet, Non-Freeze	2	4.08%	13	2.25%
5	Arkansas	Wet, Non-Freeze	7	14.29%	57	9.88%
9	Connecticut	Wet, Freeze	1	2.04%	18	3.12%
10	Delaware	Wet, Non-Freeze	1	2.04%	10	1.73%
17	Illinois	Wet, Freeze	2	4.08%	24	4.16%
18	Indiana	Wet, Freeze	2	4.08%	23	3.99%
20	Kansas	Wet, Freeze	5	10.20%	79	13.69%
21	Kentucky	Wet, Freeze	1	2.04%	5	0.87%
22	Louisiana	Wet, Non-Freeze	1	2.04%	6	1.04%
26	Michigan	Wet, Freeze	1	2.04%	18	3.12%
27	Minnesota	Wet, Freeze	8	16.33%	101	17.50%
28	Mississippi	Wet, Non-Freeze	1	2.04%	11	1.91%
29	Missouri	Wet, Freeze	6	12.24%	67	11.61%
34	New Jersey	Wet, Non-Freeze	1	2.04%	13	2.25%
36	New York	Wet, Freeze	2	4.08%	28	4.85%
39	Ohio	Wet, Freeze	1	2.04%	5	0.87%
42	Pennsylvania	Wet, Freeze	1	2.04%	14	2.43%
48	Texas	Wet, Non-Freeze	5	10.20%	66	11.44%
54	West Virginia	Wet, Freeze	1	2.04%	19	3.29%
Total 49 Sections and 577 Data points						

5.4.1 Database Development

Output Variables

IRI is considered as the output variable in the pavement performance modeling process for this research. The IRI measurements are from 1989 to 2017. Each section has two types of

IRI measurements, IRI inside/left wheel path and IRI outside/right wheel path. A mean roughness index Mean IRI is calculated by averaging the IRI inside/left wheel path and IRI outside/right wheel path measurements. In each visit date, several IRI measurement runs were completed for each section. By averaging the IRI measurement runs, a single IRI measurement was obtained for IRI inside/left wheel path, IRI outside/right wheel path, and mean IRI for each visit date. By doing this, a dataset was created which has 577 data points for 49 JRCP sections. A t-test done in section 4.8.1 showed that IRI outside wheel path (m/km) is significantly higher than IRI inside wheel path (m/km) for the JPCP section. Hence, IRI outside wheel path (m/km) was used as the output variable for JRCP performance model development. Figure 110 shows the IRI Measurements for Outside Wheel Path.

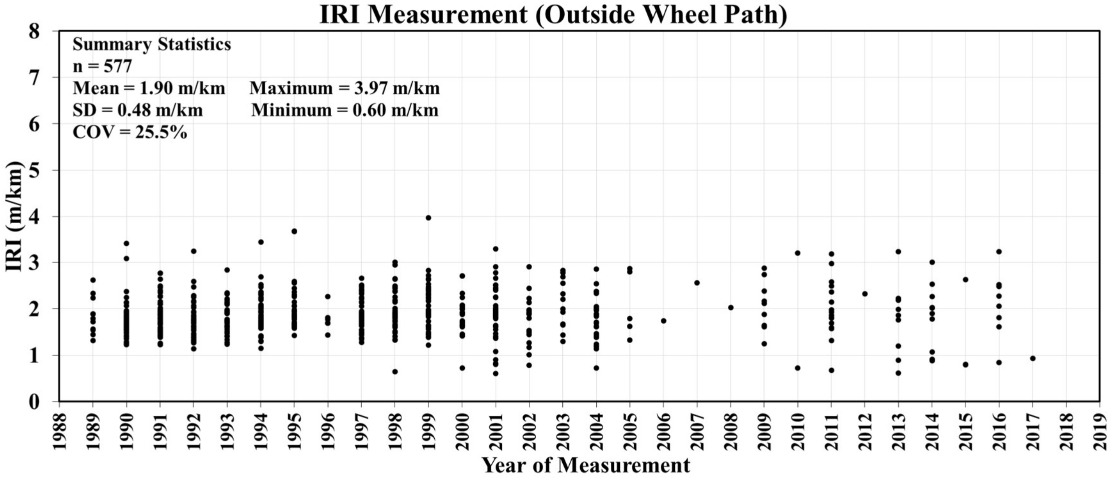

Figure 110 IRI Measurement (Outside Wheel Path) of JRCP Sections

Input Variable

The input variables were kept the same as found from the investigation done developing JPCP performance models. For the JRCP model, the input variables were collected from the

LTPP database corresponded to the output variable (IRI outside wheel path) measurement taken date (visit date). The relationship between each input variable and output variable (IRI outside wheel path) was studied by creating several plots.

Initial IRI (Outside Wheel Path) (m/km):

The initial IRI outside wheel path (m/km) represents the first IRI value measured in the outside wheel path for a specific pavement section of the LTPP database. The first measurement is usually done when the pavement was built and opened to traffic or the pavement was first included in the LTPP study. It indicates the road surface condition at the beginning of the analysis period. Initial IRI has a range of a minimum of 1.23 m/km to a maximum of 3.08 m/km. Figure 111 shows the plot of the initial IRI outside wheel path (m/km) against the IRI outside wheel path (m/km).

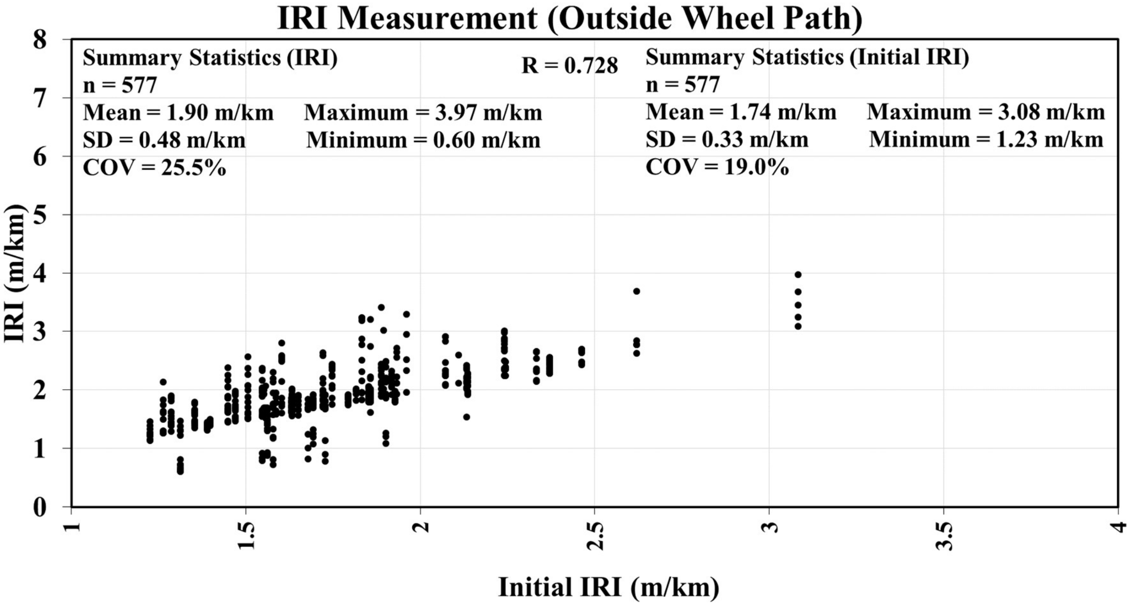

Figure 111 Initial IRI vs. IRI Measurement (Outside Wheel Path) of JRCP Sections

Age:

The variable age is calculated by subtracting the year when the section was opened to traffic from the year IRI measurement was collected. This variable represents the time pavement was expose to climate and traffic loads. Age is also a fundamental variable to be used as an input variable to predict pavement performance for future years. The mean pavement age for the 49 JRCP section is 20 years. But for some pavement sections, some IRI data were collected when the pavement age was as little as three years, and for some pavement sections that age was as high as 46 years. Figure 112 shows the pavement age when IRI measurements were collected.

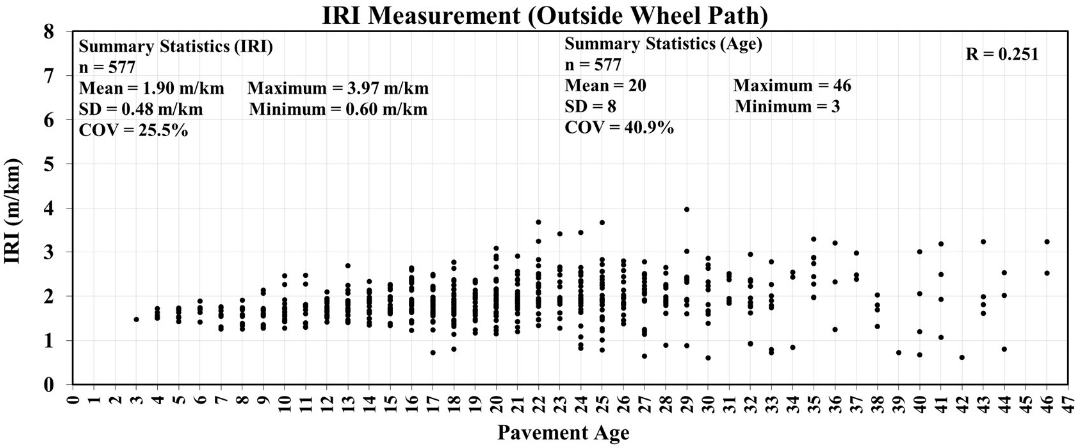

Figure 112 Age vs. IRI Measurement (Outside Wheel Path) of JRCP Sections

Concrete Pavement Thickness (in):

Concrete pavement thickness represents the thickness of the concrete and steel mesh layer in a JRCP pavement section that is laid over the base/subbase layer. This layer is exposed to climate and endures the traffic loads throughout pavements life. Concrete layer thickness plays an important role in JRCP performance. The average concrete layer thickness is 9.5 in with a standard deviation of 0.73 in. The maximum concrete layer thickness is 11.4 in and the minimum is 7.9 in. Figure 113 shows the concrete layer thickness of JRCP sections and IRI outside wheel path measurements.

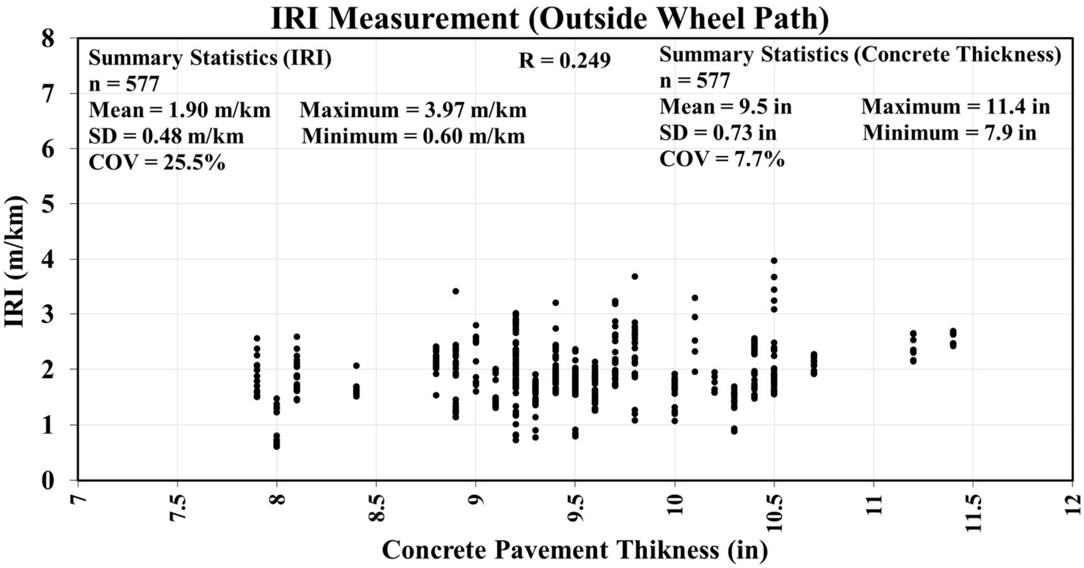

Figure 113 Concrete Pavement Thickness vs. IRI Measurement (Outside Wheel Path) of JRCP Sections

Base/Subbase Thickness (in):

Base/subbase pavement thickness represents the thickness of the base/subbase layer in a JRCP pavement section that is laid over the subgrade layer. Some JRCP sections have both base and subbase layers on the other hand some JRCP sections have only a base layer underneath the concrete layer, over the subgrade layer. Traffic loads transfer from concrete layer to base/subbase layer and this layer is also affected by precipitation. Therefore, base/ subbase thickness is an important input variable for JRCP performance modeling. The average base/subbase thickness is 5.6 in. The maximum base/subbase thickness is 15 in.

Average Contraction Spacing (m)

The average contraction spacing represents the joint spacing in JRCP sections. This joint spacing controls the natural cracks in a pavement section. Therefore, it will be useful to use the average contraction spacing of joints as an input variable for JRCP performance modeling. The mean average contraction spacing is 13.8 m with a standard deviation of 4.5 m. The maximum average contraction spacing is 23.84 m and the minimum is 4.57 m.

Cumulative ESAL:

CESAL is the sum of annual ESAL data over the years. ESAL represents a mixed stream of traffic of different axle loads and axle configurations predicted over the design or analysis period and then converted into an equivalent number of 18,000-lb. single axle loads summed over that period. ESAL represents the effects of traffic loads on the pavement over time. In some years, the LTPP database did not have ESAL information corresponding to the IRI measurements data. Interpolation and extrapolation procedures were applied using known data points to compute ESAL for the missing years. Cumulative ESAL represents the cumulative traffic load that was endured by the pavement over pavements' life. CESAL has one of the most important effects on pavement deterioration. Hence, it is vital to use in performance modeling. CESAL has a mean of 7,148,272 and a standard deviation of 7,686,590. Figure 114 shows the CESAL values corresponded to the IRI outside wheel path measurements for JRCP sections included in this study.

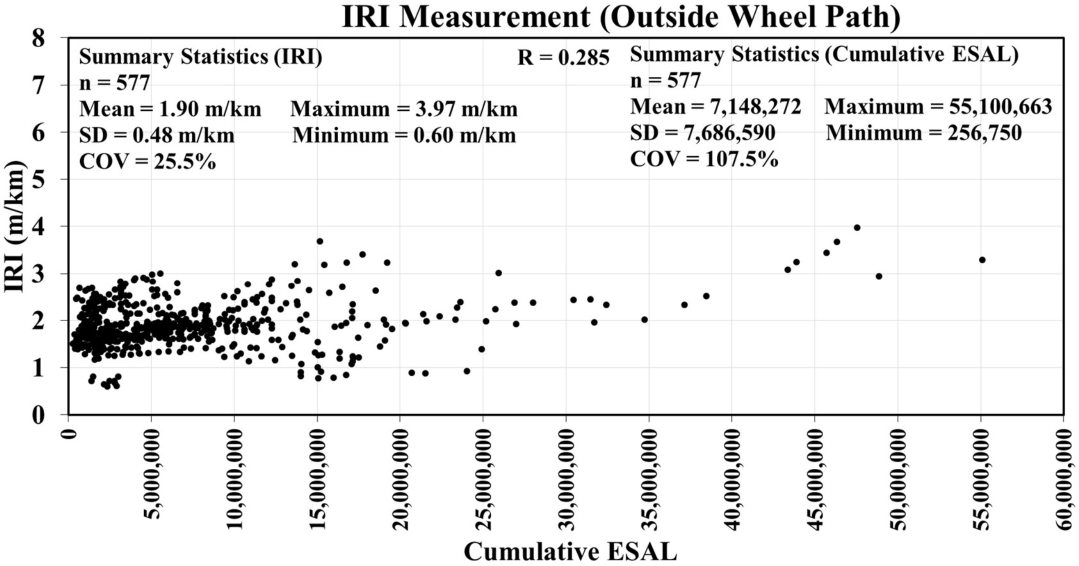

Figure 114 Cumulative ESAL vs. IRI Measurement (Outside Wheel Path) of JRCP Sections

A correlation analysis was performed to obtain the Pearson correlation coefficient (r) between all variables. The correlation matrix summarizes the correlation coefficient (r) values between all the variables and it is easy to observe if the variables are correlated with each other. This correlation coefficient (r) only provides a linear association between variables, if the data is not linearly correlated it will have a low correlation value. Table 38 summarizes the descriptive statistics of input variables used in this study and the correlation between each input variable and the output variable (IRI outside wheel path).

The four highest correlations between input variables and IRI outside wheel path (m/km) were observed with the variable initial IRI (outside wheel path) (m/km) (0.728) followed by CESAL (0.285), age (0.251), and concrete pavement thickness (in) (0.249). The lowest correlation was with base/subbase thickness (in) (0.017). However, these variables might follow a non-linear correlation with IRI outside wheel path (m/km) that cannot be identified by the correlational analysis. Therefore, even though some correlation coefficient values were low, all input variables were used in this study for the development of ANN models.

Table 38 Descriptive Statistics of Input Variables for JRCP Model

Statistics	Mean	SD	COV	Maximum	Minimum	Correlation with IRI (outside wheel path), R
Initial IRI (Outside Wheel Path) (m/km)	1.743	0.330	18.95%	3.08	1.23	0.728
Age	20	8	40.89%	46	3	0.251
Concrete Pavement Thickness (in.)	9.495	0.733	7.72%	11.4	7.9	0.249
Base/Subbase Thickness (in)	5.592	2.777	49.66%	15	0	0.017
Average Contraction Spacing (m)	13.799	4.483	32.49%	23.84	4.57	0.187
Cumulative ESAL	7,148,272	7,686,590	107.53%	55,100,663	256,750	0.285

Some variables were dummy coded as 0 and 1 for modeling purposes. The climatic region represents the climate zones defined by the LTPP which consists of four different regions, wet non-freeze, dry non-freeze, dry freeze, wet freeze. JRCP sections included in the LTPP GPS-4 study are only from wet, non-freeze, and wet, freeze climatic zone. The base/subbase materials represents the type of base/subbase materials used in the pavement section which consists of two types, unbound (granular) or bound (stabilized). For JPCP, model A4a was developed without using categorical variable season which turned out to be a better model than model A4 with the categorical variable season. Thus, the categorical variable season was not used in the development of the JRCP performance model.

5.4.2 Maintenance and Rehabilitation Actions

The t-test in section 4.8.2 established that there is a significant change in IRI value after M&R actions are done on a pavement section. Hence, it is important to incorporate pavement M&R history in the JRCP performance model. An in-depth study of the M&R history provided in the LTPP database for JRCP has been carried out in this research. The process is as follows:

- The M&R actions (improvement done on pavement) history was collected from the LTPP database. The M&R action was provided as IMP_TYPE code that is assigned by the LTPP. The description of IMP_TYPE code is described in Table 26 gathered from the LTPP user guide [74]. This table contained the type of improvements for both concrete and asphalt pavement. For this research, only concrete pavement improvement types (M&R actions) were further investigated.
- The M&R action corresponded to each IRI data point was obtained from Table 26. The IMP_TYPE and the description for the type of improvements for concrete pavements are described in Table 27. The M&R actions can be characterized in two categories: major M&R and local/minor M&R. Table 27 described the designation of M&R categories for the different types of improvement [75]. The improvement description and designated M&R action category were obtained for each IRI data point using Table 27.

The CN_Code categorical variable was developed to represent the M&R action done on a pavement section. The LTPP database has the Construction Number (CN) corresponded to each IRI data point and the description is given in Section 4.7. But this CN is not an accurate representation of the improvement action done on pavement. For this reason, this doctoral research assigned CN_Code for each IRI data point based on IRI value improvement, the M&R action done before the collection of IRI measurements, and the type of M&R action (major, local/minor). Three CN_Code were developed for JRCP pavement to achieve the most accurate model that will provide an accurate future prediction of IRI and incorporate the M&R actions in the developed model. The developed CN_Code reflects the learning from the development of JPCP performance models. The description of each CN_Code is given below:

(1) The first CN_Code was developed based on the original CN collected from the LTPP database corresponded to each IRI data point. If no M&R action (CN1 in the original LTPP database) was done, the CN_Code was categorized as '0', and this 0 was continued until an M&R action was performed. The first M&R action (CN2 in the original LTPP database) was categorized as '1', and this 1 was continued until the end of the section.

(2) The second CN_Code was also developed based on the original CN collected from the LTPP database corresponded to each IRI data point. If no M&R action (CN1 in the original LTPP database) was done, the CN_Code was categorized as '1', and this 1 was continued until an M&R action was performed. The first M&R action (CN2 in the original LTPP database) was categorized as '2', and this 2 was continued until the second M&R action. The second M&R action (CN3 in the original LTPP database) was categorized as '3', and this 3 was continued until the third M&R action. This CN_Code assignment continued until all the M&R actions done on a pavement section were categorized.

(3) The third and the last CN_Code was also developed based on the IRI value improvement and the type of M&R action provided in Table 27. If no M&R action was done and the

improvement of IRI value was very low, the CN_Code was categorized as ‘0’, and this 0 continued until an M&R action was performed or the IRI value improved significantly. The first data point found with an M&R action done or a significant improvement of IRI values was assigned as ‘1’ CN_Code and this 1 continued until the next M&R action was performed or the IRI value improved significantly. The next data point found with an M&R action done or a significant improvement of IRI values was assigned as ‘2’ CN_Code and this 2 continued until the next M&R action was found or the IRI value improved significantly. This CN_Code assignment process continued until all the IRI data points were categorized for a pavement section.

5.4.3 Database Summary

The input and output variables are thoroughly discussed in section 5.4.1. Table 39 shows the key input variables for JRCP models. The maintenance and rehabilitation (M&R) history is represented as CN_Code. Table 39 also shows the CN_Code used in these models. CN_Code descriptions are discussed in section 5.4.2. Three models were tried to find the most accurate model that can predict IRI incorporating the M&R history of the pavement sections.

Table 39 Input Variables Used in JRCP Performance Models

No.	**Input Variables**	**Model 1**	**Model 2**	**Model 3**
1	IRI_0 (Initial IRI Outside Wheel Path) (m/km)	Initial IRI Outside Wheel Path (m/km)	Initial IRI Outside Wheel Path (m/km)	Initial IRI Outside Wheel Path (m/km)
2	Age (Pavement age, years)	Age	Age	Age
3	$h_{concrete}$ (Concrete pavement	$h_{concrete}$	$h_{concrete}$	$h_{concrete}$

No.	**Input Variables**	**Model 1**	**Model 2**	**Model 3**
	thickness, in)			
4	$h_{base/subbase}$ (Base/Subbase thickness, in)	$h_{base/subbase}$	$h_{base/subbase}$	$h_{base/subbase}$
5	Average Contraction spacing (m)	Average Contraction spacing (m)	Average Contraction spacing (m)	Average Contraction spacing (m)
6	CESAL (Cumulative Equivalent Single Axel Load)	CESAL	CESAL	CESAL
7	Base/Subbase Materials (Categorical variable for Base/Subbase materials)	Unbound (Granular) Base/ Subbase Bound (Treated) Base/ Subbase	Unbound (Granular) Base/ Subbase Bound (Treated) Base/ Subbase	Unbound (Granular) Base/ Subbase Bound (Treated) Base/ Subbase
8	Climatic Region (Categorical variable for LTPP climatic region)	Wet, Non-Freeze Wet, Freeze	Wet, Non-Freeze Wet, Freeze	Wet, Non-Freeze Wet, Freeze
9	CN (Construction Number, variable for M & R)	CN Categorical: No M&R Action 0 M&R Action 1	CN Original Continuous: (1,1,2,2…) No M&R Action 1 M&R Action 2,3,4….	CN Continuous: (1,1,2,2,3,3,…..) (Based on IRI value improvement and the type of M&R action provided in Table 27) No IRI Improvement and/or M&R Action 1 IRI Improvement and/or M&R Action 2,3,4

5.5 ANN Models

5.5.1 ANN Model Architecture

In the final research, using the developed model database, three models were tried with the same input variables from Table 39 only changing CN_Code described. The output variable is IRI outside wheel path (m/km) for all three models. These three models have six continuous variables, two categorical variables, and CN_Code.

5.5.2 ANN Model Selection

Three best performing networks from each model (Model 1, Model 2, and Model 3) were selected based on statistical measures such as minimum values of MARE, Averaged-Squared-ASE, and maximum values of R^2. A total of 577 datasets were used to build the desired database; 297, 140, and 140 subdatabases were used, respectively, for training, testing, and validation purposes. Datasets that include minimum and maximum values of each variable were included in the training phase for the network to represent the characteristics of the response. The maximum and minimum ranges of each input/output variable for ANN model development were chosen on purpose to be wider than their actual ranges for better mathematical mapping [54].

Model 1

The inputs for Model 1 are initial IRI, age, concrete pavement thickness, base/subbase thickness, average contraction spacing, CESAL, base/subbase materials type, climatic region, and construction number and output is IRI (outside wheel path) (m/km) as shown in Table 39. The CN_Code used in this model is based on the original CN collected from the LTPP database. No M&R action was assigned as 0 and M&R actions were assigned as 1. This CN_Code is a categorical variable. Four model networks were chosen after training and testing to compare the accuracy of the models after validation and all data. Table 40 shows the statistical accuracy of the four chosen networks. Based on the ASE, MARE, and R^2, the chosen best model network is 11-19-20000 (Input Variables-FinalHN-Iteration). The best network's ASE values for training, testing, validation, and all data are 0.00395, 0.00465, 0.00413, and 0.00089, respectively. Though three other model networks have lower ASE in validation, the chosen best model network has the lowest ASE in testing, training, and all data. R^2 values for this model are as follows: 0.953 for the training, 0.695 for the testing, 0.720 for the validation, and 0.934 for all data. The chosen model network's R^2 value is highest for training, testing, and all data. The final architecture of this model is 11-19-1, where 11 is the number of inputs, 19 is the number of hidden nodes and 1 is the number of output.

Table 40 Statistical Accuracy Measures of Four Chosen Model Networks for Model 1

InitialHN-FinalHN-Iteration		Best Model 11-19-20000	3-19-20000	6-17-20000	7-15-20000
Training	MARE	4.871	5.464	5.569	6.039
	R^2	0.953	0.943	0.938	0.935
	ASE	0.00395	0.00450	0.00614	0.00520
Testing	MARE	8.226	8.304	10.444	10.365
	R^2	0.695	0.673	0.562	0.630
	ASE	0.00465	0.00536	0.00705	0.00620
Validation	MARE	8.501	8.084	9.188	9.039
	R^2	0.720	0.771	0.738	0.761
	ASE	0.00413	0.00333	0.00404	0.00344

InitialHN-FinalHN-Iteration		Best Model 11-19-20000	3-19-20000	6-17-20000	7-15-20000
All Data	MARE	4.841	5.221	5.930	5.769
	R^2	0.934	0.927	0.910	0.909
	ASE	0.00089	0.00098	0.00120	0.00122
Final Structure (Input Variables-FinalHN-Iteration)		11-19-20000	11-19-20000	11-17-19100	11-15-20000

Model 2

The inputs and output of this model are very similar to model 1. The CN_Code used in this model is also based on the original CN collected from the LTPP database. No M&R action was assigned as 1 and M&R actions were assigned as 2, 3, and so on. This CN_Code is a continuous variable where 2, 3 is the frequency of M&R actions done on pavement. Five model networks were chosen after training and testing to compare the accuracy of the models after validation and all data. Table 41 shows the statistical accuracy of the five chosen networks. Based on the ASE, MARE, and R^2, the chosen best model network is 11-18-20000 (Input Variables-FinalHN-Iteration). The best network's ASE values for training, testing, validation, and all data are 0.00058, 0.00278, 0.00353, and 0.00104, respectively. Though the 11-19-20000 network has lower ASE in validation and all data, the chosen best model network has the lowest ASE in testing and training. R^2 values for this model are as follows: 0.961 for the training, 0.768 for the testing, 0.751 for the validation, and 0.922 for all data. The chosen model network's R^2 value is the highest for testing, and validation. The MARE value (4.491) for the chosen best model network is the lowest in training. The final architecture of this model is 11-18-1, where 11 is the number of inputs, 18 is the number of hidden nodes and 1 is the number of output.

Table 41 Statistical Accuracy Measures of five Chosen Model Networks for Model 2

InitialHN-FinalHN-Iteration		Best Model 8-18-20000	13-18-20000	1-18-8100	6-17-20000	4-19-20000
Training	MARE	4.491	4.607	4.556	4.578	4.908
	R^2	0.961	0.953	0.960	0.962	0.948
	ASE	0.00058	0.00069	0.00064	0.00058	0.00077
Testing	MARE	8.197	8.469	8.342	8.177	8.526
	R^2	0.768	0.763	0.755	0.746	0.736
	ASE	0.00278	0.00282	0.00296	0.00312	0.00316
Validation	MARE	9.118	9.850	10.587	10.218	8.204
	R^2	0.751	0.706	0.648	0.636	0.735
	ASE	0.00353	0.00410	0.00546	0.00583	0.00346
All Data	MARE	5.419	6.051	6.709	5.516	5.326
	R^2	0.922	0.903	0.896	0.919	0.925
	ASE	0.00104	0.00130	0.00143	0.00108	0.00101
Final Structure (Input Variables-FinalHN-Iteration)		11-18-20000	11-18-20000	11-18-8100	11-17-20000	11-19-20000

Model 3

The inputs and outputs of this model are very similar to model 1 and model 2. The CN_Code used in this model was developed based on the IRI value improvement and the type of M&R action provided in Table 27. If no M&R action was done and the improvement of IRI value was very low, the CN_Code was categorized as ‘1’. If M&R action was done or there was a significant improvement of IRI value, the CN_Code was assigned as 2, 3, and so on. This CN_Code is a continuous variable where 2, 3 is the frequency of M&R actions and/or IRI value improvements. Five model networks were chosen after training and testing to compare the accuracy of the models after validation and all data. Table 42 shows the statistical accuracy of the five chosen networks. Based on the ASE, MARE, and R^2, the chosen best model network is 11-19-20000 (Input Variables-FinalHN-Iteration). The best network's ASE values for training, testing, validation, and all data are 0.00052, 0.00183, 0.00192, and 0.00064, respectively. The chosen best model network has the lowest ASE in validation. R^2 values for this model are as follows: 0.965 for the training, 0.852 for the testing, 0.853 for the validation, and 0.952 for all data. The chosen model network's R^2 value is the highest for validation. The final architecture of this model is 11-19-1, where 11 is the number of inputs, 19 is the number of hidden nodes and 1 is the number of output.

Table 42 Statistical Accuracy Measures of five Chosen Model Networks for Model 3

InitialHN-FinalHN-Iteration		4-19-20000	5-19-20000	Best Model 8-19-20000	13-19-20000	17-19-20000
Training	MARE	4.041	4.133	4.217	3.904	5.949
	R²	0.963	0.963	0.965	0.969	0.937
	ASE	0.00054	0.00053	0.00052	0.00046	0.00103
Testing	MARE	6.909	6.596	7.249	7.332	7.926
	R²	0.873	0.873	0.852	0.849	0.883
	ASE	0.00155	0.00156	0.00183	0.00189	0.00180
Validation	MARE	7.387	8.046	7.430	8.082	8.042
	R²	0.762	0.788	0.853	0.822	0.772
	ASE	0.00330	0.00288	0.00192	0.00240	0.00329
All Data	MARE	4.701	4.200	4.358	4.548	5.231
	R²	0.941	0.954	0.952	0.945	0.930

InitialHN-FinalHN-Iteration		4-19-20000	5-19-20000	Best Model 8-19-20000	13-19-20000	17-19-20000
	ASE	0.00078	0.00061	0.00064	0.00074	0.00094
Final Structure (Input Variables-FinalHN-Iteration)		11-19-20000	11-19-20000	11-19-20000	11-19-20000	11-19-20000

Three best performing networks from each model (Model 1, Model 2, and Model 3) are showed in Table 43. Model 3 has the lowest ASE, MARE, and highest R^2 for training, testing, validation, and all dataset. Thus, model 3 has been chosen as the best network.

Table 43 Best Networks from Each Model

Models		Model 1	Model 2	Best Model Model 3
Structure Initial Nodes-Final Nodes-Iterations		11-19-20000	8-18-20000	8-19-20000
Training	MARE	4.871	4.491	4.217
	R^2	0.953	0.961	0.965
	ASE	0.00395	0.00058	0.00052
Testing	MARE	8.226	8.197	7.249
	R^2	0.695	0.768	0.852
	ASE	0.00465	0.00278	0.00183
Validation	MARE	8.501	9.118	7.430
	R^2	0.720	0.751	0.853
	ASE	0.00413	0.00353	0.00192
All Data	MARE	4.841	5.419	4.358
	R^2	0.934	0.922	0.952
	ASE	0.00089	0.00104	0.00064
Final Structure Input Variables-Final Nodes-Iterations		11-19-20000	11-18-20000	11-19-20000

5.5.3 ANN Model Results

The discussion in the previous section demonstrates that model 3 is the best performing network based on all statistical measures (ASE, MARE, and R^2 value). The final model structure has 11 inputs of independent variables, 19 hidden nodes, and 1 output (11-19-1) (Figure 115). The comparison of the prediction accuracy measures for ANN model 3 is graphically presented in Figure 116.

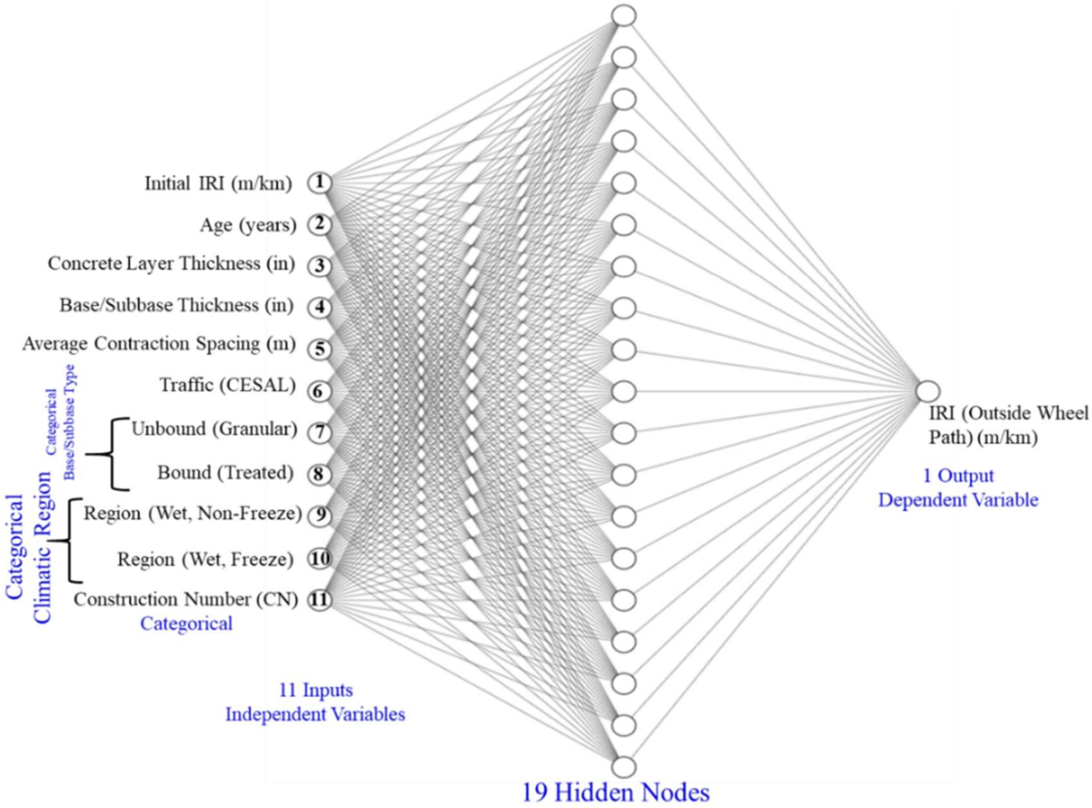

Figure 115 Network Architecture for Best Model (Model 3, Structure: 11-19-1)

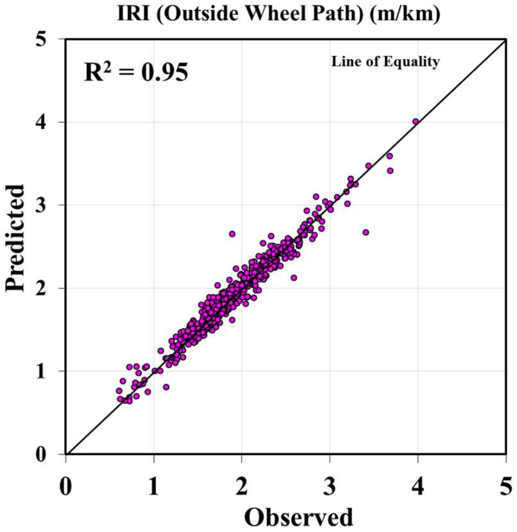

Figure 116 Observed IRI (Outside Wheel Path) (m/km) vs. Predicted IRI (Outside Wheel Path) (m/km)

The 577 data points are assigned section sequence numbers from 1 to 577. Figure 117 shows the observed and Model 3 predicted IRI outside wheel path (m/km) values. From Figure 117, it is demonstrated that the predicted IRI has apprehended most of the variability in the IRI observed values.

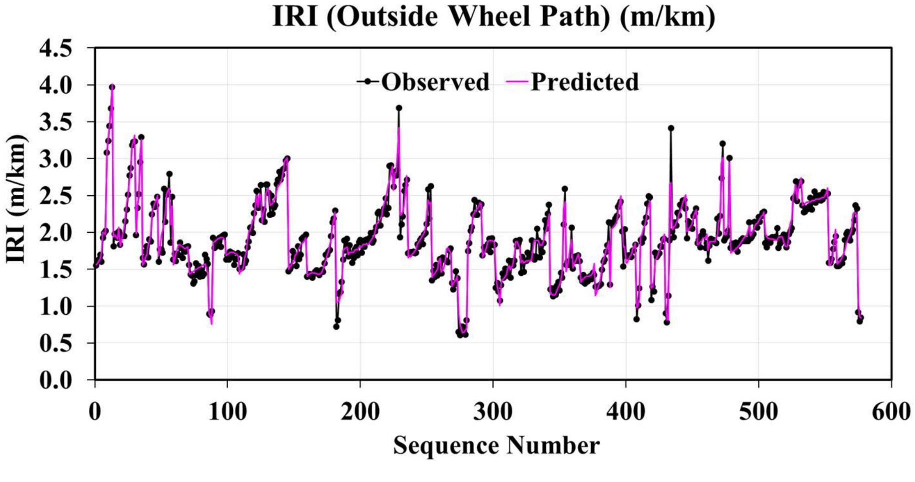

Figure 117 Observed and Predicted IRI (Outside Wheel Path) (m/km) Plot

Figure 118 shows the observed and predicted IRI for Section 20-4052, in Kansas. The predicted values follow the observed values closely. The difference in the mean values of observed and predicted is 0.6%.

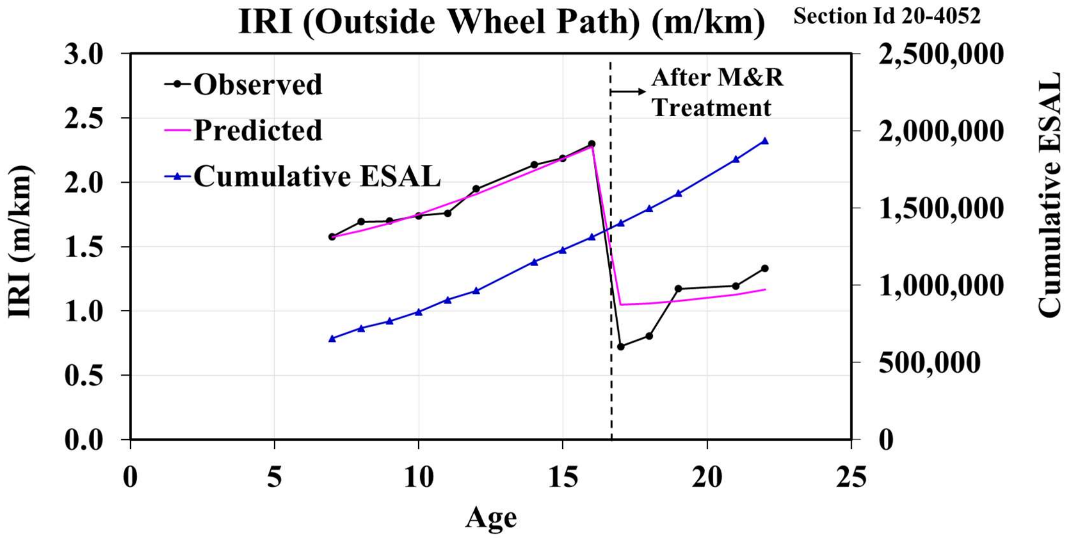

Figure 118 Observed and Predicted IRI (Outside Wheel Path) (m/km) plot of JRCP section in Kansas

5.5.4 Sensitivity Analysis

A sensitivity analysis was carried out to evaluate the significance of the inputs on the output. A GUI was developed by importing all the final ANN model parameters into an excel spreadsheet. To examine the models, some input was changed while keeping the other inputs constant. In this paper, the sensitivity analysis of model 3 is presented since it is the best model in terms of statistical accuracy measures. All model 3 inputs were kept constant except age and CESAL that were changed to generate predictions of IRI. The CESAL values were calculated using the previous year's data. A randomly selected section with one M&R action done was used to show the sensitivity analysis. Figure 119 that the IRI prediction model follows the trend of the observed values. Additionally, it can estimate the increase of IRI values with time and decrease of IRI value after M&R action. Usually, without any rehabilitation, pavement deteriorates over time, therefore, IRI increases.

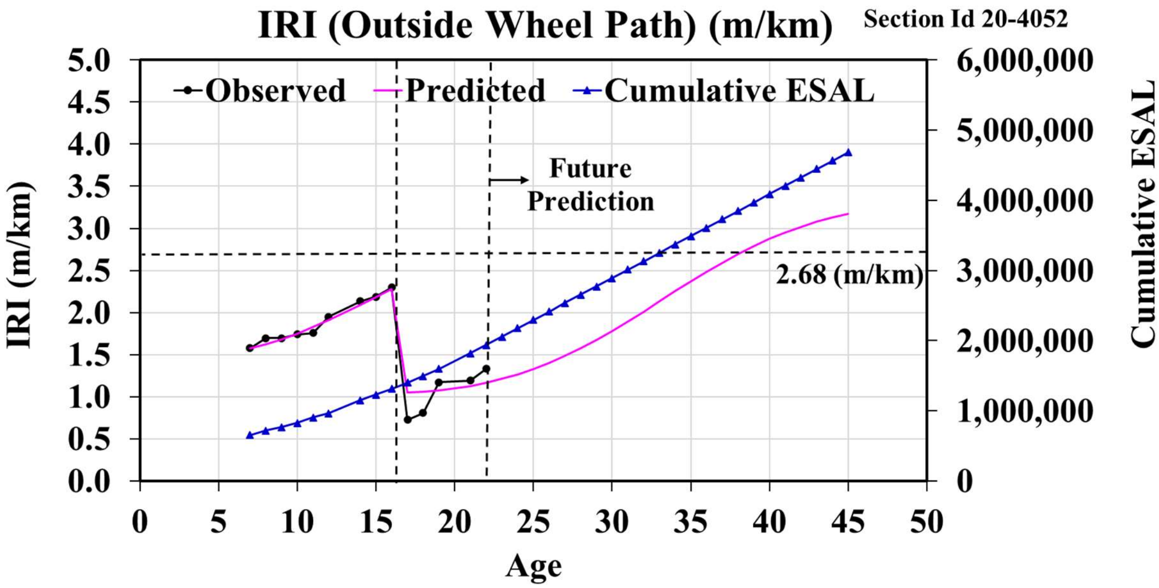

Figure 119 ANN Future Prediction Plot of IRI (Outside Wheel Path) (m/km) for JRCP Section in Kansas

Figure 119 shows that with the increase of CESAL value, the IRI value increases more than 2.68 m/km when a pavement is considered as very poor condition [10]. At this point, a new M&R action should be done to improve pavement performance. By changing CN_Code frequency using GUI, a future M&R action was provided in the section. Figure 120 shows that with CESAL value increasing over time in the future, the IRI value decreased when future M&R action was done, which means pavement condition improved.

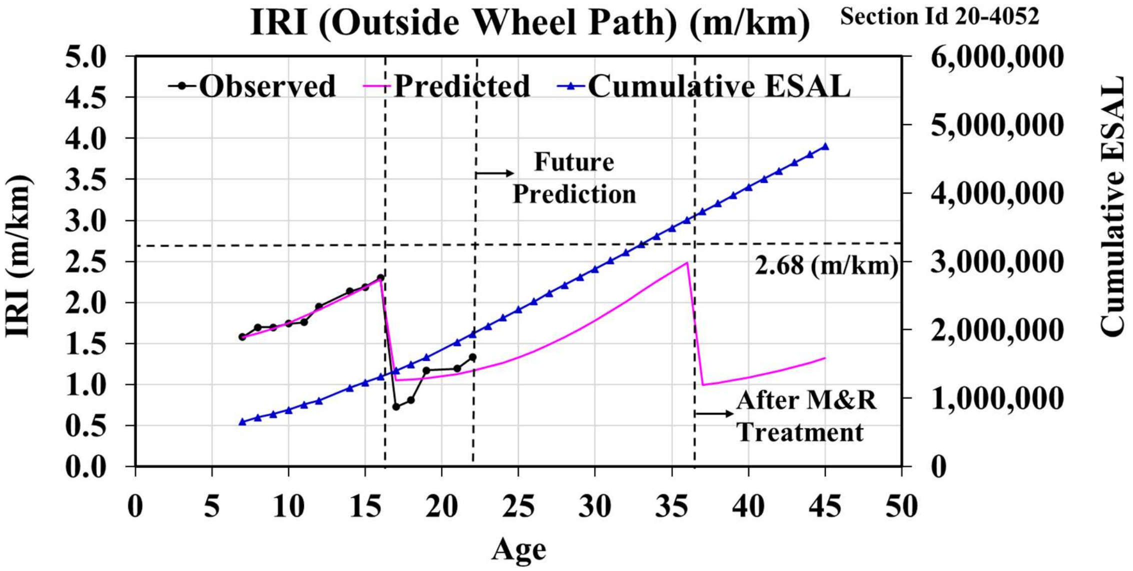

Figure 120 ANN Future Prediction Plot of IRI (Outside Wheel Path) (m/km) after M&R Action

5.6 Multiple Linear Regression Analysis for JRCP Performance Model

A MLR analysis was conducted to develop the JRCP performance model. This MLR model will be compared with the best model developed using the ANN modeling technique. The best performing model was model 3 for JRCP discussed in section 5.5.3. The input and output variables are the same as model 3. The input variables are initial IRI, age, concrete pavement thickness, base/subbase thickness, average contraction spacing, CESAL, base/subbase materials type, climatic region, and CN_Code. The output variable is IRI (outside wheel path) (m/km). The input variables have six continuous variables, two categorical variables, and CN_Code. The CN_Code was developed based on the IRI value improvement and the type of M&R action provided in Table 27. If no M&R action was done and the improvement of IRI value was very low, the CN_Code was categorized as ‘1’. If M&R action was done or there was a significant improvement of IRI value, the CN_Code was assigned as 2, 3, and so on. This CN_Code is a continuous variable where 2, 3 is the frequency of M&R actions and/or IRI value improvements.

IRI (outside wheel path) (m/km) was normally distributed. Standard residuals were normally distributed. Scatterplots were analyzed, and no curvilinear relationships between the criterion variable and predictor variables or heteroscedasticity were evident. There was a statistically significant relationship between input variables and output variable, F (10, 576) = 78.34, $p < 0.001$. The MLR model accounted for 58% of the variance in the model with $R^2 = 0.581$.

5.6.1 MLR Model Results and Comparison between ANN Model and MLR Model

The developed MLR model equation is given below:

$$\begin{aligned} &IRI\ (Outside\ Wheel\ Path)(m/km) \\ &\qquad = 1.215 + 1.070 \times IRI_0 + 0.004 \times Age + 0 \times Wet, Non-Freeze \\ &\qquad + [(-0.081) \times Wet, Freeze] + [(-0.154) \times Granular\ Base/\ Subbase \\ &\qquad + [(-0.118) \times Treated\ Base/\ Subbase + [(-0.101) \times CN_{Code}] \\ &\qquad + [(-0.085) \times h_{concrete}] + 0.003 \times h_{base/subbase} \\ &\qquad + [(-0.016) \times Average\ Contraction\ Spacing\ (m)] + 8.191 \times 10^{-9} \times CESAL \end{aligned}$$

Where, IRI_0 = Initial IRI Outside Wheel Path (m/km); Wet, Non-Freeze and Wet, Freeze = Categorical variable for climatic region; Granular Base/Subbase, Treated Base/Subabse = Categorical variable for base/subbase material type; CN_Code = Continuous variable for Maintenance and Rehabilitation (M&R) frequency; $h_{concrete}$ = Concrete pavement thickness, in; $h_{base/subbase}$ = Base/Subbase thickness, in; CESAL = Cumulative Equivalent Single Axel Load.

The comparison of the prediction accuracy measures for the MLR model is graphically presented in Figure 121. From Figure 121, it is evident that the model prediction is scattered and far away from the line of equality. The MLR model accounted for only 58% variability whereas the ANN model accounted for 95% variability in the model.

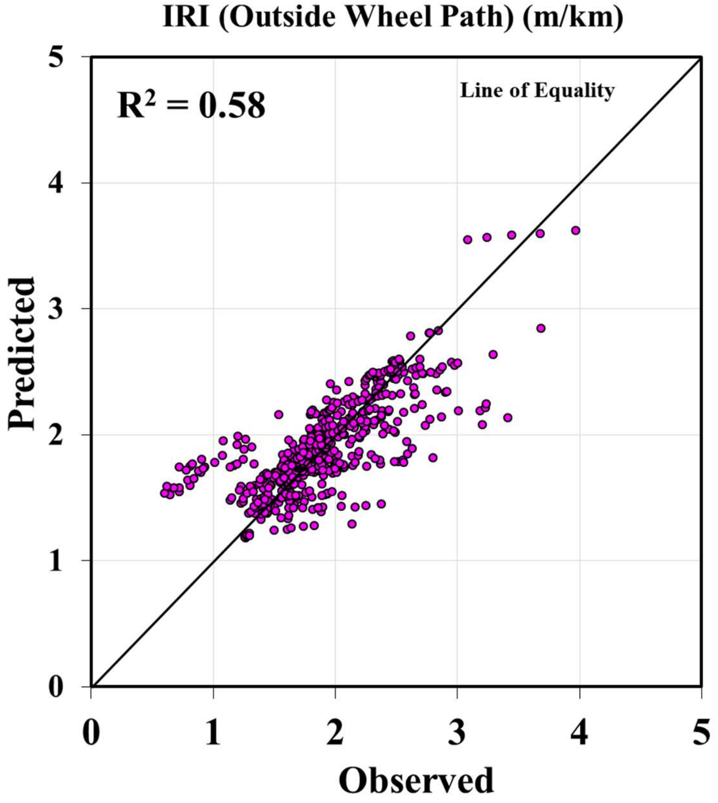

Figure 121 Observed IRI (Outside Wheel Path) (m/km) vs. Predicted IRI (Outside Wheel Path) (m/km)

The 577 data points are assigned section sequence numbers from 1 to 577. Figure 122 shows the observed and MLR model predicted IRI (outside wheel path) values. From Figure 122, it is demonstrated that the predicted IRI could not apprehend most of the variability in the IRI observed values.

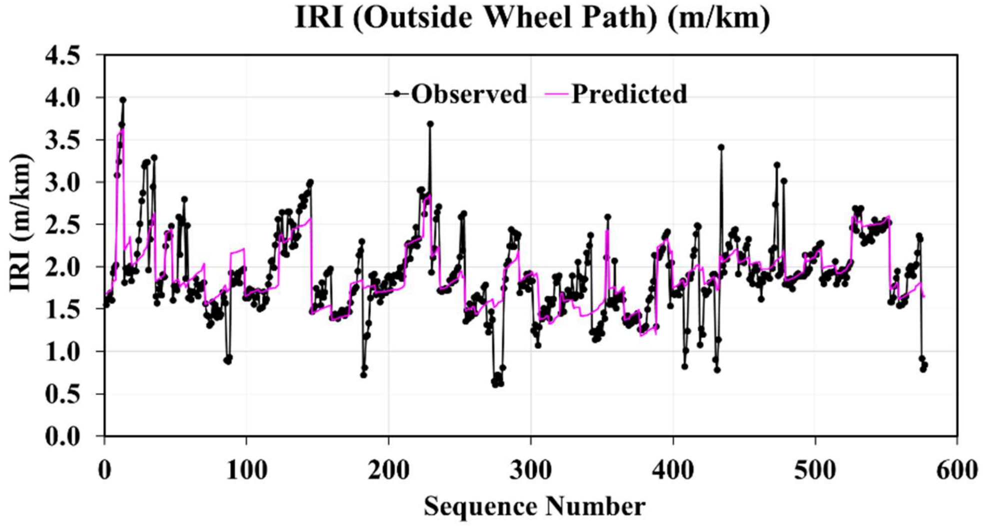

Figure 122 Observed and Predicted IRI (Outside Wheel Path) (m/km) Plot

Figure 123 shows the observed and predicted IRI for Section 20-4052, in Kansas. The predicted values do not follow the observed values closely. The difference in the mean values of observed and predicted is 13.1% whereas the difference is 0.6% for ANN Model.

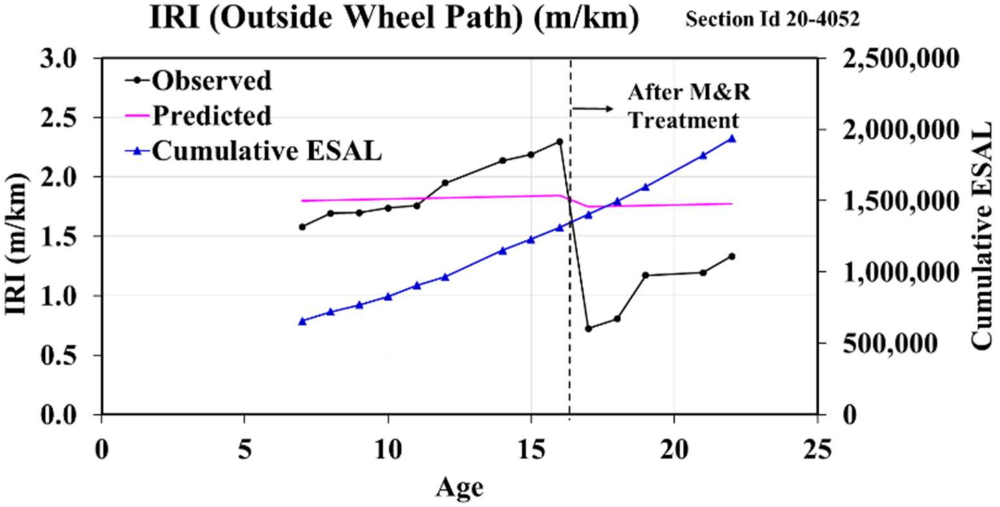

Figure 123 Observed and Predicted IRI (Outside Wheel Path) (m/km) Plot of JRCP Section in Kansas

5.7 Concluding Remarks

Based on the materials discussed in this chapter, the key concluding remarks are summarized below:

- The LTPP database contained 49 JRCP sections under the GPS-4 study. All the pavements are in the wet, freeze and wet, non-freeze climatic regions.
- An in-depth study of M&R history collected from the LTPP database for JRC pavement produced several CN_Code. The best model was found with the CN_Code developed based on the IRI value improvement and the type of M&R action provided in Table 27 and the variable is a continuous variable where number increment indicates the frequency of M&R action provided in the pavement section.
- The best performing ANN model has a network structure of 11-19-1 (i.e. 11 inputs, 19 hidden nodes, and 1 output). The ANN model to predict IRI has an R^2 value of 0.95. The total data points used to develop the IRI prediction ANN model were 577.
- The developed IRI prediction model can successfully characterize the behavior (i.e. the increase of IRI values with time and decrease of IRI value after maintenance and rehabilitation). The ANN model can be used to provide future M&R action by changing CN_Code frequency and the model successfully distinguishes the behavior of IRI (i.e. decrease of IRI after M&R action and increase of IRI with time as CESAL increases).
- The developed MLR model to predict IRI has an R^2 value of 0.58. The ANN model shows better accuracy compared to the MLR model developed in this study. The ANN model

accounted for 95% variability in the model whereas the MLR model accounted for only 58% variability.

CHAPTER VI: DEVELOPMENT OF PERFORMANCE MODELS FOR CONTINUOUS REINFORCED CONCRETE PAVEMENTS

6.1 Background

Continuously reinforced concrete pavement (CRCP) is becoming increasingly popular across the United States and around the world. It has the potential to provide a long-term service life under heavy traffic loadings and challenging environmental conditions, provided proper design and quality construction practices are utilized. A reasonably regular transverse cracking pattern with desirable crack spacing (2 to 8 ft (0.6 to 2.4 m)) is a good identifier for a well-performing CRC pavement [78]. This in turn keeps the cracks tight and provides a high level of load transfer across the cracks. Figure 124 shows the controlled cracks and embedded reinforcement steel in a CRC pavement [78].

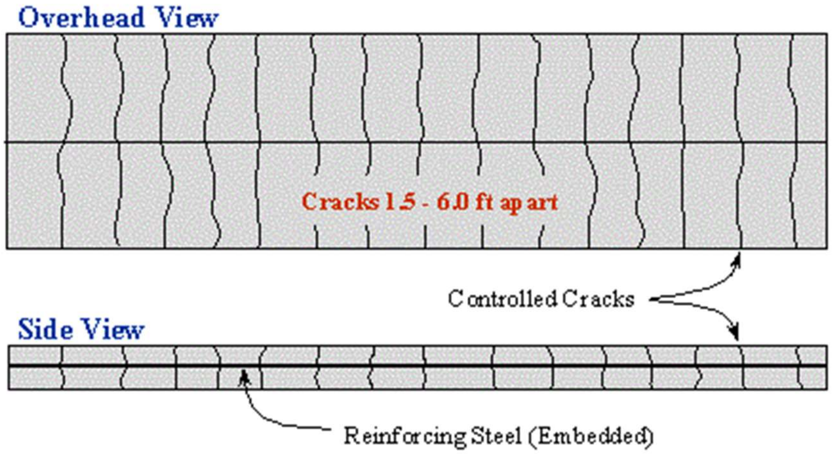

Figure 124 Cross-section and top view of Continuously Reinforced Concrete Pavement [78]

6.2 Methodology

The methodology of developing the CRCP performance model is similar to the JPCP performance model described in section 4.2. The model development process for CRCP is, as follows:

(1) Conduct a literature review of past research studies to identify independent and categorical variables that influence pavement performance.
(2) Assemble databases for JRCP model development from the LTPP database, which must include the variables identified in step (1).
(3) Evaluate the quality of databases and identify missing/erroneous data items.
(4) Develop procedures for estimating important missing data in the time series.
(5) Develop pavement performance models using ANN and multiple linear regression modeling techniques.
(6) Select the appropriate IRI model form (should be capable of estimating the increase of IRI value with time and decrease of IRI value after maintenance and rehabilitation).
(7) Evaluate accuracy and verification of developed performance prediction models for JRCP.
(8) Perform sensitivity analysis for developed performance models.
(9) Implement selected performance models.

6.3 Literature Review

The literature review related to smoothness (IRI) prediction modeling for CRCP pavement are discussed below:

In the MEPDG study of NCHRP 1–37 A [15], the CRCP smoothness model was developed using distress variables to be compatible with the other distress models that will be used in the pavement design. The model developed for predicting the smoothness of CRCP pavements is as follows:

$IRI = IRII + 0.003*TC + 0.008*PUNCH + 0.45*SF + 0.2*PATCH$ (21)

$N = 94$; $R^2 = 60$ percent; $SEE = 0.23$ m/km

where

IRII = initial IRI, m/km; TC = number of medium- and high-transverse cracks/km; PUNCH = number of medium- and high-severity punchouts/km; PATCH = percentage pavement surface with patching (M-H severity flexible and rigid); Site Factor (SF) = $Age*(1+FI)*(1+P_{200})/1000000$; Age = pavement age in years; FI = freezing index, °C days; and P_{200} = percent subgrade material passing the 0.075-mm sieve

Johnston and Surdahl [79] analyzed the LTPP CRC data by using multiple regression techniques. The database used in this study contained 85 CRC pavement sections from 29 states across the U.S. The study found significant correlations between cracks and steel depth, cracks and steel size, and cracks and pavement thickness.

Gharaibeh et al. [80] reviewed the design and performance of continuously reinforced concrete pavement (CRCP) in Illinois. The study investigated the effect of key design and construction parameters on long-term CRCP performance by using a database based on field surveys conducted from 1977 to 1994 compiled by the Illinois Department of Transportation. The study found that the following variables have significant effects on CRCP performance:

longitudinal reinforcement content (greatest effect of all variables), slab thickness (also very significant), traffic load applications, depth of reinforcement, base type, and D-cracking of concrete. The study also found that CRCP sections with a slab 178 mm (7 in.) thick and steel content less than 0.6 percent developed the most structural failures and CRCP sections with a slab 254 mm (10 in.) thick and steel content from 0.7 to 0.8 percent developed the fewest failures.

Yaserar et al. [50] developed a performance model for CRC pavement using the ANN modeling technique for Mississippi. This study used maintenance and rehabilitation actions as an input in the model. The database used in this study contained 69 CRCP pavement sections that resulted in 212 datasets from 2010 to 2018. The ANN model was trained using 25% data, then tested with 25% data and the other 25% of data was employed to validate the model by comparing ANN predicted IRI and measured IRI. The study developed a model employing an 11-18-1 ANN structure with the accuracy of 0.0012 ASE, 5.923 MARE, and 0.872 R^2 statistical measures.

6.4 Data Collection for CRCP Performance Models

The data were collected from the LTPP database of CRCP, which is GPS-5 [71]. A total of 53 GPS-5 CRCP pavement sections are included in the LTPP that are located throughout the United States. The IRI measurements are from 1989 to 2017. By averaging the IRI value from one run, a dataset was created which has 575 data points. Figure 125 shows the spatial map of CRCP sections included in the LTPP database. CRCP sections included in the LTPP database are located in four climatic regions. Table 44 shows that 60.38% (32 of 53) sections are in the wet, non-freeze climatic region and 28.3% (15 of 53) sections are in the wet, freeze climatic region. The IRI data points follow the same statistics, higher in wet, non-freeze (60.7%, 349 of 575) region than wet, freeze (25.74%, 148 of 575) region.

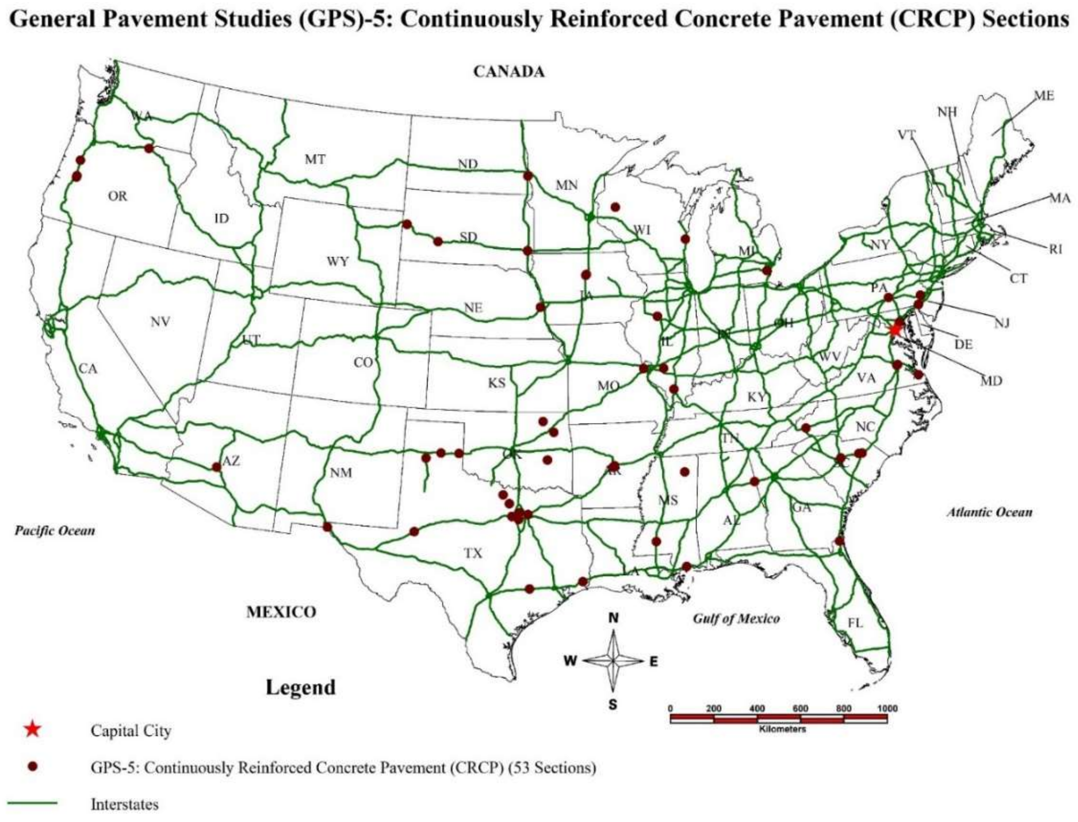

Figure 125 Spatial Map of CRCP Sections in the USA

Table 44 Distribution of Pavement Sections and IRI Data Points in Different Climatic Region

Climatic Region	Number of Sections	% of Sections	Number of Data Points	% of Data Points
Wet, Non-Freeze	32	60.38%	349	60.70%
Dry, Non-Freeze	5	9.43%	64	11.13%
Dry, Freeze	1	1.89%	14	2.43%
Wet, Freeze	15	28.30%	148	25.74%
Total	53	100.00%	575	100.00%

Table 45 shows the distribution of pavement sections and IRI data points by state. Texas has the highest 13 pavement sections out of 53 and 25.39% (146 of 575) IRI data points. Oregon has 4 sections and it contains the second highest IRI data points of 12.35% (71 of 575).

Table 45 Distribution of Pavement Sections and IRI Data Points by States

State Code	State Name	Climatic Zone	Number of Sections	% of Sections	Number of Data Points	% of Data points
1	Alabama	Wet, Non-Freeze	1	1.89%	8	1.39%
4	Arizona	Dry, Non-Freeze	1	1.89%	10	1.74%
5	Arkansas	Wet, Non-Freeze	2	3.77%	20	3.48%
10	Delaware	Wet, Non-Freeze	1	1.89%	6	1.04%
13	Georgia	Wet, Non-Freeze	1	1.89%	6	1.04%
17	Illinois	Wet, Freeze	3	5.66%	38	6.61%
19	Iowa	Wet, Freeze	2	3.77%	22	3.83%
24	Maryland	Wet, Non-Freeze	1	1.89%	12	2.09%
26	Michigan	Wet, Freeze	1	1.89%	7	1.22%
28	Mississippi	Wet, Non-Freeze	3	5.66%	22	3.83%
29	Missouri	Wet, Freeze	1	1.89%	10	1.74%
31	Nebraska	Wet, Freeze	1	1.89%	6	1.04%
37	North Carolina	Wet, Non-Freeze	1	1.89%	10	1.74%
38	North Dakota	Wet, Freeze	1	1.89%	7	1.22%
40	Oklahoma	Wet, Non-Freeze	3	5.66%	35	6.09%
41	Oregon	Wet, Non-Freeze, Dry, Non-Freeze	4	7.55%	71	12.35%
42	Pennsylvania	Wet, Freeze	2	3.77%	20	3.48%
45	South Carolina	Wet, Non-Freeze	3	5.66%	23	4.00%
46	South Dakota	Wet, Freeze, Dry, Freeze	3	5.66%	39	6.78%
48	Texas	Wet, Non-Freeze, Dry, Non-Freeze	13	24.53%	146	25.39%
51	Virginia	Wet, Non-Freeze	3	5.66%	44	7.65%
55	Wisconsin	Wet, Freeze	2	3.77%	13	2.26%
Total 53 Sections and 575 Data points						

6.4.1 Database Development

Output Variables

IRI is considered as the output variable in the pavement performance modeling process for this research. The IRI measurements are from 1989 to 2017. Each section has two types of IRI measurements, IRI inside/left wheel path and IRI outside/right wheel path. A mean roughness index Mean IRI is calculated by averaging the IRI inside/left wheel path and IRI outside/right wheel path measurements. In each visit date, several IRI measurement runs were completed for each section. By averaging the IRI measurement runs, a single IRI measurement was obtained for IRI inside/left wheel path, IRI outside/right wheel path, and mean IRI for each visit date. By doing this, a dataset was created which has 575 data points for 53 CRCP sections. Figure 126 shows the IRI Measurements for Inside Wheel Path and Outside Wheel Path.

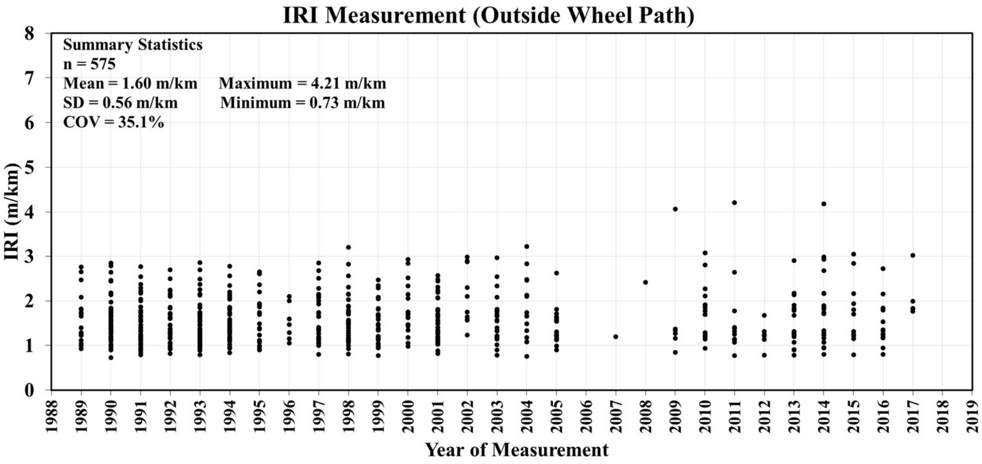

Figure 126 IRI Measurement (Outside Wheel Path) of CRCP Sections

Input Variables

The input variables were kept similar to JPCP performance models. The literature review shows the properties related to reinforcement play an important role in CRCP performance. Clear cover of concrete layer and steel density were included for the CRCP performance model. For the CRCP performance model, the input variables were collected from the LTPP database corresponded to the output variable (IRI outside wheel path) measurement taken date (visit date). The relationship between each input variable and output variable (IRI outside wheel path) was studied by creating several plots.

Initial IRI (Outside Wheel Path) (m/km):

The initial IRI outside wheel path (m/km) represents the first IRI value measured in the outside wheel path for a specific pavement section of the LTPP database. The first measurement is usually done when the pavement was built and opened to traffic or the pavement was first included in the LTPP study. It indicates the road surface condition at the beginning of the analysis period. Initial IRI has a range of a minimum of 0.73 m/km to a maximum of 2.85 m/km. Figure 127 shows the plot of the initial IRI outside wheel path (m/km) against IRI outside wheel path (m/km).

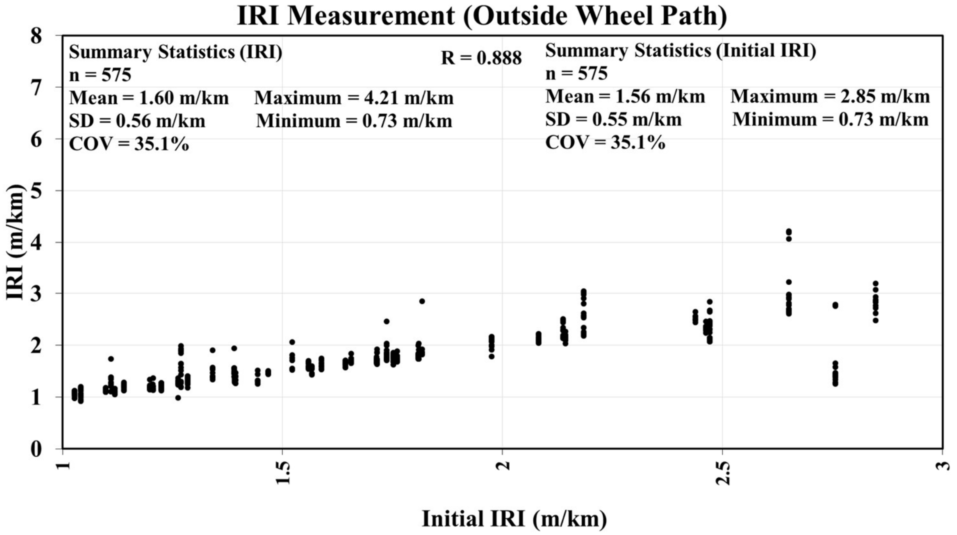

Figure 127 Initial IRI vs. IRI Measurement (Outside Wheel Path) of CRCP Sections

Age:

The variable age is calculated by subtracting the year when the section was opened to traffic from the year IRI measurement was collected. This variable represents the time pavement was expose to climate and traffic loads. Age is also a fundamental variable to be used as an input variable to predict pavement performance for future years. The mean pavement age 53 CRCP section is 20 years. But for some pavement sections, some IRI data were collected when the pavement age was as little as one year, and for some pavement sections that age was as high as 43 years. Figure 128 shows the pavement age when IRI measurements were collected.

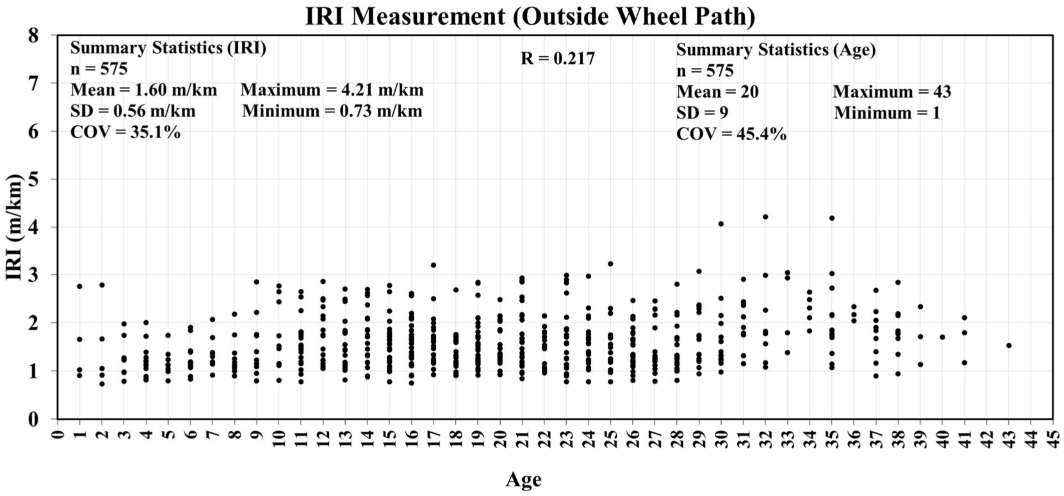

Figure 128 Age vs. IRI Measurement (Outside Wheel Path) of CRCP Sections

Concrete Pavement Thickness (in):

Concrete pavement thickness represents the thickness of concrete and steel mesh layer in a CRC pavement section that is laid over the base/subbase layer. This layer is exposed to climate and endures the traffic loads throughout pavements life. Concrete pavement thickness plays an important role in CRCP performance. The average concrete layer thickness is 9.02 in with a standard deviation of 1.31 in. The maximum concrete layer thickness is 12.8 in and the minimum is 6.2 in. Figure 129 shows the concrete layer thickness of CRCP sections and IRI outside wheel path measurements.

Base/Subbase Thickness (in):

Base/subbase pavement thickness represents the thickness of the base/subbase layer in a CRC pavement section that is laid over the subgrade layer. Some CRCP sections have both base and subbase layers underneath the concrete layer, over the subgrade layer. Traffic loads transfer from concrete layer to base/subbase layer and this layer is also affected by precipitation. Therefore, base/ subbase thickness is an important input variable for CRCP performance modeling. The average base/subbase thickness is 5.304 in. The maximum base/subbase thickness is 15.1 in and the minimum thickness is 1.6 in.

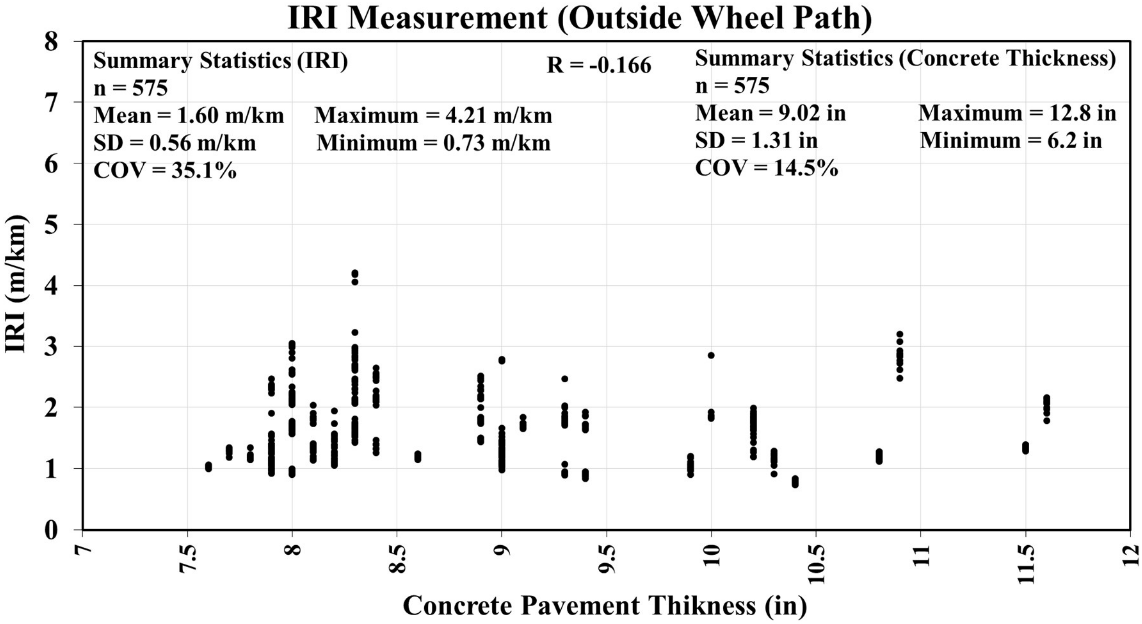

Figure 129 Concrete Pavement Thickness vs. IRI Measurement (Outside Wheel Path) of CRCP Sections

Depth of Concrete Cover to Reinforcement (in)

Depth of concrete cover to reinforcement (in) or clear cover represents the space between the concrete top to reinforcement. The mean clear cover is 3.87 in. with a standard deviation of 0.74 in. The maximum clear cover is 5.5 in and the minimum is 2.5 in. Figure 130 shows the depth of concrete cover to reinforcement of CRCP sections and IRI outside wheel path measurements.

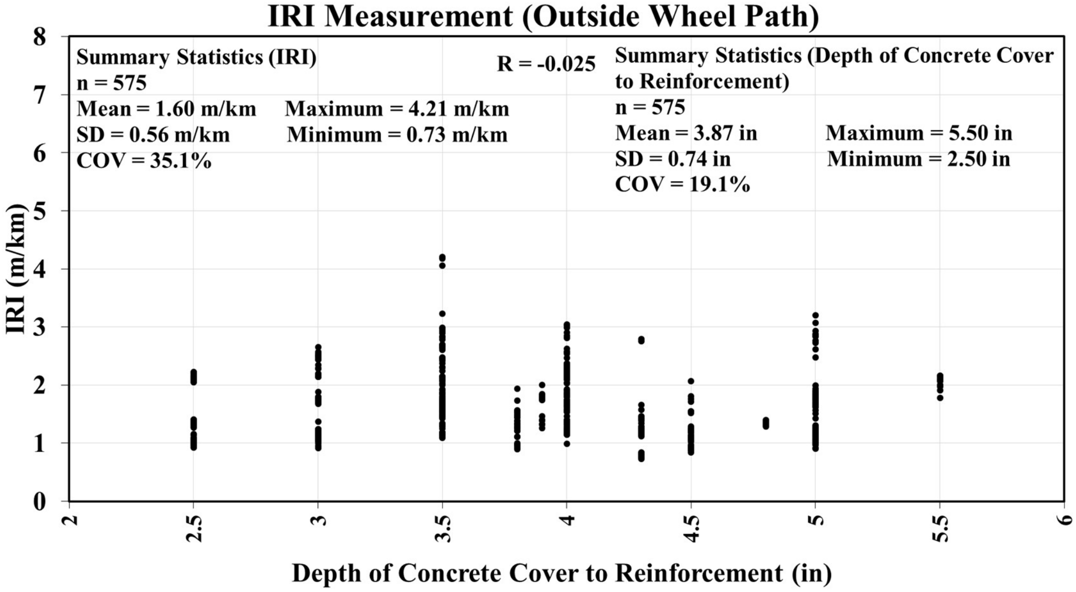

Figure 130 Depth of Concrete Cover to Reinforcement vs. IRI Measurement (Outside Wheel Path) of CRCP Sections

Design Percentage of Longitudinal Steel

The design percentage of longitudinal steel represents the steel density in a CRCP section. The amount of steel has a profound effect on the strength of the concrete pavement. Therefore, it will be useful to use the steel density as an input variable for CRCP performance modeling. The mean steel density is 0.61 percent with a standard deviation of 0.1 percent. The maximum steel density is 1.16 percent and the minimum is 0.5 percent. Figure 131 shows the steel density and IRI outside wheel path measurements.

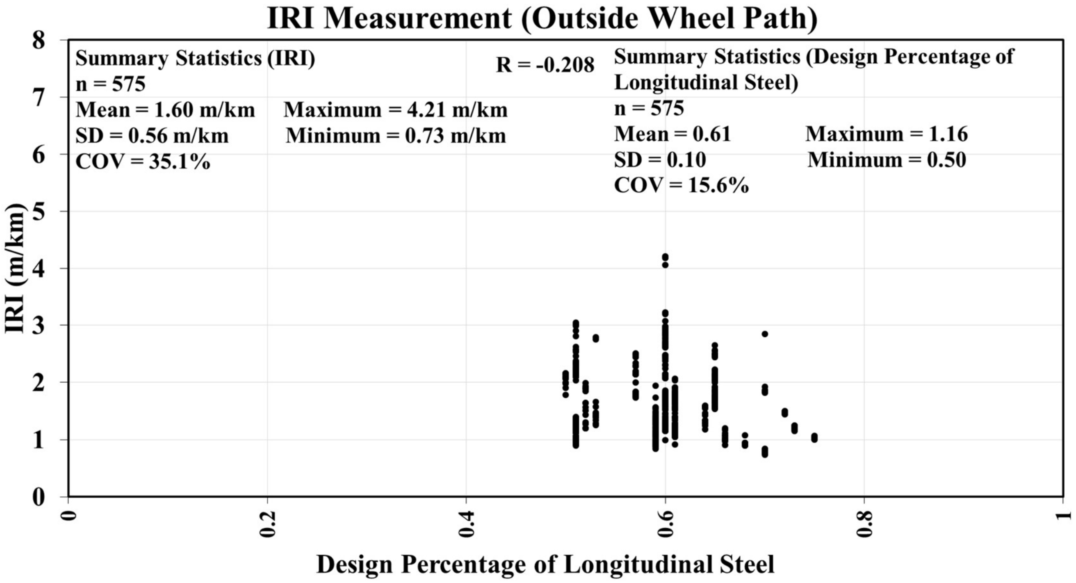

Figure 131 Design Percentage of Longitudinal Steel vs. IRI Measurement (Outside Wheel Path) of CRCP Sections

Cumulative ESAL:

CESAL is the sum of annual ESAL data over the years. ESAL represents a mixed stream of traffic of different axle loads and axle configurations predicted over the design or analysis period and then converted into an equivalent number of 18,000-lb. single axle loads summed over that period. ESAL represents the effects of traffic loads on the pavement over time. In some years, the LTPP database did not have ESAL information corresponding to the IRI measurements data. Interpolation and extrapolation procedures were applied using known data points to compute ESAL for the missing years. Cumulative ESAL represents the cumulative traffic load that was endured by the pavement over pavements’ life. CESAL has one of the most important effects on pavement deterioration. Hence, it is vital to use in performance modeling. CESAL has a mean of 10,031,067 and a standard deviation of 12,019,369. Figure 132 shows the CESAL values corresponded to the IRI outside wheel path measurements for JPCP sections included in this study.

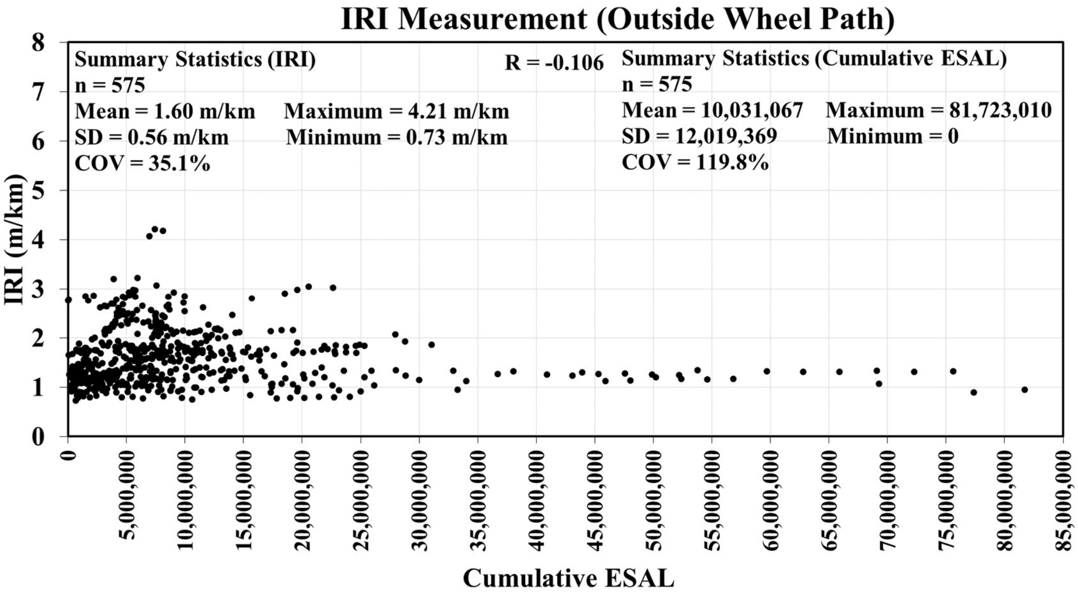

Figure 132 Cumulative ESAL vs. IRI Measurement (Outside Wheel Path) of CRCP Sections

A correlation analysis was performed to obtain the Pearson correlation coefficient (r) between all variables. The correlation matrix summarizes the correlation coefficient (r) values between all the variables and it is easy to observe if the variables are correlated with each other. This correlation coefficient (r) only provides a linear association between variables, if the data is not linearly correlated it will have a low correlation value. Table 46 summarizes the descriptive statistics of input variables used in this study and the correlation between each input variable and the output variable (IRI outside wheel path).

The three highest correlations between input variables and IRI outside wheel path (m/km) were observed with the variable initial IRI (outside wheel path) (m/km) (0.888) followed by age (0.217), and steel density (-0.208). Other variables show low correlation coefficient (r) values, which means they are not linearly correlated with the output variable. However, these variables might follow a non-linear correlation with IRI outside wheel path (m/km) that cannot be identified by the correlational analysis. Therefore, even though some correlation coefficient values were low, all input variables were used in this study for the development of ANN models.

Table 46 Descriptive Statistics of Input Variables for CRCP Model

Statistics	Mean	SD	COV	Maximum	Minimum	Correlation with IRI (outside wheel path), R
Initial IRI (Outside Wheel Path) (m/km)	1.560	0.547	35.09%	2.85	0.73	0.888
Age	20	9	45.39%	43	1	0.217
Concrete Pavement Thickness (in.)	9.021	1.310	14.52%	12.8	6.2	-0.166
Base/Subbase Thickness (in)	5.304	2.939	55.41%	15.1	1.6	-0.147
Depth of Concrete cover to reinforcement (in)	3.869	0.739	19.11%	5.5	2.5	-0.025
Design percentage of longitudinal steel	0.610	0.095	15.63%	1.16	0.5	-0.208
Cumulative ESAL	10,031,068	12,019,369	119.82%	81,723,010	0	-0.106

Some variables were dummy coded as 0 and 1 for modeling purposes. The climatic region represents the climate zone defined by the LTPP which consists of four different regions, wet non-freeze, dry non-freeze, dry freeze, wet freeze. The base/subbase materials represent the type of base/subbase materials used in the pavement section which consists of two types, unbound (granular) or bound (stabilized). For JPCP, model A4a was developed without using categorical variable season which turned out to be a better model than model A4 with the categorical variable season. Thus, the categorical variable season was not used in the development of the CRCP performance model.

6.4.2 Maintenance and Rehabilitation Actions

The t-test in section 4.8.2 established that there is a significant change in IRI value after M&R actions are done on a pavement section. Hence, it is important to incorporate pavement M&R history in the CRCP performance model. An in-depth study of M&R history provided in the LTPP database for CRCP has been carried out in this research. The process is as follows:

- The M&R actions (improvement done on pavement) history was collected from the LTPP database. The M&R action was provided as IMP_TYPE code that is assigned by the LTPP. The description of IMP_TYPE code is described in Table 26 gathered from the LTPP user guide [74]. This table contained the type of improvements for both concrete and asphalt pavement. For this research, only concrete pavement improvement types (M&R actions) were further investigated.
- The M&R action corresponded to each IRI data point was obtained from Table 26. The IMP_TYPE and the description for the type of improvements for concrete pavements are described in Table 27. The M&R actions can be characterized in two categories: major M&R and local/minor M&R. Table 27 described the designation of M&R categories for the different types of improvement [75]. The improvement description and designated M&R action category were obtained for each IRI data point using Table 27.

The CN_Code categorical variable was developed to represent the M&R action done on a pavement section. The LTPP database has the Construction Number (CN) corresponded to each IRI data point and the description is given in Section 4.7. But this CN is not an accurate representation of the improvement action done on pavement. For this reason, this doctoral research assigned CN_Code for each IRI data point based on IRI value improvement, the M&R action done before the collection of IRI measurements, and the type of M&R action (major, local/minor). Four CN_Code were developed for CRCP pavement to achieve the most accurate model that will provide an accurate future prediction of IRI and incorporate the M&R actions in the developed model. The developed CN_Code reflects the learning from the development of JPCP performance models. The description of each CN_Code is given below:

(1) The first CN_Code was developed based on the original CN collected from the LTPP database corresponded to each IRI data point. If no M&R action (CN1 in the original LTPP database) was done, the CN_Code was categorized as ‘0’, and this 0 was continued until an M&R action was performed. The first M&R action (CN2 in the original LTPP database) was categorized as ‘1’, and this 1 was continued until the end of the section.

(2) The second CN_Code was also developed based on the original CN collected from the LTPP database corresponded to each IRI data point. If no M&R action (CN1 in the original LTPP database) was done, the CN_Code was categorized as ‘1’, and this 1 was continued until an M&R action was performed. The first M&R action (CN2 in the original LTPP database) was categorized as ‘2’, and this 2 was continued until the second M&R action. The second M&R action (CN3 in the original LTPP database) was categorized as ‘3’, and this 3 was continued

until the third M&R action. This CN_Code assignment continued until all the M&R actions done on a pavement section were categorized.

(3) The CRCP sections included in the LTPP study are not much aged. There were not many M&R actions done on the pavement sections and the IRI value improvement is not significant for all the sections. Thus, the third CN_Code was also developed based on the IRI value improvement of more than 0.1 m/km and the type of M&R action provided in Table 27. If no M&R action was done and the improvement of IRI value was less than 0.1 m/km, the CN_Code was categorized as ‘0’, and this 0 continued until an M&R action was performed or the IRI value improved more than 0.1 m/km. The first data point found with an M&R action done or IRI value improvement more than 0.1 m/km, was assigned as ‘1’ CN_Code and this 1 continued until the next M&R action was performed or the IRI value improved more than 0.1 m/km. The next data point found with an M&R action done or IRI value improvement more than 0.1 m/km, was assigned as ‘2’ CN_Code and this 2 continued until the next M&R action was found or the IRI value improved more than 0.1 m/km. This CN_Code assignment process continued until all the IRI data points were categorized for a pavement section.

(4) The fourth and the last CN_Code was also developed based on the IRI value improvement of more than 10% and the type of M&R action provided in Table 27. If no M&R action was done and the improvement of IRI value was less than 10%, the CN_Code was categorized as ‘0’, and this 0 continued until an M&R action was performed or the IRI value improved more than 10%. The first data point found with an M&R action done or IRI value improvement of

more than 10%, was assigned as ‘1’ CN_Code and this 1 continued until the next M&R action was performed or the IRI value improved more than 10%. The next data point found with an M&R action done or IRI value improvement of more than 10%, was assigned as ‘2’ CN_Code and this 2 continued until the next M&R action was found or the IRI value improved more than 10%. This CN_Code assignment process continued until all the IRI data points were categorized for a pavement section.

6.4.3 Database Summary

The input and output variables are thoroughly discussed in section 6.4.1. Table 47 shows the key input variables for CRCP models. The maintenance and rehabilitation (M&R) history is represented as CN_Code. Table 47 also shows the CN_Code used in these models. CN_Code descriptions are discussed in section 6.4.2. Four models were tried to find the most accurate model that can predict IRI incorporating the M&R history of the pavement sections.

Table 47 Input Variables Used in CRCP Performance Models

No.	**Input Variables**	**Model 1**	**Model 2**	**Model 3**	**Model 4**
1	IRI_0 (Initial IRI Outside Wheel Path) (m/km)	Initial IRI Outside Wheel Path (m/km)	Initial IRI Outside Wheel Path (m/km)	Initial IRI Outside Wheel Path (m/km)	Initial IRI Outside Wheel Path (m/km)
2	Age (Pavement age, years)	Age	Age	Age	Age
3	$h_{concrete}$ (Concrete pavement thickness, in)	$h_{concrete}$	$h_{concrete}$	$h_{concrete}$	$h_{concrete}$
4	$h_{base/subbase}$ (Base/Subbase thickness, in)	$h_{base/subbase}$	$h_{base/subbase}$	$h_{base/subbase}$	$h_{base/subbase}$
5	Depth of Concrete cover to	Clear Cover (in)	Clear Cover (in)	Clear Cover (in)	Clear Cover (in)

No.	**Input Variables**	**Model 1**	**Model 2**	**Model 3**	**Model 4**
	reinforcement (in)				
6	Design percentage of longitudinal steel	Steel Density	Steel Density	Steel Density	Steel Density
7	CESAL (Cumulative Equivalent Single Axel Load)	CESAL	CESAL	CESAL	CESAL
8	Base/Subbase Materials (Categorical variable for Base/Subbase materials)	Unbound (Granular) Base/ Subbase Bound (Treated) Base/ Subbase	Unbound (Granular) Base/ Subbase Bound (Treated) Base/ Subbase	Unbound (Granular) Base/ Subbase Bound (Treated) Base/ Subbase	Unbound (Granular) Base/ Subbase Bound (Treated) Base/ Subbase
9	Climatic Region (Categorical variable for LTPP climatic region)	Wet, Non-Freeze Dry, Non-Freeze Wet, Freeze Dry, Freeze	Wet, Non-Freeze Dry, Non-Freeze Wet, Freeze Dry, Freeze	Wet, Non-Freeze Dry, Non-Freeze Wet, Freeze Dry, Freeze	Wet, Non-Freeze Dry, Non-Freeze Wet, Freeze Dry, Freeze
10	CN (Construction Number, variable for M & R)	CN Categorical: No M&R Action 0 M&R Action 1	CN Original Continuous: (1,1,2,2…) No M&R Action 1 M&R Action 2,3,4….	CN Continuous: (1,1,2,2,3,3,…..) (Based on IRI value improvement of more than 0.1 m/km and the type of M&R action provided in Table 27) No IRI Improvement and/or M&R Action 1 IRI Improvement and/or M&R Action 2,3,4	CN Continuous: (1,1,2,2,3,3,…..) (Based on IRI value improvement of more than 10% and the type of M&R action provided in Table 27) No IRI Improvement and/or M&R Action 1 IRI Improvement and/or M&R Action 2,3,4

6.5 ANN Models

6.5.1 ANN Model Architecture

In this research, using the developed model database, four models were tried with the same input variables from Table 47 only changing CN_Code described. The output variable is IRI outside wheel path (m/km) for all four models. These models have seven continuous variables, two categorical variables, and CN_Code.

6.5.2 ANN Model Selection

Four models (Model 1, Model 2, Model 3, and Model 4) were developed. A total of 575 datasets were used to build the desired database; 299, 138, and 138 subdatabases were used, respectively, for training, testing, and validation purposes. Datasets that include minimum and maximum values of each variable were included in the training phase for the network to represent the characteristics of the response. The maximum and minimum ranges of each input/output variable for ANN model development were chosen on purpose to be wider than their actual ranges for better mathematical mapping [54].

Model 1

The inputs for Model 1 are initial IRI, age, concrete pavement thickness, base/subbase thickness, clear cover, steel density, CESAL, base/subbase materials type, climatic region, and CN_Code and output is IRI (outside wheel path) (m/km) as shown in Table 47. The CN_Code used in this model is based on the original CN collected from the LTPP database. No M&R action was assigned as 0 and M&R actions were assigned as 1. This CN_Code is a categorical variable. Four model networks were chosen after training and testing to compare the accuracy of the models after validation and all data. Table 48 shows the statistical accuracy of the four chosen networks. Based on the ASE, MARE, and R^2, the chosen best model network is 14-8-20000 (Input Variables-FinalHN-Iteration). The best network's ASE values for training, testing, validation, and all data are 0.000476, 0.001015, 0.001422, and 0.000490, respectively. Though the other three model networks have lower ASE in testing and validation, the chosen best model network has the lowest ASE in training and all data. R^2 values for this model are as follows: 0.973 for the training, 0.939 for the testing, 0.924 for the validation, and 0.971 for all data. The chosen model network's R^2 value is the highest for training and all data. The chosen best model network has the lowest MARE in training, testing, and all data. The final architecture of this model is 14-8-1, where 14 is the number of inputs, 8 is the number of hidden nodes and 1 is the number of output.

Table 48 Statistical Accuracy Measures of Four Chosen Model Networks for Model 1

InitialHN-FinalHN-Iteration		1-4-20000	Best Model 4-8-20000	1-6-20000	16-16-16000
Training	MARE	4.488	3.811	4.289	4.153
	R^2	0.959	0.973	0.964	0.964
	ASE	0.000720	0.000476	0.000627	0.000640
Testing	MARE	5.556	5.438	5.712	5.453
	R^2	0.943	0.939	0.934	0.948
	ASE	0.000933	0.001015	0.001083	0.000854
Validation	MARE	5.660	6.073	5.985	6.022
	R^2	0.931	0.924	0.928	0.909
	ASE	0.001305	0.001422	0.001370	0.001700
All Data	MARE	4.759	3.857	4.461	4.200
	R^2	0.952	0.971	0.955	0.963
	ASE	0.000809	0.000490	0.000748	0.000616
Final Structure (Input Variables-FinalHN-Iteration)		14-4-20000	14-8-20000	14-6-20000	14-16-16000

Model 2

The inputs and output of this model are very similar to model 1. The CN_Code used in this model is also based on the original CN collected from the LTPP database. No M&R action was assigned as 1 and M&R actions were assigned as 2, 3, and so on. This CN_Code is a continuous variable where 2, 3 is the frequency of M&R actions done on pavement. Five model networks were chosen after training and testing to compare the accuracy of the models after validation and all data. Table 49 shows the statistical accuracy of the five chosen networks. Based on the ASE, MARE, and R^2, the chosen best model network is 14-19-20000 (Input Variables-FinalHN-Iteration). The best network's ASE values for training, testing, validation, and all data are 0.000288, 0.000725, 0.000846, and 0.000304, respectively. Though the other four model networks have lower ASE in testing and validation, the chosen best model network has the lowest ASE in training and all data. R^2 values for this model are as follows: 0.984 for the training, 0.952 for the testing, 0.950 for the validation, and 0.982 for all data. The chosen model network's R^2 value is the highest for all data. The MARE value (3.354) for the chosen best model network is the lowest in all data. The final architecture of this model is 14-19-1, where 14 is the number of inputs, 19 is the number of hidden nodes and 1 is the number of output.

Table 49 Statistical Accuracy Measures of Five Chosen Model Networks for Model 2

InitialHN-FinalHN-Iteration		3-17-20000	3-18-20000	Best Model 3-19-20000	6-12-20000	14-19-20000
Training	MARE	3.355	3.315	3.284	3.743	2.924
	R^2	0.983	0.983	0.984	0.980	0.988
	ASE	0.000300	0.000293	0.000288	0.000349	0.000220
Testing	MARE	5.296	5.267	5.253	5.584	5.019
	R^2	0.953	0.953	0.952	0.949	0.949

InitialHN-FinalHN-Iteration		3-17-20000	3-18-20000	Best Model 3-19-20000	6-12-20000	14-19-20000
	ASE	0.000717	0.000719	0.000725	0.000772	0.000775
Validation	MARE	5.363	5.303	5.271	5.652	5.133
	R^2	0.951	0.951	0.950	0.948	0.951
	ASE	0.000834	0.000836	0.000846	0.000889	0.000832
All Data	MARE	3.401	3.380	3.354	3.736	3.374
	R^2	0.981	0.981	0.982	0.976	0.981
	ASE	0.000318	0.000311	0.000304	0.000400	0.000324
Final Structure (Input Variables-FinalHN-Iteration)		14-17-20000	14-18-20000	14-19-20000	14-12-20000	14-19-20000

Model 3

The inputs and output of this model are very similar to model 1and model 2. The CN_Code used in this model was developed based on the IRI value improvement and the type of M&R action provided in Table 27. If no M&R action was done and the improvement of the IRI value was less than 0.1 m/km, the CN_Code was categorized as ‘1’. If M&R action was done or there was an improvement in the IRI value more than 0.1 m/km, the CN_Code was assigned as 2, 3, and so on. This CN_Code is a continuous variable where 2, 3 is the frequency of M&R actions and/or IRI value improvement of more than 0.1 m/km. Five model networks were chosen after training and testing to compare the accuracy of the models after validation and all data. Table 50 shows the statistical accuracy of the five chosen networks. Based on the ASE, MARE, and R^2, the chosen best model network is 14-19-20000 (Input Variables-FinalHN-Iteration). The best network’s ASE values for training, testing, validation, and all data are 0.000320, 0.000720, 0.001020, and 0.000296, respectively. The chosen best model network has the lowest ASE in testing and validation. R^2 values for this model are as follows: 0.982 for the training, 0.958 for the testing, 0.945 for the validation, and 0.982 for all data. The chosen model network's R^2 value is the highest for testing and validation. The final architecture of this model is 14-19-1, where 14 is the number of inputs, 19 is the number of hidden nodes and 1 is the number of output.

Table 50 Statistical Accuracy Measures of Five Chosen Model Networks for Model 3

InitialHN-FinalHN-Iteration		Best Model 9-19-20000	1-11-20000	15-16-9100	10-19-20000	4-19-19900
Training	MARE	3.029	3.749	4.166	2.936	3.128
	R^2	0.982	0.973	0.965	0.983	0.983
	ASE	0.000320	0.000478	0.000616	0.000303	0.000298
Testing	MARE	4.799	5.299	5.724	4.651	5.078
	R^2	0.958	0.945	0.947	0.944	0.945
	ASE	0.000720	0.000923	0.000930	0.000987	0.001005
Validation	MARE	5.520	5.575	5.865	5.137	5.738
	R^2	0.945	0.943	0.940	0.936	0.933
	ASE	0.001020	0.001072	0.001044	0.001222	0.001268
All Data	MARE	3.089	4.012	3.920	3.055	2.974
	R^2	0.982	0.970	0.972	0.982	0.984
	ASE	0.000296	0.000508	0.000471	0.000298	0.000267
Final Structure (Input Variables-FinalHN-Iteration)		14-19-20000	14-11-20000	14-16-9100	14-19-20000	14-19-19900

Model 4

The inputs and output of this model are very similar to model 3. The CN_Code used in this model was developed based on the IRI value improvement and the type of M&R action provided in Table 27. If no M&R action was done and the improvement of IRI value was less than 10%, the CN_Code was categorized as '1'. If M&R action was done or there was an improvement in the IRI value more than 10%, the CN_Code was assigned as 2, 3, and so on. This CN_Code is a continuous variable where 2, 3 is the frequency of M&R actions and/or IRI value improvement of more than 10%. Five model networks were chosen after training and testing to compare the accuracy of the models after validation and all data. Table 51 shows the statistical accuracy of the five chosen networks. Based on the ASE, MARE, and R^2, the chosen best model network is 14-19-20000 (Input Variables-FinalHN-Iteration). The best network's ASE values for training, testing, validation, and all data are 0.000254, 0.000526, 0.000651, and 0.000319, respectively. The chosen best model network has the lowest ASE in testing, validation, and all data. R^2 values for this model are as follows: 0.986 for the training, 0.965 for the testing, 0.961 for the validation, and 0.981 for all data. The chosen model network's R^2 value is the highest for training, validation, and all data. The MARE value for the chosen best model network is the lowest for training, validation, and all data. The final architecture of this model is 14-19-1, where 14 is the number of inputs, 19 is the number of hidden nodes and 1 is the number of output.

Table 51 Statistical Accuracy Measures of Five Chosen Model Networks for Model 4

InitialHN-FinalHN-Iteration		9-14-20000	Best Model 9-19-20000	4-10-5000	11-15-20000	7-15-20000
Training	MARE	3.081	2.779	3.853	3.497	3.298
	R^2	0.982	0.986	0.974	0.977	0.981
	ASE	0.000309	0.000254	0.000464	0.000408	0.000330
Testing	MARE	4.196	4.327	4.791	5.012	4.766
	R^2	0.971	0.965	0.960	0.961	0.961
	ASE	0.000448	0.000526	0.000605	0.000610	0.000619
Validation	MARE	5.044	4.903	5.824	5.806	5.459
	R^2	0.961	0.961	0.952	0.949	0.954
	ASE	0.000651	0.000651	0.000825	0.000886	0.000812
All Data	MARE	3.659	3.150	4.114	3.432	3.310
	R^2	0.971	0.981	0.969	0.978	0.979
	ASE	0.000484	0.000319	0.000517	0.000377	0.000343
Final Structure (Input Variables-FinalHN-Iteration)		14-14-20000	14-19-20000	14-10-5000	14-15-20000	14-15-20000

Four best performing networks from each model (Model 1, Model 2, Model 3, and Model 4) are showed in Table 43. Model 3 has the lowest ASE, MARE, and the highest R^2 for all datasets. Model 4 has the lowest ASE, MARE, and the highest R^2 for training, testing, and validation. Thus, model 4 has been chosen as the best network.

Table 52Best Networks from Each Model

Models		Model 1	Model 2	Model 3	Best Model Model 4
Structure Initial Nodes-Final Nodes-Iterations		4-8-20000	3-19-20000	9-19-20000	9-19-20000
Training	MARE	3.811	3.284	3.029	2.779
	R^2	0.973	0.984	0.982	0.986
	ASE	0.000476	0.000288	0.000320	0.000254
Testing	MARE	5.438	5.253	4.799	4.327
	R^2	0.939	0.952	0.958	0.965
	ASE	0.001015	0.000725	0.000720	0.000526
Validation	MARE	6.073	5.271	5.520	4.903
	R^2	0.924	0.950	0.945	0.961
	ASE	0.001422	0.000846	0.001020	0.000651
All Data	MARE	3.857	3.354	3.089	3.150
	R^2	0.971	0.982	0.982	0.981
	ASE	0.000490	0.000304	0.000296	0.000319
Final Structure Input Variables-Final Nodes-Iterations		14-8-20000	14-19-20000	14-19-20000	14-19-20000

6.5.3 ANN Model Results

The discussion in the previous section establishes that model 4 is the best performing network based on all statistical measures (ASE, MARE, and R^2 value). The final model structure has 14 inputs of independent variables, 19 hidden nodes, and 1 output (11-19-1) (Figure 133).

The comparison of the prediction accuracy measures for ANN model 4 is graphically presented in Figure 134.

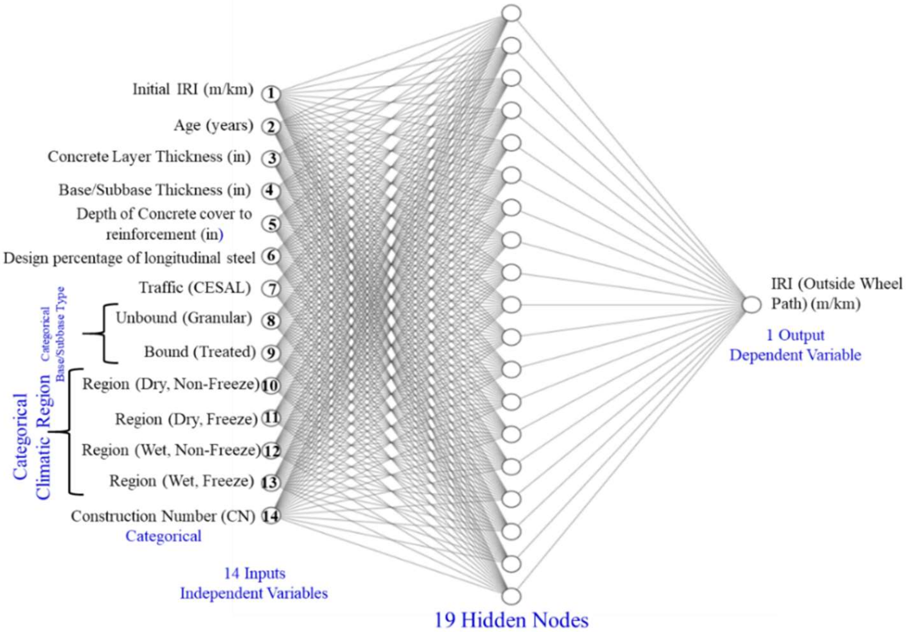

Figure 133 Network Architecture for Best Model (Model 4, Structure: 14-19-1)

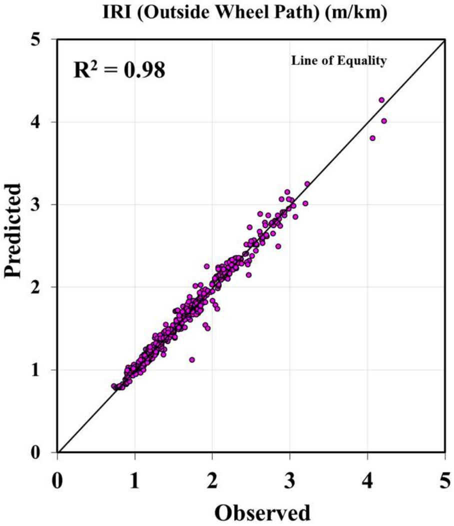

Figure 134 Observed IRI (Outside Wheel Path) (m/km) vs. Predicted IRI (Outside Wheel Path) (m/km)

The 575 data points are assigned section sequence numbers from 1 to 575. Figure 135 shows the observed and Model 4 predicted IRI outside wheel path (m/km) values. From Figure 133, it is revealed that the predicted IRI has apprehended most of the variability in the IRI observed values.

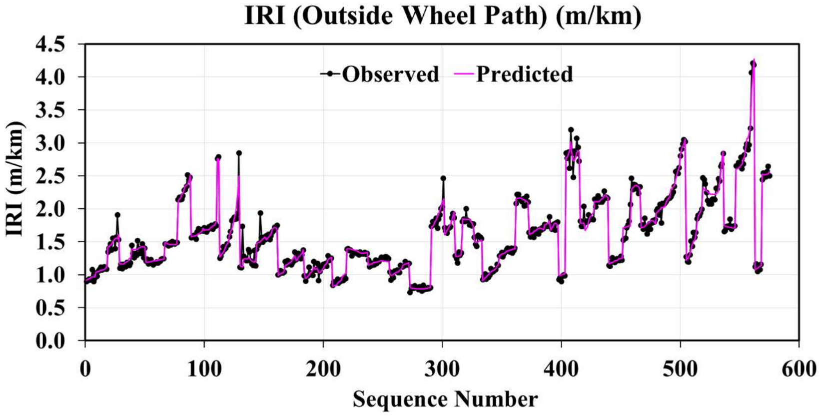

Figure 135 Observed and Predicted IRI (Outside Wheel Path) (m/km) Plot

Figure 136 shows the observed and predicted IRI for Section 24-5807, in Maryland. The predicted values follow the observed values closely. The difference in the mean values of observed and predicted is -0.13%.

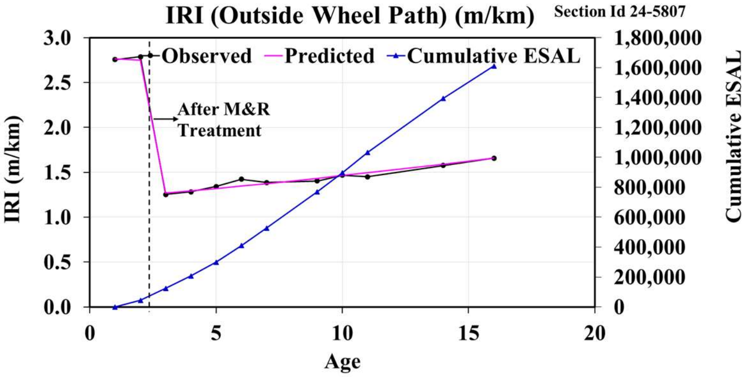

Figure 136 Observed and Predicted IRI (Outside Wheel Path) (m/km) plot of CRCP section in Maryland

6.5.4 Sensitivity Analysis

A sensitivity analysis was carried out to evaluate the significance of the inputs on the output. A GUI was developed by importing all the final ANN model parameters into an excel spreadsheet. To examine the models, some input was changed while keeping the other inputs constant. In this paper, the sensitivity analysis of model 4 is presented since it is the best model in terms of statistical accuracy measures. All model 3 inputs were kept constant except age and CESAL that were changed to generate predictions of IRI. The CESAL values were calculated using the previous year's data. A randomly selected section with one M&R action done was used to show the sensitivity analysis. Figure 137 that the IRI prediction model follows the trend of the observed values. Additionally, it can estimate the increase of IRI values with time and decrease of IRI value after M&R action. Usually, without any rehabilitation, pavement deteriorates over time, therefore, IRI increases.

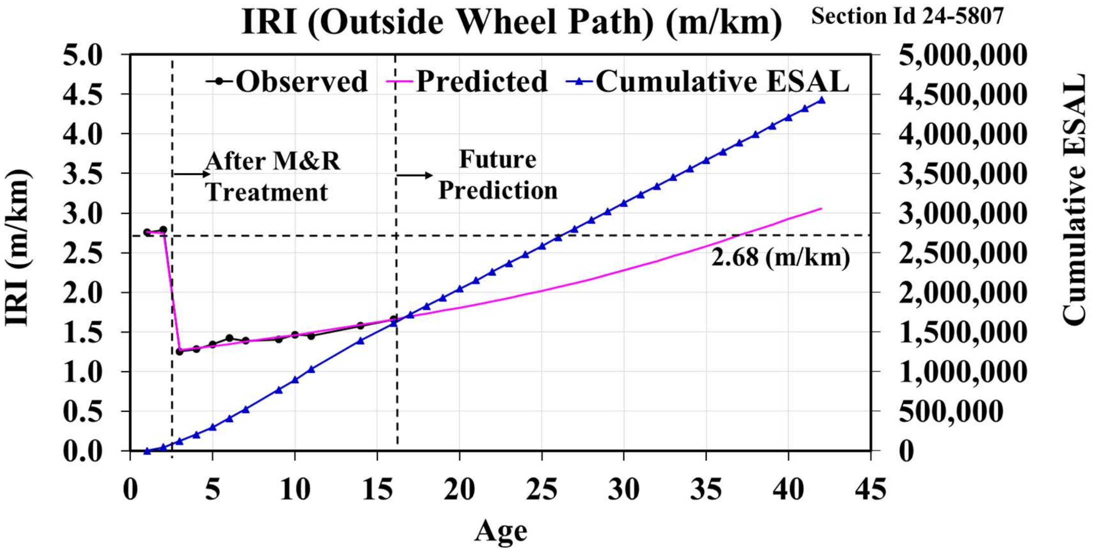

Figure 137 ANN Future Prediction Plot of IRI (Outside Wheel Path) (m/km) for CRCP Section in Maryland

Figure 137 shows that with the increase of CESAL value, the IRI value increases more than 2.68 m/km when a pavement is considered as very poor condition [10]. At this point, a new M&R action should be done to improve pavement performance. By changing CN_Code frequency using GUI, a future M&R action was provided in the section. Figure 138 shows that with CESAL value increasing over time in the future, the IRI value decreased when future M&R action was done, which means pavement condition improved.

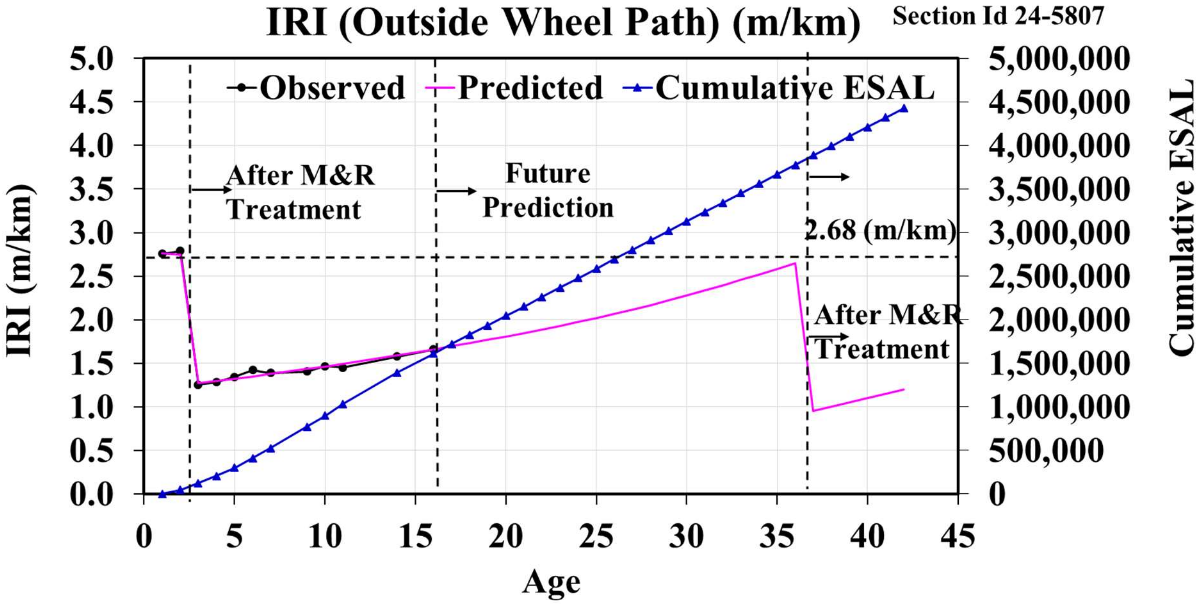

Figure 138 ANN Future Prediction Plot of IRI (Outside Wheel Path) (m/km) after M&R Action

6.6 Multiple Linear Regression Analysis for CRCP Performance Model

A MLR analysis was conducted to develop the CRCP performance model. This MLR model will be compared with the best model developed using the ANN modeling technique. The best performing model was model 4 for CRCP discussed in section 6.5.3. The input and output variables are the same as model 4. The input variables are initial IRI, age, concrete pavement thickness, base/subbase thickness, clear cover, steel density, CESAL, base/subbase materials type, climatic region, and CN_Code. The output variable is IRI (outside wheel path) (m/km). The input variables have seven continuous variables, two categorical variables, and CN_Code. The CN_Code was developed based on the IRI value improvement and the type of M&R action provided in Table 27. If no M&R action was done and the improvement of IRI value was less than 10%, the CN_Code was categorized as ‘1’. If M&R action was done or there was an improvement of IRI value more than 10%, the CN_Code was assigned as 2, 3, and so on. This CN_Code is a continuous variable where 2, 3 is the frequency of M&R actions and/or IRI value improvement of more than 10%.

IRI (outside wheel path) (m/km) was normally distributed. Standard residuals were normally distributed. Scatterplots were analyzed, and no curvilinear relationships between the criterion variable and predictor variables or heteroscedasticity were evident. There was a statistically significant relationship between input variables and output variable, F (12, 574) = 230.259, $p < 0.001$. The MLR model accounted for 83% of the variance in the model with $R^2 = 0.831$.

6.6.1 MLR Model Results and Comparison between ANN Model and MLR Model

The developed MLR model equation is given below:

$$
\begin{aligned}
&IRI\ (Outside\ Wheel\ Path)(m/km) \\
&\quad = -0.322 + 0.922 \times IRI_0\ + 0.014 \times Age + 0 \times Wet, Non-Freeze \\
&\quad + [(-0.049) \times Dry, Non-Freeze] + [(-0.126) \times Dry, Freeze] \\
&\quad + [(-0.063) \times Wet, Freeze] + 0 \times Granular\ Base/\ Subbase \\
&\quad + [(-0.067) \times Treated\ Base/\ Subbase + [(-0.228) \times CN_{Code}] \\
&\quad + 0.044 \times h_{concrete} + \left[(-0.002) \times h_{base/subbase}\right] + 0.044 \times Clear\ Cover \\
&\quad + 0.227 \times Steel\ Density + [(-4.129 \times 10^{-9}) \times CESAL]
\end{aligned}
$$

Where,

IRI_0 = Initial IRI Outside Wheel Path (m/km); Dry, Non-Freeze, Dry, Freeze, Wet, Non-Freeze and Wet, Freeze = Categorical variable for climatic region; Granular Base/Subbase, Treated Base/Subabse = Categorical variable for base/subbase material type; CN_Code = Continuous variable for Maintenance and Rehabilitation (M&R) frequency; $h_{concrete}$ = Concrete pavement thickness, in; $h_{base/subbase}$ = Base/Subbase thickness, in; Clear Cover = Depth of Concrete cover to reinforcement (in); Steel Density = Design Percentage of Longitudinal Steel; CESAL = Cumulative Equivalent Single Axel Load.

The comparison of the prediction accuracy measures for the MLR model is graphically presented in Figure 139. From Figure 139, it is evident that the model prediction is somewhat scattered and cluttered around the line of equality. The MLR model accounted for 83% variability whereas the ANN model accounted for 98% variability in the model.

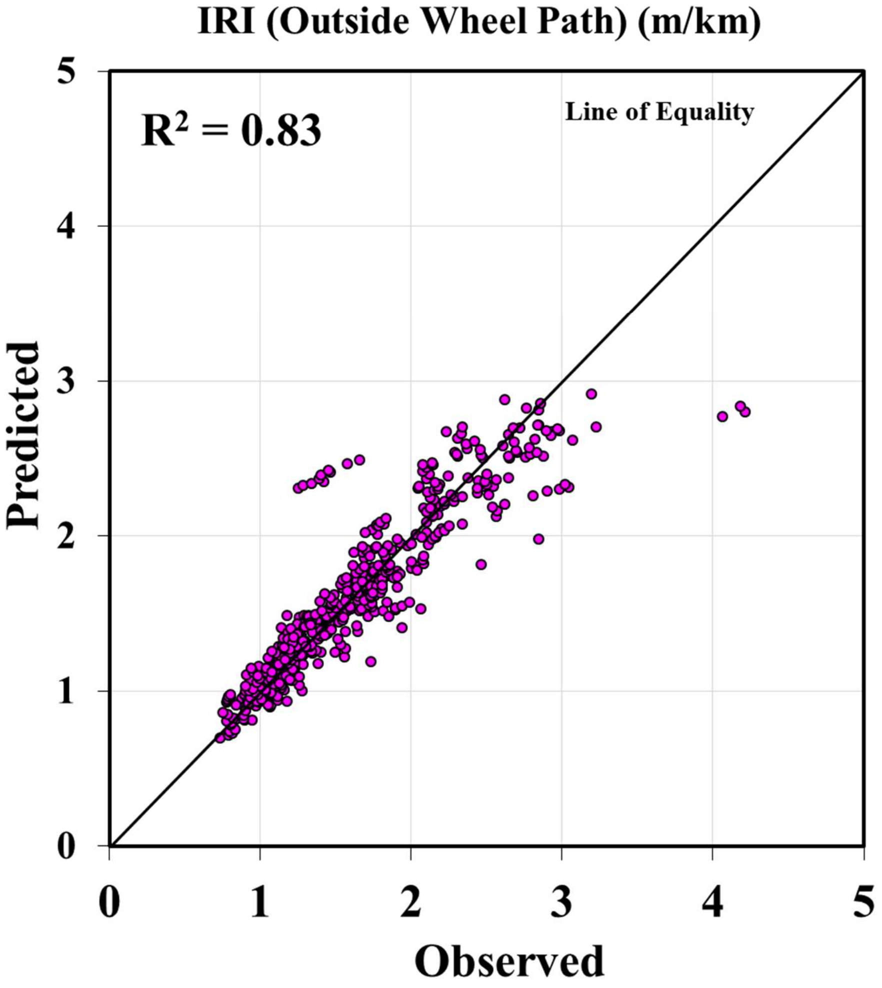

Figure 139 Observed IRI (Outside Wheel Path) (m/km) vs. Predicted IRI (Outside Wheel Path) (m/km)

The 575 data points are assigned section sequence numbers from 1 to 575. Figure 140 shows the observed and MLR model predicted IRI (outside wheel path) values. From Figure 140, it is revealed that the predicted IRI could apprehend some of the variability in the IRI observed values.

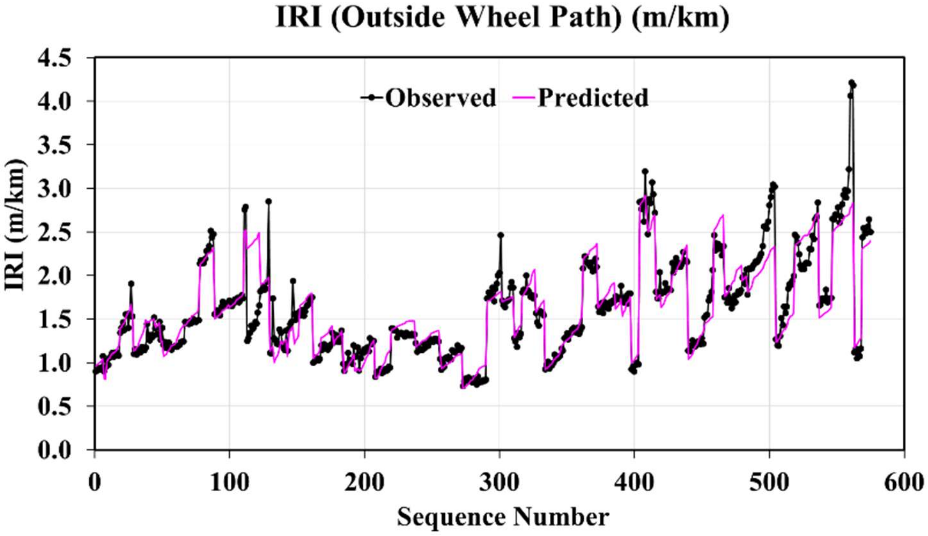

Figure 140 Observed and Predicted IRI (Outside Wheel Path) (m/km) Plot

Figure 141 shows the observed and predicted IRI for Section 24-5807, in Maryland. The predicted values do not follow the observed values closely. The difference in the mean values of observed and predicted is 46.1% whereas the difference is -0.13% for ANN Model.

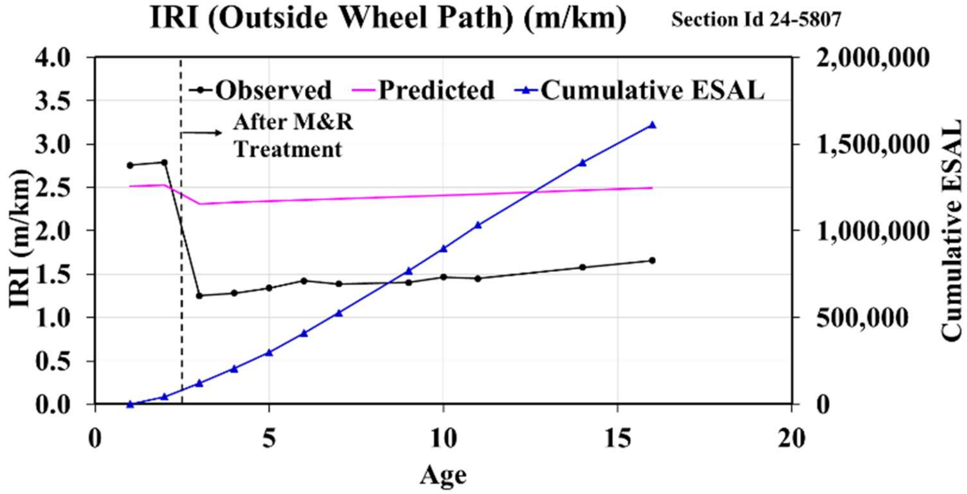

Figure 141 Observed and Predicted IRI (Outside Wheel Path) (m/km) Plot of CRCP Section in Maryland

6.7 Concluding Remarks

Based on the materials discussed in this chapter, the key concluding remarks are summarized below:

- The LTPP database contained 53 CRCP sections under the GPS-5 study. Most data points are from the wet, freeze and wet, non-freeze climatic regions.
- An in-depth study of M&R history collected from the LTPP database for CRC pavement produced several CN_Code. The best model was found with the CN_Code developed based on the IRI value improvement and the type of M&R action provided in Table 27 and the variable is a continuous variable where number increment indicates the frequency of M&R action provided in the pavement section.
- The best performing ANN model has a network structure of 14-19-1 (i.e. 14 inputs, 19 hidden nodes, and 1 output). The ANN model to predict IRI has an R^2 value of 0.98. The total data points used to develop the IRI prediction ANN model were 575.
- The developed IRI prediction model can successfully characterize the behavior (i.e. the increase of IRI values with time and decrease of IRI value after maintenance and rehabilitation). The ANN model can be used to provide future M&R action by changing CN_Code frequency and the model successfully distinguishes the behavior of IRI (i.e. decrease of IRI after M&R action and increase of IRI with time as CESAL increases).
- The developed MLR model to predict IRI has an R^2 value of 0.83. The ANN model shows better accuracy compared to the MLR model developed in this study. The ANN model

accounted for 98% variability in the model whereas the MLR model accounted for 83% variability.

CHAPTER VII: IMPLEMENTATION OF PERFORMANCE MODELS FOR CONCRETE PAVEMENT ASSET MANAGEMENT

7.1 Implementation of Developed Performance Model

An Excel-based program was developed using Visual Basic programing language for the utilization of the performance models. Connection weights, threshold values, and coefficients for best performing networks were imported into an excel worksheet to develop the Excel-based program. The connection weights, threshold values, and input values were used to perform the Feed-forward calculations using Excel functions. A programming code with Visual Basic language was written to automatically generate predictions for repeated years. Figure 142 shows the excel-based user interface developed for CRC pavement for example.

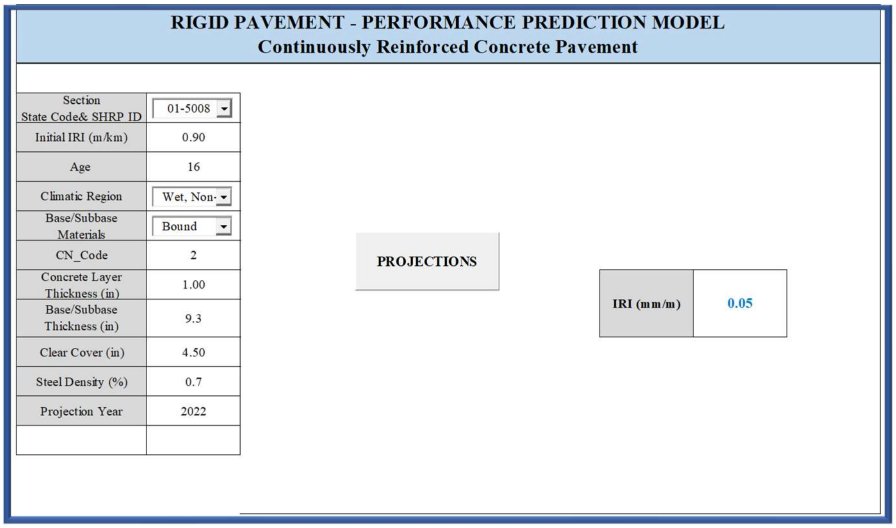

RIGID PAVEMENT - PERFORMANCE PREDICTION MODEL
Continuously Reinforced Concrete Pavement

Section State Code& SHRP ID	01-5008
Initial IRI (m/km)	0.90
Age	16
Climatic Region	Wet, Non-
Base/Subbase Materials	Bound
CN_Code	2
Concrete Layer Thickness (in)	1.00
Base/Subbase Thickness (in)	9.3
Clear Cover (in)	4.50
Steel Density (%)	0.7
Projection Year	2022

IRI (mm/m) 0.05

Figure 142 Graphical User Interface

7.1.1 Application of IRI Performance Condition Deterioration Model

The performance model can be implemented very easily using the program developed in section 7.1. Some of the input variables are constant for each section. After selecting a new section in Figure 142, those variables will be automatically updated. Three variables need to be provided by the user to generate predictions for a specific pavement section. The input variables that need to be provided by the user are discussed below:

- Pavement age (year) is calculated from the initial year when the road was opened to the traffic. If a pavement was opened to traffic in 1991, the pavement age in 2021 is 31 years. If a prediction has to be made in 2030, the pavement age will be 40 years.
- Estimate the CESAL for the projected years based on a known traffic growth factor. If the recent CESAL is 500,000 in 2021, and the annual traffic growth factor is 1%, the estimated CESAL in 2030 is 546,843 and will be used in the model.
- For the maintenance and rehabilitation (M&R) action (CN_Code) variable, assign 1 if there is no M&R has taken place. If a new pavement action needs to be done, add one to the previous CN_Code. If no new M&R action needs to be done, keep the same CN_Code.

Users can update the projection year and the age will be calculated based on the given projection year. By clicking the “Projections” button shown in Figure 142, a submenu will be displayed. This submenu is shown in Figure 143. This submenu will allow the user to select how they want to provide the information about CESAL. Either, the user can provide each year’s ESAL and the program will calculate the CESAL using the ESAL information. Or, the user can provide percent increase/ ESAL growth information for the highway, the program will calculate the CESAL using equations embedded in the coding. Users can give the information about rehabilitation to occur at a specific year shown in Figure 144. The model considers the effect of rehabilitation for the year assigned and then goes back to the trend of deterioration.

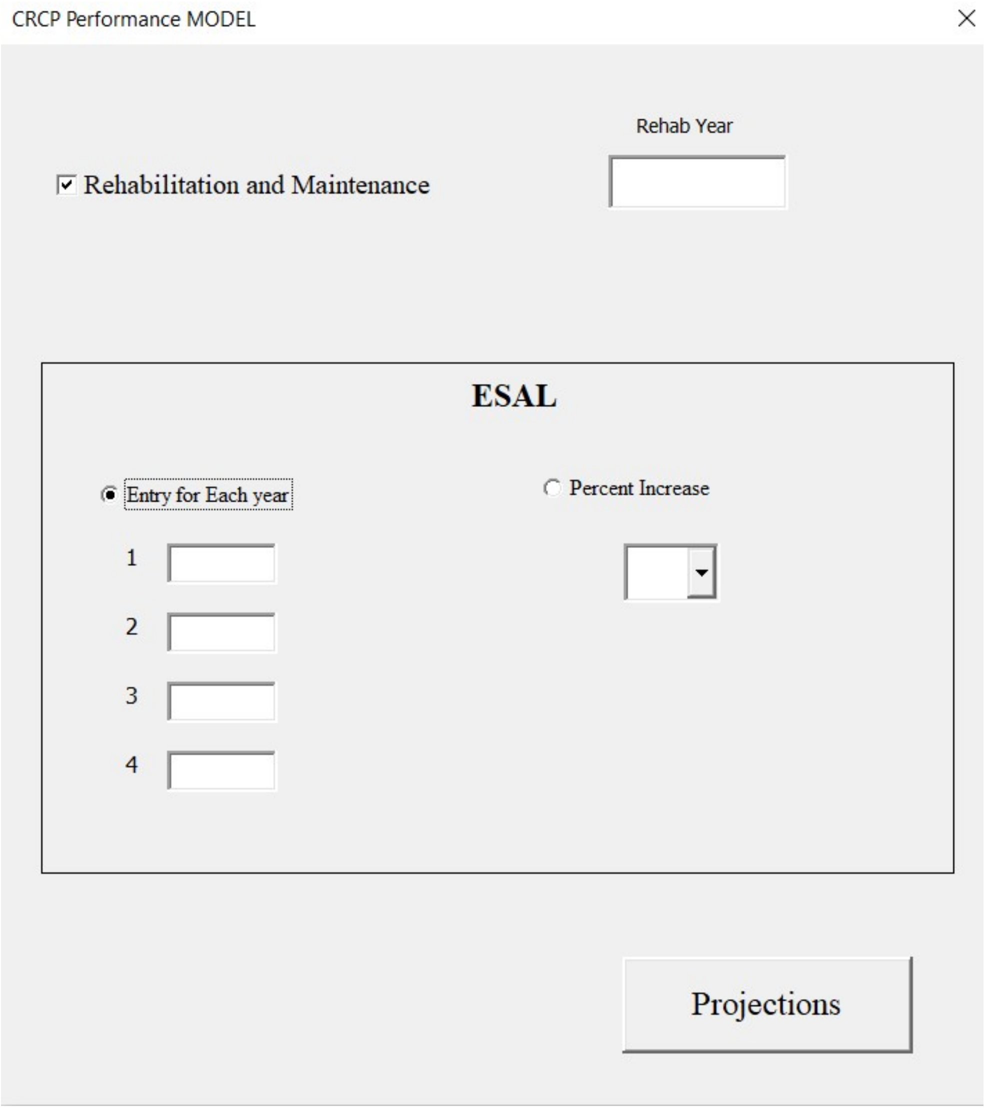
☑ Rehabilitation and Maintenance

● Entry for Each year

○ Percent Increase

Figure 143 Graphical User Interface Submenu for ESAL Information

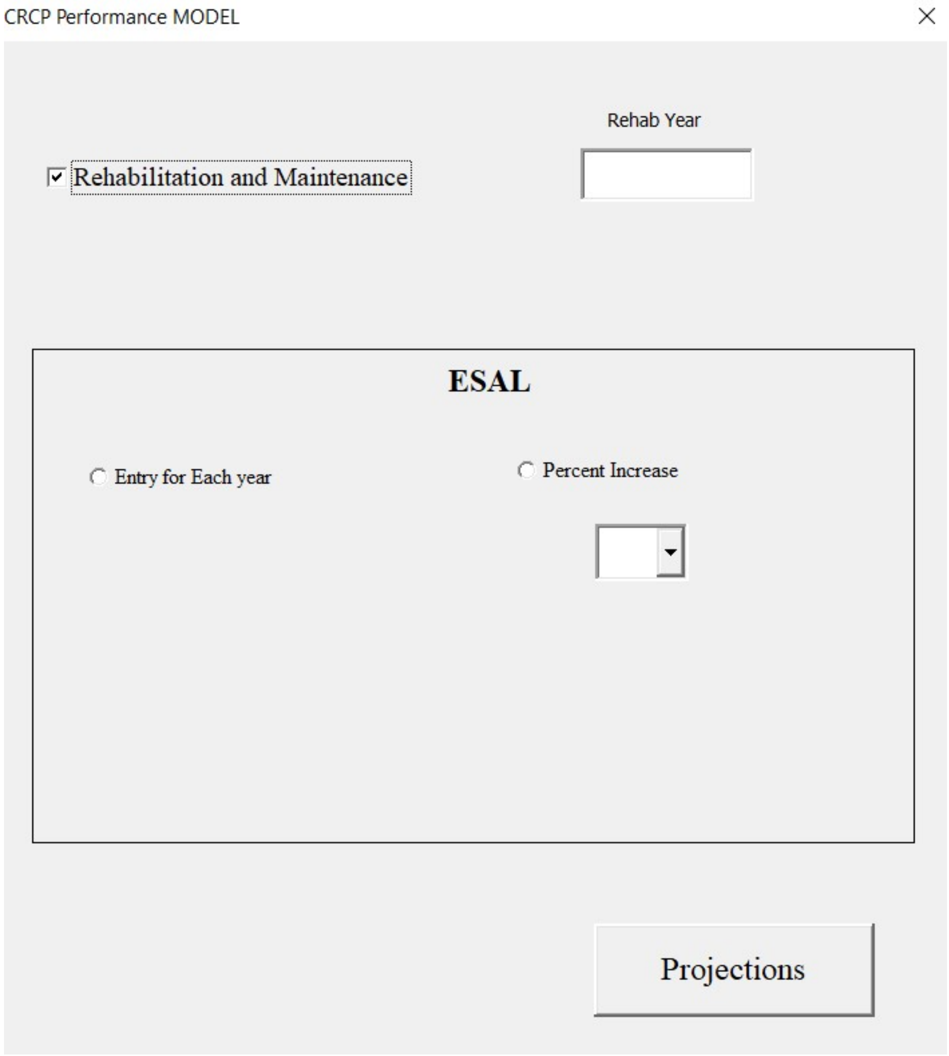

Figure 144 Graphical User Interface Submenu for Maintenance and Rehabilitation Information

7.2 Application of Performance Models for Concrete Pavement Asset Management

Figure 142 shows an enhanced Pavement Asset Management (PAM) framework [9], which was developed based on the U.S. Governmental Accounting Standards Board (GASB) Statement 34 framework [81]. The influence of life-cycle M&R is significant for longer performing highway conditions, as shown in Figure 143. It is recommended to implement the pavement condition deterioration model developed in this research for life-cycle asset management and M&R programs. A simplified M&R intervention criterion for PAM is shown in Table 53 [75].

The performance model developed in this research can successfully predict when a new M&R will be needed for a pavement section. Table 53 can be used to decide what type of M&R actions should be provided in the section. A present worth analysis can be done to identify what type of M&R will be less costly but sustainable for the pavement. A life cycle cost analysis can also be done use performance prediction. This can be helpful to the agencies for budget allocation and prioritize urgent M&R actions.

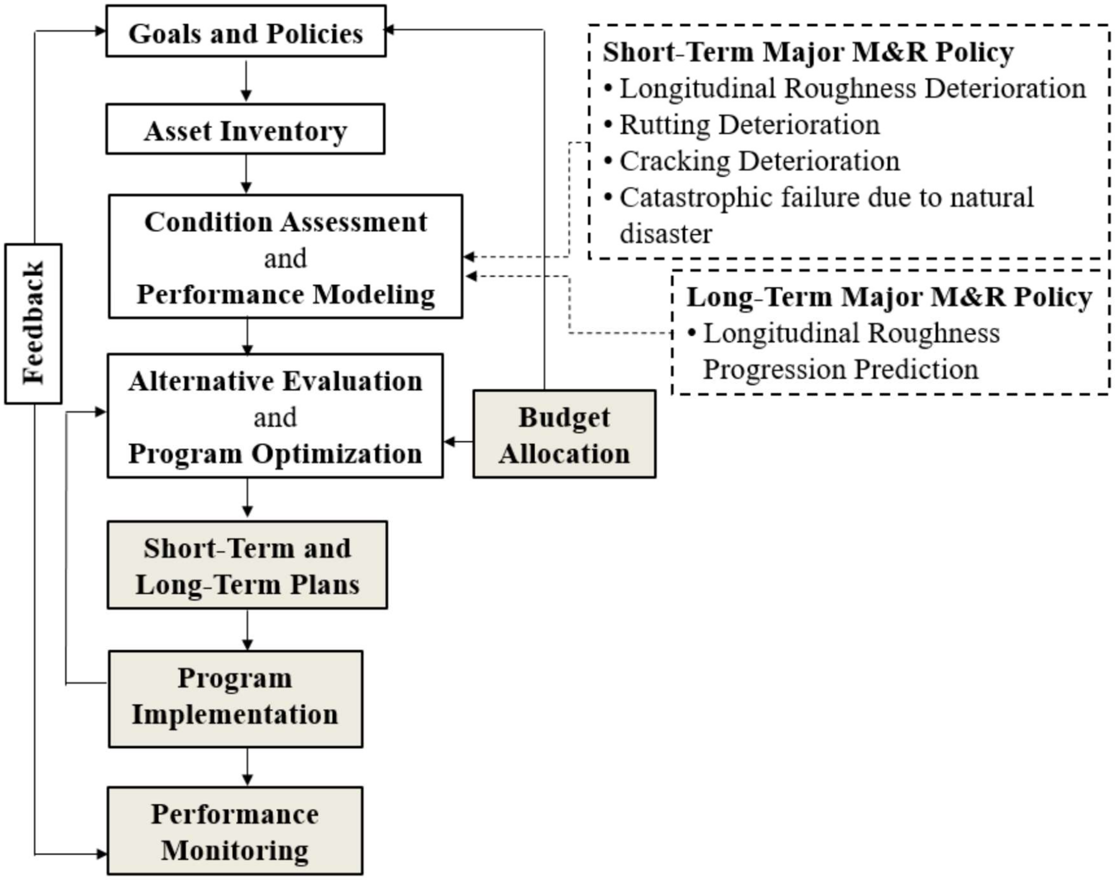

Figure 145 An Enhanced Pavement Asset Management (PAM) Framework [9]

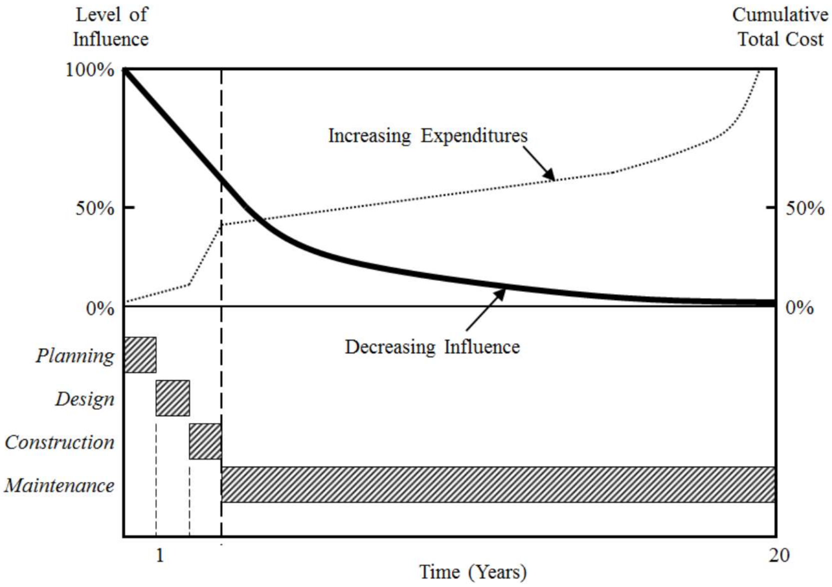

Figure 146 Basic Concept of Life Cycle Cost (LCC) [9]

Table 53 Simplified M&R Intervention Criteria for Pavement Asset Management [75]

1. Short Term or Single Year M, R&R Intervention Policy			
	Asphalt Pavement M, R&R	Intervention Criteria	M, R&R Treatment
(a)	Total Distress Area Low (L), Medium (M), High (H)	(L, M, H Severity) > 60%	**Asphalt Pavement:** M1 for freeway and highway; M2 for other roads **Concrete Pavement:** M1P for freeway and highway; M2P (extensive) for other roads
(b)	Cracking Area	< 60% H - Severity ≥ 20%	**Asphalt Pavement:** M3 (Minor, seal coat) **Concrete Pavement:** M2P (extensive)
(c)	Rutting Area	< 60% H - Severity ≥ 20%	**Asphalt Pavement:** M2 (Milling and inlay)
(d)	Total Distress Area	< 60% H - Severity < 20%	**Asphalt Pavement:** M4 **(**Local minor maintenance) **Concrete Pavement:** M4P (Local)
(e)	Longitudinal Roughness	IRI exceeds 5.2 m/km (Rough & Unsafe)	**Asphalt Pavement:** M3 **(**Minor, seal coat) **Concrete Pavement:** M2P (Extensive)
	(Only if distress repairs are not being applied)		

1. Short Term or Single Year M, R&R Intervention Policy			
(f)	Catastrophic Failure Policy (Flood due to rain, hurricane, river overflow), Others: Earthquake	Rapid Condition Assessment to Identify: (1) Local Failure (> 60% area) (2) Mitigation by Major Maintenance & Rehabilitation	**Asphalt Pavement:** M3 **Concrete Pavement:** M2P Reconstruction as needed
Asphalt Pavement Treatment Codes		**Unit Cost, US $**	
M1	Major maintenance, rehabilitation	1.5 inch milling, 4 inches asphalt overlay on freeways and highways, $6.0/sq. yard on 100% area	
M2	Major, Milling and inlay	1.5 inch milling and asphalt inlay, $3.0/sq. yard on 100% area	
M3	Minor, seal coat	Asphalt slurry seal or microsurfacing, $1.5/sq. yard on 100% area	
M4	Local, minor for H - severity	Asphalt patching $2.5/sq. yard for rutted area; Crack sealing $1.5/sq. yard for cracked area	
(If both M2 and M3 are selected then use **only** M2 for freeways and highways and use **only** M3 for other types of roads)			
Concrete Pavement M, R&R Treatment Codes		**Unit Cost, US $**	
M1P	Major maintenance, rehabilitation	4 inches asphalt overlay on freeway and highway; $8.0/sq. yard on 100% area	
M2P	Concrete pavement restoration	Extensive; $7.0/sq. yard on distressed area	
M4P	Concrete pavement restoration	Local; $6.0/sq. yard on distressed area	
2. Long Term or Multi Year M,R&R Intervention Policy			
Asphalt Pavement Intervention Criteria Based on Longitudinal Roughness		M2 if IRI equals or exceeds 5.2 m/km	
Concrete Pavement Intervention Criteria		M1P if PSR equals or < 2.0	

7.3 Concluding Remarks

The developed condition deterioration models for concrete highway pavement present a significant improvement on the models currently used in the mechanistic-empirical pavement design method. It is recommended to implement the pavement condition deterioration model developed in this research for life-cycle asset management and M&R programs.

CHAPTER VIII: SUMMARY, CONCLUSIONS, AND RECOMMENDATIONS

8.1 Summary

Road and highway infrastructures performance in any country is impacted by load repetitions and it is further compromised by climate attributes and extreme weather events. Damages to roads and bridges are among the infrastructure failures that have occurred during these extreme events. A disruption in any one system affects the performance of others. For example, damages in road and bridge infrastructure will delay the recovery operation after a disaster. The model predictions of the climate attributes can be used to understand and assess the future climate change in different climate zones worldwide. This understanding of climate changes and future predictions of climate attributes will help to develop climate adaptation strategies and better prepare the communities for extreme weather-related natural disaster occurrences.

The importance of considering maintenance and rehabilitation action in the condition deterioration model was never considered. This research considered the maintenance and rehabilitation history in the development and implementation of pavement condition deterioration models. The development of the IRI prediction model considered the LTPP climatic regions, pavement structural properties, and traffic. The developed models are more objective, incorporate important input variables that are easily available and easy to implement in decision making. The concrete highway pavement IRI deterioration prediction models were developed and evaluated in this research for LTPP datasets of 1,482 for JPCP, 577 for JRCP, and 575 for CRCP. Comparatively, the AASHTO MEPDG performance equations were developed using fewer test sections.

8.2 Conclusions

8.2.1 Review and Enhancement of Climate Attributes Models

Several climate attribute models were developed in this research. The key concluding remarks for these models are discussed below:

- The best model found for sea surface temperature (SST) is the seasonal ARIMA model (24,0,0) (24,0,36). The model successfully predicted the 2018-2019 El Niño year. The model prediction shows that the next El Niño years will be 2021-22 and 2025-26. The model prediction also shows that the next La Niña year will be 2028-29.
- The best model found for global mean sea level (GMSL) is the seasonal ARIMA model (12,0,0) (12,0,24). The predicted annual rate of change in GMSL is 0.6 mm/year from 2013 to 2050. But a higher annual rate of change (1.4 mm/year) is predicted from 2031 to 2050.
- The best model found for northern hemisphere sea ice extent and southern hemisphere sea ice extent is the seasonal ARIMA model (1,0,18) (1,0,24) and (12,0,18) (12,0,24), respectively. The model prediction shows that the total loss of northern hemisphere sea ice extent in 2050 will be 1.66 million km^2. But the total gain of southern hemisphere sea ice extent will be 1.24

million km^2. The net change of global sea ice extent will be -0.24 million km^2, which indicates a loss of sea ice.

8.2.2 Development of Condition Deterioration Progression Models for Concrete Pavements

Three performance models were developed for three different concrete pavement types. The key conclusions from all three models are summarized below:

- The hypothesis testing in this study confirmed that IRI outside wheel path has significantly higher values than IRI inside wheel path. Therefore, the ANN and MLR models were developed for IRI outside wheel path.
- The climatological variables have a strong linear association with climatic regions. The climatological variables also need to be predicted before using in the prediction models for future IRI predictions. Hence, climatological variables were not used in the model development.
- The exclusion of categorical variable season helped to develop a better ANN performance model for JPCP. Hence, the categorical variable season was not used in the development of JRCP and CRCP performance models.
- The hypothesis testing in this study demonstrated that it is imperative to use the maintenance and rehabilitation history of the pavement in the development of the IRI prediction model. An in-depth study of M&R history collected from the LTPP database for all concrete pavement produced several CN_Code. The best model was found with the CN_Code developed based on the IRI value improvement and the type of M&R action provided in

Table 27 and this variable is a continuous variable where number increment indicates the frequency of M&R action provided in the pavement section.

- The ANN models show better accuracy in predicting pavement performance compare to the multiple regression models for all types of concrete pavement.
- The developed IRI prediction models can successfully characterize the behavior (i.e. the increase of IRI values with time and decrease of IRI value after maintenance and rehabilitation). The ANN models can be used to provide future M&R action by changing CN_Code frequency and the model successfully distinguishes the behavior of IRI (i.e. decrease of IRI after M&R action and increase of IRI with time as CESAL increases).

The results of JPCP performance models are discussed below:

- The LTPP database contained 107 JPCP sections under the GPS-3 study. Most data points are from the wet, freeze and wet, non-freeze climatic regions.
- The best performing ANN model has a network structure of 13-19-1 (i.e. 13 inputs, 19 hidden nodes, and 1 output). The ANN model to predict IRI has an R^2 value of 0.94. The total data points used to develop the IRI prediction ANN model were 1,355. From Table 18, it is evident that the developed ANN model in this study has higher accuracy than the previously developed models via multiple regression and ANN models.
- The developed MLR model to predict IRI has an R^2 value of 0.49. The verification of this MLR model generated a mean difference of 1.49%, RMSE of 0.370, and MARE of 19.3%

- The ANN model shows better accuracy compared to the MLR model developed in this study. The ANN model accounted for 94% variability in the model whereas the MLR model accounted for only 49% variability.

The outcomes of JRCP performance models are summarized below:

- The LTPP database contained 49 JRCP sections under the GPS-4 study. All the pavements are in the wet, freeze and wet, non-freeze climatic regions.
- The best performing ANN model has a network structure of 11-19-1 (i.e. 11 inputs, 19 hidden nodes, and 1 output). The ANN model to predict IRI has an R^2 value of 0.95. The total data points used to develop the IRI prediction ANN model were 577.
- The developed MLR model to predict IRI has an R^2 value of 0.58. The ANN model shows better accuracy compared to the MLR model developed in this study. The ANN model accounted for 95% variability in the model whereas the MLR model accounted for only 58% variability.

The results of CRCP performance models are discussed below:

- The LTPP database contained 53 CRCP sections under the GPS-5 study. Most data points are from the wet, freeze and wet, non-freeze climatic regions.
- The best performing ANN model has a network structure of 14-19-1 (i.e. 14 inputs, 19 hidden nodes, and 1 output). The ANN model to predict IRI has an R^2 value of 0.98. The total data points used to develop the IRI prediction ANN model were 575.
- The developed MLR model to predict IRI has an R^2 value of 0.83. The ANN model shows better accuracy compared to the MLR model developed in this study. The ANN model

accounted for 98% variability in the model whereas the MLR model accounted for 83% variability.

8.3 Recommendations for Future Research

The models developed in this research have some limitations. The recommendations for future researches to overcome these limitations are discussed below:

- The climate attribute models developed in this research can be updated incorporating the latest year’s data.
- The developed ANN models for concrete highway pavements are not recommended to be used outside of their applicable ranges for extrapolation.
- All the ANN models developed in this research are static. Dynamic sequential modeling technique where predictions for the future years will be used as input to predict the next year’s value; can be developed for concrete pavements using the same LTPP database.
- These performance models can be incorporated in the life cycle cost (LCC) analysis of pavements.
- These performance models can be implemented for highway pavement asset management.

LIST OF REFERENCES

[1] Central Intelligence Agency (CIA). https://www.cia.gov/index.html Accessed 14 March 2019.

[2] Gopisetti, L. S. P. International Roughness Index Prediction of Flexible and Rigid Pavements Using Climate and Traffic Data. Ms. Thesis, Department of Civil Engineering, Bradley University, 2017.

[3] Highway Length References, US Department of Transportation, Federal Highway Administration, Policy and Governmental Affairs, Office of Highway Policy Information https://www.fhwa.dot.gov/policyinformation/statistics/2016/, Accessed May 7, 2021.

[4] Congress of the United States, Congressional Budget Office (CBO). "The Highway Trust Fund and the Treatment of Surface Transportation Programs in the Federal Budget, June 2014," http://www.cbo.gov/sites/default/files/cbofiles/attachments/45416/TransportationScoring.pdf Accessed 8 September 2015.

[5] USDOT. "Highway Trust Fund Ticker," https://www.transportation.gov/highway-trust-fund Ticker. Accessed 8 September 2015.

[6] EM-DAT. The International Disaster Database. Center for Research on the Epidemiology of Disasters - CRED. http://www.emdat.be/advanced_search/index.html. Accessed May 3, 2021.

[7] Lindsey, R.Climate Change: Global Sea Level. https://www.climate.gov/news features/understanding-climate/climate-change-global-sea-level.19 November 2019. Accessed 15

September 2019.

[8] National Ocenic and Atmoshpheric Adminstration (NOAA). Equatorial Pacific Sea Surface Temperatures. https://www.ncdc.noaa.gov/teleconnections/enso/indicators/sst/#oni Accessed 7 August 2018.

[9] Uddin, W., W.R. Hudson, Ralph Haas. Public Infrastructure Asset Management. McGraw-Hill, Inc., New York, 2013. ISBN 0071820116 ISBN-13: 978-0071820110.

[10] El-Hakim, R. A., and S. El-Badawy. "International roughness index prediction for rigid pavements: An artificial neural network application." 2013.

[11] Reynolds R, Dettinger M, Cayan D, Stephens D, Highland L, Wilson R. Effects of El Niño on streamflow, lake level, and landslide potential. U.S. Geological Survey Open file report. 1997.

[12] Wieczorek GF.Landslide triggering mechanisms. In: Turner AK, Schuster RL (eds) Landslides: investigation and mitigation: Special Report 247; Transportation Research Board, National Research Council, 1988,pp 76–90.

[13] Yu, H.T., M.I. Darter, K.D. Smith, J. Jiang and L. Khazanovich. Performance of Concrete Pavements Volume III - Improving Concrete Pavement Performance. Report No. FHWA-RD-95-111, Washington, DC: Federal Highway Administration, January.

[14] Al-Omari, B. and M.I. Darter. Relationships Between IRI and PSR. Report Number UILU-ENG-92-2013. Springfield, IL: Illinois Department of Transportation, 1992.

[15] TRB. "Development of the 2002Guide for the Design of New and Rehabilitated Pavement

Structures: Phase II.” NCHRP 01-37A, Transportation Research Board (TRB). http://apps.trb.org/cmsfeed/TRBNetProjectDisplay.asp?ProjectID=218 Accessed 9 September 2015.

[16] Naguib, Ahmed M. Sherif M. EL-Badwy, Murad H. Ibrahim. International Roughness Index Predictive Model for Rigid Pavements based on LTPP Data. ResearchGate. 2019. https://www.researchgate.net/publication/330993303 Accessed 19 February 2020.

[17] R. Abd El-Hakim, S. El-Badawy, "International Roughness Index Prediction for Rigid Pavements: An Artificial Neural Network Application", Advanced Materials Research, Vol 723, pp. 854-860, August 2013.

[18] Bayrak,M.B., Egemen Teomete and Manish Agrawal. Use of Artificial Neural Networks for Predicting Rigid Pavement Roughness, Midwest Transportation Consortium Fall Student Conference, Ames, Iowa, 19 November 2004.

[19] Mohamed Jaafar, Z. F. Computational Modeling and Simulations of Condition Deterioration to Enhance Asphalt Highway Pavement Design and Asset Management. *Ph.D. Dissertation*, Department of Civil Engineering, The University of Mississippi, Oxford, August 2019.

[20] NOAA. Climate.gov. https://www.climate.gov/maps-data/primer/climate-data-primer Accessed 13 April 2020.

[21] McCleary, R., R. A. Hay Jr. Applied Time Series Analysis for the Social Sciences. Sage Publications. Beverly Hills, California, 1980.

[22] Uddin, W., B. F. McCullough, and M. M. Crawford. Methodology for Forecasting Air Travel and Airport Expansion Needs. Transportation Research Record, Vol. 1025, pp. 9-10, 1985.

[23] IBM (2017). IBM SPSS software, IBM SPSS Statistics 25. International Business Machine.https://www.ibm.com/analytics/data-science/predictive-analytics/spss-statistical-software Accessed June 1, 2018.

[24] Sea Level Rise. Understanding the past-improving projection for the future http://www.cmar.csiro.au/sealevel/sl_data_cmar.html Accessed 22 March 2019.

[25] National Snow and Ice Data Center (NSIDC). Sea Ice and Snow Cover Extent. https://www.ncdc.noaa.gov/snow-and-ice/extent/sea-ice/N/0 Accessed 11 September 2019.

[26] Wieczorek GF. Landslide triggering mechanisms. In: Turner AK, Schuster RL (eds) Landslides: investigation and mitigation: Special Report 247; Transportation Research Board, National Research Council, 1988, pp 76–90.

[27] Remote Sensing System. Sea Surface Temperature. http://www.remss.com/measurements/sea-surface-temperature/ Accessed 28 February 2019.

[28] Remote Sensing System. TMI. http://www.remss.com/missions/tmi/ Accessed 28 February 2019.

[29] Space Science and Engineering Center. University of Wisconsin-Madison. https://www.ssec.wisc.edu/data/sst/ Accessed 28 February 2019.

[30] Remote Sensing System. GMI. http://www.remss.com/missions/gmi/ Accessed 28

February 2019.

[31] Remote Sensing System. AMSR. http://www.remss.com/missions/amsr/ Accessed 28 February 2019.

[32] Smith, Catherine A., Prashant D. Sardeshmukh. The Effect Of ENSO on The Intraseasonal Variance of Surface Temperatures in winter. Int. J. Climatol. 20: 1543–1557 (2000).

[33] Liang, I., Xiu-Qun Yang , De-Zheng Sun.The Effect of ENSO Events on the Tropical Pacific Mean Climate: Insights from an Analytical Model. Journal of Climate. Vol. 25. 2012.

[34] Sun, X., Benjamin Renard, Mark Thyer, Seth Westra, Michel Lang. A global analysis of the asymmetric effect of ENSO on extreme Precipitation. Journal of Hydrology. 530. 2015. 51–65.

[35] Moreiras, Stella M. Climatic effect of ENSO associated with landslide occurrence in the Central Andes, Mendoza Province, Argentina. Landslides. 2005. 2:53–59.

[36] Tote, C., Gerard Govers, Stijn Van Kerckhoven, Isabel Filiberto, Gert Verstraeten, and Herman Eerens. Effect of ENSO events on sediment production in a large coastal basin in northern Peru. Earth Surface Processes and Landforms. Earth Surf. Process. Landforms 36, 1776–1788. 2011.

[37] Sea Level Rise. Historical Sea Level Changes. http://www.cmar.csiro.au/sealevel/sl_hist_last_decades.html Accessed 21 March 2019.

[38] IPCC. Climate Change 2007: Impacts, Adaptation and Vulnerability. Contribution of Working Group II to the Fourth Assessment Report of the Intergovernmental Panel on Climate

Change In M. L. Parry, O. F. Canziani, J. P. Palutikof, P. J. van der Linden, & C. E. Hanson (Eds.). Cambridge: Cambridge University Press.2007.

[39] Meier, Walter N, J Scott Stewart. Assessing uncertainties in sea ice extent climate indicators. United States of America Environ. Res. Lett. 14 (2019) 035005.

[40] National Ocenic and Atmoshpheric Adminstration (NOAA). https://oceanservice.noaa.gov/facts/sea-ice-climate.html. https://oceanservice.noaa.gov/facts/sea-ice-climate.html Accessed 3 May 2021.

[41] Lin, J., J.-T. Yau, and L.H. Hsiao. Correlation analysis between international roughness index (IRI) and pavement distress by neural network. In Proc., 82nd Transportation Research Board Annual Meeting. Washington, DC. Transportation Research Board. 2003.

[42] Hossain, M. I., A.M., L. S. P. Gopisetti, S.M., and M. S. Miah. International Roughness Index Prediction of Flexible Pavements Using Neural Networks. J. Transp. Eng., Part B: Pavements, 2019, 145(1).

[43] Duckworth, P. T. Evaluation of Flexible Pavement Performance Models in Mississippi: A Neural Network Approach. *M.S. Thesis*, Department of Civil Engineering, The University of Mississippi, Oxford, August 2020.

[44] Najjar, Yacoub M., et al. “Neuronet-Based Approach to Modeling the Durability of Aggregate in Concrete Pavement Construction.” Transportation Research Record: Journal of the Transportation Research Board, vol. 1582, no. 1, 1997, pp. 29–33., doi:10.3141/1582-05.

[45] Najjar, Yacoub, and Xiaobin Zhang. “Characterizing the 3D Stress-Strain Behavior of

Sandy Soils: A Neuro-Mechanistic Approach." Numerical Methods in Geotechnical Engineering, 2000, pp. 43–57., doi:10.1061/40502(284)4.

[46] Al-masaeid, H. H. Utilizing of Magnesium Oxysulfate Binders for Additive Construction Applications. *Ph.D. Dissertation*, Department of Civil Engineering, The University of Mississippi, Oxford, December 2018.

[47] Qatu, K. M. Optimizing the Performance of Complex Engineering Systems Aided by Artificial Neural Networks. *Ph.D. Dissertation*, Department of Civil Engineering, The University of Mississippi, Oxford, December 2019.

[48] Zupan, Jure, and J. Gasteiger. Neural Networks for Chemists. Wiley-VCH, 1999.

[49] Yasarer, Hakan, and Yacoub M. Najjar. "Characterizing the Permeability of Kansas Concrete Mixes Used in PCC Pavements." International Journal of Geomechanics, vol. 14, no. 4, 2014, doi:10.1061/(asce)gm.1943-5622.0000362.

[50] Hakan Yasarer, H., Mohammad Najmush Sakib Oyan, and Yacoub Najjar. "A Performance Prediction Model for Continuously Reinforced Concrete Pavement Using Artificial Neural Network." Proceedings of the 9th International Conference on Maintenance and Rehabilitation of Pavements—Mairepav9, Lecture Notes in Civil Engineering 76, 2020, pp. 771-782., https://doi.org/10.1007/978-3-030-48679-2_72

[51] Yasarer, H. I. Characterizing the Permeability of Concrete Mixes Used in Transportation Applications: A Neuronet Approach, Master's Thesis, Kansas State University, Manhattan, KS, 2010. 105 pp.

[52] Najjar, Y. M. and Mryyan, S. “ANN-Based Profiling: Data Importance,” Intelligent Engineering Systems through Artificial Neural Networks, Vol. 19, pp. 155-162.

[53] Najjar Y. Quick Manual for the Use of ANN program TRSEQ1. Department of Civil Engineering, Kansas State University, Manhattan, Kansas, USA. 1999.

[54] Yasarer, H. and Najjar, Y. Development of a Mix-Design Based Rapid Chloride Permeability Assessment Model Using Neuronets. Proceedings of International Joint Conference on Neural Networks, San Jose, California, USA, July 31 – August 5, 2011.

[55] FHWA. About Long-Term Pavement Performance. Federal Highway Administration (FHWA), Research and Technology, 20 January 2015. cms7.fhwa.dot.gov/research/long-term-infrastructure-performance/ltpp/long-term-pavement-performance Accessed 11 October 2019.

[56] FHWA. About Long-Term Pavement Performance. Federal Highway Administration (FHWA), Research and Technology, 20 January 2015. http://www.fhwa.dot.gov/research/tfhrc/programs/infrastructure/pavements/ltpp/ Accessed 25 February 2015

[57] Pierce, L. M. and McGovern, G. NCHRP Synthesis 457, Implementation of the AASHTO Mechanistic Empirical Pavement Design Guide and Software - A Synthesis of Highway Practice. 2014.

[58] Sayers, M. W., Gillespie, T. D., Queiroz, Cesar A.V., The International Road Roughness Experiment (IRRE): establishing correlation and a calibration standard for measurements (English). World Bank technical paper ; no. WTP 45. Washington, DC, The World Bank,1986.

[59] ACAP. Jointed Plain Concrete Pavement (JPCP). http://wikipave.org/index.php?title=Jointed_Plain_Concrete_Pavement_(JPCP) Accessed 3 May 2021.

[60] Oh, Han Jin, Jun Young Park, Hyung Bae Kim, Won Kyong Jung, and Jung Hun Lee. Performance Evaluation of JPCP with Changes of Pavement Mix Design Using Pavement Management Data. Advances in Civil Engineering. Volume 2019, Article ID 8763679, 10 Pages.https://doi.org/ 10.1155/2019/8763679.

[61] Zhizhong, Z., and GUO Zhongyin. Prediction of Asphalt Pavement International Roughness Index (IRI) By Combined Approach of Empirical Regression and Markov. ASCE. 2013.

[62] Wang, Kelvin C.P. and Qiang Li. Pavement Smoothness Prediction Based on Fuzzy and Gray Theories. Computer-Aided Civil and Infrastructure Engineering 26 (2011) 69–76.

[63] Naguib, Ahmed M., Sherif M. EL-Badwy, and Murad H. Ibrahim. International Roughness Index Predictive Model for Rigid Pavements based on LTPP Data. ResearchGate. 2019. https://www. researchgate.net/publication/330993303 Accessed 19 February 2020.

[64] Rahman, M., M. Majbah Uddin, and Sarah L. Gassman. Pavement Performance Evaluation Models for South Carolina. KSCE Journal of Civil Engineering (2017) 21(7):2695-2706. DOI 10.1007/s12205-017-0544-7.

[65] Attoh-Okine, N. O. Predicting Roughness Progression in Flexible Pavements Using Artificial Neural Networks. In Proc., 3rd Int. Conf. on Managing Pavements. Washington, DC. Transportation Research Board. 1994.

[66] Lin, J., J.-T. Yau, and L.H. Hsiao. Correlation analysis between international roughness index (IRI) and pavement distress by neural network. In Proc., 82nd Transportation Research Board Annual Meeting. Washington, DC. Transportation Research Board. 2003.

[67] Mazari, M., and D. D. Rodriguez. "Prediction of Pavement Roughness Using A Hybrid Gene Expression Programming-Neural Network Technique." J. Traffic Transp. Eng. 3 (5): 448-455. 2016. https://doi.org/10.1016/j.jtte.2016.09.007.

[68] Ziari, H., J. Sobhani, J. Ayoubinejad, and T. Hartmann. 2016. "Prediction of IRI In Short and Long Terms for Flexible Pavements: ANN and GMDH Methods." Int. J. Pavement Eng. 17 (9): 776–788. https://doi.org/10.1080/10298436.2015.1019498.

[69] Georgiou, P., Christina Plati, and Andreas Loizos. Soft Computing Models to Predict Pavement Roughness: A Comparative Study. Advances in Civil Engineering. Volume 2018, Article ID 5939806, 8 pages. https://doi.org/10.1155/2018/5939806.

[70] Hossain, M., Gopisetti, L.S.P. & Miah, M.S. Artificial Neural Network Modelling to Predict International Roughness Index of Rigid Pavements. *Int. J. Pavement Res. Technol.* **13,** 229–239 (2020). https://doi.org/10.1007/s42947-020-0178-x

[71] FHWA. Long Term Pavement Performance (LTPP) Info Pave: Data. LTPPInfoPaveTM. U.S. Department of Transportation Federal Highway Administration (FHWA). https://infopave. fhwa.dot.gov/Data/DataSelection Accessed 11 November 2019.

[72] AASHTO. "Mechanistic-Empirical Pavement Design Guide, Interim Edition: A Manual of Practice," American Association of State and Highway Transportation Officials, Washington, DC, 2008.

[73] Mohamed Jaafar, Z. F., and Uddin. W. “Modeling of Pavement Roughness Performance Using the LTPP Database for Southern Region in the U.S.” Proc., 6th International Conference Bituminous Mixtures and Pavements, Thessaloniki, Greece, 2015, pp. 714-722.

[74] FHWA. Long-Term Pavement Performance. Information Management System User Guide. U.S. Department of Transportation. Federal Highway Administration. FHWA-RD-03-088 (Final). June 2019.

[75] Uddin, W. 2020. CE570-Infrustructure Management. Course Lecture Notebook, University of Mississippi, August 2020.

[76] ACAP. Jointed Reinforced Concrete Pavement (JRCP). http://wikipave.org/index.php?title=Jointed_Reinforced_Concrete_Pavement_(JRCP) Accessed 3 May 2021.

[77] Yu, H.T., M.I. Darter, K.D. Smith, J. Jiang and L. Khazanovich. Performance of Concrete Pavements Volume III - Improving Concrete Pavement Performance. Report No. FHWA-RD-95-111, Washington, DC: Federal Highway Administration, January 1998.

[78] ACAP. Continuously Reinforced Concrete Pavement (CRCP). http://wikipave.org/index.php?title=Continuously_Reinforced_Concrete_Pavement_(CRCP) Accessed 3 May 2021.

[79] Johnston, D. P. and Roger W. Surdahl. Effects of Base Type on Modeling Long-Term Pavement Performance of Continuously Reinforced Concrete Sections. Transportation Research Record: Journal of the Transportation Research Board, No. 1979, Transportation Research Board of the National Academies, Washington, D.C., 2006, pp. 93–101.

[80] Gharaibeh, N. G., M. I. Darter, and L. B. Heckel. Field Performance of Continuously Reinforced Concrete Pavement in Illinois. Transportation Research Record: Journal of the Transportation Research Board, No. 1684, Transportation Research Board of the National Academies, Washington, D.C., 1999, pp. 44-50.

[81] GASB. 2000. About Guide to Implementation of GASB Statement 34 on Basic Financial Statements and Management's Discussion and Analysis for State and Local Governments: Questions and Answers. Governmental Accounting Standards Board (GASB) of the Financial Accounting Foundation, Norwalk, CT. Library of Congress Card Number: 00-132271, ISBN 0-910065-84-5.

APPENDIX

Appendix A Step-by-Step Procedure to Diagnose Terms for ARIMA Time Series Modeling

THE UNIVERSITY OF MISSISSIPPI
DEPARTMENT OF CIVIL ENGINEERING
CENTER FOR ADVANCED INFRASTRUCTURE TECHNOLOGY

TECHNICAL MEMORANDUM

TECH MEMO: TM-SS-3 **PROJECT:** ARIMA Time Series Modeling

TO: W. Uddin, Project Director **DATE:** September 9, 2019 **REV:** December 11, 2019

AUTHOR: Salma Sultana, PhD Graduate Research Assistant

SUBJECT: Step-by-Step Procedure to Diagnose Terms for ARIMA Time Series Modeling

ARIMA Modeling for Highly Autocorrelated Cyclic Seasonal Time Series Data

Use the following step-by-step procedure to diagnose appropriate terms for Auto Regressive Integrated Moving Average (ARIMA) modeling [1, 2].

1. Plot time series, x (year or month) y (observation) with marker (symbol) and connecting lines, as shown in Figure A for global natural disaster time series. The requirement for minimum data points is preferably 50 for ARIMA modeling.

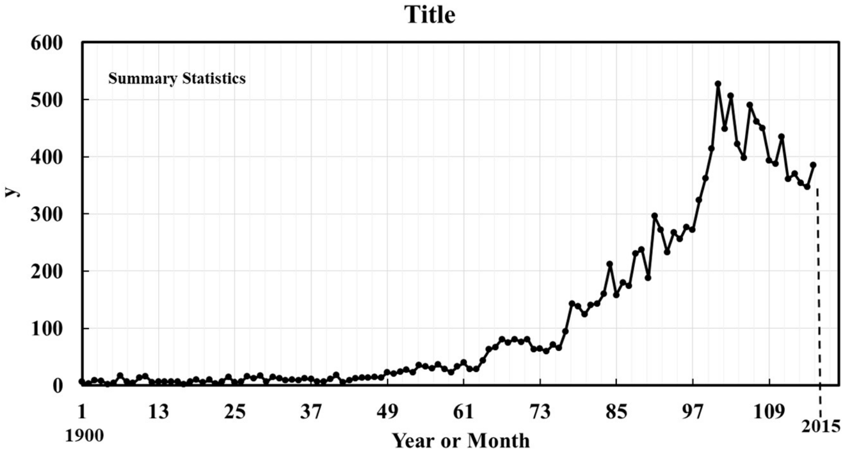

Figure A. Time series plot of annual global natural disasters

2. Conduct Normality test (Kolmogorov-Smirnov and Shapiro-Wilk). If it is significant and fails the Normality test then regression model is invalid and ARIMA modeling is preferred.

3. Calculate autocorrelation R at Lag-1. (High R ≥ 0.4 means serial correlation; therefore, regression model and linear trend line are invalid.) The SPSS statistical software [3] includes an option to create Autocorrelation (ACF) plot and Partial Autocorrelation (PACF) plot up to 60 lags or more. The command is: **Analysis** > **Forecasting** > **Autocorrelation.**

In the case of global disaster time series data, the data has decaying ACF and spiking PACF (Figure A1).

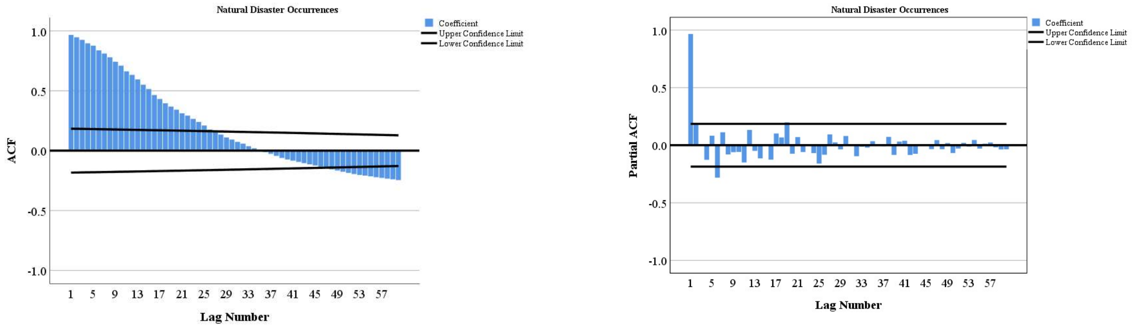

Figure A1. ACF and PACF plot

4. Study the time series plot (Figure A) to identify trend and seasonality pattern in the data.

5. If trend and seasonality are present, as shown in Figure A then calculate R-values for differencing order-1 and moving average (2,3,4,6,9,12…..) in an Excel table.

5a. Plot order-1 differencing (d) time series (y_1-y_2) and calculate correlation R-value with the original time series. Figure B shows differencing order-1. If the differencing series does not increase or decline with time, then it implies linear trend can be removed by differencing.

If R-value of differencing series with the original time series is generally equal or less than 0.2, the series can be made stationary by differencing. Use d = 1and d = 2 if appropriate. In that case run ACF and PACF plots using differencing series to select ARIMA terms.

If differencing R-value with the original time series is more than 0.2, don't use differencing operator (d). Use d = 0.

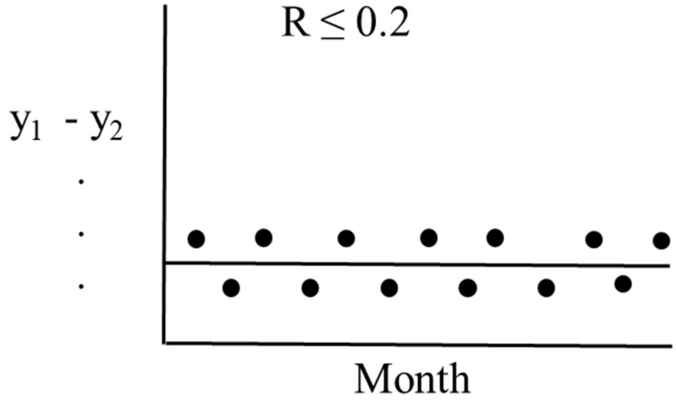

Figure B. Differencing-1 plot

5b. Identify high R-values for moving average (MA) terms (Step 5) to select appropriate MA term (q order). It is advised not to use q order 1.

6. Select (p,0,q) terms if differencing is not used where p is the order of Autoregressive (AR) term , 0 for no differencing, and q order of MA term.

If differencing order-d is applicable then select (p,d,q) terms.

7. Use the following diagnosis steps to select the initial ARIMA model for appropriate order of AR,d,MA terms (p,d,q):

7a. Rule for selecting differencing order-d is explained in Step 5a.

7b. Rules to interpret ACF and PACF of the original time series output for selecting p,q and seasonal terms are, as follows:

1. AR Process (p, d, 0): Decaying ACF and spiking PACF (p non-zero spike from PACF plot). Select AR term p by number of spike(s) with high R-value in PACF plot. Figure C shows an example of the AR process (p,0,0) without differencing ($d = 0$).

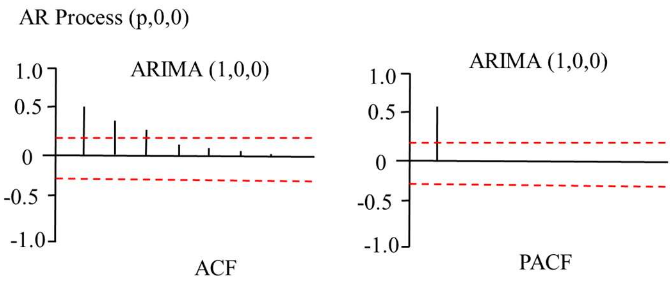

Figure C. AR Process (p,0,0)

2. MA Process (0, d, q): Spiking ACF and decaying PACF (q non-zero spike from ACF plot). Identify MA term q with high R-value (Steps 5, 5b). Figure D shows an example of the MA process (0,0,q) without differencing (d = 0).

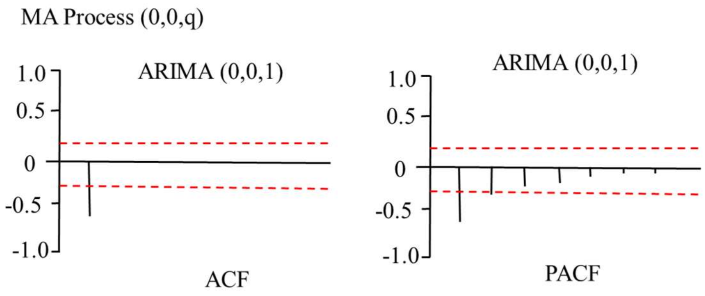

Figure D. MA Process (0,0, q)

3. AR, d, MA process (p, d, q): Both ACF and PACF decaying. Select AR term p by number of spike(s) with high R-value in PACF plot. Identify MA term q with high R-value (Steps 5, 5b). Figure E shows an example process (p,0,q) without differencing (d = 0).

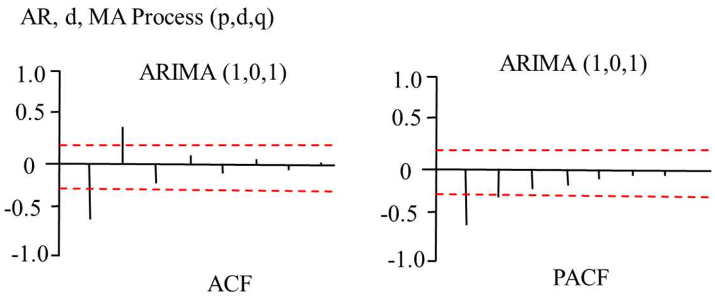

Figure E. AR, d, MA Process (p,0,q)

8. Select P and Q seasonal model terms for seasonal ARIMA model.

8a. Use PACF plot to determine the term of P (use the selected p for P).

8b. Use d as used in the ARIMA model terms.

8c. Use ACF plot to determine the term of seasonal Q.

Additionally, look at R in combined Excel table created in steps 5 for Q, using the MA term with the highest value.

9. Analyze ARIMA model.

The SPSS command is: **Analyze > Forecasting > Create Traditional Models.**

9a. Use reasonable forecast number of years, which should be lesser than the total years of the historical time series data. For example, forecasts up to future years 2030 and/or 2050 can be used for modeling of climate attribute time series data up to the previous years.

10. Conduct diagnostic evaluation.

10a. Investigate and interpret residual ACF plot and residual PACF plot (Figure F), prediction of the verification year, and the predictions for the future years.

10b. If necessary, change the ARIMA model terms as appropriate. Repeat steps 10a.

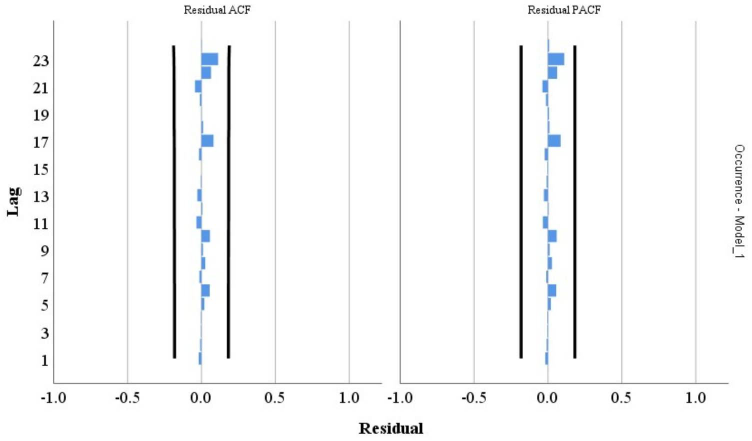

Figure F. Residual ACF and PACF

11. Continue post-diagnostics for enhancing the term of ARIMA model, as necessary for improving the results.

11a. The final ARIMA (p,0,q) model for the annual global natural disaster time series (Figure A) is (1,0,34).

11b. Note this is not a seasonal ARIMA model because of the annual time series. If monthly time series is analyzed, then the model will be seasonal ARIMA model (p,0,q) (P,0,Q).

12. The following examples illustrate writing formats for ARIMA models.

12a. Example of AR process ARIMA (1,0,0) model equation:

$Y_t = C + (1 - \phi_1 B) * a_t$

Y_t = Data time series (Dependent or response variables)

C = Constant

$1 - \phi_1 B$ = Regular Autoregressive process of order one

a_t = random shock term; normally distributed, independent with zero mean, and variance equal to σ_a

12b. Example of MA process ARIMA (0,1,3) model equation:

$\nabla^1 * Y_t = C + (1 - \theta_1 B - \theta_2 B^2 - \theta_3 B^3) * a_t$

Y_t = Data time series (Dependent or response variables)

∇^1 = Regular Differencing operator of order one

C = Constant

$1 - \theta_1 B - \theta_2 B^2 - \theta_3 B^3$ = Regular Moving Average process of order three

a_t = random shock term; normally distributed, independent with zero mean, and variance equal to σ_a

12c. Example of **(**AR, d, MA) process ARIMA (1,1,3) model equation:

$\nabla^1 * Y_t = C + (1 - \phi_1 B) * (1 - \theta_1 B - \theta_2 B^2 - \theta_3 B^3) * a_t$

Y_t = Data time series (Dependent or response variables)

∇^1 = Regular Differencing operator of order one

C = Constant

$1 - \phi_1 B$ = Regular Autoregressive process of order one

$1 - \theta_1 B - \theta_2 B^2 - \theta_3 B^3$ = Regular Moving Average process of order three

a_t = random shock term; normally distributed, independent with zero mean, and variance equal to σ_a

Concluding Remarks:

The above step-by-step procedure (steps 1 to 12) should be followed for identifying appropriate ARIMA model terms for the data time series.

Acknowledgements:

The procedure described in this tech memorandum was conducted at the Center for Advanced Infrastructure Technology (CAIT) at the University of Mississippi. Thanks are due to doctoral student Rulian Barros for assistance.

References:

[1] McCleary, Richard (1982). *Applied time series analysis for the social sciences*. SAGE Publications, Inc., Beverly Hills, California.

[2] Box, George E. P. (1994). *Time series analysis: forecasting and control*. Englewood Cliffs, N.J.: Prentice Hall, 1994.

[3] IBM (2017). IBM SPSS software, IBM SPSS Statistics 25. International Business Machine. https://www.ibm.com/analytics/data-science/predictive-analytics/spss-statistical-software Accessed June 1, 2018.

VITA

Salma Sultana was born June 26, 1992, in Lakshmipur, Bangladesh. Salma received her bachelor’s degree in Civil Engineering from Bangladesh University of Engineering and Technology (BUET) in 2015. After obtaining her bachelor’s degree, she started working as a research assistant at the Bureau of Research, Testing, and Consultancy (BRTC) in a project about updating pavement design guidelines for the Local Government Engineering Department (LGED). Her profound interest in pavement led her to pursue higher studies in transportation engineering. She joined as a Ph.D. student at the University of Mississippi in 2018. She worked as a research assistant under the supervision of Dr. Waheed Uddin in a project funded by the Mississippi Department of Transportation (MDOT) about vehicle detection sensors. She also worked with various climate attributes and the effect of climate on infrastructure. She worked on the application of artificial neural networks in pavement performance modeling. She has several publications in civil engineering journals and presented at the Transportation Research Board meetings. She received Gulf Region ITS (GRITS) Graduate Scholarship Award in 2018. She worked as a teaching assistant and was awarded the ‘Outstanding Teaching Assistant Award’ in 2019. She received the Fall Dissertation Fellowship award in 2020 awarded by the University of Mississippi. She is a student member of the American Society of Civil Engineers (ASCE) and Gulf Region ITS (GRITS) and is an engineer-in-training (E.I.T.) in the state of Mississippi. She aims to be a part of the research and development area of the transportation engineering sector.